A High-Resolution Study of the High-Redshift Intergalactic Medium

Thesis by
George D. Becker

In Partial Fulfillment of the Requirements
for the Degree of
Doctor of Philosophy

California Institute of Technology
Pasadena, California

2007

(Defended July 24, 2006)

For my family,
who have supported me at every step,
and for Molly,
my constant inspiration

Acknowledgements

It is a pleasure to thank some of the many people from whom I have received support, although there are far too many to be listed here. I received early support from my undergraduate advisor, Bob O'Connell, who introduced me to research and encouraged me to do my graduate work at Caltech, and from Ray Ohl, whose enthusiasm helped many in my class at UVa to pursue the sciences. While at Indiana, I was fortunate to receive additional encouragement and direction from Mike Pierce.

Nearly all of the observations presented here were performed at the Keck telescopes in Hawaii, and I am deeply indebted to the Keck staff for their patient assistance through many nights of observing. Closer to home, I am thankful to the staff in Robinson, particularly Gina Armas, Gita Patel, and Diane Fujitani for making all of the practical aspects of life at Caltech easy. I am especially grateful to our systems administration team of Patrick Shopbell, Anu Mahabal, and Cheryl Southard. Their tremendous expertise and hard work make all scientific progress in the department possible.

My thanks to Judith Mack for opening her home on many occasions - and for the flan.

It has been a great pleasure to be part of an exceptional community of grad students. Their talents are remarkable, both in astronomy and far beyond, and I have leaned a great deal from each of them. Lunches were one of the best times to reflect and relax, and I was privileged to enjoyed the regular company of David Kaplan, Dawn Erb, Micol Christopher, Jackie Kessler-Silacci, and Naveen Reddy, as well as most of the other grad students at different times.

Many thanks to my enjoyable and accommodating office mates: Anu Mahabal, Pranjal Trivedi, Edo Berger, Matt Hunt, Bryan Jacoby, Laura Hainline, and Stuartt Corder. I am also grateful to the fun and always tolerant people with whom I shared a roof: Noah Robinson, Jon Sievers, Milan Bogosavljevic, Francis O'Donovan, Jennifer Carron, Dan Stark, and Adam Krauss.

The astronomy department's soccer, basketball, and softball teams have been a welcome outlet, and I thank Mike Santos, Rob Simcoe, Micol Christopher, and Larry Weintraub for organizing these. Opportunities to make music have been indispensable, and I am grateful to the Angeles Chorale and the Caltech Thursday Jazz Band for the chance to perform with many exceptional musicians. In particular, I would like to thank Bill Bing for lending his

time and talent to lead the Caltech Bands. Bill is an invaluable resource for the Caltech community.

My thanks to Rob Simcoe for showing me the ropes of quasar absorption line research as I was beginning at Caltech. I am also grateful to Michael Rauch, who has been a great source of encouragement and a reliable sounding board. I have greatly enjoyed the trips with Michael to observe in Chile, even if we had to spend hours deciding who would go first down the mountain.

Finally, I could not have asked for a better thesis advisor than Wal Sargent. Wal possesses an astounding wealth of knowledge, astronomical and otherwise, and I have greatly enjoyed our many conversations. I have been particularly pleased to share with Wal a love of music. On observing runs, we seemed to agree the most on Baroque composers, but could also entertain a rare moment of jazz (when he was willing). Dinners at Merriman's were always a favorite (thanks, Ira). Most importantly, though, Wal provided me with every opportunity to do good science, and allowed me to find my own way with only a gentle nudge here and there. To be "team" is to have a great Coach.

Abstract

We measure the spatial coherence of filamentary structures in the intergalactic medium (IGM) at $z \sim 4$. The transmitted flux in the Lyα forest is significantly cross-correlated in the spectra of two pairs of QSOs at $z \sim 4$ with angular separation $\Delta\theta \sim 30''$. This strongly suggests that some fraction of the absorbing structures span the ~ 1 comoving Mpc separation between paired sightlines.

We further present measurements of the ionization state of the high-redshift IGM using three approaches: a search for low-ionization metal lines at $z > 5$, a study of the evolution of Lyα optical depths over $2 \lesssim z \lesssim 6$, and a measurement of the UV background at $4 \lesssim z \lesssim 5$ using the quasar proximity effect. We identify six O I systems in the HIRES spectra of nine QSOs with redshifts $4.9 \leq z_{\rm QSO} \leq 6.4$. Four of these systems lie towards SDSS J1148+5251 ($z_{\rm QSO} = 6.4$). This excess at $z \sim 6$, however, is unlikely to indicate a significantly neutral IGM suggestive of the end of reionization, since the O I falls over a redshift interval that also shows transmission in Lyα and Lyβ. In contrast, we find no O I towards SDSS J1030+0524 ($z_{\rm QSO} = 6.30$), whose spectrum shows a broad Gunn-Peterson trough. That sightline must also be highly ionized, therefore, or else chemically pristine. The relative abundances of O, Si, and C in the systems we detect are consistent with enrichment from Type II supernovae, with an upper limit of 30% on the amount of metals contributed by supermassive stars.

We examine the evolution of Lyα optical depth using the transmitted flux probability distribution function (PDF) in the spectra of 63 QSOs spanning absorption redshifts $1.7 < z < 5.8$ to predictions from two theoretical τ distributions. For an isothermal IGM and a uniform UV background, the optical depth distribution computed from a density model that has been used to make claims of late reionization produces poor fits to the observed flux PDF unless significant corrections to the QSO continua are applied. In contrast, a lognormal τ distribution fits the data at all redshifts with only minor changes in the continua. A simple linear fit to the redshift evolution of the lognormal parameters at $z < 5.4$ reproduces the observed mean Lyα and Lyβ transmitted fluxes over $1.6 < z < 6.2$. Assuming the density field, temperature, and UV background vary slowly at $z < 5$, this suggests that no sudden change in the IGM due to late reionization is necessary to explain the lack of transmitted flux at $z \gtrsim 6$.

Finally, we measure the metagalactic UV background at $4 \lesssim z \lesssim 5$ using the quasar proximity effect in a sample of 16 QSOs. Accurate redshifts were obtained from Mg II emission lines, supplemented by estimates from the start of the Lyα forest and CO emission. We use a new method for directly estimating the size of a QSO's proximity region based on the observed transmitted flux distribution. The relative sizes of the proximity regions are consistent with the expected trend in QSO luminosity, although the proximity regions around faint QSOs may be disproportionately small. Our estimate of the background H I ionization rate, $\Gamma^{\rm bg} = (1.4^{+1.6}_{-0.7}) \times 10^{-12}\ {\rm s}^{-1}$, is consistent with no evolution from $z \gtrsim 2$ based on other measurements using the proximity effect, the mean opacity of the Lyα forest, and the integrated ionizing output of star-forming galaxies and QSOs.

Contents

1 Introduction 1

1.1 Overview 1

1.2 Scientific Background 2

1.2.1 The Metagalactic Ionizing Background 3

1.2.2 Reionization 5

1.3 Thesis Outline 6

2 Large-Scale Correlations in the Lyα Forest at $z = 3 - 4$ 10

2.1 Introduction 11

2.2 The Data 13

2.3 Comparison of Sightlines 18

2.3.1 Correlation Functions 18

2.3.2 Flux Distributions 21

2.4 Effects of Photon Noise and Instrumental Resolution 25

2.5 Metal Systems 31

2.5.1 Q1424+2255 31

2.5.2 Q1439−0034A & B 33

2.6 Conclusions 36

3 Discovery of excess O I absorption towards the $z = 6.42$ QSO SDSS J1148+5251 41

3.1 Introduction 42

3.2 The Data 43

3.3 O I Search 45

3.3.1 Technique 45

3.4 Overabundance of O I systems towards SDSS J1148+5251 56
  3.4.1 Comparison with Lower-Redshift Sightlines 60
  3.4.2 Comparison with Damped Lyα and Lyman Limit System Populations 61
3.5 Metal Abundances 62
3.6 Discussion 67
3.7 Summary 70

4 The Evolution of Optical Depth in the Lyα Forest: Evidence Against Reionization at $z \sim 6$ 72
4.1 Introduction 73
4.2 The Data 75
4.3 Flux Probability Distribution Functions 79
  4.3.1 Observed PDFs 79
  4.3.2 Theoretical PDFs 80
  4.3.3 Fitting the observed PDFs 83
4.4 Redshift Evolution of Optical Depth 92
  4.4.1 Lognormal Parameters 92
  4.4.2 Mean transmitted flux 96
  4.4.3 UV background 102
4.5 An inverse temperature-density relation? 104
4.6 Conclusions 105

5 The Metagalactic UV Background at $z = 4-5$ Measured Using the Quasar Proximity Effect 120
5.1 Introduction 121
5.2 The Data 124
  5.2.1 Optical Spectra 124
  5.2.2 IR Spectra 124
  5.2.3 Redshifts 126
  5.2.4 QSO Luminosities 130
5.3 Proximity Effect Model 136
  5.3.1 Transmitted Flux Distribution 137

5.3.2 Maximum Likelihood Method 138

5.4 Results 140

5.4.1 Maximum Likelihood Estimates of $\Gamma^{\rm bg}$ 140

5.4.2 Luminosity Dependence of Proximity Region Size 141

5.4.3 Median Transmitted Flux 142

5.5 Comparison with Previous Results 147

5.6 Conclusions 148

6 Epilogue **152**

Bibliography **154**

List of Figures

1.1 The HIRES high-z sample 8

2.1 Keck/ESI spectra of Q1422+2309 and Q1422+2255 15
2.2 Keck/ESI spectra of Q1439−0034A and Q1439−0034B 15
2.3 Lyα forest in Q1422+2309 and Q1422+2255 17
2.4 Lyα forest in Q1439−0034A and Q1439−0034B 17
2.5 Flux correlation functions 20
2.6 Distribution of pixel fluxes in Q1422+2309 and Q1422+2255 23
2.7 Distribution of pixel fluxes in Q1439−0034A and Q1439−0034B 24
2.8 Effects of noise on the autocorrelation function 27
2.9 Effects of resolution on the autocorrelation function 28
2.10 Relative effects of resolution on the auto- and cross-correlation functions . 30
2.11 The $z \approx 3.1$ C IV systems in Q1422+2309 and Q1422+2255 34
2.12 The $z \approx 3.4$ C IV systems in Q1439−0034B 35
2.13 The $z \approx 1.7$ Mg II systems in Q1439−0034A and Q1439−0034B 38

3.1 The $z = 5.3364$ O I system in SDSS J0231−0728 49
3.2 The $z = 5.8408$ O I system in SDSS J1623+3112 51
3.3 The $z = 6.0097$ O I system in SDSS J1148+5251 52
3.4 The $z = 6.1293$ O I system in SDSS J1148+5251 53
3.5 The $z = 6.1968$ O I system in SDSS J1148+5251 54
3.6 The $z = 6.2555$ O I system in SDSS J1148+5251 55
3.7 Sensitivity curves for O I detection 58
3.8 Effective O I absorption pathlength interval 59
3.9 Relative metal abundances in O I systems 64

3.10 Upper limit on $N_{\rm H\,I}$ for the $z = 5.3364$ O I systems in SDSS J0231−0728 . 66

3.11 Upper limit on $N_{\rm H\,I}$ for the $z = 6.0097$ O I systems in SDSS J1148+5251 . 66

4.1 Fits to the Lyα flux PDFs at $4.254 \leq \langle z \rangle \leq 5.614$ 85

4.2 Fits to the Lyα flux PDFs at $3.126 \leq \langle z \rangle \leq 4.234$ 86

4.3 Fits to the Lyα flux PDFs at $2.652 \leq \langle z \rangle \leq 3.061$ 87

4.4 Fits to the Lyα flux PDFs at $2.374 \leq \langle z \rangle \leq 2.643$ 88

4.5 Fits to the Lyα flux PDFs at $1.797 \leq \langle z \rangle \leq 2.370$ 89

4.6 Reduced χ^2 values for PDF fits: continuum and zero point fixed 90

4.7 Reduced χ^2 values for PDF fits: continuum and zero point allowed to vary 91

4.8 Continuum adjustments for PDF fits as a function of redshift 93

4.9 Examples of continuum adjustments overlaid on spectra 94

4.10 Lognormal τ distribution parameters 95

4.11 Redshift evolution of theoretical τ and flux distributions 97

4.12 Evolution of $\tau^{\alpha}_{\rm eff}$ over $3 \leq z \leq 6.2$ (linear) 99

4.13 Evolution of $\tau^{\alpha}_{\rm eff}$ over $1.6 \leq z \leq 6.2$ (logarithmic) 100

4.14 Evolution of $\tau^{\beta}_{\rm eff}$ over $3 \leq z \leq 6.2$ (linear) 101

4.15 H I ionization rates determined from flux PDFs 103

4.16 Example fits to Lyα flux PDFs using a non-isothermal MHR00 model . . . 106

5.1 NIRSPEC H-band spectra of QSO Mg II emission lines 128

5.2 Proximity regions in QSO with $1^{\rm h} < {\rm RA} < 3^{\rm h}$ 131

5.3 Proximity regions in QSO with $3^{\rm h} < {\rm RA} < 8^{\rm h}$ 132

5.4 Proximity regions in QSO with $8^{\rm h} < {\rm RA} < 11^{\rm h}$ 133

5.5 Proximity regions in QSO with $12^{\rm h} < {\rm RA} < 23^{\rm h}$ 134

5.6 Theoretical flux PDFs in a QSO proximity region 139

5.7 Proximity region size as a function of QSO luminosity 144

5.8 Median flux in QSO proximity regions 146

5.9 Measurements of $\Gamma^{\rm bg}$ at $2 \lesssim z \lesssim 5$ 149

List of Tables

2.1 Summary of QSO Pairs Observations 14
2.2 Lyα Forest Cross-Correlation Values 21
2.3 Q1424+2255 Metal Systems 32
2.4 Q1439$-$0034A Metal Systems 36
2.5 Q1439$-$0034B Metal Systems 37

3.1 Summary of Observations for O I Search 44
3.2 Measured Properties of O I Systems 46
3.2 Measured Properties of O I Systems 47
3.2 Measured Properties of O I Systems 48
3.3 Abundance Measurements 63
3.4 Comoving Mass Densities 67

4.1 Fitted Lyα Forest Regions 76
4.1 Fitted Lyα Forest Regions 77
4.1 Fitted Lyα Forest Regions 78
4.2 Best-Fit MHR00 Model Parameters (Isothermal) 108
4.2 Best-Fit MHR00 Model Parameters (Isothermal) 109
4.2 Best-Fit MHR00 Model Parameters (Isothermal) 110
4.2 Best-Fit MHR00 Model Parameters (Isothermal) 111
4.3 Best-Fit Lognormal Parameters 112
4.3 Best-Fit Lognormal Parameters 113
4.3 Best-Fit Lognormal Parameters 114
4.3 Best-Fit Lognormal Parameters 115
4.4 Best-Fit MHR00 Model Parameters (Non-Isothermal) 116

4.4 Best-Fit MHR00 Model Parameters (Non-Isothermal) 117
4.4 Best-Fit MHR00 Model Parameters (Non-Isothermal) 118
4.4 Best-Fit MHR00 Model Parameters (Non-Isothermal) 119

5.1 Summary of Proximity Effect Observations 125
5.2 QSO Redshifts 127
5.3 QSO Continuum Properties 135
5.4 UV Background Measurements 141
5.5 Individual Proximity Region Estimates 143

Chapter 1

Introduction

1.1 Overview

The past two decades have witnessed tremendous advances in the study of the high-redshift intergalactic medium (IGM). Sky surveys have made the detection of quasars out to $z \sim 6$ nearly routine. At the same time, numerical simulations of large-scale structure are able to reproduce many of the observed properties of quasar absorption lines, particularly the complex patter of H I absorption known as the Lyα forest. This concordance between observations and simulations has secured the "cosmic web", a self-gravitating network of filaments, sheets, and voids, as the standard model for the IGM. The scaffolding for the web is provided by dark matter, whose evolution from a set of initial conditions can be realistically simulated for an assumed set of cosmological parameters, given the limits set by the resolution and size of the simulation box. Baryons will tend to follow the dark matter, but are further subject to hydrodynamics, ionization, heating, and other complicating factors such as chemical and mechanical feedback from galaxies. Many properties of the IGM are therefore difficult to determine from first principles and must be constrained observationally. These include the size of absorbing structures, the intensity of the ionizing radiation field, and the composition and distribution of heavy elements. Perhaps the largest unknowns concern the timing and mechanisms of cosmic reionization. The fact that Lyα photons reach us from quasars out to $z \sim 6$ implies that the hydrogen in the IGM was already ionized by that epoch, but how much further back reionization occurred and what sources were responsible remain contentious issues. Ultimately, placing clear constraints on reionization will allow us to better understand the nature of the first luminous sources.

This work aims to shed light on several aspects of the evolution of the high-redshift IGM using multiple unique observations of quasars at $z > 4$. In Chapter 2 (reprinted from the *Astrophysical Journal*, v. 613, p. 61, written with W. Sargent and M. Rauch), we use two widely spaced pairs of $z \sim 4$ quasars to demonstrate that absorbing structures are correlated out to at least 1 comoving Mpc. Chapters 3 and 4 utilize the first high-resolution spectra of quasars at $4.9 \leq z \leq 6.4$ to examine the evolution of the Lyα forest and metal lines at these epochs, and to test the plausibility of reionization at $z \sim 6.2$. In Chapter 3 (reprinted from the *Astrophysical Journal*, v. 640, p. 69, written with W. Sargent, M. Rauch, and R. Simcoe), we conduct a search for O I as a potential tracer of chemically enriched, neutral gas. In Chapter 4 (submitted to the *Astrophysical Journal*, written with M. Rauch and W. Sargent), we test the ability of two models for the distribution of Lyα optical depths to produce the observed transmitted flux distribution. The evolution of the optical depths is then used to explain the disappearance of transmitted flux at $z > 6$. Finally, in Chapter 5, we employ a large set of quasars with accurate Mg II redshifts to measure the intensity of the metagalactic ionizing background at $4 \lesssim z \lesssim 5$ using the quasar proximity effect.

1.2 Scientific Background

Many of the basic properties of the IGM have been established since the late 1970's and early 1980's, when sensitive detectors became available for use on 4-5m telescopes. Sargent et al. (1980) demonstrated that the numerous Lyα absorption lines seen in quasar spectra are associated with weakly clustered, low density, photoionized parcels of intergalactic gas with temperatures of $T \sim 10^4$ K. More recently, high-resolution spectrographs on 8-10m ground-based telescopes (in particular, HIRES on Keck and UVES on the VLT) have allowed the $z > 2$ Lyα forest to be studied with great sensitivity (e.g., Hu et al. 1995). Ultraviolet spectrographs on board the space-based telescopes have, meanwhile, opened up the IGM down to $z = 0$ (e.g., Penton et al. 2000). With a long baseline over which to study the evolution of the Lyα forest, statistics such as the distributions of H I column densities, the distribution of Doppler widths, and the flux power spectrum are now established out to $z \sim 5$.

During the 1980s, Lyα absorbers were primarily thought of as isolated clouds that were pressure confined by a hot intercloud medium. However, with the advent of numerical simulations capable of following the growth of large-scale structure (e.g., Cen et al. 1993), an interconnected network of dark matter and baryons formed from the gravitational collapse of density perturbations left over from the Big Bang has become the standard paradigm. The "cosmic web" (Bond & Wadsley 1997) model of the IGM has proven remarkably successful in reproducing the observed properties of the Lyα forest, such that synthetic spectra from simulations are, in many (though not all) ways, indistinguishable from real data. This agreement has been one of the great successes in the study of the high-redshift Universe.

The gravitational collapse model has been the backdrop for a number of experiments that use the IGM as a cosmic laboratory. The opacity of the forest can be used to set limits on the baryon density (Rauch et al. 1997). The temperature-density relation of the IGM can be measured from the distribution of observed line widths (Schaye et al. 2000; McDonald et al. 2001). Correlations in the Lyα forest probe density fluctuations down to scales of $\lesssim 1$ comoving Mpc. When combined with measurements out to horizon scales from the cosmic microwave background (CMB), these correlations place tight constraints on the amplitude and slope of the matter power spectrum (e.g., Spergel et al. 2003; Viel et al. 2006). The better we understand the fundamental properties and evolution of the IGM, the more reliably such tests can be performed.

1.2.1 The Metagalactic Ionizing Background

Most of the evolution of the Lyα forest can be explained by the expansion of the Universe, the gravitational collapse of large-scale structures, and the evolution of the ionizing background (e.g., Davé et al. 1999). Among these factors, the ionizing background is the most difficult to constrain theoretically, as it depends not only on the rates of star formation and quasar activity, which are highly non-linear processes, but on the fraction of ultraviolet photons that escape from ionizing sources into the IGM (e.g., Steidel et al. 2001). Much of the integrated UV output of star-forming galaxies and quasars will come from faint sources, which require deep observations to detect at high redshift (e.g., Hunt et al. 2004; Yan & Windhorst 2004). Furthermore, in a highly ionized Universe, the mean free path of ionizing photons will be set by the number density of optically thick Lyman limit systems (absorbers with H I column densities $N_{\rm H\,I} \geq 10^{17.2}$ cm^{-2}). Numerical simulations are generally not able to resolve these systems, and their incidence rate must be determined observationally.

Given these factors, independent estimates of the UV background are valuable both for determining the ionization state of the IGM and for constraining models of galaxy and quasar formation.

In principle, the intensity of the UV background can be determined from the mean level of transmitted flux in the Lyα forest. In creating artificial quasar spectra from simulations, the background level is typically 'tuned" such that the optical depths in the simulation produce transmitted flux levels that match the real data. However, the hydrogen neutral fraction, and hence the Lyα optical depth, also depends on the density and temperature of the gas. The non-linear relationship between optical depth and transmitted flux further means that the mean transmitted flux will depend on the *distribution* of optical depths (e.g., Songaila & Cowie 2002). For a given simulation, this will depend not only on the density distribution, which is sensitive to the cosmological parameters, but also on assumptions about the thermal state of the gas. It is common to assume either a uniform temperature or a simple monotonic relationship between temperature and density. Radiative transfer effects, however, may complicate the temperature distribution considerably (Bolton et al. 2004).

In order to disentangle the ionization rate from the density and temperature of the gas, independent measurements of the ionizing background must be made. At $z \approx 0$ the UV background can be estimated from the truncation of H I disks in spiral galaxies (e.g., Sunyaev 1969; Dove & Shull 1994). Ratios of metal species with different ionization potentials can be used to constrain the strength and shape of the radiation field, assuming that the species populations are set by photoionization (e.g., Songaila 1998). However, strong metal absorption systems are typically associated with galaxies. (e.g., Boksenberg et al. 2003). Their ionization state may therefore depend more on the local ionizing output of the galaxy than on a truly metagalactic background.

The quasar proximity effect offers an alternate means of measuring the ionizing background using the Lyα forest. The amount of absorption in the forest generally increases with redshift. However, near a quasar, the absorption tends to decrease. This is generally attributed to locally enhanced photoionization by the quasar itself. Knowing the luminosity of the quasar, the intensity of the UV background can be inferred by determining the distance out to which the quasar dominates the ionizing flux (e.g., Carswell et al. 1987;

Bajtlik et al. 1988). The most successful applications of the proximity effect have been at $z < 4$, where individual Lyα lines can be easily identified and large samples of quasar spectra can be used to overcome the variance in the forest (e.g., Scott et al. 2000, 2002). At higher redshifts the measurements have been more sparse. In addition, previous studies have not demonstrated that the extent of the proximity region depends correctly on the luminosity of the quasar, and hence that the values obtained for the UV background are accurate. Proximity effect measurements would be particularly valuable at $z > 4$, where the ionizing output of galaxies and quasars becomes increasingly difficult to measure directly. A consensus between galaxy/quasar counts, the mean transmitted flux in the Lyα forest, and the proximity effect would imply a genuine understanding of the ionization state of the high-redshift IGM.

1.2.2 Reionization

As pointed out by Gunn & Peterson (1965), Scheuer (1965), and Shklovskii (1965), an expanding Universe filled with neutral hydrogen would produce a tremendous Lyα optical depth ($\tau_{\mathrm{Ly}\alpha} \sim 10^5$). The fact that we observe transmitted flux in the Lyα forest, therefore, implies that the IGM must now be highly ionized. Following recombination at $z \approx 1100$, when the Universe transitioned from being predominantly ionized to being predominantly neutral, the IGM would have remained opaque to UV photons until enough luminous sources were formed that were able to reionize the vast majority of the hydrogen (and later helium). Determining when and how reionization occurred is one of the primary challenges of modern cosmology, with implications both for the nature of the first luminous sources and for the subsequent growth of small-scale structure.

Observations of the cosmic microwave background (CMB) provide an upper limit on the redshift of reionization. Thomson scattering by free electrons produces linear polarization in the CMB, which can be used to infer the total electron optical depth to the surface of last scattering. A higher τ_{e} would mean that CMB photons had encountered greater numbers of free electrons, which would require an earlier reionization. The most recent CMB measurements indicate that $\tau_{\mathrm{e}} \sim 0.09$ (Spergel et al. 2006). If reionization occurred all at once, than this would imply a reionization redshift of $z_{\mathrm{reion}} \sim 11$. A more prolonged reionization, however, could have begun much earlier ($z_{\mathrm{reion}} \gtrsim 25$).

High-redshift quasar can be used as a second probe of reionization. In the past seven years, the Sloan Digital Sky Survey has uncovered significant numbers of quasars out to $z = 6.4$ (Fan et al. 2006b, and references therein). The absence of complete Lyα absorption (so-called "Gunn-Peterson troughs") at $z < 6$ implies that the Universe was already highly ionized one billion years after the Big Bang. However, the discovery of extended absorption troughs in the spectra of the highest-redshift objects has led to claims that reionization may have ended as late as $z \sim 6$ (Djorgovski et al. 2001; Becker et al. 2001; Fan et al. 2002, 2006a). As noted above, a trace amount of neutral hydrogen is sufficient to produce a large Lyα optical depth. Therefore, the rapid evolution of transmitted flux at $z > 5.7$, rather than the mere appearance of Gunn-Peterson troughs, has been the primary evidence for reionization lasting until $z \sim 6$ (e.g., Fan et al. 2006a).

Late reionization remains strongly debated, however. Perhaps the best evidence against a significantly neutral IGM at $z \sim 6$ is the transmitted Lyα, Lyβ, and Lyγ flux seen towards the highest-redshift known quasar, SDSS J1148+5251 ($z = 6.42$) (Oh & Furlanetto 2005; White et al. 2005). In addition, no large change is seen in the luminosity function or emission line profiles of Lyα-emitting galaxies between $z \sim 5.7$ and $z \sim 6.5$ that would suggest absorption by a highly-neutral IGM at $z > 6$ (e.g., Malhotra & Rhoads 2004; Hu & Cowie 2006). Theoretically, late reionization remains a flexible issue. A combination of the clustering of ionizing sources, the uneven growth of ionized bubbles, and the inhomogeneity of the IGM can be invoked to accommodate nearly all of the current observations, either in support of or against late reionization (e.g., Wyithe & Loeb 2004a; Lidz et al. 2006b; Furlanetto et al. 2006). New types of observations are therefore needed to clarify whether dramatic changes in the IGM are occuring at $z \sim 6$.

1.3 Thesis Outline

To address these issues, we have obtained a variety of unique moderate- and high-resolution spectra of quasars at $z \gtrsim 4$. In Chapter 2, we examine ESI spectra of two sets of quasar pairs at $z \sim 4$ with angular separation $\Delta\theta \approx 30''$. We demonstrate that the transmitted flux is significantly correlated between paired sightlines, which implies that filaments in the IGM are coherent on scales of > 1 comoving Mpc. We further investigate the effects of noise and spectral resolution on the agreement between the flux autocorrelation and cross-correlation functions, a measurement that can be used to determine the cosmological constant. We conclude that spectral resolution must be carefully accounted for when making this comparison.

Much of this work utilizes a new set of HIRES spectra of 11 quasars at $4.9 \leq z \leq 6.4$ (Figure 1.1). These are the first high-resolution spectra of any quasars at $z > 4.8$, giving us an unprecedented view of the Lyα forest and metal absorption lines at these redshifts. The observations were made possible due largely to the recently upgraded detector on HIRES. Even so, many of these objects are at the sensitivity limits of current instruments, and the total sample represents over 100 hours of integration.

In Chapter 3, we use the HIRES high-z sample to search for O I absorption as a probe of neutral gas at $z > 5$. We uncover six systems, four of which lie towards our highest-redshift objects, SDSS J1148+5251 ($z = 6.42$). We demonstrate that this is a statistically significant excess, but that it is unlikely to indicate a highly-neutral IGM since this sightline also shows Lyα and Lyβ transmission over the same redshift interval as the O I. We use the lack of O I detected towards SDSS J1030+0524 ($z = 6.30$) to argue that that sightline must be highly ionized, despite the presence of an extended Gunn-Peterson trough, or else chemically pristine. We further show that the relative metal abundances in the six O I systems are consistent with enrichment from Type II supernovae, rather than hypothetical supermassive stars.

In Chapter 4, we combine our high-z sample with HIRES data for a large number of quasars at $2.0 \leq z \leq 4.7$ to study the evolution of Lyα optical depth from $z \sim 2$ to the proposed epoch of reionization. We compare the observed flux probability distribution function (PDF) to predictions from an IGM model that has been used to infer a drop in the H I ionization rate at $z \sim 6$. We find that the agreement is generally poor unless large corrections to the quasar continua are made. In constant, we show that a simple lognormal optical depth distribution provides a good fit to the observed flux PDF at all redshifts. We further show that a steady evolution in the lognormal τ distribution reproduces the evolution in the mean transmitted flux over $1.6 < z < 6.2$. We use this fact to argue that if the evolution of transmitted flux at $z < 5$ reflects slowly-varying conditions in the IGM, then the evolution at $z > 6$ should not require any abrupt change that could be attributed to late reionization.

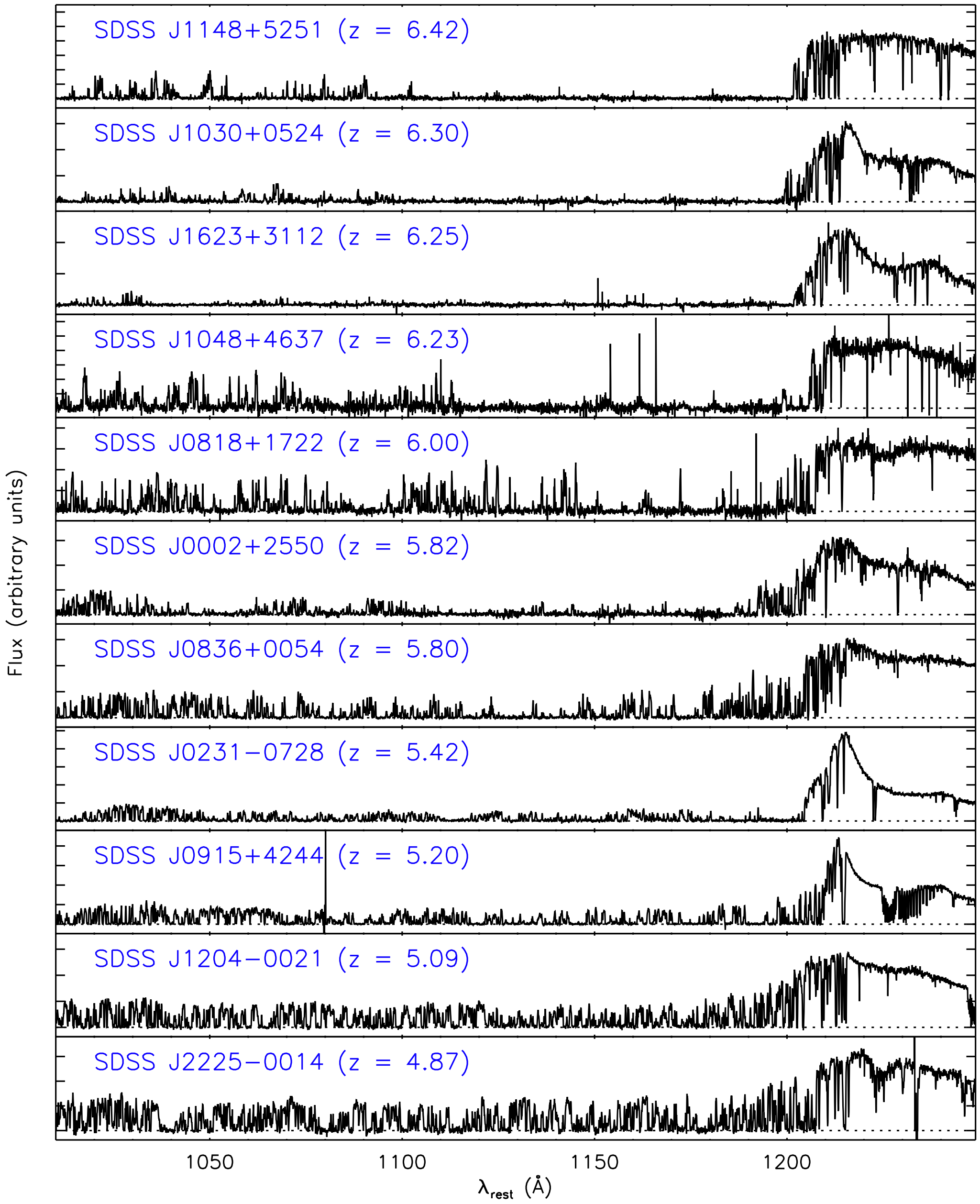

Figure 1.1 The HIRES high-z sample. Spectra are plotted as a function of rest wavelength. The Lyα forest extends blueward of the Lyα emission line at 1216 Å. Metal lines can be seen reward of Lyα.

In Chapter 5, we use the quasar proximity effect to measure the UV background at $4 \lesssim z \lesssim 5$. These are the first proximity effect measurements at $z > 4$ using a large number of quasars. We measure accurate systemic redshifts using infrared spectra of Mg II emission lines. In order to deal with line blending in the Lyα forest at $z > 4$, we present a new method for determining the size of a quasar's proximity region based on the distribution of transmitted fluxes near the quasar redshift. We also test the photoionization model of the proximity effect by comparing the proximity regions sizes of quasars with different luminosities. We find that proximity region size has roughly the correct dependence on quasar luminosity, but with a large scatter. We further show that our value for the H I ionization rate is consistent with no evolution in the UV background over $2 \lesssim z \lesssim 5$, and that proximity effect measurements at high redshift are consistent with the opacity of the Lyα forest and the combined ionizing output of star forming galaxies and quasars.

Finally, we conclude with an epilogue outlining some of the possible future directions for this work.

Chapter 2

Large-Scale Correlations in the Lyα Forest at $z = 3 - 4$[1]

Abstract

We present a study of the spatial coherence of the intergalactic medium toward two pairs of high-redshift quasars with moderate angular separations observed with Keck/ESI, Q1422 +2309A & Q1424+2255 ($z_{em} \approx 3.63$, $\Delta\theta = 39''$) and Q1439−0034A & B ($z_{em} \approx 4.25$, $\Delta\theta = 33''$). The cross-correlation of transmitted flux in the Lyα forest shows a $5 - 7\sigma$ peak at zero velocity lag for both pairs. This strongly suggests that at least some of the absorbing structures span the $230 - 300\ h_{70}^{-1}$ proper kpc transverse separation between sightlines. We also statistically examine the similarity between paired spectra as a function of transmitted flux, a measure which may be useful for comparison with numerical simulations. In investigating the dependence of the correlation functions on spectral characteristics, we find that photon noise has little effect for $S/N \gtrsim 10$ per resolution element. However, the agreement between the autocorrelation along the line sight and the cross-correlation between sightlines, a potential test of cosmological geometry, depends significantly on instrumental resolution. Finally, we present an inventory of metal lines. These include a a pair of strong C IV systems at $z \approx 3.4$ appearing only toward Q1439B, and a Mg II + Fe II system present toward Q1439 A and B at $z \approx 1.68$.

---

[1] Originally published in *The Astrophysical Journal*, v. 613, p. 61; written with W. L. W. Sargent and M. Rauch (Copyright 2004, The American Astronomical Society)

2.1 Introduction

Multiply-imaged lensed quasars and close quasar pairs provide valuable probes of structure in the intergalactic medium. By comparing the absorption patterns in the spectra of adjacent quasar images one can gauge the similarity in the underlying matter distributions along the lines of sight and hence constrain the sizes of absorbing structures. Previous studies at small separations ($\Delta\theta \lesssim 10''$) have typically provided lower limits to the scale of Lyα absorbers over a wide range in redshift, with weak upper constraints of ~ 400 comoving kpc derived by assuming spherical clouds (Weymann & Foltz 1983; Foltz et al. 1984; McGill 1990; Smette et al. 1992; Dinshaw et al. 1994; Bechtold et al. 1994; Bechtold & Yee 1995; Smette et al. 1995; Fang et al. 1996). Observations of pairs at wider separations ($\Delta\theta \approx 0.5' - 3'$) have shown evidence that some Lyα absorbers span $\gtrsim 1$ comoving Mpc (Petitjean et al. 1998; Crotts & Fang 1998; D'Odorico et al. 1998, 2002; Young et al. 2001; Aracil et al. 2002) and possibly up to 30 comoving Mpc (Williger et al. 2000).

The majority of studies on lensed quasars and quasar pairs have relied on matching individual absorption lines between spectra. High-resolution spectra (FWHM $\lesssim 20$ km s^{-1}) are required to completely resolve these features, however. In addition, the crowding of lines in the high-redshift Lyα forest often prevents the identification of single absorbers. Liske et al. (2000) instead used transmitted flux statistics as a function of smoothing length to identify significantly underdense or overdense regions. Their analysis of paired sightlines at $z \sim 2-3$ suggests that absorbing structures may span $\gtrsim 3$ comoving Mpc. An alternate approach reflecting the continuity of the underlying density field is to compute the correlation of transmitted flux along parallel lines of sight. This robust statistic is quickly computed and can be easily compared to numerical simulations of large-scale structure (e.g., Viel et al. 2002).

As an extension to studying the matter distribution, correlations in the Lyα forest have been proposed as a tool for constraining the cosmological constant through a variant of the Alcock-Paczyński test (Alcock & Paczynski 1979). The Alcock-Paczyński test takes advantage of the fact that, for a homogeneous sample of objects, the characteristic radial and transverse sizes should be equal. In the case of the Lyα forest, one can compare the correlation length of absorbing structures along the line of sight to the correlation length in the transverse direction. The velocity separation, $\Delta v_{\|}$, between objects along the line of sight is simply given by their redshifts,

$$\Delta v_{\parallel} = \frac{\Delta z}{1+z} c \, . \tag{2.1}$$

In contrast, the transverse velocity separation, $\Delta v_{\perp}$, between objects at redshift z with angular separation $\Delta\theta$ depends on the cosmological parameters implicit in the Hubble constant, $H(z)$, and angular diameter distance, $D_A(z)$, as

$$\Delta v_{\perp} = H(z) \Delta l = H(z) D_A(z) \Delta\theta \, , \tag{2.2}$$

where Δl is the proper linear separation. One approach to exploiting the difference between $\Delta v_{\parallel}$ and $\Delta v_{\perp}$ is to directly compare the autocorrelation of transmitted flux along single lines of sight to the cross-correlation between spectra of sources at a variety of angular separations (Hui et al. 1999; Lidz et al. 2003). An alternate method compares observed cross-correlations to those determined from linear theory (McDonald & Miralda-Escudé 1999) or from artificial spectra drawn from numerical simulations (Lin & Norman 2002). Recently, Rollinde et al. (2003) found agreement between the cross-correlations and autocorrelations among spectra of several $z \sim 2$ quasar pairs over a wide range in separation (although see the discussion on spectral resolution below). In the future, large surveys such as the Sloan Digital Sky Survey (York et al. 2000) should greatly increase the number of quasar pairs available for such studies.

We present results for two pairs of quasars at a novel combination of high redshift and moderate separation. The closely separated A and C images ($\Delta\theta = 1\farcs3$) of the bright $z = 3.63$ lensed system Q1422+2309 (Patnaik et al. 1992) have been previously examined by Rauch et al. (1999, 2001a) and Rauch et al. (2001b). Adelberger et al. (2003) recently discovered an additional faint source, Q1424+2255 ($z = 3.62$) (therein referred to as Q1422b), at a separation $\Delta\theta = 38\farcs5$ from the lensed system. In this study, we compare the sightlines toward Q1422+2309A (herein referred to as Q1422) and Q1424+2255 (herein referred to as Q1424 to avoid confusion with the B image of Q1422). We additionally investigate the $\Delta\theta = 33\farcs4$ pair at $z = 4.25$ discovered in the Sloan Digital Sky Survey, SDSSp J143952.58 − 003359.2 (herein Q1439A) and SDSSp J143951.60 − 003429.2 (herein Q1439B) (Schneider et al. 2000). For each pair, the similarity in quasar redshifts allows us to study the transverse properties of the Lyα forest and intervening metal systems over a large pathlength. Our results should provide a valuable resource for comparison with numerical simulations of large-scale structure.

The remainder of the paper is organized as follows: In §2.2 we present our observations together with a general overview of the data. We compute the flux correlation functions in the Lyα forest in §2.3 and statistically examine the similarity between sightlines as a function of flux. In §2.4 we analyze the effects of photon noise and instrumental resolution on the correlation functions. Finally, we present an inventory of unpublished metal absorption systems presented in §2.5. Our results are summarized in §2.6.

Throughout this paper we adopt $\Omega_{\rm m} = 0.3$, $\Omega_\Lambda = 0.7$, and $H_0 = 70$ km s^{-1} Mpc^{-1}.

2.2 The Data

Our observations are summarized in Table 2.1. We observed all four quasars under good to excellent seeing conditions over the period 2000 March to 2002 June using the Keck Echellette Spectrograph and Imager (ESI) (Sheinis et al. 2002) in echellette mode. Additional observations of Q1424 were provided by C. Steidel while additional observations of Q1439A were provided by L. Hillenbrand. All exposures were taken at the parallactic angle except for one exposure of Q1439B at an airmass near 1.0, where chromatic atmospheric dispersion is only a minor concern.

The raw CCD frames for Q1422, Q1439A, and Q1439B were processed and the 2-D echelle spectra extracted using the MAKEE software package. Reduction of Q1424 data was performed using a suite of IRAF scripts, as described in Adelberger et al. (2003). For each night we used the extracted orders from at least one standard star (Feige 34, BD+284211, and/or HZ 44) to determine an instrumental response function with which to derive relative flux calibrations. The calibrated orders of all exposures from all nights were then converted to vacuum heliocentric wavelengths and combined to produce a single continuous spectrum per object (Figures 2.1 and 2.2). We use a binned pixel size of 20 km s^{-1}. Normalized spectra were produced by fitting continua to the final reduced versions.

The majority of observations were made using a $0\farcs75$ slit. However, inspection of the spectra extracted from exposures taken with different slits widths revealed very little difference in resolution, likely due to favorable seeing. For the combined spectra we adopt

Table 2.1. Summary of QSO Pairs Observations

Object	Date[a]	Exp. time (s)	FWHM[b] (km s^{-1})
	Keck/ESI		
Q1422+2309A	2000 Mar 03-04	1200[c]	~ 55
Q1424+2255	2000 Mar 03 – 2001 Apr 21	44900[d]	~ 55
Q1439−0034A	2001 Jan 26 – 2002 Jun 10	8000[e]	~ 55
Q1439−0034B	2001 Apr 19 – 2002 Jun 10	42400[f]	~ 55
	Keck/HIRES		
Q1422+2309A	1998 Jan 30 – 1998 Apr 15	31600[g]	4.4

[a] Interval over which observations were made.

[b] Spectral resolution.

[c] 600 s with $0''.75$ slit, 600 s with $1''.0$ slit.

[d] 43100 s with $0''.75$ slit (including 20900 s by C. Steidel), 1800 s with $1''.0$ slit.

[e] 5000 s with $0''.75$ slit, 3000 s with $0''.5$ slit (L. Hillenbrand).

[f] $0''.75$ slit.

[g] 9000 s with UV cross-disperser, 22600 s with red cross-disperser

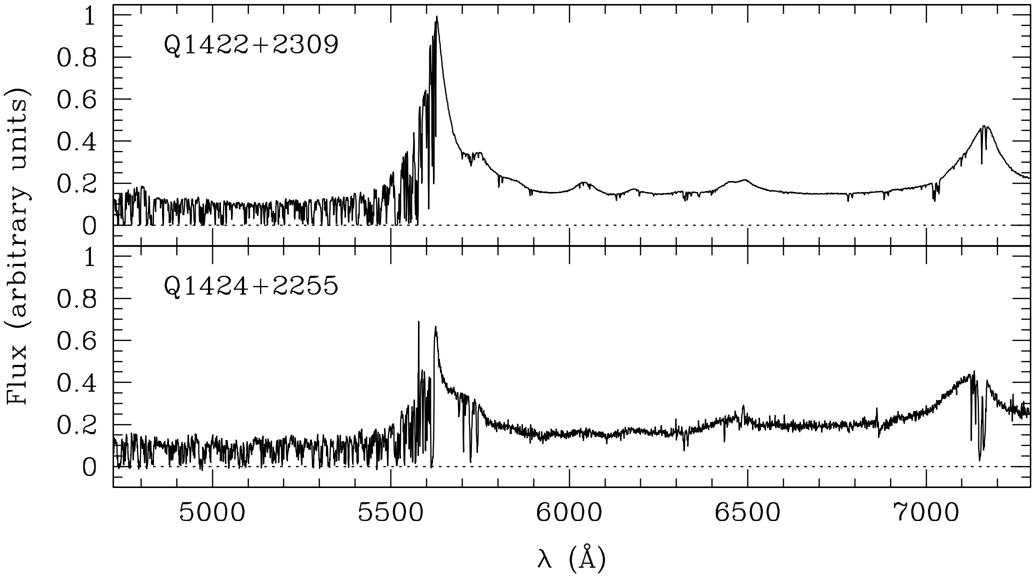

Figure 2.1 Keck/ESI spectra covering the rest wavelength region from Lyβ to C IV in Q1422 (*top*) and Q1424 (*bottom*). Spectra have been binned in wavelength using 40 km s^{-1} pixels for display. Contamination from the [O I] λ5577 skyline can be seen in the spectrum of Q1424.

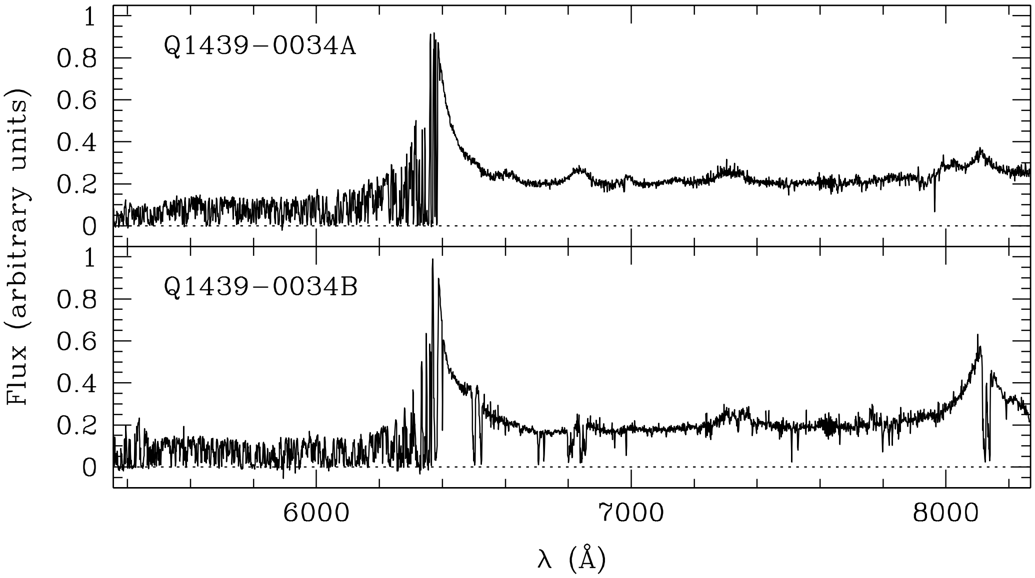

Figure 2.2 Same as Figure 2.1, here for Q1439A (*top*) and Q1439B (*bottom*).

a measured spectral resolution FWHM = 55 km s^{-1}. The final ESI spectra for Q1424, Q1439A, and Q1439B have typical $S/N \approx 13-30$ per resolution element in the Lyα forest, while Q1422 has $S/N \approx 150$.

We restrict our analysis of the Lyα forest to the the wavelength region between each quasar's Lyα and O VI emission lines. To avoid a proximity effect from the quasar, we include only those pixels at least 10,000 km s^{-1} blueward of the quasar's Lyα emission. We further include only pixels at least 1,000 km s^{-1} redward of Lyβ and O VI emission to avoid any confusion with the Lyβ forest or intrinsic O VI absorption. For Q1422 and Q1424 this yields a redshift interval $\Delta z = 0.50$ with mean redshift $\langle z \rangle = 3.22$. For Q1439 A and B, $\Delta z = 0.58$ and $\langle z \rangle = 3.79$. Due to the high redshift of Q1439 A and B, the Lyα forest in the spectra of these sources extends over the strong night sky lines [O I] λ5577 and Na I λ5890,5896. In our analysis, we exclude the narrow ($2-3$ Å) regions around these lines.

A visual comparison of the Lyα forest in the paired spectra suggests that the most striking similarity occurs among the strongest absorption features (see Figures 2.3 and 2.4). These regions often appear to be similar along adjacent lines of sight, as do regions where the absorption is nearly zero (possible "voids" relatively free of absorbing material). Matches among intermediate strength features are less obvious, which suggests that the structures giving rise to those lines may not be as coherent over the separation between sightlines. Many strong lines and regions of nearly zero absorption that do not coincide between spectra, however, can also be identified. The alignment of a subset of features may occur purely by chance.

Our spectral coverage also allows us to investigate the extent to which metal systems span parallel lines of sight. Two strong C IV systems appear toward Q1439B at $z \approx 3.4$, separated by 1700 km s^{-1}. Each system has a large rest equivalent width, $W_{\rm rest}(1548) \sim 1.5$ Å. No C IV appears at this redshift toward Q1439A, however. In contrast, a low-ionization system containing Mg II and Fe II does appear along both sightlines at $z \approx 1.68$, separated by only $\sim$ 400 km s^{-1}. A single, extended absorber responsible for the low-ionization features would have a linear size $\gtrsim 280\ h_{70}^{-1}$ proper kpc. These lines may alternatively arise from the chance intersection of separate, clustered absorbers. Weaker C IV systems appear in both Q1422 and Q1424 separated by $\sim$ 440 km s^{-1} at $z \approx 3.08$, where the separation between sightlines is 290 h_{70}^{-1} proper kpc. We expand further on the properties of metal

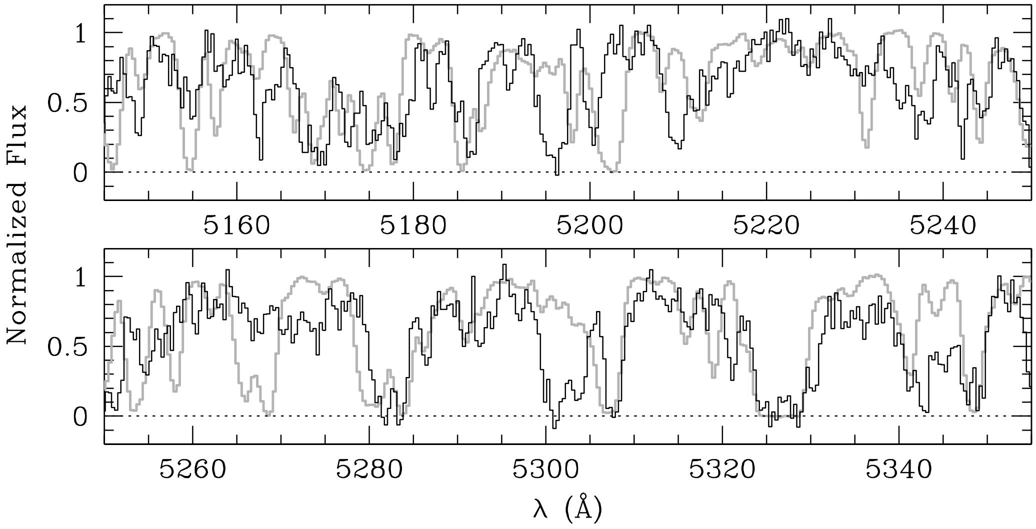

Figure 2.3 A representative section of the Lyα forest in the normalized spectra of Q1422 (grey line) and Q1424 (black line).

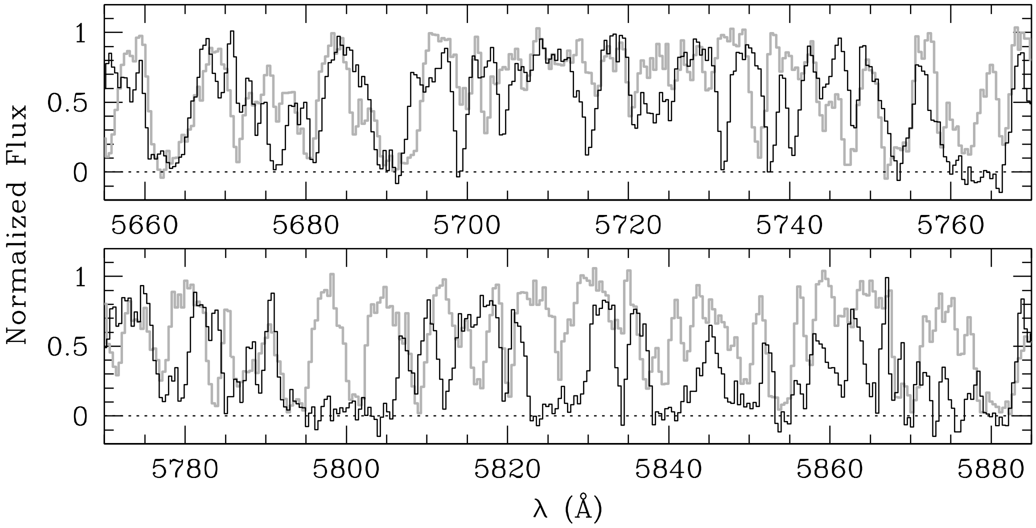

Figure 2.4 Same as Figure 2.3, here for Q1439A (grey line) and Q1439B (black line).

systems in the appendix.

In order to assess the effect of spectral characteristics on our Lyα forest results, we additionally employed a deep, high-resolution spectrum of Q1422+2309A. Observations were made with the Keck High Resolution Echelle Spectrometer (HIRES) (Vogt et al. 1994) using a $0\farcs574$ slit. This yields a spectral resolution FWHM = 4.4 km s^{-1}. Reductions were performed as described Rauch et al. (2001a). In addition to the data from that work, which used the red cross-disperser only, we include subsequent exposures taken with the UV-blazed cross-disperser installed to provide additional coverage of the Lyα forest. The final spectrum was binned to give a constant velocity width for each pixel of 2.1 km s^{-1}, with a typical S/N per resolution element of $50 - 90$.

2.3 Comparison of Sightlines

2.3.1 Correlation Functions

The correlation of transmitted flux in the spectra of closely separated quasars provides a simple means of quantifying the degree of similarity in the matter distribution along adjacent sightlines. We define the un-normalized correlation, ξ, of the spectra of two sources separated on the sky by an angle $\Delta\theta$ as

$$\xi(\Delta\theta, \Delta v_{\|}) = \frac{1}{N} \sum \left[F(\Delta\theta, v_{\|} + \Delta v_{\|}) - \bar{F}(\Delta\theta)\right] \left[F(0, v_{\|}) - \bar{F}(0)\right] , \tag{2.3}$$

where F is the continuum-normalized flux, $\bar{F}(\Delta\theta)$ and $\bar{F}(0)$ are the mean fluxes along the two sightlines, $v_{\|}$ is the line-of-sight velocity, $\Delta v_{\|}$ is the longitudinal velocity lag, and N is the total number of pixels in each spectrum within the region of interest. The sum is performed over all available pixels at a given velocity lag, of which there will be

$$n_{\mathrm{pix}}(\Delta v_{\|}) = N - \frac{\Delta v_{\|}}{\delta v_{\mathrm{pix}}} \tag{2.4}$$

for a pixel size δv_{pix}. The normalized correlation value can be computed by dividing equation (2.3) by the standard deviation in each input spectrum.

We have chosen a pixel size for the combined spectra to give roughly 3 pixels/resolution element. We note, however, that the $1/N$ factor in equation (2.3) implies that the value of the correlation will be insensitive to pixel size so long as the spectrum is well sampled. The increase in the sum created by using a larger number of smaller pixels will be offset by the increase in N so long as there are $\gtrsim 2$ pixels/resolution element. Using pixels larger than the spectral resolution will introduce smoothing effects (see §2.4).

In order to assess the coherence of absorbing structures across adjacent sightlines, we compute the cross-correlation of transmitted flux in the Lyα forest in the spectra of our quasar pairs. As a reference, we also determine the autocorrelation, $\xi(0, \Delta v_{\|})$, along lines of sight toward individual objects. At these high redshifts, H I Lyα absorption will strongly dominate over contaminating absorption from lower-redshift metals such as C IV and Mg II. The correlation functions should therefore accurately reflect the distribution of neutral hydrogen to within the present measurement errors. All correlations are computed in single-pixel steps, which are 20 km s^{-1} for the ESI data. Figure 2.5 displays the autocorrelation function for each quasar along with the cross-correlation functions between adjacent sightlines. Both in the case of Q1422/Q1424 and Q1439A/B, a clear peak in the cross-correlation at zero lag indicates a genuine similarity between sightlines.

Undulations in the correlation functions arising from the chance superposition of unrelated lines constitute the dominant source of uncertainty in the peak values (see discussion on photon noise below). Pixel-to-pixel variations in the correlations are themselves clearly correlated. We find, however, that the overall distributions of values away from the central peaks are very nearly Gaussian. We therefore take the standard deviation of pixels in the "noise" region, which we define to be where 2000 km s^{-1} $\leq |\Delta v_{\|}| \leq$ 18000 km s^{-1}, as the 1σ error in a correlation peak value. In this region we expect no underlying signal, however the correlation is still computed from at least half of the available pixels. Since the sum in equation (2.3) is computed over fewer pixels as the velocity lag increases, yet the factor $1/N$ remains constant, the amplitude of the noise features will tend to diminish as $\sqrt{n_{\rm pix}(\Delta v_{\|})}$, where $n_{\rm pix}(\Delta v_{\|})$ is the number of pixels included in the sum in equation (2.3) at lag $\Delta v_{\|}$. Therefore, in order to match the amplitude of the noise at $\Delta v_{\|} = 0$, we multiply the correlation at each lag by a scale factor s before computing the standard deviation, where

$$s = \sqrt{\frac{n_{pix}(0)}{n_{\rm pix}(\Delta v_{\|})}} = \sqrt{\frac{N}{N - \Delta v_{\|}/\delta v_{\rm pix}}} \, . \tag{2.5}$$

For the range in velocity lag defined above this is a modest correction. Including only lags

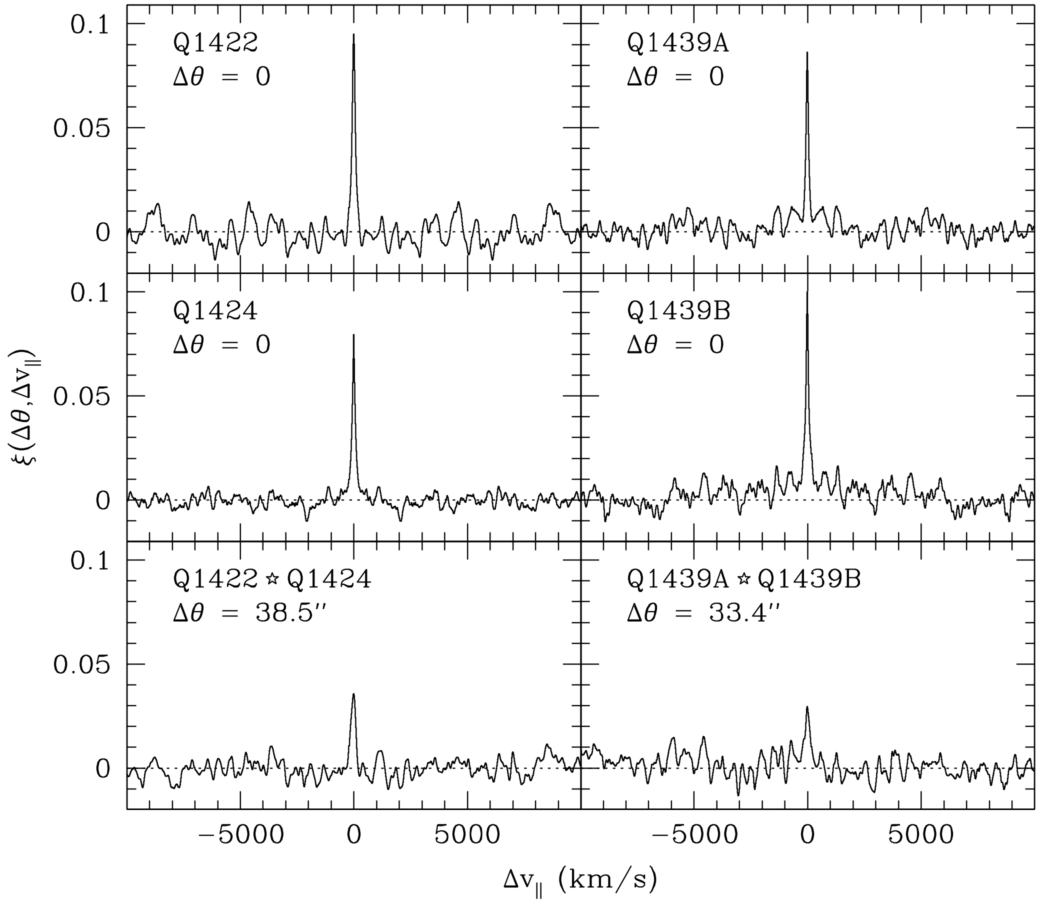

Figure 2.5 Flux correlation functions computed from the Lyα forest plotted vs. longitudinal velocity lag. *Top four panels:* Autocorrelation functions for Q1422 (*top left*), Q1424 (*middle left*), Q1439A (*top right*), and Q1439B (*middle right*). Negative velocity lags have been included for consistency. *Bottom panels:* Cross-Correlation functions for Q1422/Q1424 (*bottom left*) and Q1439A/B (*bottom right*).

Table 2.2. Lyα Forest Cross-Correlation Values

QSO Pair	$\Delta\theta$[a]	$z_{\mathrm{Ly}\alpha}$[b]	Δl[c]	$\Delta v_{\perp}$[d]	$\xi(\Delta\theta, 0)$	
			h_{70}^{-1} proper kpc	km s^{-1}	Un-normalized[e]	Normalized[f]
Q1422/Q1424	38.″5	$2.965 - 3.466$	$283 - 298$	97.8	0.0358 ± 0.0049	0.412 ± 0.057
Q1439A/B	33.″4	$3.496 - 4.075$	$230 - 245$	96.3	0.0296 ± 0.0057	0.319 ± 0.062

[a] Angular separation of the QSO pair.

[b] Redshift interval used in computing the correlation values for the Lyα forest.

[c] Linear separation between the lines of sight for the given redshift interval, computed for $\Omega_{\mathrm{m}} = 0.3$, $\Omega_{\Lambda} = 0.7$, and $H_0 = 70$ km s^{-1} Mpc^{-1}.

[d] Transverse velocity separation between the lines of sight for our adopted cosmology at the mean redshift in the given interval.

[e] Cross-Correlation at zero lag computed from equation (2.3).

[f] Cross-Correlation at zero lag computed from equation (2.3) divided by the standard deviation of the Lyα forest flux in each input spectrum.

where at least half of the $\sim$ 1800 Lyα pixels in each spectrum overlap limits s to at most $\sqrt{2}$. For the range in velocity lag shown in Figure 2.5, $s < 1.2$.

Our results for the cross-correlations are summarized in Table 2.2. Using the above estimate for the error, the peak in the cross-correlation for Q1422/Q1424 (Q1439A/B) is significant at the 7σ (5σ) level. This strongly suggests coherence in the absorbing structures on the scale of the $230 - 300$ h_{70}^{-1} proper kpc transverse separation between sightlines. The marginal consistency of the peak values with one another likely reflects the similarity in sightline separation and redshift for the two quasar pairs. The zero-lag values of the autocorrelations, which give the variance in the flux for these sections of the Lyα forest, are 0.0950 for Q1422, 0.0796 for Q1424, 0.0862 for Q1439A, and 0.1000 for Q1439B. Thus, the normalized cross-correlation peaks are $41.2 \pm 5.7\%$ for Q1422/Q1424 and $31.9 \pm 6.2\%$ for Q1439A/B.

2.3.2 Flux Distributions

The flux cross-correlations demonstrate that at least some Lyα absorbers span the separation between our paired lines of sight. It does not, however, indicate whether the similarity between sightlines depends on the strength of the absorber. The crowded nature of the

Lyα forest at $z \sim 4$, together with the present spectral resolution, greatly inhibits a study of individual lines. We are, however, able to look at the agreement between absorption features on a pixel-by-pixel basis.

Our goal is to determine whether the similarity in flux between paired spectra depends on the amount of absorption for an individual pixel. First, we first select those Lyα forest pixels in one spectrum (Q1422 or Q1439A) whose flux falls within a specified range. We then identify the pixels in the companion spectrum with matching wavelengths and compute their flux distribution. Comparing the distribution in this subsample to that in all Lyα forest pixels in the companion spectrum allows us to evaluate whether there exists an overabundance of pixels in the specified flux range relative to that expected on random chance.

The results for Q1422/Q1424 and Q1439A/B are shown in Figures 2.6 and 2.7, respectively. Each panel shows the normalized distribution of Q1424 or Q1439B pixels in the indicated subsample along with the distribution of all Lyα forest pixels in that spectrum. The range of flux in Q1422 or Q1439A for each subsample is chosen to be significantly larger than the typical flux uncertainty. In each case, we compute the two-sided Kolmogorov-Smirnov statistic, which is the maximum difference between the cumulative fractions of pixels in the subsample and of all pixels in the forest, along with the associated likelihood of randomly obtaining a smaller statistic than the one observed. The number of pixels in each subsample is also shown.

The clearest results occur at extreme levels of absorption. Pixels in Q1422 (Q1439A) either near saturation, $F < 0.2$, or near the continuum, $F > 0.8$, tend to strongly coincide with pixels of similar flux in Q1424 (Q1439B). Intermediate flux pixels appear to be less strictly matched, with the exception of pixels in Q1422 with $0.4 < F < 0.6$. For certain subsamples, namely $0.6 < F < 0.8$ in Q1422 and $0.4 < F < 0.6$ in Q1439A, the distribution of fluxes in the companion spectrum is consistent with a random selection. This seems to confirm the visual appraisal that strong absorbers and regions relatively free of absorbing material tend to span adjacent lines of sight more readily than do absorbers of intermediate strength.

While each sample includes enough pixels to produce a statistically significant result, a few caveats are worth considering. Systematic errors in continuum fitting might artificially

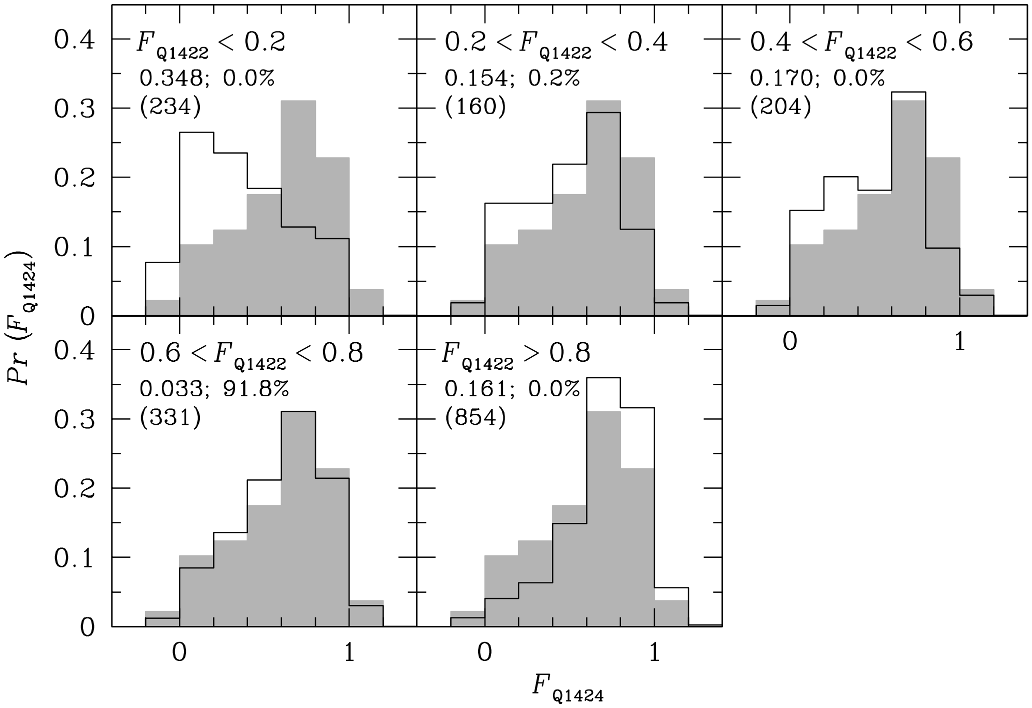

Figure 2.6 Distributions of continuum-normalized pixel fluxes in the Lyα region of Q1424 as a function of the flux in Q1422. Unshaded histograms show the flux probability distribution for the subsample of pixels in Q1424 corresponding in wavelength to those pixels in Q1422 that have fluxes in the indicated range. Shaded histograms show the probability distribution for all Q1424 pixels in the Lyα region. For each range of flux in Q1422, the two-sided Kolmogorov-Smirnov statistic for the subsample and full sample of Q1424 flux values is presented along with the associated likelihood, expressed as a percent, of obtaining a higher value if the the two samples were drawn from the same distribution. The number of pixels in each subsample is given in parentheses. The full sample contains 1783 pixels.

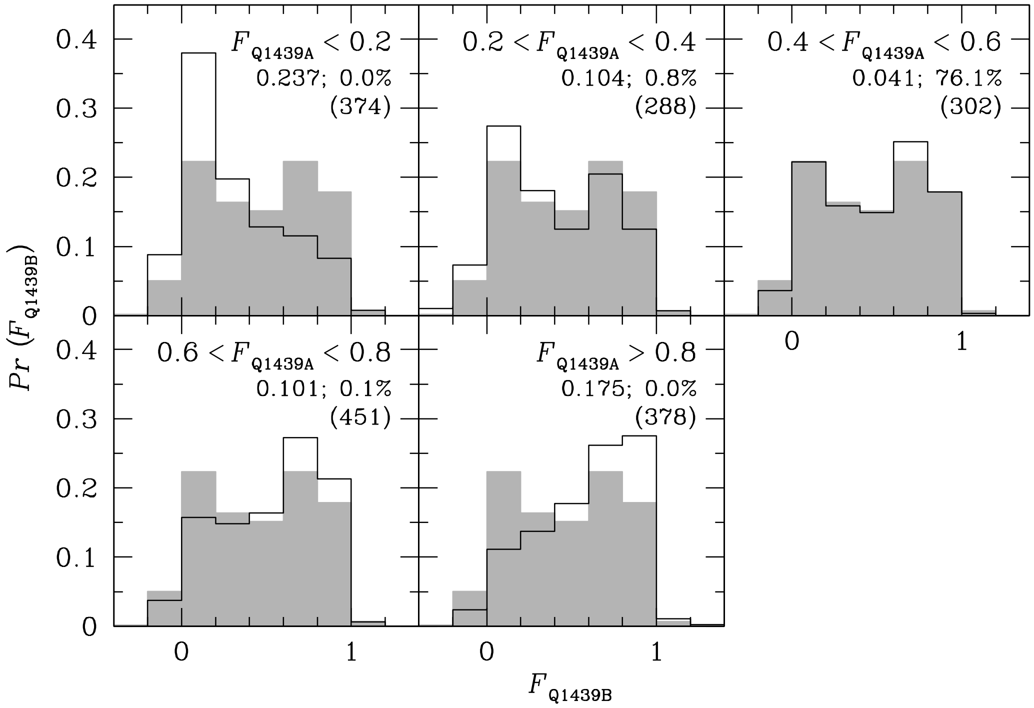

Figure 2.7 Same as Figure 2.6, here for pixel fluxes in the Lyα region of Q1439B as a function of the flux in Q1439A. The full sample contains 1793 pixels.

create clusters of pixels with low absorption near the same wavelength in pairs of spectra. Similarly, errors in sky-subtraction that are repeated between spectra might create false coincidences of pixels near zero flux. Multiple independent continuum fits resulted in typical differences of $\sim 10\%$ in flux on scales of ~ 100 Å. We likewise find no evidence for large systematic errors in the sky subtraction. Given that the resulting uncertainties are significantly smaller than the range in flux used to define a subsample in Figures 2.6 & 2.7, these effects should only be a minor concern.

We stress that comparing transmitted fluxes does not strictly yield a clear physical interpretation. Pixels of intermediate flux commonly occur along the wings of strong features. They will therefore tend to cluster less readily than pixels near the continuum or near saturation, especially if the strong lines shift in velocity between spectra. Moreover, agreement in flux does not necessarily indicate agreement in optical depth. Since transmitted flux decreases exponentially with optical depth, τ, the difference in flux for a given fractional change in τ will depend on the value of τ itself. For a small characteristic change between sightlines, $\Delta\tau/\tau \ll 1$, the greatest scatter in flux is expected for $\tau \sim 1$, with the scatter decreasing as $\tau \rightarrow 0$ or as $\tau \rightarrow \infty$. It is, therefore, unclear whether the enhanced agreement in flux among pixels with flux near the continuum or near saturation indicates that the corresponding gas is more homogeneous on these scales than the gas giving rise to intermediate absorption features. More specific insights may be drawn by comparing our measured flux distributions to those derived from numerical simulations.

2.4 Effects of Photon Noise and Instrumental Resolution

Comparing the longitudinal and transverse flux correlation functions (or power spectra, equivalently) in the Lyα forest has been been explored by several authors as a means of measuring the cosmological geometry via the Alcock-Paczyński test. This application primarily requires a sample of sightlines large enough to overcome cosmic variance. Some question remains, however, regarding the dependence of the correlation functions on data characteristics such as signal-to-noise ratio and resolution. It is particularly important to know to what extent the autocorrelation measures the physical correlation length along the line of sight rather than the instrumental resolution. For additional discussion on the effects of spectral characteristics see, e.g., Lin & Norman (2002) and Croft et al. (1998).

In the preceding analysis we assumed that the chance alignment of unrelated absorption features dominated over photon noise in producing uncertainty in the flux correlations. To justify this, we recomputed the autocorrelation for the ESI spectrum of Q1422 after adding increasing levels of Gaussian random noise. The results appear nearly identical for $S/N \gtrsim 10$ per resolution element (Figure 2.8). A spike at $\Delta v_{\parallel} = 0$ appears in the autocorrelation function as the S/N decreases because the variance in the noise becomes comparable to the intrinsic variance in the absorption features. No such jump is expected to occur, however, in the cross-correlation since the photon noise in the two spectra should be uncorrelated. Large sets of moderate S/N spectra may therefore be more useful than smaller sets of high S/N for this type of work.

To address the effects of spectral resolution on the autocorrelation we have synthesized moderate- and low-resolution spectra from a high-quality Keck HIRES spectrum of Q1422 (resolution FWHM = 4.4 km s^{-1}). In each test case we first tune the spectral resolution by convolving the HIRES data with a Gaussian kernel and then compute the resulting autocorrelation function. The results for spectra with resolution FWHM = 4.4 (unsmoothed), 15, 55, and 200 km s^{-1} are plotted in Figure 2.9. Very little difference exists between the autocorrelation functions computed from the unsmoothed HIRES data and from the data smoothed to FWHM = 15 km s^{-1}. Thus, we may conclude that the correlation in the unsmoothed HIRES data is an accurate measure of the intrinsic correlation in the Lyα forest (subject to cosmic variance and redshift-space distortions). The Lyα lines are already smoothed by their thermal width and easily resolved with HIRES. However, when the spectrum is degraded to FWHM = 55 km s^{-1}, similar to ESI data, the autocorrelation is clearly broadened and diminished in amplitude. (We note that the autocorrelation measured from this “synthetic” ESI spectrum is nearly identical to that computed from the real ESI data.) At even lower resolution, comparable to Keck/LRIS or VLT/FORS2, the spectral resolution dominates over the intrinsic correlation length.

As the spectral resolution decreases, the peak of the autocorrelation also incorporates more of the outlying noise (random undulations in the correlation function at $\Delta v \gg 0$). At large velocity lags ($\Delta v_{\parallel} \gg 200$ km s^{-1}), disagreement between the high-resolution and low-resolution cases may be due in part to these noise features. Better agreement may result when the correlation function is averaged over many sightlines.

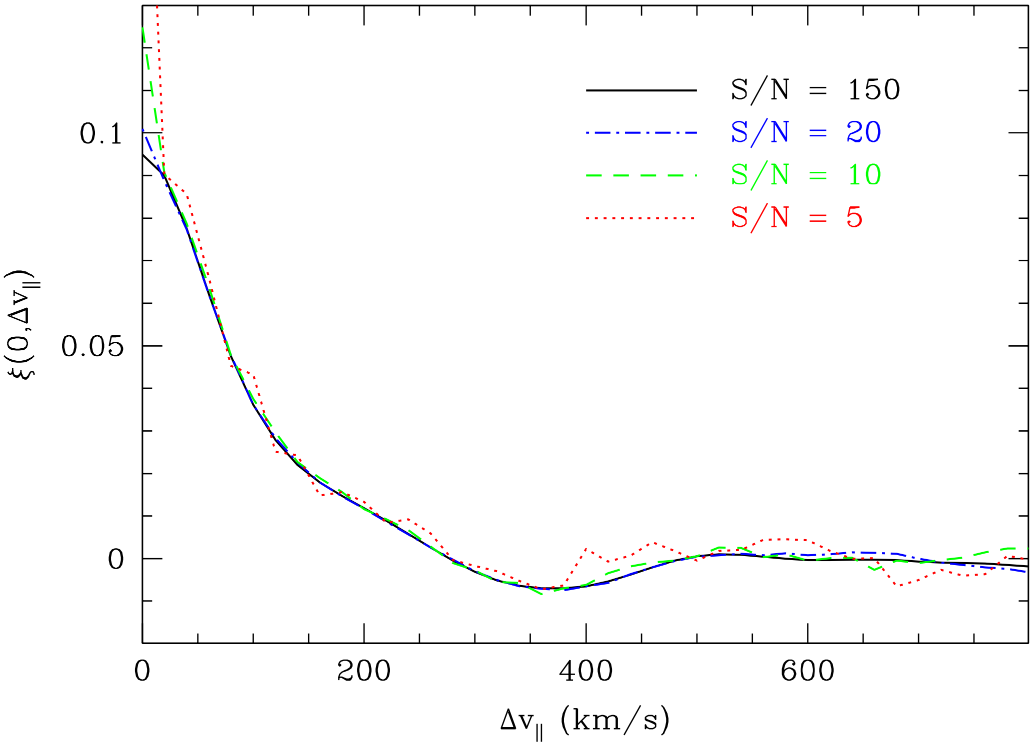

Figure 2.8 The effects of photon noise on the shape of the autocorrelation function. The solid line shows the autocorrelation computed from our original ESI spectrum of Q1422 (FWHM = 55 km s^{-1}, $S/N = 150$ per resolution element). Additional lines show the autocorrelation recomputed after adding random Gaussian noise to the original spectrum such that the resulting S/N per resolution element is 20 (dash-dotted line), 10 (dashed line), and 5 (dotted line). Autocorrelation functions were computed in longitudinal velocity lag steps of 20 km s^{-1}. The spike at $\Delta v_{\parallel} = 0$ reflects only a single point for each curve.

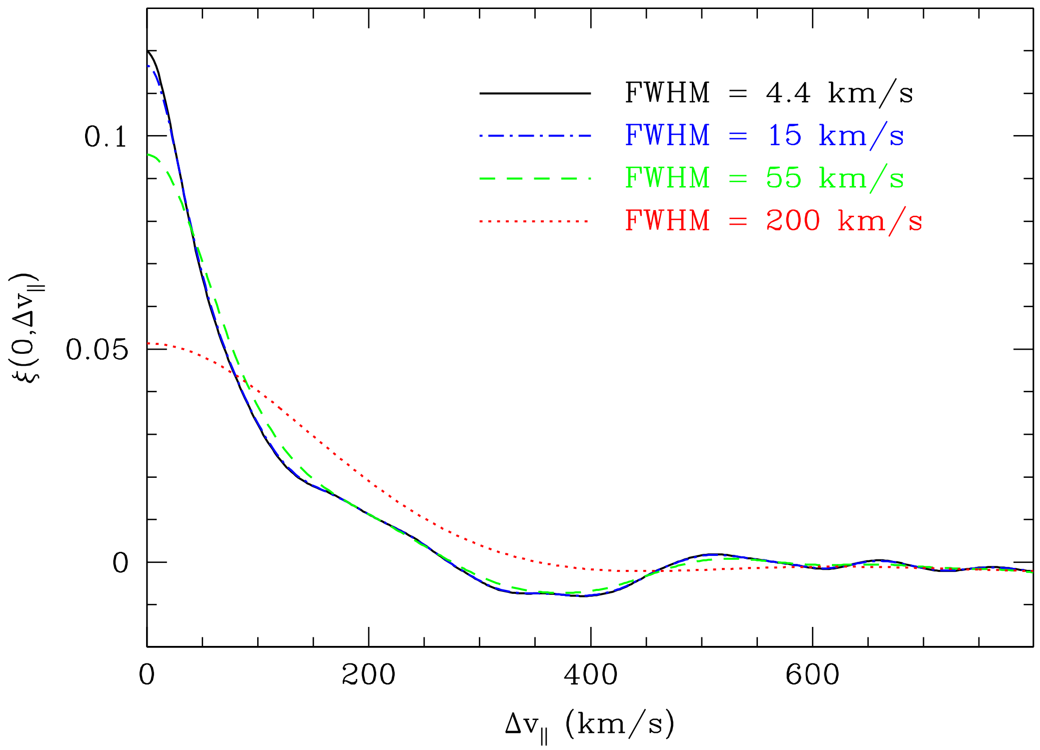

Figure 2.9 The effects of spectral resolution on the shape of the autocorrelation function. The solid line shows the autocorrelation computed from our original HIRES spectrum of Q1422 (FWHM = 4.4 km s^{-1}). Additional lines show the autocorrelation recomputed after smoothing the HIRES data to a spectral resolution FWHM of 15 km s^{-1} (dash-dotted line), 55 km s^{-1} (dashed line), and 200 km s^{-1} (dotted line).

A more subtle issue is how spectral resolution affects the agreement between autocorrelation and cross-correlation functions. To address this, we degraded the resolution of our ESI data to mimic observations using a lower resolution instrument (FWHM $= 200$ km s^{-1}) and then recomputed the correlations. Figure 2.10 contrasts the results from the original spectra with those from the smoothed versions. In each case we plot the autocorrelation functions computed from single sightlines and overplot the peak of the corresponding cross-correlation at a velocity lag equal to the transverse velocity separation between the lines of sight ($\Delta v_{\perp} = 98$ km s^{-1} for Q1422/Q1424, $\Delta v_{\perp} = 96$ km s^{-1} for Q1439A/B for the case of $\Omega_{\rm m} = 0.3$, $\Omega_{\Lambda} = 0.7$, and $H_0 = 70$ km s^{-1} Mpc^{-1}).

The differences shown in Figure 2.10 between the ESI and low-resolution cases suggest a significant dependence on spectral resolution. At ESI resolution the concordance between auto- and cross-correlations appears to be very good for both pairs of sightlines. At low resolution, however, the peaks of the cross-correlation functions fall well below the values of the autocorrelation functions at the same total velocity separation. While part of this effect may be due to noise in the correlations, the general dependence on resolution can be understood in regions where the intrinsic correlation function is non-linear on scales smaller than the width of the smoothing kernel. (This includes the region around the peak at zero lag, since the correlation is expected to be symmetric about $\Delta v_{\parallel} = 0$.) Convolving the input spectra with a smoothing kernel produces a correlation function that has been convolved twice with the same kernel, once for each spectrum. The resulting un-normalized autocorrelation function may therefore be higher or lower at a particular velocity lag, depending on the shape of the correlation function at that point. Since the peak of the cross-correlation function is already a maximum, however, it can only decrease as a result of smoothing (apart from the effects of noise). Thus, if we adjust our cosmology such that, at high spectral resolution, the composite cross-correlation function built up from pairs at many different separations agrees with the mean autocorrelation function (ignoring redshift-space distortions), this agreement may not hold with low-resolution data. Spectral resolution must therefore be considered carefully when performing this type of comparison, for example by referring to artificial spectra drawn from numerical simulations of large-scale structure.

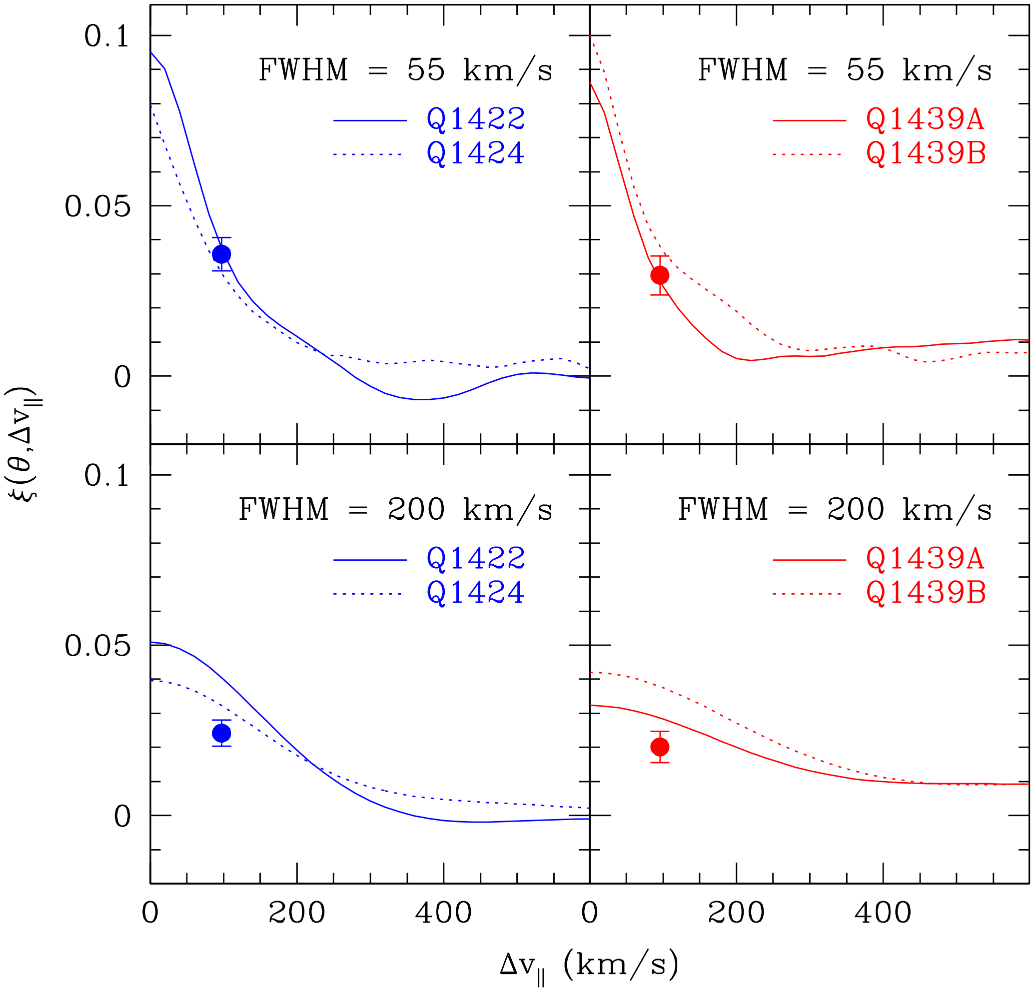

Figure 2.10 The relative effects of spectral resolution on auto- and cross-correlations. *Top panels*: Autocorrelation functions computed from the Lyα regions in the indicated unsmoothed ESI spectra (FWHM = 55 km s^{-1}) (solid and dotted lines) overlaid with the peak value of the cross-correlation computed between those spectra (filled circles). The peak of the cross-correlation is plotted at a velocity lag equal to the transverse separation between the two lines of sight for the case of $\Omega_{\rm m} = 0.3$, $\Omega_\Lambda = 0.7$, and $H_0 = 70$ km s^{-1} Mpc^{-1}. *Bottom panels*: Same as the top panels, here after smoothing the ESI spectra to a resolution of 200 km s^{-1}.

2.5 Metal Systems

Previous studies using quasar pairs and multiply-imaged lensed quasars have demonstrated spatial coherence in metal systems over a variety of length scales. Differences between metal systems in narrowly-separated lines of sight suggest that the absorbers giving rise to individual lines seen in high-resolution spectra span at most a few kiloparsecs, both for high-ionization systems seen in C IV and for low-ionization systems seen in Mg II(Lopez et al. 1999; Petitjean et al. 2000; Rauch et al. 2001a, 2002; Churchill et al. 2003; Tzanavaris & Carswell 2003; Ellison et al. 2004). However, these absorbers may be part of larger structures extending $\gtrsim 20\ h_{70}^{-1}$ kpc (Smette et al. 1995) and even $\gtrsim 100\ h_{70}^{-1}$ kpc for highly ionized material (Petitjean et al. 1998; Lopez et al. 1999, 2000).

The present data afford us a unique opportunity to probe the coherence of metal systems on scales of $\sim 300\ h_{70}^{-1}$ proper kpc. Unfortunately, modest signal-to-noise and significant contamination from skylines in the red part of our spectra greatly limit our sensitivity and hinder completeness estimates. Our detections are limited to relatively strong lines and lines that fall in regions of unusually high S/N.

Line lists for Q1424, Q1439A, and Q1439B are presented in Tables 2.3, 2.4, and 2.5, respectively. In the following sections we briefly comment on some of the more interesting systems. Results for Q1422 are presented in detail elsewhere (Rauch et al. 2001a; Bechtold & Yee 1995; Petry et al. 1998). For each line we measure the wavelength centroid and equivalent width. Weighted mean redshifts are given where multiple lines are measured for a single ion. In the case of blended lines we attempt to alleviate the overlap by fitting Voigt profiles to any unblended transitions of the same ions using VPFIT and then dividing by the inferred model profiles. This typically allows us to obtain values for at least the strongest blended components.

2.5.1 Q1424+2255

Strong associated broad absorption lines (BALs) at $z = 3.62$ are seen in C IV and N V along with weaker associated absorption in Si IV (although the Si IV appears affected by skyline contamination). Isolated components of C IV and N V appear up to 1000 km s^{-1} blueward of the BAL. These suggest small pockets of outflowing material moving at a higher velocity than the material responsible for the bulk of the broad absorption. C IV is also seen at

Table 2.3. Q1424+2255 Metal Systems

$\lambda_{\rm obs}$ (Å)	Line ID	$z_{\rm obs}$[a]	$W_{\rm rest}$ (Å)
		Intervening	
5692.34 ± 0.12	Si IV $\lambda1394$	3.08417 ± 0.00009	0.29 ± 0.02
6323.34 ± 0.14	C IV $\lambda1548$	3.08433 ± 0.00007	0.50 ± 0.03
6333.93 ± 0.17	C IV $\lambda1550$	3.08433 ± 0.00007	0.37 ± 0.03
		Associated	
5704.76 ± 0.08	N V $\lambda1239$	3.60499 ± 0.00007	0.34 ± 0.01
5709.70 ± 0.11	N V $\lambda1239$	3.60898 ± 0.00009	0.11 ± 0.01
5724.81 ± 0.08	N V $\lambda1239$	3.62118 ± 0.00005	0.96 ± 0.02
5743.22 ± 0.09	N V $\lambda1243$	3.62118 ± 0.00005	0.75 ± 0.02
6437.34 ± 0.17	Si IV $\lambda1394$	3.61865 ± 0.00009	0.24 ± 0.03
6478.79 ± 0.21	Si IV $\lambda1403$	3.61865 ± 0.00009	0.16 ± 0.02
7129.64 ± 0.08	C IV $\lambda1548$	3.60511 ± 0.00005[b]	0.36 ± 0.01
7135.69 ± 0.16	C IV $\lambda1548$	3.60902 ± 0.00010	0.10 ± 0.01
7141.28 ± 0.08	C IV $\lambda1550$	3.60511 ± 0.00005[b]	$\lesssim 0.37$[c]
7144.70 ± 0.13	C IV $\lambda1548$	3.61484 ± 0.00008	0.08 ± 0.01
7153.99 ± 0.07	C IV $\lambda1548$	3.62085 ± 0.00004	1.82 ± 0.03
7165.96 ± 0.11	C IV $\lambda1550$	3.62085 ± 0.00004	1.44 ± 0.06

[a] Weighted mean redshift from all available transitions.

[b] C IV doublet redshift computed from the $\lambda1548$ line only.

[c] 3σ upper limit (possible blend).

$z = 3.62$ toward Q1422A. (Rauch et al. 2001a). Since the absorption is associated with the quasar in both cases, however, these features are unlikely to be related.

An intervening C IV system appears at $z = 3.084$. We additionally identify the line at 5692.3 Å to be Si IV $\lambda1394$ at the same redshift, where Si IV $\lambda1403$ is blended with N V $\lambda1239$ at $z = 3.621$. A C IV complex with possible Si IV appears at $z = 3.090$ toward both the A and C images of Q1422 (Rauch et al. 2001a; Boksenberg et al. 2003), implying a transverse size $\gtrsim 290\ h_{70}^{-1}$ proper kpc for a single structure spanning all three lines of sight. Figure 2.11 shows the C IV absorption at this redshift in Q1424 and Q1422. The systems are narrowly separated along the line of sight, with $\Delta v \approx 440$ km s^{-1}. However, Boksenberg et al. (2003) find ~ 25 C IV systems per unit redshift at $z = 3$ for systems with total column density $N_{\rm syst}(\mbox{C IV}) > 10^{12}$ cm^{-2}. This translates to a typical spacing between systems of only ~ 3000 km s^{-1}. It is therefore reasonable to suspect that this superposition of relatively modest C IV absorbers toward Q1422 and Q1424 occurs by chance. Significant H I absorption occurs along both lines of sight in the velocity interval spanned by these systems, though this may be due to the crowded state of the Lyα forest at $z \sim 3$.

2.5.2 Q1439−0034A & B

Two broad C IV complexes at $z \approx 3.4$ form the most conspicuous metal absorption features in the spectrum of Q1439B (Figure 2.12). The systems are separated by 1700 km s^{-1}, and each has a velocity width of ~ 400 km s^{-1}. Neither complex is observed toward Q1439A. The individual components are unlikely to be resolved with ESI. However, we can place a lower limit on the column density of these systems by assuming that the weaker transition (C IV λ1551) falls on the linear part of the curve-of-growth. In that case, the column density, $N_{\rm syst}$, is related to rest equivalent with, $W_{\rm rest}$, as

$$W_{\rm rest} = \frac{\pi e^2}{m_e c^2} f \lambda_0^2 N_{\rm syst} \, , \tag{2.6}$$

for a transition with rest wavelength λ_0 and oscillator strength f. For the lower-equivalent width system ($z_{\rm abs} = 3.402$, $W_{\rm rest}(1551) \approx 1.1$ Å), this gives $N_{\rm syst}(\mbox{C IV}) \gtrsim 5 \times 10^{14}$ cm^{-2}. If we adopt a power-law column density distribution $d^2\mathcal{N}/dN_{\rm syst}dz \propto N_{\rm syst}^{-\beta}$, where $\mathcal{N}$ is the number of systems, then we would expect $\lesssim 0.6$ systems per unit redshift in this column density range based on the above Boksenberg et al. (2003) results and adopting their value of $\beta = 1.6$. The narrow redshift spacing of these two systems ($\Delta z = 0.025$) therefore strongly suggests that they are related. One explanation is that the absorption complexes arise from two sides of an intervening galactic outflow. Alternatively, the high levels of H I absorption seen at both C IV redshifts may indicate a pair of galaxy halos.

Mg II + Fe II systems appear toward both Q1439 A and B at $z \approx 1.68$, separated between spectra by 410 km s^{-1} along the line of sight (Figure 2.13). From Churchill et al. (1999), the number of Mg II systems per unit redshift with rest equivalent width $W_{\rm rest}(2796) > 0.02$ Å is expected to be ≈ 2.7. The probability of randomly finding a system within this velocity

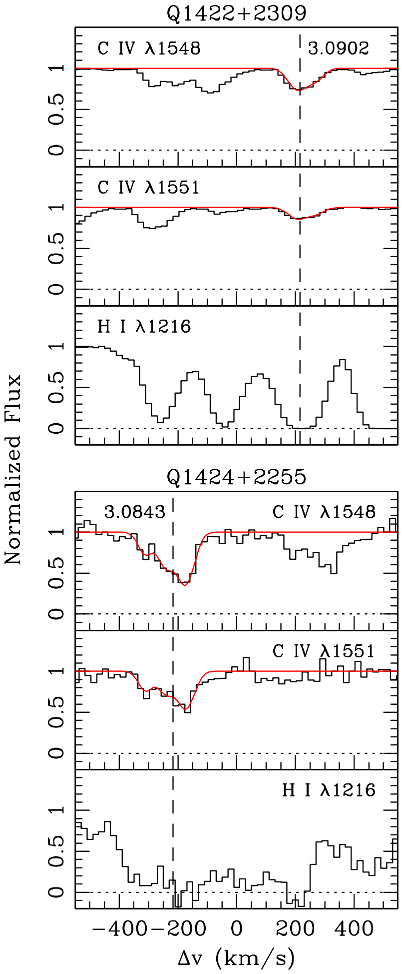

Figure 2.11 *Top three panels:* Continuum-normalized ESI spectrum of Q1422 (histogram) showing the C IV and H I absorption for the system at $z = 3.0902$ reported by Rauch et al. (2001a). The continuous lines show the Voigt profile fits computed from HIRES data where the profiles have been smoothed to ESI resolution. *Bottom three panels:* Continuum-normalized ESI spectrum of Q1424 (histogram) showing the C IV and H I absorption for the system measured herein at $z = 3.0843$. The continuous lines show Voigt profile fits computed from the ESI data. All components in both spectra are placed on a common velocity scale in order to demonstrate the longitudinal velocity separation between these systems.

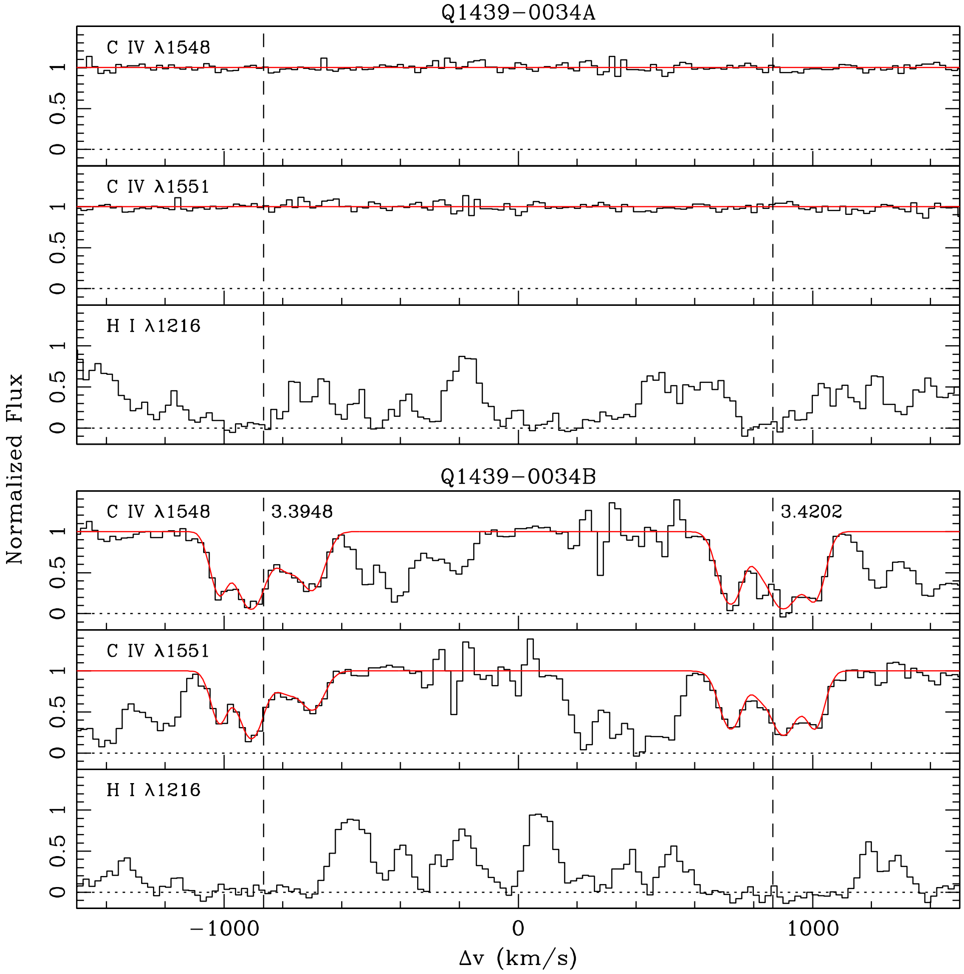

Figure 2.12 *Top three panels:* Continuum-normalized ESI spectrum of Q1439A (histogram) covering the C IV and H I regions near $z = 3.4$. The continuous lines in the top two panels demonstrate the absence of C IV over this interval. *Bottom three panels:* Continuum-normalized spectrum of Q1439B (histogram) showing the C IV and H I absorption for the systems at $z = 3.3948$ and $z = 3.4202$. The continuous lines show the Voigt profile fits to the C IV absorption. Several of the C IV $\lambda1548$ pixels near 850 km s^{-1} in this plot are heavily affected by skylines and have been excluded from the fit. All components in both spectra are placed on a common velocity scale in order to demonstrate the longitudinal velocity separation between these systems.

Table 2.4. Q1439−0034A Metal Systems

$\lambda_{\rm obs}$ (Å)	Line ID	$z_{\rm obs}$[a]	$W_{\rm rest}$ (Å)
6393.06 ± 0.10	Fe II $\lambda2383$	1.68304 ± 0.00004	0.07 ± 0.01
7502.82 ± 0.12	Mg II $\lambda2796$	1.68305 ± 0.00004	0.18 ± 0.02
7521.87 ± 0.19	Mg II $\lambda2804$	1.68305 ± 0.00004	0.10 ± 0.02
9134.29 ± 0.14	Mg II $\lambda2796$	2.26645 ± 0.00004	0.30 ± 0.03
9157.37 ± 0.18	Mg II $\lambda2804$	2.26645 ± 0.00004	0.32 ± 0.04

[a] Weighted mean redshift from all available transitions.

separation is therefore ~ 0.02, or a factor of three lower if we restrict ourselves to strong ($W_{\rm rest}(2796) > 0.3$) systems (Steidel & Sargent 1992). Thus, there is a high likelihood that these systems are related. Both Mg II and Fe II appear stronger toward B than toward A, with a factor of seven difference between sightlines in the equivalent widths of Mg II $\lambda2804$ and Fe II $\lambda2384$. These features may arise either from a single absorber spanning the 280 h_{70}^{-1} proper kpc between sightlines or from a pair of clustered objects. Two additional strong Mg II systems appear along only a single sightline, one toward A at $z = 2.266$ and another toward B at $z = 1.399$.

Q1439B is a BAL quasar showing high levels of associated absorption in C IV and N V. We identify the O I absorption reported by Fukugita et al. (2004) as the strong C IV systems at $z \approx 3.4$ mentioned above. No strong associated absorption is seen for Q1439A. As noted by Fukugita et al. (2004), the difference in associated absorption features supports the hypothesis that Q1439 A and B are a true binary and not a lensed pair.

2.6 Conclusions

We have analyzed the transverse properties of the Lyα forest at $3.0 \lesssim z \lesssim 4.1$ on scales of ~ 1 h_{70}^{-1}comoving Mpc ($230 - 300$ h_{70}^{-1} proper kpc) toward the $z \approx 3.63$ quasar pair Q1422+2309A/Q1424+2255 and the $z \approx 4.25$ pair Q1439−0034A/B. Strong peaks at zero velocity lag in the flux cross-correlations between paired sightlines indicate coherence in the H I absorbers on these scales. The crowded nature of the Lyα forest at these redshifts

Table 2.5. Q1439−0034B Metal Systems

$\lambda_{\rm obs}$ (Å)	Line ID	$z_{\rm obs}$[a]	$W_{\rm rest}$ (Å)
		Intervening	
6402.03 ± 0.06	Fe II $\lambda2382$	1.68680 ± 0.00002	0.51 ± 0.01
6602.02 ± 0.13	C IV $\lambda1548$	3.26419 ± 0.00006	0.15 ± 0.02
6612.57 ± 0.14	C IV $\lambda1551$	3.26419 ± 0.00006	0.13 ± 0.02
6704.31 ± 0.11	C IV $\lambda1548$	3.33041 ± 0.00006	0.14 ± 0.02
6707.40 ± 0.06	Mg II $\lambda2796$	1.39863 ± 0.00002	1.18 ± 0.03
6709.91 ± 0.11	Si II $\lambda1527$	3.39502 ± 0.00007	0.17 ± 0.02
6715.59 ± 0.19	C IV $\lambda1551$	3.33041 ± 0.00006	0.09 ± 0.02
6724.68 ± 0.07	Mg II $\lambda2804$	1.39863 ± 0.00002	0.91 ± 0.03
6804.02 ± 0.07	C IV $\lambda1548$	3.39476 ± 0.00003	1.48 ± 0.02
6815.18 ± 0.08	C IV $\lambda1551$	3.39476 ± 0.00003	1.09 ± 0.02
6843.29 ± 0.06	C IV $\lambda1548$	3.42022 ± 0.00003	1.58 ± 0.04
6854.89 ± 0.06	C IV $\lambda1551$	3.42022 ± 0.00003	1.25 ± 0.02
6949.75 ± 0.20	Fe II $\lambda2587$	1.68680 ± 0.00002	0.26 ± 0.05
6986.15 ± 0.08	Fe II $\lambda2600$	1.68680 ± 0.00002	0.50 ± 0.02
7387.85 ± 0.14	C IV $\lambda1548$	3.77191 ± 0.00007	0.18 ± 0.02
7400.22 ± 0.19	C IV $\lambda1551$	3.77191 ± 0.00007	0.09 ± 0.02
7513.04 ± 0.08	Mg II $\lambda2796$	1.68673 ± 0.00003[b]	0.70 ± 0.03
7532.51 ± 0.15	Mg II $\lambda2804$	1.68673 ± 0.00003[b]	0.68 ± 0.13
		Associated	
6502.00 ± 0.09	N V $\lambda1239$	4.24877 ± 0.00005	1.62 ± 0.05
6523.45 ± 0.08	N V $\lambda1243$	4.24877 ± 0.00005	1.31 ± 0.02
8125.49 ± 0.04	C IV $\lambda1548$	4.24847 ± 0.00002	1.94 ± 0.01
8139.44 ± 0.04	C IV $\lambda1551$	4.24847 ± 0.00002	1.68 ± 0.01

[a] Weighted mean redshift from all available transitions.

[b] Mg II doublet redshift computed from the $\lambda2796$ line only.

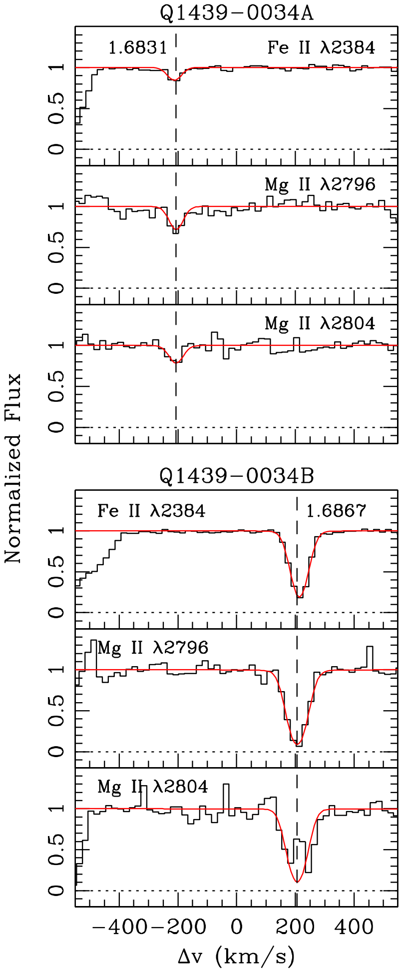

Figure 2.13 *Top three panels:* Continuum-normalized spectrum of Q1439A (histogram) showing the Mg II and Fe II absorption for the system at $z = 1.6831$. The continuous lines show Voigt profile fits. *Bottom three panels:* Same as the top panels, here for the system at $z = 1.6867$ in Q1439B. Several of the Mg II $\lambda2804$ pixels in Q1439B near 200 km s^{-1} in this plot are heavily affected by skylines and have been excluded from the fit. All components in both spectra are placed on a common velocity scale in order to demonstrate the longitudinal velocity separation between these systems.

restricts a line-by-line comparison. A statistical approach, however, suggests that the flux in paired spectra tends to be most similar in regions of either very strong or very weak absorption. The similarities at flux levels near the continuum are consistent with the large sizes of voids and low-density gaseous filaments and sheets expected to comprise much of the intergalactic medium. The more surprising similarities at low flux levels may simply reflect the limited dynamic range of transmitted flux in distinguishing among regions of high optical depth ($\tau \gg 1$). Larger differences in flux found at intermediate flux levels may relate to the increased scatter in flux naturally expected for optical depths near unity, and also to the fact that flux differences along the wings of strong lines will be sensitive to bulk velocity shifts between sightlines. Despite the difficulty in producing a clear physical interpretation from the data alone, both the correlation and flux statistics should provide a useful resource for comparison with numerical simulations.

In order to assess the dependence of the correlation functions on photon noise and spectral resolution we have employed high-quality ESI and HIRES spectra of Q1422. Adding photon noise has very little effect for $S/N \gtrsim 10$ per resolution element except to introduce a spike in the autocorrelation at zero lag. Increasing the resolution FWHM increases the velocity width of the autocorrelation and decreases its amplitude, as expected. These effects may occur unevenly, however, due to the incorporation of noise features as the peak broadens. We further tested the effects of resolution on the relative amplitudes of the autocorrelation and cross-correlation by degrading the resolution of our ESI spectra to match that of a low-resolution spectrograph such as Keck/LRIS or VLT/FORS2. For both pairs, the cross-correlation and autocorrelations agree well for our adopted cosmology when the correlations are computed from the original ESI data. Smoothing the spectra, however, substantially reduces the cross-correlation with respect to the autocorrelations. This will typically occur at any velocity lag where the intrinsic correlation function is non-linear on scales smaller than the width of the smoothing kernel. Cosmological tests making use of the Lyα forest correlation length should take this effect into account.

Finally, we present an inventory of metal lines in Q1424, Q1439A, and Q1439B in the appendix. The most noteworthy features are a pair of strong C IV complexes at $z \approx 3.4$ appearing only toward Q1439B. Given their large equivalent widths, the relatively small separation between these systems suggests that they are related, possibly arising from separate galaxy halos or two sides of a galactic outflow. Low-ionization systems containing Mg II and Fe II appear at $z \approx 1.68$ in Q1439 A and B separated by 410 km s^{-1}. These may either represent a single, extended structure ($\Delta l \gtrsim 280\ h_{70}^{-1}$ proper kpc) or separate, clustered absorbers. A C IV system appears toward Q1424 at $z = 3.084$, within 440 km s^{-1} of a known C IV system toward Q1422. A single absorber responsible for both systems would have a transverse size $\gtrsim 290\ h_{70}^{-1}$ proper kpc. The number density of weak C IV systems at this redshift, however, suggests that these lines may instead result from chance superposition.

The authors would like to thank Chuck Steidel for bringing Q1424+2255 to our attention and for the additional data on this object, Kurt Adelberger for his ESI reduction of Q1424, Lynne Hillenbrand for kindly sharing her observations of Q1439A, and Rob Simcoe for his HIRES reduction of Q1422A. We would also like to thank Tom Barlow for making public the MAKEE software package, Bob Carswell for VPFIT, and the anonymous referee for helpful comments. Finally, we are indebted to the indigenous Hawaiian community for the opportunity to conduct observations from their sacred mountain. Without their hospitality this work would not have been possible. W.L.W.S gratefully acknowledges support from the NSF through grants AST-9900733 and AST-0206067. M.R. has been supported by the NSF through grant AST-0098492 and by NASA through grant AR-90213.01A.

Chapter 3

Discovery of excess O I absorption towards the $z = 6.42$ QSO SDSS J1148+5251[1]

Abstract

We present a search for O I in the spectra of nine $4.9 \leq z_{\rm QSO} \leq 6.4$ QSOs taken with Keck/HIRES. We detect six systems with $N_{\rm O\,I} > 10^{13.7}$ cm^{-2} in the redshift intervals where O I $\lambda1302$ falls redward of the Lyα forest. Four of these lie towards SDSS J1148+5251 ($z_{\rm QSO} = 6.42$). This imbalance is unlikely to arise from variations in sensitivity among our data or from a statistical fluctuation. The excess O I occurs over a redshift interval that also contains transmission in Lyα and Lyβ. Therefore, if these O I systems represent pockets of neutral gas, then they must occur within or near regions of the IGM that are highly ionized. In contrast, no O I is detected towards SDSS J1030+0524 ($z_{\rm QSO} = 6.30$), whose spectrum shows complete absorption in Lyα and Lyβ over $\Delta z \sim 0.2$. Assuming no ionization corrections, we measure mean abundance ratios $\langle[{\rm O/Si}]\rangle = -0.04 \pm 0.06$, $\langle[{\rm C/O}]\rangle = -0.31 \pm 0.09$, and $\langle[{\rm C/Si}]\rangle = -0.34 \pm 0.07$ (2σ), which are consistent with enrichment dominated by Type II supernovae. The O/Si ratio limits the fraction of silicon in these systems contributed by metal-free very massive stars to $\lesssim 30\%$, a result which is insensitive to ionization corrections. The ionic comoving mass densities along the $z_{\rm QSO} > 6.2$ sightlines, including only the detected systems, are $\Omega_{\rm O\,I} = (7.0 \pm 0.6) \times 10^{-8}$, $\Omega_{\rm Si\,II} = (9.6 \pm 0.9) \times 10^{-9}$, and $\Omega_{\rm C\,II} = (1.5 \pm 0.2) \times 10^{-8}$.

---

[1] Originally published in *The Astrophysical Journal*, v. 640, p. 69; written with W. L. W. Sargent, M. Rauch, and R. A. Simcoe (Copyright 2006, The American Astronomical Society)

3.1 Introduction

The state of the intergalactic medium (IGM) at redshift $z \sim 6$ remains under considerable debate. Significant transmitted flux in the Lyα forest at $z \sim 5.7$ means that the IGM must have been highly ionized by at least ~ 1 Gyr after the Big Bang (Becker et al. 2001; Djorgovski et al. 2001; Fan et al. 2001, 2004). Each of the four known QSOs at $z_{\rm QSO} \geq 6.2$ show Gunn-Peterson troughs (Gunn & Peterson 1965) over at least a narrow redshift interval (Becker et al. 2001; Pentericci et al. 2002; Fan et al. 2001, 2003, 2004; White et al. 2003). This complete lack of transmitted flux has been interpreted as an indication that the tail end of cosmic reionization may extend to $z \sim 6$. Songaila (2004), however, found the evolution of transmitted flux over $2 < z < 6.3$ to be consistent with a smoothly decreasing ionization rate and not indicative of a sudden jump in the Lyα optical depth at $z \sim 6$.

Significant variations in the fraction of transmitted flux are common among sightlines at the same redshift (Songaila 2004). While the spectrum of SDSS J1030+0524 ($z_{\rm QSO} = 6.30$) shows complete absorption in Lyα and Lyβ over a redshift interval $\Delta z \approx 0.2$ (White et al. 2003), transmitted flux appears over the same redshifts in the Lyα, Lyβ, and Lyγ forests of SDSS J1148+5251 ($z_{\rm QSO} = 6.42$) (White et al. 2005; Oh & Furlanetto 2005). Either the IGM is highly ionized everywhere at $z \sim 6.3$ and long stretches of complete absorption are the result of line blending, or the neutral fraction of the IGM is patchy on large scales. A patchy IGM could result from the clumpiness of the IGM and the clustering of ionizing sources (Furlanetto & Oh 2005).

Studies of H I transmitted flux are ultimately hampered by the large optical depths expected for even a small neutral fraction. The presence of a Gunn-Peterson trough can at best constrain the volume- and mass-weighted H I neutral fractions to $\gtrsim 10^{-3}$ and $\gtrsim 10^{-2}$, respectively (Fan et al. 2002). Alternative measurements are required to probe larger neutral fractions. The non-evolution in the luminosity function of Lyα-emitting galaxies provides an independent indication that the IGM at $z \sim 6.5$ is highly ionized (e.g., Malhotra & Rhoads 2004; Stern et al. 2005), although Lyα photons may escape as a result of galactic winds (Santos 2004) or from locally ionized bubbles created by clustered sources (Furlanetto et al. 2004a). In the future, observations of redshifted 21 cm emission/absorption should trace the growth and evolution of ionized regions at $z > 6$, placing strong constraints on reionization scenarios (e.g., Tozzi et al. 2000; Kassim et al. 2004; Carilli et al. 2004; Furlanetto et al.

2004b).

A high neutral fraction must also have a measurable effect on metal absorption lines (Oh 2002; Furlanetto & Loeb 2003). Overdense regions of the IGM should be the first to become enriched, due to the presence of star-forming sources, yet the last to remain ionized, due to the short recombination times (Oh 2002). Low-ionization metal species should therefore produce numerous absorption features in the spectra of background objects prior to reionization. A particularly good candidate is O I, which has an ionization potential nearly identical to that of H I and a transition at 1302 Å that can be observed redward of the Lyα forest. Oxygen and hydrogen will lock in charge-exchange equilibrium (Osterbrock 1989), which ensures that their neutral fractions will remain nearly equal,

$$f_{\mathrm{H\,I}} \equiv \frac{n_{\mathrm{H\,I}}}{n_{\mathrm{H}}} \approx \frac{n_{\mathrm{O\,I}}}{n_{\mathrm{O}}}\,. \tag{3.1}$$

Despite the increased photo-ionization cross section of O I at higher energies, this relationship is expected to hold over a wide range in $f_{\mathrm{H\,I}}$ (Oh et al. 2005, in prep).

In this work, we present a search for O I in the spectra of nine $4.9 \leq z_{\mathrm{QSO}} \leq 6.4$ QSOs. This is the first time a set of $z_{\mathrm{QSO}} > 5$ spectra has been taken at high resolution (R = 45,000). Our sample includes three objects at $z_{\mathrm{QSO}} > 6.2$, where we might expect to see an "O I forest" (Oh 2002). In §3.2 we describe the observations and data reduction. The results of the O I search are detailed in §3.3. In §3.4 we demonstrate a significant overabundance of O I systems towards the highest-redshift object, SDSS J1148+5251 ($z_{\mathrm{QSO}} = 6.42$), and compare the overabundance to the number density of lower-redshift O I systems and other absorbers with high H I column densities. Measurements of the relative metal abundances for all the detected systems are described in §3.5. In §3.6 we discuss the significance of these excess systems for the enrichment and ionization state of the IGM at $z \sim 6$. Our results are summarized in §3.7. Throughout this paper we assume $\Omega = 1$, $\Omega_{\mathrm{m}} = 0.3$, $\Omega_{\Lambda} = 0.7$, and $H_0 = 70$ km s^{-1} Mpc^{-1}.

3.2 The Data

Observations using the Keck HIRES spectrograph (Vogt et al. 1994) were made between 2003 February and 2005 June, with the bulk of the data acquired during 2005 January and

Table 3.1. Summary of Observations for O I Search

QSO	$z_{\rm QSO}$	Dates	$\Delta t_{\rm exp}$ (hrs)[a]
SDSS J2225−0014	4.87	2004 Jun	6.7[b]
SDSS J1204−0021	5.09	2005 Jan - Feb	6.7
SDSS J0915+4244	5.20	2005 Jan - Feb	10.8
SDSS J0231−0728	5.42	2005 Jan - Feb	10.0
SDSS J0836+0054	5.80	2003 Feb - 2005 Jan	21.7[c]
SDSS J0002+2550	5.82	2005 Jan - Jun	4.2
SDSS J1623+3112	6.22	2005 Jun	12.5
SDSS J1030+0524	6.30	2005 Feb	12.0
SDSS J1148+5251	6.42	2003 Feb - 2005 Feb	22.0[d]

[a] All exposures were taken with the upgraded HIRES detector unless otherwise noted.

[b] Taken with the old HIRES detector

[c] 9.2 hrs taken with the old HIRES detector

[d] 4.2 hrs taken with the old HIRES detector

February. Our QSO sample and the observations are summarized in Table 3.1. All except the 2003 February data were taken with the upgraded HIRES detector. We used an $0''.86$ slit, which gives a velocity resolution FWHM of $\Delta v = 6.7$ km s^{-1}.

The continuum luminosities in our sample approach the practical detection limit of HIRES. In addition, the spectral regions of interest for this work lie in the far red, where skyline contamination and atmospheric absorption are major concerns. To address these difficulties, the data were reduced using a custom set of IDL routines written by one of us (GDB). This package uses optimal sky subtraction (Kelson 2003) to achieve Poisson-limited residuals in the two-dimensional sky-subtracted frame. One-dimensional spectra were extracted using optimal extraction (Horne 1986). Blueward of the Lyα emission line, the continuum for these objects is highly obscured due to strong absorption from the Lyα forest. Furthermore, single exposures were typically too faint to fit reliable continua even in unabsorbed regions. Individual orders were therefore combined by first flux calibrating each order using the response function derived from a standard star. The combined spectra were continuum-fit by hand using a cubic spline. Standards stars were also to correct for telluric absorption. Estimated residuals from continuum fitting (redward of Lyα) and atmospheric correction are typically within the flux uncertainties.

3.3 O I Search

3.3.1 Technique

At $z > 5$ it becomes increasingly difficult to identify individual Lyα lines due to the large opacity in the Lyα forest. Therefore, candidate O I lines must be confirmed using other ions at the same redshift. Si II λ1260 and C II λ1334 are the most useful for this purpose since their rest wavelengths place them redward of the Lyα forest, at least over a limited range in redshift. These transitions are also expected to be relatively strong over a range in ionization conditions. At lower redshifts where Si II λ1260 has entered the forest, we are still sensitive to Si II λ1304, although it is weaker than Si II λ1260 by a factor of 7.

We searched for O I in each sightline over the redshift range between the quasar redshift $z_{\rm QSO}$ and the redshift $z_{\rm min} = (1 + z_{\rm QSO})\lambda_{\alpha}/\lambda_{\rm O\,I} - 1$, where O I enters the Lyα forest. To identify a system, we required absorption at the same redshift in O I and either Si II λ1260 or C II λ1334, and that the line profiles for at least two of the ions be comparable. In practice, Si II λ1260 proved to be the best indicator over the lower-redshift end of each sightline, since the signal-to-noise (S/N) ratio was typically better over that region of the spectrum. At redshifts where Si II λ1260 was lost in the forest we relied solely upon C II for confirmation. By chance, the two O I systems we identified using only C II were also strong enough to be detected in Si II λ1304.

We identified six O I systems in total along our nine lines of sight. Their properties are summarized in Table 3.2. Four of the six systems appear towards SDSS J1148+5251, and we examine this potential overabundance in detail in §3.4. Voigt profiles were fitted using the VPFIT package written, by R. Carswell. Due to line blending and the modest S/N ratio over some regions of the data, it was often necessary to tie the redshift and/or Doppler parameter of one ion to those of another whose profile was more clearly defined in order to obtain a satisfactory fit. In practice, the resulting total column densities are very similar to those obtained when all parameters are allowed to vary freely, as would be expected for systems still on the linear part of the curve of growth. Comments on individual systems are given below.

Table 3.2. Measured Properties of O I Systems

Ion	z	b (km s^{-1})	$\log N$ (cm^{-2})
SDSS J0231−0728: $z_{\rm sys} = 5.3364$			
Si II	5.333982 ± 0.000008	5.38 ± 0.58	12.786 ± 0.055
C II[a]	5.333982	5.38	13.584 ± 0.068
Si II	5.335928 ± 0.000020	6.91 ± 1.33	12.514 ± 0.079
Si II	5.336337 ± 0.000019	7.62 ± 1.60	12.978 ± 0.087
Si II[b]	5.336721	12.96	12.711 ± 0.135
O I[a]	5.335928	6.91	13.982 ± 0.086
O I[a]	5.336337	7.62	14.138 ± 0.129
O I	5.336721 ± 0.000072	12.96 ± 3.23	13.972 ± 0.143
C II[a]	5.335928	6.91	13.298 ± 0.077
C II[a]	5.336337	7.62	13.454 ± 0.119
C II[b]	5.336721	12.96	13.314 ± 0.138
Si II	5.337841 ± 0.000014	10.89 ± 0.98	12.678 ± 0.040
Si II	5.338474 ± 0.000043	11.71 ± 3.39	12.233 ± 0.098
Si II	5.339301 ± 0.000016	10.44 ± 1.13	12.316 ± 0.063
C II[a]	5.337841	10.89	13.512 ± 0.051
C II[a]	5.338474	11.71	12.880 ± 0.161
C II[a]	5.339301	10.45	13.074 ± 0.097
Si IV[a]	5.337841	10.89	12.848 ± 0.051
Si IV[a]	5.338474	11.71	12.142 ± 0.192
Si IV[a]	5.339301	10.44	12.950 ± 0.049
SDSS J1623+3112: $z_{\rm sys} = 5.8408$			
O I[c]	5.836481 ± 0.000012	5.01 ± 0.59	14.376 ± 0.075
O I[c]	5.836806 ± 0.000017	4.44 ± 1.57	14.216 ± 0.111
Si II[c]	5.836423 ± 0.000029	3.63 ± 2.66	12.746 ± 0.182
Si II[c]	5.836799 ± 0.000060	10.82 ± 4.29	12.985 ± 0.124
Si II[d]	5.839938	6.37	13.279 ± 0.182
Si II[d]	5.840138	4.13	13.063 ± 0.340
Si II[b]	5.840456	6.92	12.931 ± 0.196
Si II[b]	5.840798	5.32	13.488 ± 0.060
Si II[b]	5.841113	7.33	13.271 ± 0.078
Si II[b]	5.841456	1.77	11.655 ± 1.018
Si II[d]	5.841780	6.23	12.854 ± 0.070

Table 3.2 (cont'd)

Ion	z	b (km s^{-1})	$\log N$ (cm^{-2})
O I$^{\rm d}$	5.839938	6.37	14.214 ± 0.212
O I$^{\rm d}$	5.840138	4.13	14.152 ± 0.242
O I	5.840456 ± 0.000032	6.92 ± 4.21	13.734 ± 0.206
O I	5.840798 ± 0.000014	5.32 ± 0.94	14.384 ± 0.084
O I	5.841113 ± 0.000025	7.33 ± 1.48	14.316 ± 0.073
O I	5.841456 ± 0.000014	1.77 ± 1.72	13.518 ± 0.150
O I$^{\rm d}$	5.841780	6.23	13.793 ± 0.027
C II	5.839938 ± 0.000055	6.37 ± 1.56	13.811 ± 0.231
C II	5.840138 ± 0.000039	4.13 ± 2.50	13.955 ± 0.249
C II$^{\rm b}$	5.840456	6.92	13.431 ± 0.193
C II$^{\rm b}$	5.840798	5.32	13.771 ± 0.093
C II$^{\rm b}$	5.841113	7.33	13.316 ± 0.101
C II	5.841780 ± 0.000007	6.23 ± 0.51	13.736 ± 0.055
SDSS J1148+5251: $z_{\rm sys} = 6.0097$			
Si II$^{\rm b}$	6.009119	7.02	12.126 ± 0.592
Si II$^{\rm b}$	6.009290	3.36	12.770 ± 0.137
Si II$^{\rm b}$	6.009717	8.44	13.323 ± 0.037
Si II$^{\rm b}$	6.010070	4.94	12.331 ± 0.261
O I	6.009119 ± 0.000112	7.02 ± 3.18	13.593 ± 0.371
O I	6.009290 ± 0.000012	3.36 ± 1.28	14.071 ± 0.113
O I	6.009717 ± 0.000010	8.44 ± 0.96	14.487 ± 0.030
O I	6.010070 ± 0.000034	4.94 ± 1.60	13.516 ± 0.178
C II$^{\rm b}$	6.009119	7.02	13.180 ± 0.328
C II$^{\rm b}$	6.009290	3.36	13.281 ± 0.286
C II$^{\rm b}$	6.009717	8.44	14.013 ± 0.057
C II$^{\rm b}$	6.010070	4.94	13.044 ± 0.182
SDSS J1148+5251: $z_{\rm sys} = 6.1293$			
C II$^{\rm c}$	6.127673 ± 0.000039	6.11 ± 3.03	12.916 ± 0.118
C II$^{\rm c}$	6.128589 ± 0.000037	8.08 ± 2.47	13.101 ± 0.092
Si II$^{\rm b}$	6.129267	6.51	13.273 ± 0.050
O I	6.129267 ± 0.000006	6.51 ± 0.49	14.606 ± 0.096
C II$^{\rm b}$	6.129267	6.51	13.744 ± 0.070
C II$^{\rm c}$	6.129885 ± 0.000017	2.21 ± 1.80	13.161 ± 0.186

Table 3.2 (cont'd)

Ion	z	b (km s^{-1})	$\log N$ (cm^{-2})
	SDSS J1148+5251: $z_{\rm sys} = 6.1968$		
Si II	6.196787 ± 0.000014	7.82 ± 0.84	12.277 ± 0.044
O I[a]	6.196787	7.82	13.727 ± 0.061
C II[a]	6.196787	7.82	13.027 ± 0.072
	SDSS J1148+5251: $z_{\rm sys} = 6.2555$		
C II[c]	6.255234 ± 0.000131	12.13 ± 5.51	13.159 ± 0.229
Si II	6.255496 ± 0.000004	4.30 ± 0.27	12.900 ± 0.040
O I	6.255465 ± 0.000015	5.08 ± 1.04	14.075 ± 0.087
C II[a]	6.255496	4.30	13.596 ± 0.114

[a] The z- and b-values for this component were tied to those for Si II.

[b] The z- and b-values for this component were tied to those for O I.

[c] Unconfirmed component

[d] The z- and b-values for this component were tied to those for C II.

SDSS J0231−0728: $z_{\rm sys} = 5.3364$ (Figure 3.1)

This system shows a central complex in O I, Si II, and C II that is best fit using three components with a total velocity span of $\Delta v \approx 38$ km s^{-1}. We measure the redshifts and b-parameters of the bluest two central components from Si II. The redshift and b-parameter for the reddest central component are measured from O I, which is least affected by additional lines towards the red. Leaving all parameters untied produces a two-component fit for C II, which is likely due to low S/N. However, the total column densities remain virtually unchanged.

A single component at $\Delta v \approx -115$ km s^{-1} appears in Si II and C II but not in O I. Since O I is more easily ionized than either Si II or C II ($\Delta E_{\rm O\,I} = 13.6$ eV, $\Delta E_{\rm Si\,II} = 16.3$ eV, $\Delta E_{\rm C\,II} = 24.4$ eV), this component probably arises from gas that is more highly ionized than the gas producing the O I absorption. Three additional components appear redward of the central O I complex. These are visible in Si II, C II, and Si IV and presumably correspond to

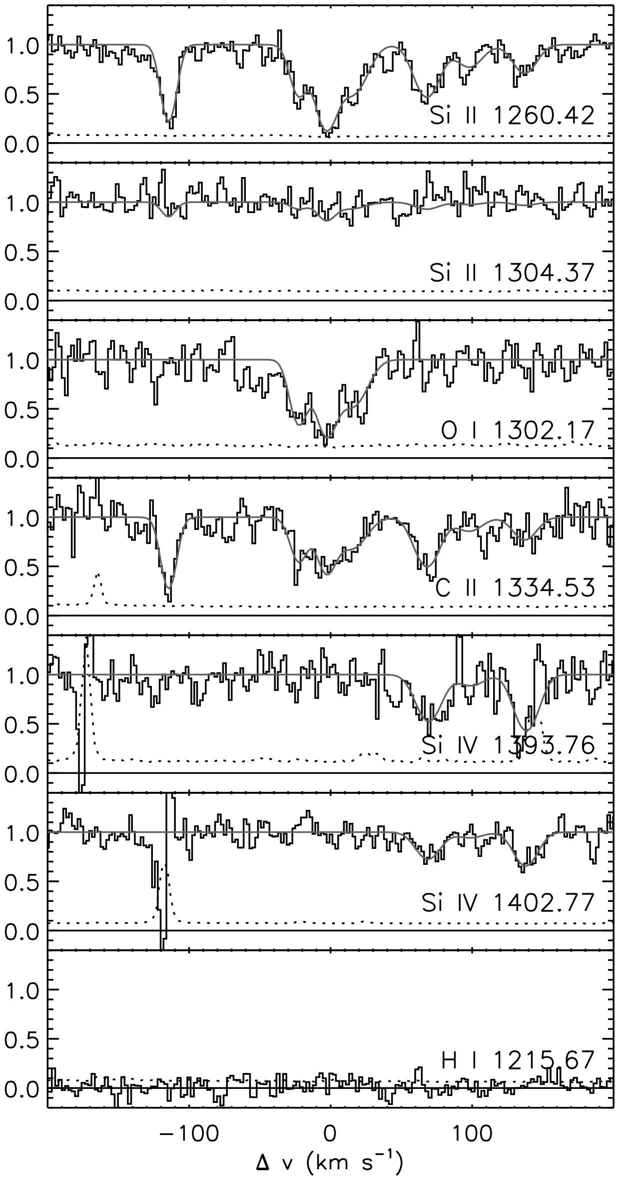

Figure 3.1 Absorption lines for the $z_{\rm sys} = 5.3364$ O I system towards SDSS J0231−0728. Regions of the spectrum covering individual transitions have been shifted onto a common velocity scale. The *histogram* shows the normalized flux. The *solid line* shows the best Voigt profile fit. The *dotted line* shows the 1σ flux error.

gas in a still higher ionization state. We use Si II to constrain the redshift and b-parameters for all the non-O I components, although fitting without tying any parameters produces very similar results.

SDSS J1623+3112: $z_{\rm sys} = 5.8408$ (Figure 3.2)

This system shows multiple components with a total velocity span of $\Delta v \approx 81$ km s^{-1}. The Si II is strong enough that the 1304 Å transition is clearly visible. Some additional absorption occurs along the blue edge of the O I complex. Since no corresponding absorption appears in C II, however, this features is unlikely to be genuine O I. We use C II to fix the redshifts and b-parameters of the bluest two components and the reddest component for all ions. The z and b values for the remaining components are tied to O I. The weakest C II component was automatically dropped by the fitting program. This should not, however, have a significant impact on the summed C II column density. No Si IV was detected down to $N_{\rm Si\ IV} > 10^{13}$ cm^{-2}.

A strong line appears at a velocity separation $\Delta v \approx -180$ km s^{-1} from the O I complex. Weak absorption appears at the same velocity in Si II λ1304. The corresponding C II region, however, is completely covered by Mg I λ2853 from a strong Mg II system at $z_{\rm abs} = 2.1979$. Therefore, while these features are plausibly associated with the O I complex, their identity cannot presently be confirmed. We do not include these lines when computing the relative abundances, although their O I/Si II ratio is consistent with those measured for the other O I systems.

SDSS J1148+5251: $z_{\rm sys} = 6.0097$ (Figure 3.3)

This system shows multiple components with a velocity span of $\Delta v \approx 41$ km s^{-1}. The Si II λ1260 transition falls in the Lyα forest. Si II λ1304, however, is clearly visible. The C II occurs among moderate-strength telluric absorption. In correcting for the atmosphere we recovered a C II velocity profile very similar to that of O I and Si II. Some additional absorption around the C II are probably telluric lines that were not completely removed. We achieved the best fit for O I using four components while allowing the continuum level to vary slightly. Using fewer components resulted in virtually the same total $N_{\rm O\ I}$, which is to be expected if the lines lie along the linear part of the curve of growth. We used the z and b

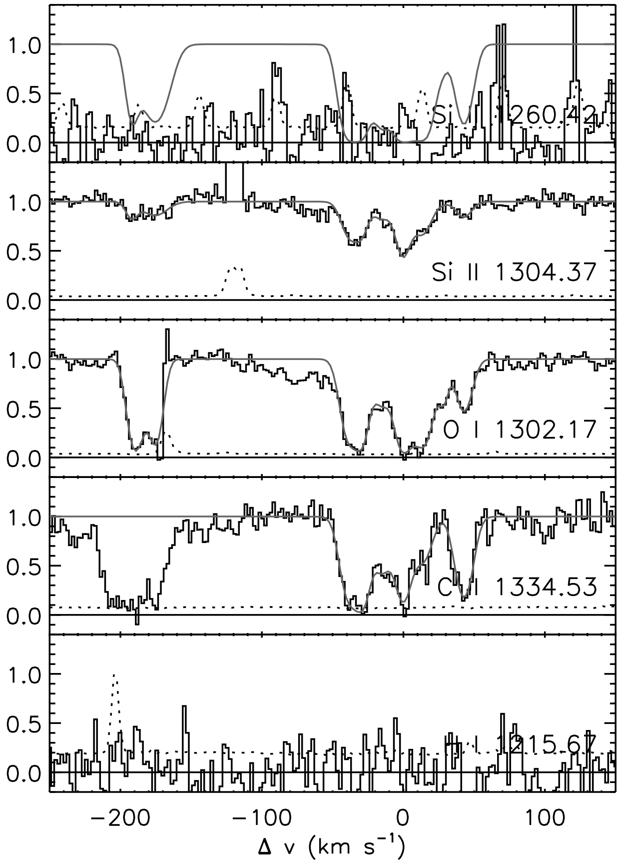

Figure 3.2 Absorption lines for the $z_{\rm sys} = 5.8408$ O I system towards SDSS J1623+3112. See Figure 3.1 for details. The sharp features around Si II $\lambda1260$ are noise in the Lyα forest. The components at $\Delta v \approx -180$ km s^{-1} are unconfirmed due to the strong $z_{\rm abs} = 2.1979$ Mg I absorption at the wavelength where we would expect to see C II.

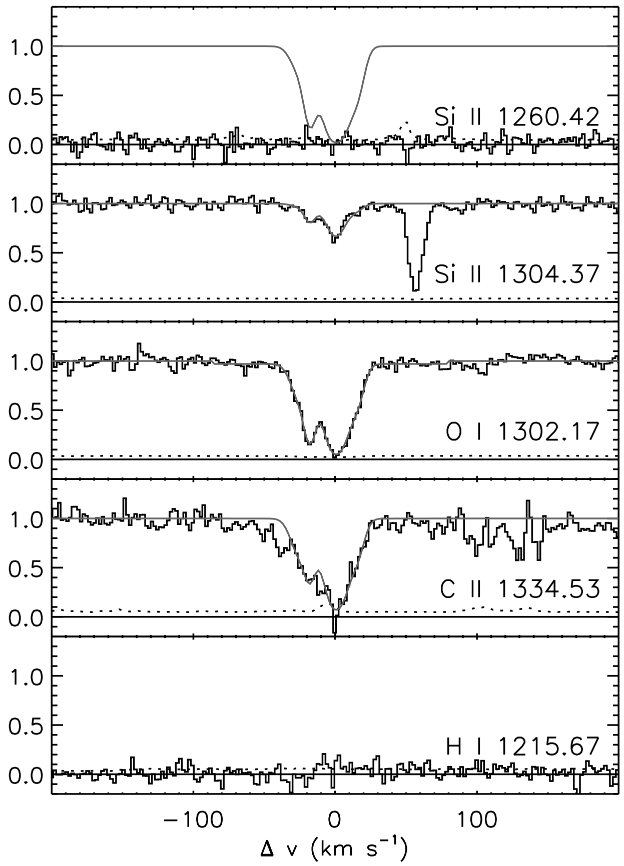

Figure 3.3 Absorption lines for the $z_{\rm sys} = 6.0097$ O I system towards SDSS J1148+5251. See Figure 3.1 for details. Si II $\lambda1260$ falls in the Lyα forest. The strong line at $\Delta v = 57$ km s^{-1} from Si II $\lambda1304$ is Si II $\lambda1260$ at $z = 6.2555$. The absorption features at $\Delta v \approx -40$ km s^{-1} and $\Delta v \approx 90 - 140$ km s^{-1} from C II are probably telluric absorption that has not been fully removed.

values for these four O I lines to determine the corresponding column densities for Si II and C II. Leaving all parameters untied resulted in small changes in the b-parameters and in the preferred number of lines used by VPFIT (3 for Si II instead of 4), but negligible changes in the total column density for each ion. We detect no Si IV down to $N_{\rm Si\,IV} > 10^{12.5}$ cm^{-2}. This system does show C IV absorption in the low-resolution NIRSPEC spectrum taken by Barth et al. (2003). The kinematic structure, however, cannot be determined from their data, and it is therefore unknown whether the C IV absorption arises from the same gas that produces the lower-ionization lines.

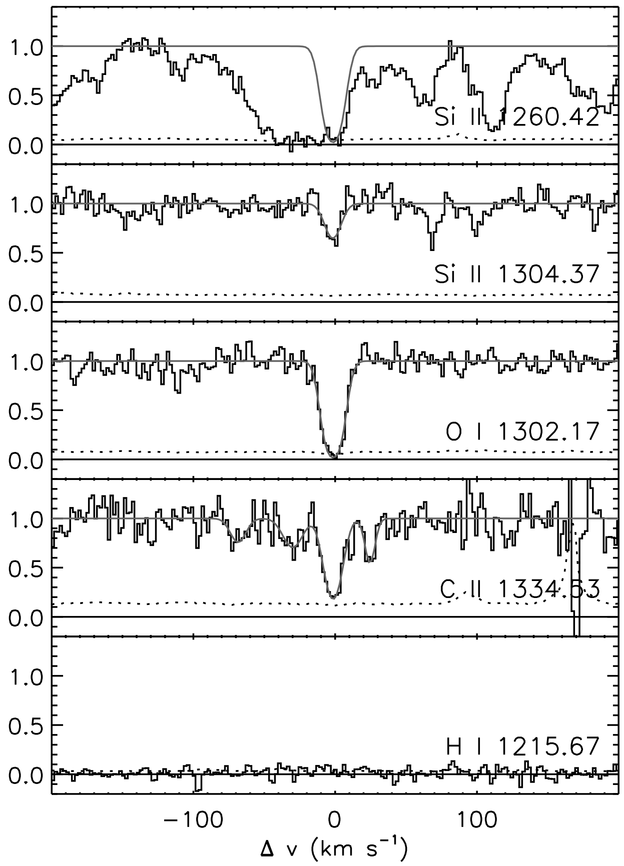

Figure 3.4 Absorption lines for the $z_{\rm sys} = 6.1293$ O I system towards SDSS J1148+5251. See Figure 3.1 for details. The features around Si II λ1260 are Lyα absorption in the quasar proximity region. The C II components at $\Delta v = -67, -29$ and 26 km s^{-1} are unconfirmed.

SDSS J1148+5251: $z_{\rm sys} = 6.1293$ (Figure 3.4)

The Si II λ1260 line for this system falls in the Lyα forest. Si II λ1304, however, is strong enough to be visible. We tie the redshifts and b-parameters for Si II and C II at $z = 6.129267$ to those for O I, which has the cleanest profile. Leaving all parameters untied produces changes in the b-parameters that are within the errors and negligible changes in the column densities. Possible additional C II lines appear at $\Delta v = -67$, -29, and 26 km s^{-1} from the strong component. These do not appear in O I and would probably be too weak to appear in Si II λ1304. We do not include them when computing the relative abundances for this system. No Si IV was detected down to $N_{\rm Si\,IV} > 10^{12.7}$ cm^{-2}.

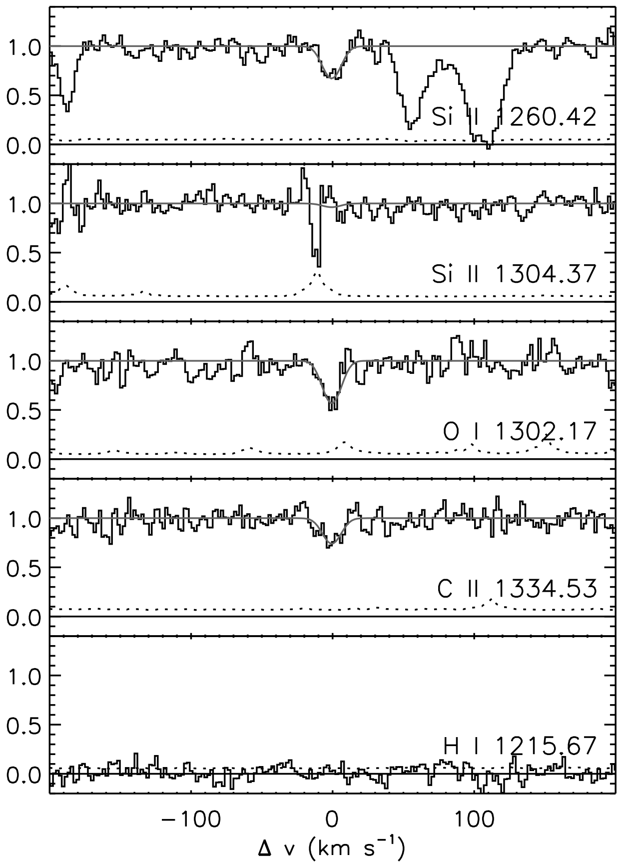

Figure 3.5 Absorption lines for the $z_{\rm sys} = 6.1968$ O I system towards SDSS J1148+5251. See Figure 3.1 for details. The features near Si II λ1260 are unrelated metal lines. The sharp feature near Si II λ1304 is the residual from a strong skyline.

SDSS J1148+5251: $z_{\rm sys} = 6.1968$ (Figure 3.5)

The Si II λ1260 and C II lines for this system occur in transparent gaps within regions of mild telluric absorption. In some of our exposures, the O I line falls on the blue wing of a strong telluric feature. The O I, however, can be clearly seen in the uncorrected 2005 January data, where the heliocentric velocity shifted the observed QSO spectrum further to the blue. We tie the redshifts and b-values for O I and C II to those of Si II, for which the line profile is the cleanest. Leaving all parameters untied produces negligible changes in the column densities.

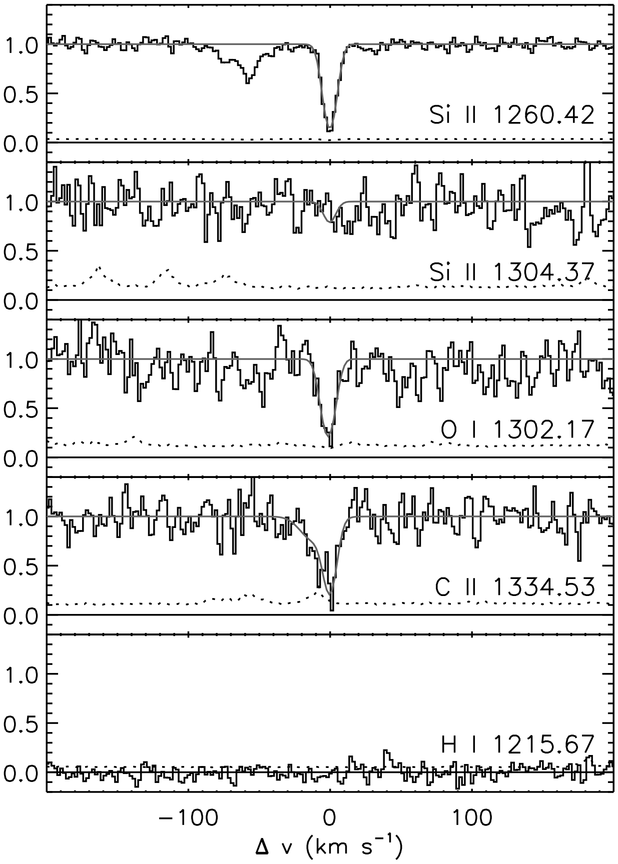

Figure 3.6 Absorption lines for the $z_{\rm sys} = 6.2555$ O I system towards SDSS J1148+5251. See Figure 3.1 for details. The absorption at $\Delta v \approx -60$ km s^{-1} from Si II λ1260 is Si II λ1304 at $z = 6.0097$. The C II fit includes an unconfirmed component on the blue edge of the profile.

SDSS J1148+5251: $z_{\rm sys} = 6.2555$ (Figure 3.6)

We use a single component for the primary fit to this system. The C II falls on a sky emission line and hence the line profile is rather noisy. We therefore tied the redshift and b-parameter for C II to those of Si II, while z and b for O I were allowed to vary freely. The fitted z and b values for O I agree with those for Si II within the fit errors. Tying z and b for O I to those of Si II produced no significant change in $N_{\rm O\,I}$. Both Si II λ1260 and O I are well fit by a single line, while the blue edge of the C II shows a possible additional component. We fit this component separately but do include it when computing relative abundances.

3.4 Overabundance of O I systems towards SDSS J1148+5251

Despite the relatively small total number of detected O I systems, a noticable overabundance appears towards SDSS J1148+5251. It should be noted that this object has one of the brightest continuum magnitudes among QSOs at $z > 5$ (Fan et al. 2003). We also spent considerable integration time on this object. Therefore, the data are among the best in our sample. In this section we address the null hypothesis that the apparent imbalance in the distribution of O I systems results from a combination of incompleteness and small number statistics.

For each sightline we used an automated scheme to determine the absorption pathlength interval ΔX over which we are sensitive to systems above a given O I column density. For a non-evolving population of sources expanding with the Hubble flow, we expect to intersect the same number of sources per unit X at all redshifts, where X is defined for $\Omega = 1$ as

$$dX = \frac{(1+z)^2}{\sqrt{\Omega_{\rm m}(1+z)^3 + \Omega_\Lambda}} dz \, . \tag{3.2}$$

At the redshift of each pixel where we are potentially sensitive to O I, we inserted artificial single-component systems containing O I, Si II, and C II with relative abundances set to the mean measured values (see §3.5) and a turbulent Doppler width of $b = 10$ km s^{-1}. The minimum $N_{\rm O\,I}$ at which the system could be detected by the automated program was then determined. A detection required that there be significant (4σ) absorption at the expected wavelengths of O I and at least one of the other two ions. The redshifts of at least two of the three fitted profiles must also agree within a tolerance of $\Delta z_{tol} = 0.0002$, and the line widths must agree to within a factor of two. In the case where the fitted profiles agree for only two of the ions, the spectrum at the wavelength of the third ion must be consistent with the expected level of absorption. This allows for one of the ions to be blended with another line or lost in Lyα forest. Lines that fell in the Fraunhofer A band were not considered. This method detected all of the known O I systems and produced only one false detection in the real data, which was easily dismissed by visual inspection. We note that this method focuses on our ability to detect systems similar to those observed towards SDSS J1148+5251. Multiple-component systems such as the two at lower redshift are in general easy to identify, even in noisy regions of the spectrum.

The results of the sensitivity measurements are shown in Figure 3.7. The solid lines show the ΔX over which we are sensitive to systems with $N_{\rm O\,I} \geq N_{\rm O\,I}^{\rm min}$. The O I column densities for the four systems seen towards SDSS J1148+5251 are marked with circles. The dashed line shows the mean ΔX as a function of $N_{\rm O\,I}^{\rm min}$ for all nine sightlines. While it is clear that the path length over which we are sensitive to low-column density systems is considerably smaller for some sightlines than for SDSS J1148+5251, there does exist significant coverage across the total sample even at the $N_{\rm O\,I}$ of the weakest system in our sample.

Completeness effects will depend on the intrinsic distribution of line strengths, in that weaker systems will more easily be lost in low-S/N sightlines. It is useful to define an effective absorption pathlength interval $\Delta X^{\rm eff}$ such that, for a sightline with a total pathlength $\Delta X^{\rm tot}$ and sensitivity $S(N)$, we would expect to detect the same number $\mathcal{N}$ of systems with $N \geq N_{\rm min}$ over $\Delta X^{\rm eff}$ if we had perfect sensitivity. For a column-density distribution $f(N) = \partial^2 \mathcal{N} / \partial N \partial X$, this gives

$$\Delta X^{\rm eff} \int_{N_{\rm min}}^{\infty} f(N)\, dN = \Delta X^{\rm tot} \int_{N_{\rm min}}^{\infty} f(N)\, S(N)\, dN\,, \tag{3.3}$$

where $S(N)$ is the fraction of the total pathlength over which we are sensitive to systems with column density N. The sensitivity function can be determined directly from Figure 3.7. We assume a conventional power-law distribution in O I column densities $f(N_{\rm O\,I}) \propto N_{\rm O\,I}^{-\alpha}$. Hence,

$$\Delta X^{\rm eff} = \Delta X^{\rm tot} \frac{\int_{N_{\rm min}}^{\infty} N^{-\alpha}\, S(N)\, dN}{\int_{N_{\rm min}}^{\infty} N^{-\alpha}\, dN}\,. \tag{3.4}$$

Taking into account our measured sensitivity, the maximum likelihood estimator for α for all six O I systems is $\hat{\alpha} = 1.7$. A K-S test allows $1.3 \leq \alpha \leq 2.1$ at the 95% confidence level.

In Figure 3.8 we plot $\Delta X^{\rm eff}$ as a function of α taking $N_{\rm min} = 10^{13.7}$ cm^{-2} as the cutoff value. The solid line shows $\Delta X^{\rm eff}$ for SDSS J1148+5251, while the dashed line shows $\Delta X^{\rm eff}$ for the remaining eight sightlines, divided by 5.7 to match SDSS J1148+5251 at $\alpha = 1.7$. It is easy to see that the ratio $\Delta X^{\rm eff}_{1148} / \Delta X^{\rm eff}_{\rm other}$ does not change significantly with α ($\lesssim 4\%$ over $1.1 \leq \alpha \leq 3.0$). This is purely a coincidence, most likely related to the fact that the overall high quality of the SDSS J1148+5251 data is balanced by the placement of the O I systems in a difficult region of the spectrum. However, it means that the relative numbers of expected O I detections for SDSS J1148+5251 and the remaining eight sightlines should

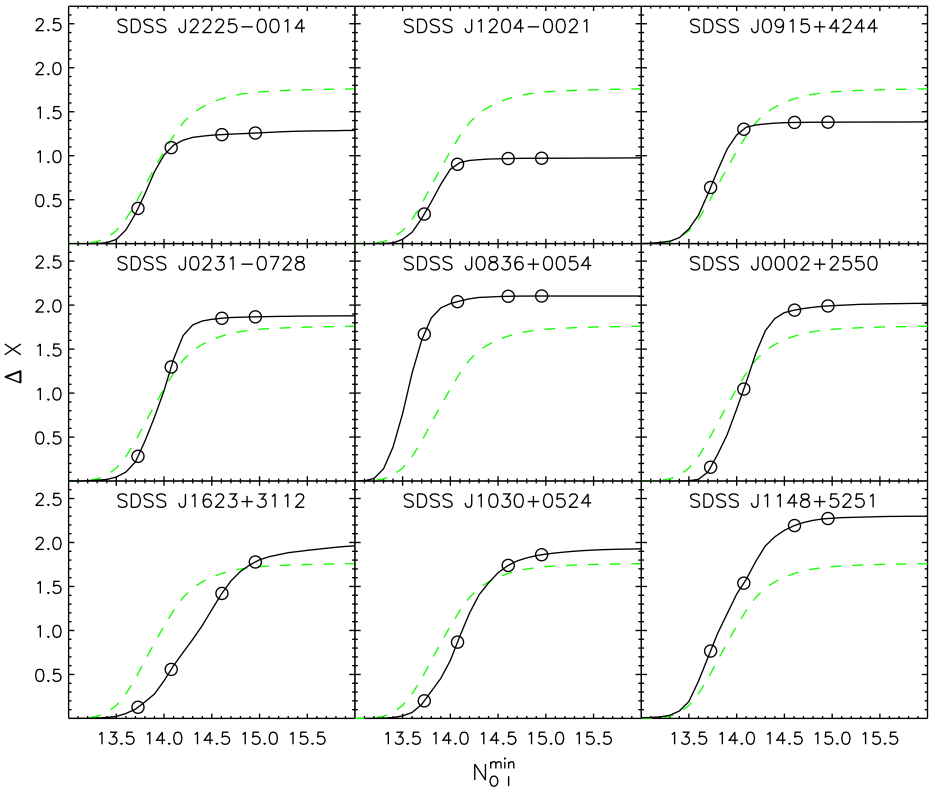

Figure 3.7 Sensitivity curves for each of our sightlines. The *solid lines* give the absorption pathlength interval over which we are sensitive to single-component O I systems with $N_{\rm O\ I} \geq N^{\rm min}_{\rm O\ I}$ and relative abundances similar to those of the O I systems in our sample. *Circles* mark the ΔX values corresponding to the $N_{\rm O\ I}$ of systems detected towards SDSS J1148+5251. The *dashed line* shows the mean ΔX as a function of $N^{\rm min}_{\rm O\ I}$ for all nine sightlines. The three lowest-redshift sightlines have smaller maximum ΔX values due in part to A-band atmospheric absorption.

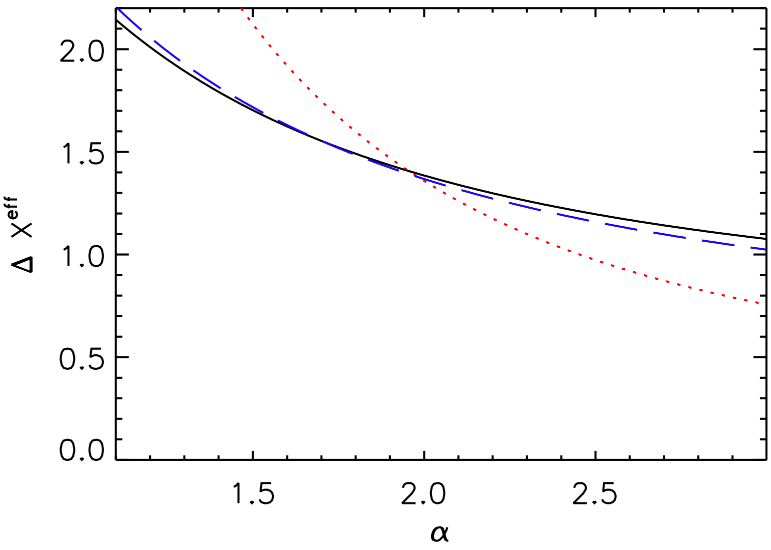

Figure 3.8 Effective absorption pathlength interval over which we are sensitive to O I systems with $N_{\rm O\,I} \geq 10^{13.7}$ cm^{-2} as a function of α, where $f(N_{\rm O\,I}) \propto N_{\rm O\,I}^{-\alpha}$ (see equation 3.3). The *solid line* shows $\Delta X^{\rm eff}$ for SDSS J1148+5251. The *dashed line* shows the summed $\Delta X^{\rm eff}$ for the remaining eight sightlines, divided by 5.7 to match SDSS J1148+5251 at $\alpha = 1.7$. The *dotted line* shows the combined $\Delta X^{\rm eff}$ for SDSS J1030+0524 and SDSS J1623+3112. For reasonable values of α, the ratio of $\Delta X^{\rm eff}$ for SDSS J1148+5251 and the remaining eight sightlines is essentially constant. We would therefore expect to see roughly six times as many O I systems along the other eight sightlines as towards SDSS J1148+5251 for a non-evolving population of absorbers.

be nearly invariant over a wide range in plausible column density distributions.

We can now evaluate the likelihood that the imbalance of O I detection results from small number sampling. For a Poisson distribution, the likelihood of detecting $\mathcal{N}$ systems when the expected number of detections is ν is given by

$$P(\mathcal{N},\nu) = \frac{\nu^{\mathcal{N}} e^{-\nu}}{\mathcal{N}}\,. \tag{3.5}$$

If we assume that the expected number of detections towards SDSS J1148+5251 is $\nu = 6\,(\Delta X^{\rm eff}_{1148}/\Delta X^{\rm eff}_{\rm all}) \simeq 0.90$, then the probability of detecting at least 4 systems is

$$P(\geq 4,\nu) = \sum_{\mathcal{N}=4}^{\infty} P(\mathcal{N},\nu) = 1 - \sum_{\mathcal{N}=0}^{3} P(\mathcal{N},\nu) = 0.013\,. \tag{3.6}$$

Similarly, if we take the number of systems observed towards SDSS J1148+5251 as a representative sample and compute the expected number of systems towards the remaining eight sightlines to be $\nu = 4\,(\Delta X^{\rm eff}_{\rm other}/\Delta X^{\rm eff}_{1148}) \simeq 23$, then the likelihood of detecting at most two systems is

$$P(\leq 2, \nu) = \sum_{\mathcal{N}=0}^{2} P(\mathcal{N}, \nu) = 3.6 \times 10^{-8}\,. \tag{3.7}$$

The probability of simultaneously detecting at least 4 systems towards SDSS J1148+5251 while detecting at most two systems along the remaining eight sightlines,

$$P\left(\frac{\partial \mathcal{N}}{\partial X}\right) = \left[1 - \sum_{\mathcal{N}=0}^{3} P(\mathcal{N}, \frac{\partial \mathcal{N}}{\partial X}\,\Delta X^{\rm eff}_{1148})\right] \left[\sum_{\mathcal{N}=0}^{2} P(\mathcal{N}, \frac{\partial \mathcal{N}}{\partial X}\,\Delta X^{\rm eff}_{\rm other})\right]\,, \tag{3.8}$$

has a maximum of $P(\partial\mathcal{N}/\partial X) = 0.0018$ at $\partial\mathcal{N}/\partial X = 0.84$, taking $\alpha \leq 3$. Thus, assuming that the O I systems are randomly distributed, we can rule out with a high degree of confidence the possibility that the excess number of detected systems towards SDSS J1148+5251 is the result of a statistical fluctuation.

3.4.1 Comparison with Lower-Redshift Sightlines

Our sample of nine $z_{\rm QSO} > 4.8$ sightlines is sufficient to demonstrate that the apparent excess of O I systems towards SDSS J1148+5251 is highly unlikely to arise from a random spatial distribution of absorbers. However, the distribution may be significantly non-random due to large-scale clustering. For example, if the line-of-sight towards SDSS J1148+5251 passes through an overdense region of the IGM then we might expect to intersect more than the typical number of absorbers.

To address this possibility, we have searched for O I in the spectra of an additional 30 QSOs with $2.6 < z_{\rm QSO} < 4.6$. The sample was taken entirely with HIRES for a variety of studies. Due to the lower QSO redshifts, the data are of significantly higher quality than the $z_{\rm QSO} > 4.8$ sample. All sightlines are complete down to $N_{\rm O\,I} = 10^{13.5}$ cm^{-2} (apart from rare wavelength coverage gaps) with the majority complete down to $N_{\rm O\,I} = 10^{13.0}$ cm^{-2}.

A detailed study of the properties of lower-redshift O I absorbers will be presented elsewhere. Here we note that 11 systems with $N_{\rm O\,I} > 10^{13.7}$ cm^{-2} were identified along all 30 sightlines in the redshift intervals where O I would occur redward of the Lyα forest. This is comparable to but slightly larger than the incidence rate among the eight lowest-redshift sightlines in our $z_{\rm QSO} > 4.8$ sample. The number density is even somewhat higher among the $z_{\rm QSO} < 4.6$ sample since the absorption pathlength intervals are shorter (cf. equation 3.2). However, many of the $z_{\rm QSO} < 4.6$ spectra were taken in order to study known damped Lyα systems (DLAs; $N_{\rm H\,I} > 10^{20.3}$ cm^{-2}), which commonly exhibit O I (e.g., Prochaska et al. 2001, 2003). We would therefore expect these sightlines to contain more than the typical number of O I systems. The important point is that no sightline contained more than a single system. If the excess towards SDSS J1148+5251 is due to the chance alignment with an overdense region of the IGM, then such a coincidence must occur in fewer than $\sim 2-3\%$ of all sightlines.

3.4.2 Comparison with Damped Lyα and Lyman Limit System Populations

We can compare the observed number of O I systems in our $z_{\rm QSO} > 4.8$ sample with the expected number of DLAs by extrapolating from lower-redshift DLA surveys. Storrie-Lombardi & Wolfe (2000) find a line number density $n_{\rm DLA}(z) = \partial\mathcal{N}_{\rm DLA}/\partial z = 0.055\,(1+z)^{1.11}$. This is consistent at high-z with the larger survey done by Prochaska et al. (2005) and with the number density evolution Rao et al. (2006) obtained by combining DLA samples over $0 \leq z \leq 4.5$. From this $n_{\rm DLA}(z)$ we would expect a total of ~ 1.5 DLAs total along all nine lines-of-sight in the redshift intervals where are sensitive to O I. This is consistent with the two O I systems seen along the eight lower-redshift sightlines. We would expect, however, to see only ~ 0.2 DLAs towards SDSS J1148+5251, which is inconsistent with the four we observe.

The disparity eases for SDSS J1148+5251 if we include all Lyman limit Systems (LLSs; $N_{\rm H\,I} > 10^{17.2}$ cm^{-2}). The line number density of LLSs at $z > 2.4$ found by Péroux et al. (2003), $n_{\rm LLS}(z) = 0.07\,(1+z)^{2.45}$, predicts ~ 4 LLSs towards SDSS J1148+5251 in the interval where we can observe O I. There should, however, also be ~ 20 LLSs along the remaining eight lines-of-sight. If the excess O I absorbers are associated with the progenitors of lower-redshift LLSs then they must evolve strongly in O I at $z \gtrsim 6$.

3.5 Metal Abundances

Absorption systems at $z > 5$ provide an opportunity to study metal enrichment when the age of the Universe was $\lesssim 1$ Gyr. The opacity of the Lyα forest at these redshifts prevents us from measuring reliable H I column densities. We are still, however, able to constrain relative abundances. In Table 3.3, we summarize the Voigt profile fitting results. Total column densities for each system include only components with confirmed O I. Relative abundances were calculated using the solar values of Grevesse & Sauval (1998) and assuming zero ionization corrections. These are plotted in Figure 3.9. The error-weighted mean values for all six systems are $\langle[\mathrm{O/Si}]\rangle = -0.04 \pm 0.06$, $\langle[\mathrm{C/O}]\rangle = -0.31 \pm 0.09$, and $\langle[\mathrm{C/Si}]\rangle = -0.34 \pm 0.07$ (2σ errors).

The uncorrected abundances are broadly consistent with the expected yields from Type II supernovae of low-metallicity progenitors (Woosley & Weaver 1995; Chieffi & Limongi 2004). Low- and intermediate-mass stars should not contribute significantly to the enrichment of these systems since these stars will not have had time to evolve by $z \sim 6$ (although see Barth et al. 2003). We can use the O/Si ratio to constrain the enrichment from zero-metallicity very massive stars (VMSs, $M_\star \sim 140 - 270\,M_\odot$). VMSs exploding as pair instability supernovae are expected to yield ~ 4 times as much silicon compared to Type II SNe for the same amount of oxygen (Schaerer 2002; Umeda & Nomoto 2002; Heger & Woosley 2002; Woosley & Weaver 1995; Chieffi & Limongi 2004). We can estimate the fraction $f_{\mathrm{Si}}^{\mathrm{VMS}}$ of silicon contributed by VMSs to these systems using the simple mixing scheme of Qian & Wasserburg (2005b,a),

$$\left(\frac{\mathrm{O}}{\mathrm{Si}}\right) = \left(\frac{\mathrm{O}}{\mathrm{Si}}\right)_{\mathrm{VMS}} f_{\mathrm{Si}}^{\mathrm{VMS}} + \left(\frac{\mathrm{O}}{\mathrm{Si}}\right)_{\mathrm{SN\,II}} \left(1 - f_{\mathrm{Si}}^{\mathrm{VMS}}\right) . \tag{3.9}$$

Adopting $[\mathrm{O/Si}]_{\mathrm{VMS}} = -0.61$ from Heger & Woosley (2002), and $[\mathrm{O/Si}]_{\mathrm{SN\,II}} = 0.00$ from Woosley & Weaver (1995), the mean uncorrected O/Si gives $f_{\mathrm{Si}}^{\mathrm{VMS}} = 0.11 \pm 0.17$ (2σ). However, this value of O/Si should be considered a lower limit. The ionization potential of O I is smaller than that of Si II ($\Delta E_{\mathrm{O\,I}} = 13.6$ eV, $\Delta E_{\mathrm{Si\,II}} = 16.3$ eV). Therefore, applying an ionization correction would increase O/Si. Taking $\langle[\mathrm{O/Si}]\rangle > -0.10$ gives $f_{\mathrm{Si}}^{\mathrm{VMS}} < 0.27$ (2σ).

The mean C/Si ratio is consistent with zero silicon contribution from VMSs, although C/Si may decrease if ionization corrections are applied ($\Delta E_{\mathrm{C\,II}} = 24.4$ eV $> \Delta E_{\mathrm{Si\,II}}$).

Table 3.3. Abundance Measurements

Sightline	$z_{\rm sys}$	$\log N_{\rm O\ I}^{\rm tot\,a}$	$\log N_{\rm Si\ II}^{\rm tot\ a}$	$\log N_{\rm C\ II}^{\rm tot\ a}$	$[\rm O/Si]^{b}$	$[\rm C/O]^{b}$	$[\rm C/Si]^{b}$	$\log N_{\rm H\ I}$
SDSS J1148+5251	6.2555	14.08 ± 0.09	12.90 ± 0.04	13.60 ± 0.11	-0.11 ± 0.08	-0.17 ± 0.15	-0.27 ± 0.12	$\cdots$
SDSS J1148+5251	6.1968	13.73 ± 0.06	12.28 ± 0.04	13.03 ± 0.07	0.17 ± 0.07	-0.39 ± 0.10	-0.22 ± 0.08	$\cdots$
SDSS J1148+5251	6.1293	14.61 ± 0.10	13.27 ± 0.05	13.74 ± 0.07	0.05 ± 0.10	-0.55 ± 0.13	-0.50 ± 0.09	$\cdots$
SDSS J1148+5251	6.0097	14.70 ± 0.05	13.48 ± 0.05	14.17 ± 0.07	-0.07 ± 0.06	-0.22 ± 0.09	-0.28 ± 0.08	$< 21.9^{c}$
SDSS J1623+3112	5.8408	14.96 ± 0.06	13.98 ± 0.06	14.50 ± 0.09	-0.31 ± 0.09	-0.15 ± 0.13	-0.45 ± 0.11	$\cdots$
SDSS J0231−0728	5.3364	14.52 ± 0.07	13.25 ± 0.06	13.84 ± 0.07	-0.02 ± 0.07	-0.37 ± 0.12	-0.39 ± 0.09	$< 20.1^{c}$

[a] Total ionic column densities summed over all components with confirmed O I absorption

[b] Relative abundances using the solar values of Grevesse & Sauval (1998) and assuming no ionization corrections

[c] Upper limit including uncertainty in the continuum level

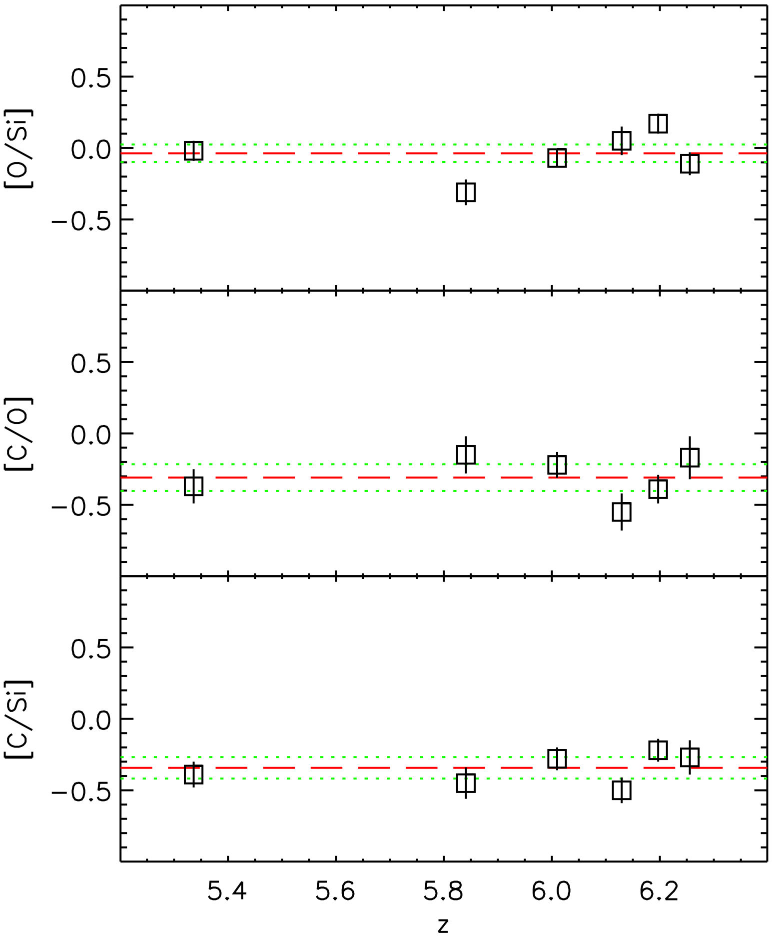

Figure 3.9 Relative metal abundances in the O I systems assuming no ionization corrections. Individual measurements plotted as *squares* with 1σ error bars are taken from Table 3.3. *Dashed lines* show the weighted mean values for all six systems. *Dotted lines* show the 2σ uncertainties in the means.
]

Dust corrections would also decrease C/Si since silicon is more readily depleted onto grains (Savage & Sembach 1996). Our upper limit of $\langle[\mathrm{C/Si}]\rangle < -0.27$ (2σ) therefore does not provide an additional constraint on $f_{\mathrm{Si}}^{\mathrm{VMS}}$. The limit set by O/Si, however, may still imply that VMSs provided a smaller fraction of the metals in these O I systems than in the general IGM. Qian & Wasserburg (2005b,a) have argued that VMSs at $z \gtrsim 15$ must have contributed $\gtrsim 50\%$ of the silicon in the IGM in order to produce $[\mathrm{Si/C}]_{\mathrm{IGM}} \sim 0.7$ at $z \approx 2-4$ (Aguirre et al. 2004). The Si/C ratio in the IGM derived from high-ionization lines, however, depends sensitively on the choice of ionizing backgrounds.

The high level of absorption blueward of the Lyα emission line at $z > 5$ prevents us from reliably fitting Voigt profiles to H I. Transmission peaks, however, in the Lyα and Lyβ forests near the O I redshifts allow us to set upper limits on the H I column density for two of our systems. Fits to these systems with the strongest allowable damping wings are shown in Figures 3.10 and 3.11, and the corresponding limits are listed in Table 3.3. The limits take into account uncertainties in the continuum level, which was set to a power-law $F_{\nu} \propto \lambda^{-\beta}$ with spectral index $\beta = 0.5$, normalized at a rest wavelength of 1280 Å. The continuum uncertainty will include the error in the amplitude of the power law at the wavelength of the damped system. Taking $\Delta\beta = 0.65$ to incorporate 95% of the scatter in QSO spectral indices (Richards et al. 2001), this error is $< 10\%$ for the system at $z_{\mathrm{sys}} = 5.3364$, for which the limit on $N_{\mathrm{H\,I}}$ was set using Lyα transmission, and $< 20\%$ for the system at $z_{\mathrm{sys}} = 6.0097$, for which the limit was set using Lyβ. Larger uncertainties in the continuum may result from errors in the relative flux calibration and the departure from a power law. We conservatively estimate both of these to be $\sim 20\%$, which translates to an uncertainty in the column density $\sigma(\log N_{\mathrm{H\,I}}) \sim 0.3$. The upper limits on $\log N_{\mathrm{H\,I}}$ listed in Table 3.3 are our "best fit" values plus this uncertainty. The corresponding limits on the absolute abundances are $[\mathrm{O/H}] > -2.4$ ($z_{\mathrm{sys}} = 5.3364$) and $[\mathrm{O/H}] > -4.1$ ($z_{\mathrm{sys}} = 6.0097$).

The comoving mass density for each ion is given by

$$\Omega_{\mathrm{ion}} = \frac{H_0 m_{\mathrm{ion}}}{c\rho_{\mathrm{crit}}} \frac{\sum N_{\mathrm{ion}}}{\Delta X^{\mathrm{tot}}} \,, \tag{3.10}$$

where m_{ion} is the mass of the ion, $\rho_{\mathrm{crit}} = 0.92 \times 10^{-29}\ h_{70}^{2}\ \mathrm{g\ cm^{-3}}$ is the cosmological closure density, and ΔX^{tot} is the total pathlength interval over which we are sensitive to O I. In Table 3.4 we list Ω_{ion} for O I, Si II, and C II summing over all $z_{\mathrm{QSO}} > 4.8$ sightlines, over the

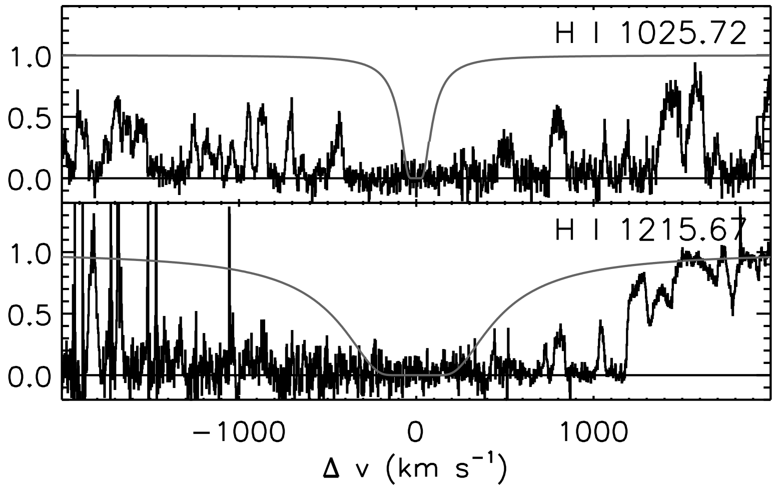

Figure 3.10 Voigt profile fit to H I Lyα and Lyβ corresponding to the upper limit on $N_{\mathrm{H\,I}}$ for the $z_{\mathrm{sys}} = 5.3364$ O I systems towards SDSS J0231−0728. In order to set an upper limit on $N_{\mathrm{H\,I}}$ we have taken $b = 1$ km s^{-1}, although the actual b-parameter is likely to be significantly larger. In this system, $N_{\mathrm{H\,I}}$ is constrained by the transmitted flux in the wings of the Lyα profile.

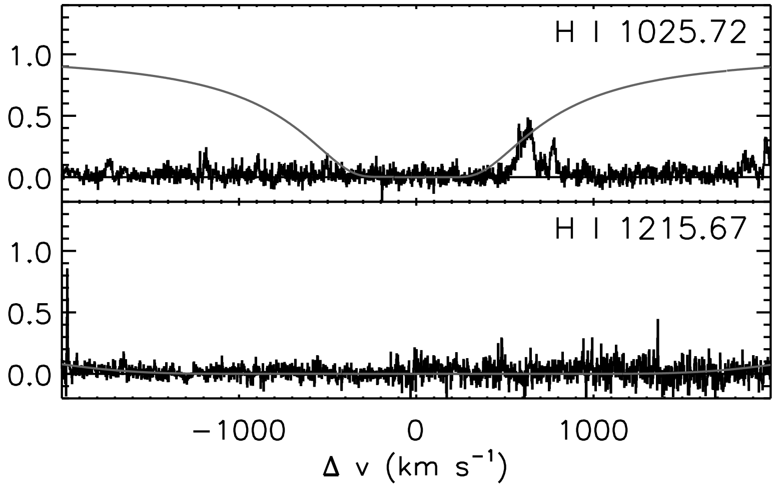

Figure 3.11 Voigt profile fit to H I Lyα and Lyβ corresponding to the upper limit on $N_{\mathrm{H\,I}}$ for the $z_{\mathrm{sys}} = 6.0097$ O I systems towards SDSS J1148+5251. In this system, $N_{\mathrm{H\,I}}$ is constrained by the transmitted flux in the red wing of the Lyβ profile.

Table 3.4. Comoving Mass Densities

Sightlines	Ω(O I) ($\times10^{-8}$)	Ω(Si II) ($\times10^{-9}$)	Ω(C II) ($\times10^{-8}$)
All	3.2 ± 0.2	4.5 ± 0.4	0.8 ± 0.1
$z_{\rm QSO} > 6.2$	7.0 ± 0.6	9.6 ± 0.9	1.5 ± 0.2
SDSS J1148+5251	10.2 ± 1.0	9.8 ± 0.7	1.8 ± 0.2

Note. — For each ion, the value of $\Omega_{\rm ion}$ computed from equation (3.10) includes all *confirmed* components listed in Table 3.2 along the indicated lines of sight, including those components without corresponding O I. These values are lower limits in the sense that we have made no attempt to correct for incompleteness. Errors are 1σ and reflect only the uncertainty in the summed column densities.

three sightlines with $z_{\rm QSO} > 6.2$ only, and over the sightline towards SDSS J1148+5251 only. The mass densities include all confirmed absorption components, including those without detected O I. We have, however, made no attempt to correct for incompleteness. The densities of low-ionization metal species along our $z_{\rm QSO} > 6.2$ sightlines are comparable to the densities of the corresponding high-ionization species at lower-redshift. Songaila (2005) measured $\Omega(\text{C IV}) \sim 3 \times 10^{-8}$ and $\Omega(\text{Si IV}) \sim 1 \times 10^{-8}$ over $1.5 < z < 4.5$, with a drop in Ω(C IV) by at least a factor of two at $z > 5$. A decrease in high-ionization metals and a correlated rise in their low-ionization counterparts with redshift might signal a change in the ionization state of the $z > 5$ IGM. However, coverage of C IV does not currently extend to $z \sim 6$, and our O I sample is probably too small to make a meaningful comparison.

3.6 Discussion

Although we observe an overabundance of O I at $z > 6$ along one of our highest-redshift sightlines, it is not clear that these four systems constitute a “forest” which would signal a predominantly neutral IGM. In the reionization phase prior to the overlap of ionized bubbles, Oh (2002) predicts tens to hundreds of O I lines with $N_{\rm O\,I} > 10^{14}$ cm^{-2}, although the number may be lower if the enriched regions have very low metallicity ($Z < 10^{-2.5} Z_\odot$), or if the volume filling factor of metals is small ($f_Z \ll 0.01$). The number of O I systems we detect is more consistent with his predictions for the post-overlap phase, although the expected number of lines depends on the ionizing efficiency of the metal-producing galaxies. The Oh (2002) model also predicts lines with $N_{\rm O\,I} > 10^{15}$ cm^{-2}, which we do not observe.

The significance of the excess O I towards SDSS J1148+5251 is complicated by the presence of Lyα and Lyβ transmission along that sightline. The O I systems occur interspersed in redshift with the Lyβ peaks, with the velocity separation from the nearest peak ranging from $\Delta v \sim 500$ to 3000 km s^{-1} ($\Delta l \sim 5$ to 30 comoving Mpc). The O I absorbers also do not appear to be clustered. Along a total redshift interval $\Delta z_{\rm tot} = 0.49$ (~ 200 comoving Mpc) where we are sensitive to O I, the detected systems are separated by $\Delta z = 0.06$ to 0.12 ($\Delta l = 24$ to 50 comoving Mpc). If any significantly neutral regions are present along this sightline, then they occur within or near regions that are highly ionized. In contrast, we find no O I towards SDSS J1030+0524, despite the fact that its spectrum shows complete absorption in Lyα and Lyβ over $\Delta z \sim 0.2$. The SDSS J1030+0524 sightline may pass through a region of the IGM that is still largely neutral and not yet enriched. Alternatively, there may be no O I because the sightline is highly ionized. In that case, a large-scale density enhancement could still produce the high Lyα and Lyβ optical depth (Wyithe & Loeb 2005b).

The overabundance of O I together with the transmission in Lyα and Lyβ indicates that the SDSS J1148+5251 sightline has experienced both significant enrichment *and* ionization. One explanation is that we are looking along a filament. The total comoving distance between O I systems towards SDSS J1148+5251 is ≈ 101 Mpc, which is smaller than the largest known filamentary structures at low redshift (e.g., Gott et al. 2005). If the line-of-sight towards SDSS J1148+5251 runs along a filament at $z \sim 6$ then we might expect to intersect more than the average number of absorbers. Galaxies along such a structure might produce enough ionizing radiation to create the transmission gaps observed in the Lyα and Lyβ forests while still allowing pockets of neutral material to persist if the ionizing background is sufficiently low. If we assume that every $z \sim 6$ galaxy is surrounded by an enriched halo, then we can calculate the typical halo radius

$$R_{\rm halo} \sim \left[\frac{\mathcal{N}}{\pi(1+z)^2 \left\langle \Phi_{\rm gal} \right\rangle \delta_{\rm gal} \Delta D}\right]^{1/2} \tag{3.11}$$

$$\begin{aligned} \sim \quad & 35 \text{ proper kpc} \left(\frac{\mathcal{N}}{4}\right)^{1/2} \left(\frac{1+z}{7.2}\right)^{-1} \left(\frac{\langle \Phi_{\rm gal} \rangle}{0.01\,{\rm Mpc}^{-3}}\right)^{-1/2} \\ & \times \left(\frac{\delta_{\rm gal}}{10}\right)^{-1/2} \left(\frac{\Delta D}{200\,{\rm Mpc}}\right)^{-1/2} . \end{aligned} \tag{3.12}$$

Here, ΔD is the total comoving distance over which we are sensitive to O I. We have used the mean comoving number of galaxies $\langle \Phi_{\rm gal} \rangle$ at $z \sim 6$ measured down to the limit of the Hubble Ultra Deep Field (UDF; Yan & Windhorst 2004; Bouwens et al. 2005), and assumed an overdensity of galaxies $\delta_{\rm gal} = \Phi_{\rm gal} / \langle \Phi_{\rm gal} \rangle = 10$ along this sightline. The absorption could be due to filled halos, shells, or other structures surrounding the galaxies. Note that by inverting equation (3.11) we can rule out the possibility that these O I systems arise from the central star-forming regions of galaxies similar those observed in the UDF. The small size $R_{\rm half-light} \sim 0.8$ kpc of galaxies at $z \sim 6$ (Bouwens et al. 2005) would require either a local galaxy overdensity $\delta_{\rm gal} \sim 10^4$ or a large number of faint galaxies to produce the observed absorption systems.

At present we can place relatively few physical constraints on these absorbers. Assuming charge-exchange equilibrium (equation 3.1), we can estimate the H I column densities as a function of metallicity,

$$\log N_{\rm H\,I} = 16.9 + \log\left(\frac{N_{\rm O\,I}}{10^{13.7}\ {\rm cm}^{-2}}\right) - [{\rm O/H}] \, . \tag{3.13}$$

For solar metallicities, even the weakest O I system in our sample must be nearly optically thick. Metal-poor absorbers with [O/H] < -2 would require column densities $N_{\rm H\,I} \gtrsim 10^{19}$ cm^{-2}, which is consistent with the indication from the relative metal abundances that these absorbers are largely neutral.

Finally, the excess O I absorbers are distinguished by their small velocity dispersions. Three out of the four systems towards SDSS J1148+5251 have single components with Doppler widths $b \approx 5-8$ km s^{-1}. We may be seeing only the low-ionization component of a kinematically more complex structure such as a galactic outflow (e.g., Simcoe et al. 2006). If there are, however, additional high-ionization components that would appear in C IV and Si IV then we might expect to see components in C II and possibly Si II without O I. This is the case in the $z_{\rm sys} = 5.3364$ system towards SDSS J0231−0728. The $z_{\rm sys} = 6.1293$ and $z_{\rm sys} = 6.2550$ systems towards SDSS J1148+5251 show potential C II lines that do not appear in O I, but these are relatively weak, and in the $z_{\rm sys} = 6.1293$ system there is no apparent strong Si IV. Among the 11 O I absorbers in the $z < 4.6$ sample, only three have a single O I component with a velocity width comparable to the three narrowest systems towards SDSS J1148+5251. The fact that the excess O I systems appear kinematically quiescent further suggests that they are a distinct class of absorbers.

3.7 Summary

We have conducted a search for O I in the high-resolution spectra of 9 QSOs at $4.8 \leq z_{\rm QSO} \leq 6.4$. In total, we detect six systems in the redshift intervals where O I $\lambda1302$ falls redward of the Lyα forest. Four of these lie towards SDSS J1148+5251 ($z_{\rm QSO} = 6.42$). This imbalance is not easily explained by small number statics or by varying sensitivity among the data. A search at lower redshift revealed no more than than one O I system per sightline in a high-quality sample of 30 QSOs with $2.6 \leq z_{\rm QSO} \leq 4.6$. The number of excess systems is significantly larger than the expected number of damped Lyα systems at $z \sim 6$, but similar to the predicted number of Lyman limit systems.

The six systems have mean relative abundances $\langle[{\rm O/Si}]\rangle = -0.04 \pm 0.06$, $\langle[{\rm C/O}]\rangle = -0.31 \pm 0.09$, and $\langle[{\rm C/Si}]\rangle = -0.34 \pm 0.07$ (2σ errors), assuming no ionization corrections. These abundances are consistent with enrichment dominated by Type II supernovae. The lower limit on the oxygen to silicon ratio $\langle[{\rm O/Si}]\rangle > -0.10$ is insensitive to ionization corrections and limits the contribution of silicon from VMSs to $< 30\%$ in these systems. The upper limits on the ratio of carbon to oxygen $[{\rm C/O}] \leq -0.13$, and carbon to silicon $[{\rm C/Si}] \leq -0.20$ are also insensitive to ionization. Integrating over only the confirmed absorption lines, the mean ionic comoving mass densities along the three $z_{\rm QSO} > 6.2$ sightlines are $\Omega_{\rm O\,I} \approx 7.0 \times 10^{-8}$, $\Omega_{\rm Si\,II} \approx 9.6 \times 10^{-9}$, and $\Omega_{\rm C\,II} \approx 1.5 \times 10^{-8}$.

The excess O I systems towards SDSS J1148+5251 occur in redshift among Lyα and Lyβ transmission features, which indicates that the IGM along this sightline has experienced both enrichment *and* significant ionization. The sightline may pass along a filament, where galaxies are producing enough ionizing photons create the transmission gaps while still allowing a few neutral absorbers to persist. In contrast, no O I was observed towards SDSS J1030+0524, whose spectrum shows complete Gunn-Peterson absorption. The SDSS J1030+0524 sightline may pass through an underdense region containing very few sources that would either enrich or ionize the IGM. Alternatively, the sightline may be highly ionized, with a large-scale density enhancement producing strong line-blending in the Lyα and Lyβ forests. Future deep imaging of these fields and near-infrared spectroscopy covering high-ionization metal lines will allow us to distinguish between these scenarios and clarify the nature of the excess O I absorbers.

The authors would like to thank the anonymous referee for helpful comments, Peng Oh for sharing his recent results on charge-exchange equilibrium ahead of publication, and Bob Carswell for VPFIT. WLWS gratefully acknowledge support from the NSF through grants AST 99-00733 and AST 02-06067. MR has been supported by the NSF under grant AST 00-98492. RAS has been supported by the MIT Pappalardo Fellowship program. Finally, we thank the Hawaiian people for the opportunity to conduct observations from Mauna Kea. Without their hospitality this work would not have been possible. In particular, we would like to thank Lono, who granted us clear skies during the overcast months of 2005 January and February.

Chapter 4

The Evolution of Optical Depth in the Lyα Forest: Evidence Against Reionization at $z \sim 6$[1]

Abstract

We examine the evolution of the IGM Lyα optical depth distribution using the transmitted flux probability distribution function (PDF) in a sample of 55 QSOS spanning absorption redshifts $1.7 < z < 5.8$. The data are compared to two theoretical τ distributions: a model distribution based on the density distribution of Miralda-Escudé et al. (2000) (MHR00), and a lognormal distribution. We assume a uniform UV background and an isothermal IGM for the MHR00 model, as has been done in previous works where transmitted flux statistics have been used to infer an abrupt change in the IGM at $z \sim 6$. Under these assumptions, the MHR00 model produces poor fits to the observed flux PDFs at redshifts where the optical depth distribution is well sampled, unless large continuum corrections are applied. The lognormal τ distribution, however, fits the data at all redshifts with only minor continuum adjustments. We use a simple parametrization for the evolution of the lognormal parameters to calculate the expected mean transmitted flux at $z > 5.4$. The lognormal τ distribution predicts the observed Lyα and Lyβ effective optical depths at $z > 5.7$ while simultaneously fitting the mean transmitted flux down to $z = 1.6$. In contrast, the best-fitting power-law underpredicts the amount of absorption both at $z > 5.7$ and at $z < 2.5$. If the evolution of the lognormal distribution at $z < 5$ reflects a slowly-evolving density field, temperature, and UV background, then no sudden change in the IGM at $z \sim 6$ due to late reionization appears

---

[1] Submitted to *The Astrophysical Journal*; written with M. Rauch and W. L. W. Sargent

necessary. We have used the lognormal optical depth distribution without any assumption about the underlying density field. If the MHR00 density distribution is correct, then a non-uniform UV background and/or IGM temperature may be required to produce the correct flux PDF. We find that an inverse temperature-density relation greatly improves the PDF fits, but with a large scatter in the equation of state index. The lognormal τ distribution therefore currently offers the best match to the observed flux PDF and the most reliable predictor for the transmitted flux at high redshift.

4.1 Introduction

The Lyα forest serves as our most fundamental probe of the evolution of the intergalactic medium (IGM). While numerous models have been proposed for the underlying density field (see Rauch 1998 for a review), the current consensus is a self-gravitating network of filamentary structures collapsing out of initially Gaussian density perturbations. Given a description of the IGM that relates density and transmitted flux, one can compute various cosmological parameters and examine the large-scale evolution of the Universe.

Perhaps the most dramatic inferences drawn from the evolution of Lyα transmitted flux is that the reionization of the IGM may have ended as late as $z \sim 6.2$ (Becker et al. 2001; White et al. 2003; Fan et al. 2002, 2006a). This conclusion is based not only on the appearance of complete Gunn-Peterson troughs in the spectra of QSOs at $z > 6$, but on the accelerated decline and increased variance in the mean transmitted flux at $z > 5.7$ (Fan et al. 2006a). Late reionization is potentially at odds with the transmitted flux seen towards the highest-redshift known QSO, SDSS J1148+5251 ($z_{\rm QSO} = 6.42$, White et al. 2003, 2005; Oh & Furlanetto 2005). In addition, the fact that the observed number density of Lyα-emitting galaxies does not evolve strongly from $z \sim 5.7$ to $z \sim 6.5$ implies that the IGM is already highly ionized at these redshifts (Hu et al. 2004; Hu & Cowie 2006; Malhotra & Rhoads 2004, 2006; Stern et al. 2005). Galactic winds (Santos 2004) or locally ionized bubbles (Haiman & Cen 2005; Wyithe & Loeb 2005a; Furlanetto et al. 2004a, 2006) may allow Lyα photons to escape even if the IGM is significantly neutral. Additional arguments may be made about the thermal history of the IGM (Theuns et al. 2002; Hui & Haiman 2003) or the apparent size of the transmission regions around $z \sim 6$ QSOs (Mesinger & Haiman 2004; Mesinger et al. 2004; Wyithe & Loeb 2004b; Fan et al. 2006a). However, the evolution of the Lyα forest remains the strongest evidence for late reionization.

Still, the significance of the disappearance of transmitted flux at $z \sim 6$ has been highly debated (Songaila & Cowie 2002; Songaila 2004; Lidz et al. 2006b). As Songaila & Cowie (2002) pointed out, the mean transmitted flux in an inhomogeneous IGM will depend strongly on the underlying density distribution, or more precisely, on the optical depth distribution. At $z \sim 6$, any transmitted flux will arise from rare voids, which lie in the tail of the optical depth distribution. Using a sample of 19 QSOs at $z > 5.7$, Fan et al. (2006a) showed that the evolution the mean transmitted flux at $z \sim 6$ diverges significantly from that expected for a commonly-used model of the IGM density (Miralda-Escudé et al. 2000, referred to herein as MHR00). The question, then, is whether the MHR00 model describes the distribution of optical depths accurately enough to make reliable predictions at very high redshift.

In this paper we examine two theoretical optical depth distributions and their predictions for the Lyα transmitted flux probability distribution function (PDF) The first is based on the gas density distribution given by MHR00, which has been used to make claims of late reionization. Their density distribution is derived from simple arguments about the dynamics of the IGM (see §4.3.2) and matches the output of an earlier numerical simulation (Miralda-Escudé et al. 1996). In order to compute optical depths, assumptions must be made about the ionizing background and the thermal state of the IGM. As other authors have done, we will primarily consider a uniform UV background and an isothermal IGM. In §4.5 we will briefly generalize to a non-isothermal equation of state.

The second case we consider is a simple lognormal optical depth distribution. This choice can be motivated in at least two ways. Initially Gaussian density perturbations will give rise to a lognormal density field when the initial peculiar velocity field is also Gaussian (Coles & Jones 1991). Indeed, Bi et al. (1992) demonstrated that a lognormal density distribution can produce many properties of the observed Lyα forest (see also Bi et al. 1995; Bi & Davidsen 1997). More generally, however, a lognormal distribution naturally arises as a result of the central limit theorem when a quantity is determined by several multiplicative factors. For optical depth, these factors are density, temperature, and ionization rate. Here we will consider the lognormal distribution to be a generic distribution with the desirable properties of being non-zero and having a potentially large variance. Our main conclusions will not depend on any assumptions about the underlying density field.

The transmitted flux PDF has been used to constrain a variety of cosmological parameters (e.g., Rauch et al. 1997; Gaztañaga & Croft 1999; McDonald et al. 2000; Choudhury et al. 2001; Desjacques & Nusser 2005; Lidz et al. 2006a), with many authors assuming an optical depth distribution similar to one we consider here. We will examine the distributions themselves and their evolution with redshift by attempting to fit the models to the observed flux PDFs from a large sample of Keck HIRES data spanning Lyα absorption redshifts $1.7 < z < 5.8$. We introduce the data in §4.2. In §4.3 the optical depth distributions are derived and used to fit the observed flux PDFs. We find that the lognormal distribution provides a better fit to the data at all redshifts where the optical depth distributions are well sampled. In §4.4 we perform a simple fit to evolution of the lognormal distribution and use it to predict the mean transmitted flux at $z > 5.7$. In §4.5 we modify the model distribution by applying a non-isothermal equation of state. Finally, our results are summarized in §4.6.

4.2 The Data

Observations were made using the HIRES spectrograph (Vogt et al. 1994) on Keck I between 1993 and 2006. Targets are listed in Table 4.1. QSOs at $z_{\rm QSO} < 4.8$ were observed using the original HIRES CCD and were reduced using the MAKEE package written by Tom Barlow. QSOs at $z_{\rm QSO} > 4.8$ were observed using the upgraded detector and reduced using a custom set of IDL routines as described in Becker et al. (2006b). The IDL package is based on the optimal sky subtraction technique of Kelson (2003). For nearly all of our observations we used an $0\farcs86$ slit, which gives a velocity resolution FWHM of $\Delta v = 6.7$ km s^{-1}.

Table 4.1. Fitted Lyα Forest Regions

QSO	$z_{\rm QSO}$	$\langle z_{\rm abs}\rangle^{\rm a}$	$z_{\rm abs}^{\rm min}$	$z_{\rm abs}^{\rm max}$	median flux error
SDSS J1148+5251	6.42	5.614	5.430	5.802	0.05
SDSS J1030+0524	6.30	5.514	5.339	5.692	0.11
SDSS J1623+3112	6.25	5.522	5.339	5.709	0.15
SDSS J1048+4637	6.23	5.516	5.339	5.696	0.15
SDSS J0818+1722	6.00	5.590	5.417	5.766	0.10
		5.221	5.066	5.417	0.07
SDSS J0002+2550	5.82	5.465	5.339	5.592	0.12
		5.076	4.910	5.245	0.11
SDSS J0836+0054	5.80	5.455	5.339	5.573	0.05
		5.067	4.893	5.245	0.04
SDSS J0231−0728	5.42	5.043	4.885	5.206	0.11
		4.730	4.563	4.885	0.09
SDSS J0915+4244	5.20	4.849	4.707	4.993	0.07
		4.509	4.373	4.647	0.07
SDSS J1204−0021	5.09	4.747	4.582	4.887	0.09
		4.428	4.277	4.582	0.09
SDSS J2225−0014	4.87	4.513	4.381	4.647	0.10
		4.234	4.087	4.381	0.11
BRI1202−0725	4.69	4.074	3.929	4.214	0.10
BRI2237−0607	4.56	4.254	4.126	4.377	0.07
Q0246+1750	4.44	4.123	3.988	4.260	0.05
		3.851	3.716	3.988	0.07
Q1055+4611	4.15	3.846	3.719	3.975	0.02
		3.591	3.460	3.719	0.03
Q0000−263	4.13	3.833	3.704	3.961	0.05
		3.574	3.447	3.704	0.05
Q1645+5520	4.10	3.798	3.672	3.927	0.01
		3.543	3.417	3.672	0.02
BRI0241−0146	4.08	3.779	3.652	3.906	0.05
		3.523	3.398	3.652	0.06
Q0827+5255	3.91	3.623	3.503	3.748	0.01
		3.389	3.265	3.503	0.02
Q0055−2659	3.65	3.381	3.266	3.499	0.05
		3.149	3.033	3.266	0.06
Q1422+2309A	3.63	3.358	3.243	3.475	0.02
		3.126	3.011	3.243	0.02
Q0930+2858	3.44	2.955	2.845	3.067	0.07

Table 4.1 (cont'd)

QSO	$z_{\rm QSO}$	$\langle z_{\rm abs}\rangle^{\rm a}$	$z_{\rm abs}^{\rm min}$	$z_{\rm abs}^{\rm max}$	median flux error
Q0642+44	3.40	2.927	2.818	3.037	0.08
Q0956+1217	3.31	3.061	2.954	3.169	0.04
		2.845	2.738	2.954	0.05
HS0741+4741	3.23	2.772	2.664	2.876	0.03
Q0636+6801	3.18	2.931	2.827	3.036	0.02
		2.720	2.618	2.827	0.02
Q1140+3508	3.16	2.916	2.813	3.021	0.03
		2.708	2.605	2.813	0.03
HS1011+4315	3.14	2.766	2.657	2.869	0.04
Q0449−1326	3.10	2.860	2.757	2.962	0.04
		2.654	2.552	2.757	0.07
Q0940−1050	3.08	2.844	2.743	2.947	0.04
		2.639	2.538	2.743	0.05
HS1946+7658	3.07	2.627	2.524	2.728	0.03
Q2231−0015	3.02	2.780	2.680	2.881	0.05
		2.578	2.479	2.680	0.07
Q1107+487	2.98	2.546	2.446	2.646	0.04
Q1437+3007	2.98	2.746	2.648	2.846	0.04
		2.547	2.448	2.648	0.05
Q0216+0803	2.98	2.748	2.659	2.843	0.12
		2.574	2.487	2.658	0.15
Q1244+3133	2.97	2.541	2.439	2.638	0.10
Q1511+0907	2.89	2.658	2.562	2.756	0.06
		2.464	2.368	2.562	0.08
Q1132+2243	2.88	2.652	2.556	2.750	0.06
		2.456	2.361	2.556	0.09
HS0119+1432	2.87	2.643	2.547	2.740	0.03
		2.452	2.353	2.547	0.04
Q1549+1919	2.84	2.613	2.517	2.707	0.01
		2.419	2.324	2.517	0.01
Q0528−250	2.81	2.595	2.492	2.683	0.05
		2.398	2.302	2.492	0.07
Q2344+1228	2.79	2.374	2.280	2.470	0.09
HS1700+6416	2.74	2.525	2.432	2.619	0.01
		2.339	2.244	2.432	0.02
Q1442+2931	2.66	2.264	2.169	2.352	0.03
Q1009+2956	2.65	2.436	2.345	2.527	0.02

Table 4.1 (cont'd)

QSO	$z_{\rm QSO}$	$\langle z_{\rm abs}\rangle^{\rm a}$	$z_{\rm abs}^{\rm min}$	$z_{\rm abs}^{\rm max}$	median flux error
		2.252	2.162	2.343	0.02
Q1358+1134	2.58	2.370	2.282	2.461	0.15
Q2343+1232	2.58	2.190	2.101	2.281	0.10
Q2206−199N	2.57	2.356	2.269	2.447	0.03
		2.188	2.105	2.269	0.04
Q1623+2653	2.53	2.323	2.235	2.411	0.06
		2.146	2.058	2.235	0.10
Q0841+1256	2.51	2.127	2.038	2.214	0.12
Q0237−233	2.24	2.050	1.966	2.128	0.06
Q1225+3145	2.21	2.016	1.938	2.098	0.03
		1.857	1.777	1.938	0.04
Q0421+019	2.05	1.870	1.795	1.947	0.08
Q0119−0437	1.98	1.807	1.733	1.876	0.14
Q0058+0155	1.96	1.797	1.734	1.859	0.12

[a] Mean absorption redshift.

We will return to the issue of continuum fitting in §4.3.3. For now, we will describe our baseline fitting procedure for quasars at various redshifts. For objects at $z_{\rm QSO} < 4.8$, individual exposures were typically bright enough that a continuum could be fit to individual orders. This was done by hand using a slowly varying spline fit. The orders were then normalized prior to combining. At higher redshifts, we performed a relative flux calibration of each exposure using standard stars. The individual exposures were then combined prior to continuum fitting. A spline fit was again used for QSOs at $z_{\rm QSO} \leq 5.4$. Since the transmission regions at $z > 5$ rarely, if ever, reach the continuum, the fits at these redshifts were of a very low order and intended only to emulate the general structure of continua observed in lower redshift QSOs (e.g., Telfer et al. 2002; Suzuki 2006). For $z_{\rm QSO} > 5.7$ we used a power law fit to the continuum of the form $f_\nu \propto \nu^{-0.5}$.

Determining a quasar continuum is generally a subjective process whose accuracy will depend strongly on how much of the continuum has been absorbed (see Lidz et al. 2004b for a discussion). At $z \sim 3$, much of the spectrum will still be unabsorbed and errors in the continuum fit will depend on signal-to-noise of the data and the personal bias of the individual performing the fit. For high-quality data, errors in the continuum at $z \sim 3$ should be

$\lesssim 1\%$. This uncertainty will increase with redshift as more of the continuum gets absorbed. By $z \sim 5.5$, very few transmission regions remain and the continuum must be inferred from the slope of the spectrum redward of the Lyα emission line. The spectral slope, however, may have an unseen break near Lyα. In addition, echelle data are notoriously difficult to accurately flux calibrate. We therefore expect our power-law continuum estimates at $z \sim 6$ to be off by as much as a factor of two.

4.3 Flux Probability Distribution Functions

4.3.1 Observed PDFs

Observed transmitted flux probability distribution functions (PDFs) were taken from spectra of the 55 quasars listed in Table 4.1. In order to avoid contamination from the proximity region and from O VI/Lyβ absorption, we limited our analysis to pixels 10000 km s^{-1} blueward of the Lyα emission line and 5000 km s^{-1} redward of the O VI emission line. The offsets were made intentionally large to account for possible errors in the QSO redshifts. In order for each region to contain enough pixels to be statistically significant yet avoid strong redshift evolution within a sample, we divided the Lyα forest in each sightline into two sections covering ~ 60 Å rest wavelength. Regions containing damped Lyα systems were discarded. We further exclude wavelengths covered by the telluric A and B bands. Other atmospheric absorption due to water vapor was typically weak compared to the Lyα absorption at the same wavelength and so was ignored. Table 4.1 lists the redshift interval for each region of the Lyα forest we examine.

Metal lines can be a significant contaminant in the Lyα forest, particularly at lower redshifts. We therefore removed as many lines as could be identified either by damped Lyα absorption or from multiple metal lines at the same redshift. In addition to the doublets C IV, Si IV, and Mg II, we searched for coincidences of Si II, Si III, C II, O I, Fe II, Al II, and Al III. For exceptionally strong systems we also masked weaker lines such as Cr II, Ti II, S II, and Zn II. Lines in the forest were masked according to the structure and extent of lines identified redward of Lyα emission. Very strong line that could be identified only from their presence in the Lyα forest (e.g., saturated C IV) were also masked. We did not mask, however, weak lines found in the forest without counterparts redward of Lyα emission.

Doing so would preferentially discard pixels with low Lyα optical depth (where the metal lines can be seen), introducing a potentially larger bias in the PDF than the one incurred by leaving the contaminated pixels in the sample. In any case, our primary concern is with strong metal lines that could mimic saturated Lyα absorption. Weak metal lines are not expected to significantly alter the flux PDF.

The observed transmitted flux PDF for each region was computed in normalized flux bins of 0.02. Errors were computed using bootstrap resampling (Press et al. 1992). Each region was divided into many short sections spanning 200 km s^{-1}, and 1000 replicates of each region were constructed by randomly drawing sections with replacement. For this work we have used only the diagonal elements of the error matrix. As noted by McDonald et al. (2000) and Desjacques & Nusser (2005), ignoring the off-diagonal elements when performing χ^2 fitting can have a significant effect on the width of the χ^2 distribution, but has only a small effect on the values of the best-fit parameters. For comparison, we have repeated the analyses presented in this paper using purely Poisson errors and have obtained nearly identical results.

4.3.2 Theoretical PDFs

We will examine two possible distributions for Lyα optical depths: one based on the gas density distribution given by MHR00, and the other a lognormal distribution. In this section we derive the expected flux PDF for each case.

MHR00 model

The MHR00 gas density distribution is derived analytically based on assuming that the density fluctuations are initially Gaussian, that the gas in voids is expanding at constant velocities, and that the densities are smoothed on the Jeans length of the photoionized gas. The resulting parametric form for the volume-weighted density distribution is

$$P_{\Delta}^{\mathrm{MHR00}}(\Delta) = A \exp\left[-\frac{(\Delta^{-2/3} - C_0)^2}{2(2\delta_0/3)^2}\right]\Delta^{-\beta}\,, \tag{4.1}$$

where $\Delta \equiv \rho/\bar{\rho}$ is the gas overdensity and A, C_0, δ_0, and β are constants. We take $\delta_0 = 7.61/(1+z)$ and β from Table 1 of MHR00, which produces good fits to ΛCDM

($\Omega_{\rm m} = 0.4$) simulation of Miralda-Escudé et al. (1996). We then set A and C_0 such that the total area under $P_\Delta^{\rm MHR00}(\Delta)$ and the mean overdensity are both equal to one. Parameters for redshifts other than those listed in MHR00 are linearly interpolated.

To convert from densities to optical depths, assumptions must be made about the ionizing background radiation and the thermal state of the gas. The Lyα optical depth of a uniform IGM would be

$$\tau_u = \frac{\pi e^2}{m_e c} f_\alpha \lambda_\alpha H^{-1}(z) n_{\rm H\,I}\,, \tag{4.2}$$

where f_α is the Lyα oscillator strength, $\lambda_\alpha = 1216$ Å, and $H(z)$ is the Hubble constant at redshift z (Gunn & Peterson 1965). In the case of photoionization equilibrium, the optical depth $\tau(\Delta)$ for an overdensity Δ can be expressed in terms of the H I ionization rate Γ, and the recombination coefficient α as (Weinberg et al. 1997)

$$\tau(\Delta) \propto \frac{(1+z)^{4.5}(\Omega_{\rm b}h^2)^2\alpha[T(\Delta)]}{h\Gamma(\Delta,z)\Omega_{\rm m}^{0.5}}\Delta^2\,, \tag{4.3}$$

where α depends on the temperature as $\alpha(T) \propto T^{-0.7}$ for $T \sim 10^4$ K (Abel et al. 1997). The IGM temperature will generally depend on the density, which is typically expressed as a power-law equation of state, $T(\Delta) = T_0\Delta^{1-\gamma}$ (e.g., Hui & Gnedin 1997). As other authors have done, however, we will assume a uniform UV background and an isothermal IGM (Songaila & Cowie 2002; Songaila 2004; Fan et al. 2002, 2006a). Following Fan et al. (2002), we can then express the optical depth as a function of density,

$$\tau(\Delta) = \tau_0 \left(\frac{1+z}{7}\right)^{4.5} \left[\frac{0.05}{\Gamma_{-12}(z)}\right] \Delta^2\,, \tag{4.4}$$

where Γ_{-12} is the H I ionization rate in units of 10^{-12} s^{-1}. For comparison to other works (McDonald et al. 2001; Fan et al. 2002, 2006a), we take $\tau_0 = 82$, although the normalization depends on the choice of cosmology. Equations (4.1) and (4.4) can then be used to determine the expected distribution of optical depths,

$$P_\tau^{\rm MHR00}(\tau) = \frac{AG^{(\beta-1)/2}}{2\tau^{(\beta+1)/2}} \exp\left[-\frac{\left(G^{1/3}\tau^{-1/3} - C_0\right)^2}{2(2\delta_0/3)^2}\right], \tag{4.5}$$

where

$$G \equiv \tau_0 \left(\frac{1+z}{7}\right)^{4.5} \left[\frac{0.05}{\Gamma_{-12}(z)}\right] . \tag{4.6}$$

Finally, we can convert to the expected distribution of normalized fluxes, $F = e^{-\tau}$,

$$P_F^{\mathrm{MHR00}}(F) = \frac{AG^{(\beta-1)/2}}{2(-\ln F)^{(\beta+1)/2} F} \exp\left[-\frac{\left(G^{1/3}(-\ln F)^{-1/3} - C_0\right)^2}{2(2\delta_0/3)}\right] \tag{4.7}$$

for $0 \leq F \leq 1$, 0 otherwise. The distribution of fluxes at a particular z is then fully specified by the ionization rate Γ_{-12}.

Lognormal τ distribution

For the lognormal optical depth distribution, we make no assumptions about the underlying density field, temperature, or ionization rate. As discussed above, a lognormal distribution can be motivated either from arguments about the evolution of an initially Gaussian density field (Coles & Jones 1991; Bi et al. 1992) or by the central limit theorem. Here we consider it to be a generic model that may plausibly describe the distribution of optical depths. The lognormal distribution is described by two parameters, $\mu = \langle \ln \tau \rangle$, and σ, which is the standard deviation of $\ln \tau$,

$$P_\tau^{\mathrm{Lognormal}}(\tau) = \frac{1}{\tau\sigma\sqrt{2\pi}} \exp\left[-\frac{(\ln \tau - \mu)^2}{2\sigma^2}\right] . \tag{4.8}$$

This gives an expected distribution of transmitted fluxes,

$$P_F^{\mathrm{Lognormal}}(F) = \frac{1}{(-\ln F) F \sigma\sqrt{2\pi}} \exp\left[-\frac{(\ln(-\ln F) - \mu)^2}{2\sigma^2}\right] \tag{4.9}$$

for $0 \leq F \leq 1$, 0 otherwise. There are obvious similarities between the MHR00 and lognormal distributions, which should not be surprising if they are both expected to at least roughly describe the data. We will examine the differences between the two cases more closely in §4.4.1.

4.3.3 Fitting the observed PDFs

In order to match the observed flux PDF, we must account for various imperfections in the data. The most important of these is noise in the flux measurements, which will smooth out the PDF and create pixels with $F < 0$ and $F > 1$. We incorporate this effect by convolving the ideal flux PDFs given by equations (4.7) and (4.9) with a smoothing kernel constructed separately for each flux bin. (Numerically, the smoothing is performed on bins much narrower than those used for the final PDFs). The kernel for a particular bin is a weighted sum of Gaussian kernels whose widths and weights are determined from the distribution of formal flux errors of pixels in that bin. The result is typically a kernel with a narrow core to account for pixels with low noise, and an extended tail for noisier pixels. This allows us to fit regions of the Lyα forest where the data quality is highly inhomogeneous.

Errors in the continuum level and the flux zero point will also affect the the observed PDF. A change in the continuum will cause the observed PDF to be stretched or compressed in proportion to the flux level. An error in the zero point, which may result either from imperfect sky subtraction or from spurious counts (i.e., cosmic rays) improperly handled by the spectrum extraction or combination routines, will also stretch or compress the observed PDF from the low-flux end. In fitting the PDFs we consider two cases: first, where we assume there are no errors in either the continuum or the zero point, and second, where the continuum level and zero point are treated as free parameters. We define the preferred continuum and zero point levels to be those which, if applied to the data, would allow the theoretical distributions to produce the best. When performing the fits, however, the adjustments are applied to the models and not to the data. The continuum and zero points are treated independently, such that a change in the zero point does not require a change in the continuum, and visa versa. We do not allow zero point corrections at $z < 3$, where few pixels have zero flux. This was found to have no significant impact on the other parameters.

The results of the χ^2 minimization fitting are summarized in Tables 4.2 and 4.3 for the MHR00 and lognormal cases, respectively. The best-fitting PDFs are plotted in Figures 4.1 through 4.5. For each region, we show the observed PDF along with the best-fitting theoretical PDFs in the cases where no continuum or zero point corrections are made and where the continuum and zero point are allowed to vary. At $z > 5$, the MHR00 and lognormal distribution provide very similar fits. This is not a surprise since, at these redshifts, we are sampling the low-optical depth tail of both distributions. The differences in the distributions increase at lower redshift. At $3 < z < 5$, the best-fit MHR00 distribution significantly underpredicts the number of pixels with very low optical depth unless a continuum correction is applied. In contrast, the best-fit lognormal distributions provide a reasonable fit to the data at all redshifts, with or without a change in the continuum. Both models underpredict the number of saturated pixels in some cases, although the discrepancy tends to be much larger for the MHR00 distribution.

In Figure 4.6 we compare the minimum reduced χ^2 values for both models in the case where the continua and zero points are held fixed. At $z < 2$, there is a roughly even divide between regions that are better fit by the MHR00 distribution and those that prefer the lognormal distribution. In most instances, however, where the MHR00 distribution is preferred, the fit is relatively poor ($\chi^2_{\mathrm{r}} > 2$). At $z > 5$, the fits are mostly comparable, as noted above. For $3 < z < 4$, the lognormal distribution provides a reasonable fit and is strongly preferred over the MHR00 model.

The fits improve for both models when the continua and zero points are allowed to vary. Most of this improvement is the result of the continuum corrections. The effect is particularly large for the MHR00 distribution, which implies that the MHR00 model tends to require that a significant continuum correction be applied to the data in order to produce a good fit. In Figure 4.7 we plot the reduced χ^2 values for these more general fits. As was the case without continuum and offset adjustments, the two distributions produce comparable fits at $z > 5$. At all lower redshifts, however, the lognormal distribution is preferred.

As noted above, even at low redshift, where extended regions of the spectrum have very little absorption, the continuum fit may be in error due to a combination of noise and the personal bias of the individual applying the fit. At $z < 4$, however, the continuum error should be less than a few percent for reasonably high signal-to-noise data. In Figure 4.8 we plot the continuum correction preferred for both distributions as a function of redshift. The MHR00 model requires the continuum to steadily increase with redshift over the continuum drawn by hand in order to account for the lack of pixels predicted to lie near the continuum (i.e., pixels with very low optical depth). In contrast, the lognormal τ distribution naturally accommodates fluxes near the continuum and does not require a large continuum correction for $z < 4.5$. At $z > 5.4$, the preferred continuum adjustment has a large scatter for both

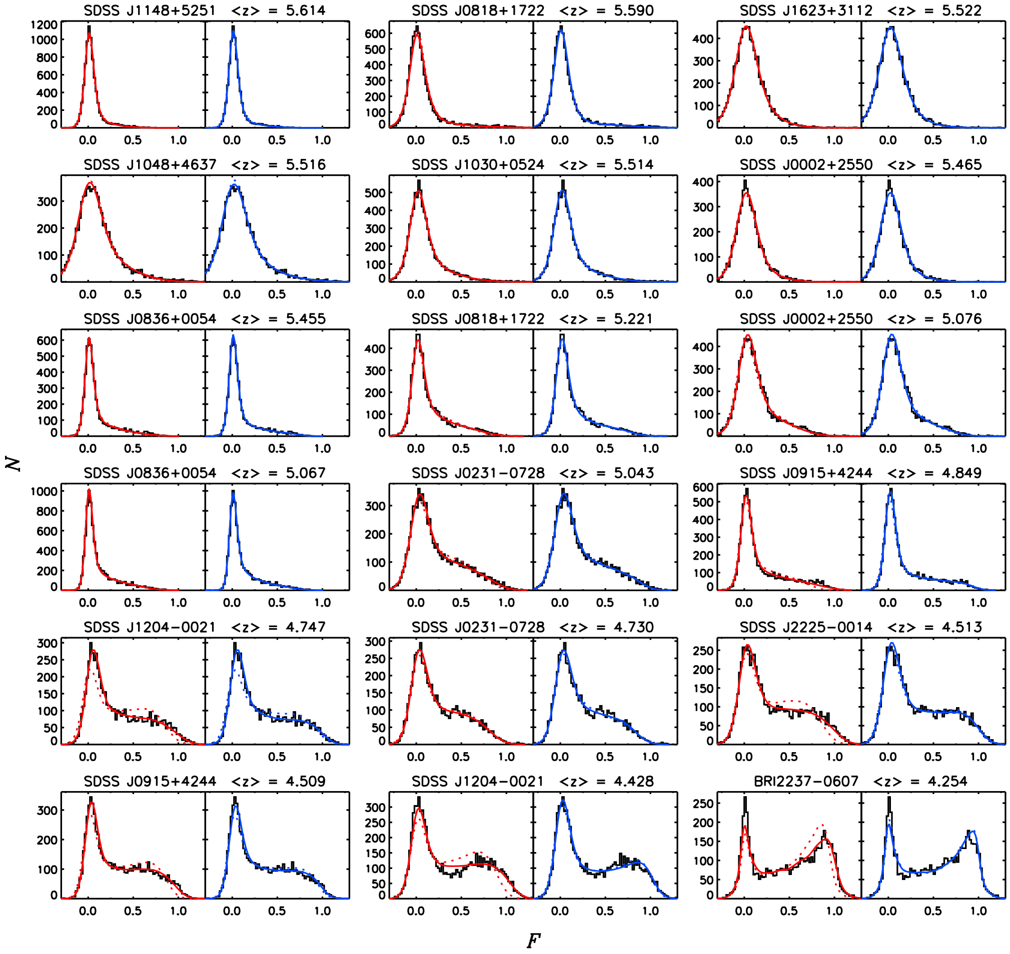

Figure 4.1 Fits to the Lyα flux probability distribution functions for QSOs in our sample. Each set of panels is labeled with the QSO name and the mean absorption redshift. Histograms show the observed PDF. For each region, MHR00 model fits assuming an isothermal IGM are shown on the left-hand side (red lines), while fits based on a lognormal τ distribution are shown on the right-hand side (blue lines). Dotted lines indicate the best fit without adjusting either the continuum or the zero point. Solid lines show the best fits when the continuum and zero point are allowed to vary. The lognormal τ distribution generally produces a good fit without large adjustments to the continuum, whereas at $3 < z < 5$ the MHR00 model fits tend to be poor unless a significant continuum adjustment is made.

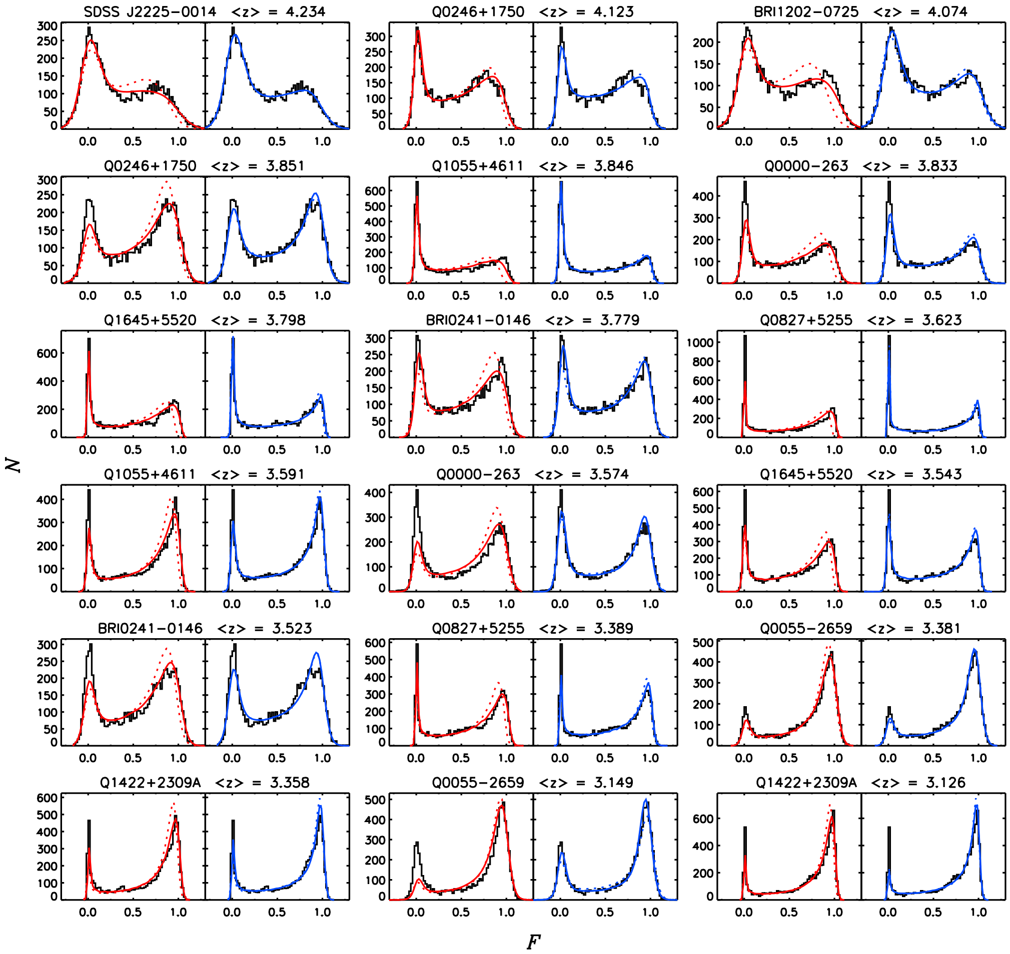

Figure 4.2 Fits to the Lyα flux probability distribution functions for QSOs in our sample, continued from Figure 4.1.

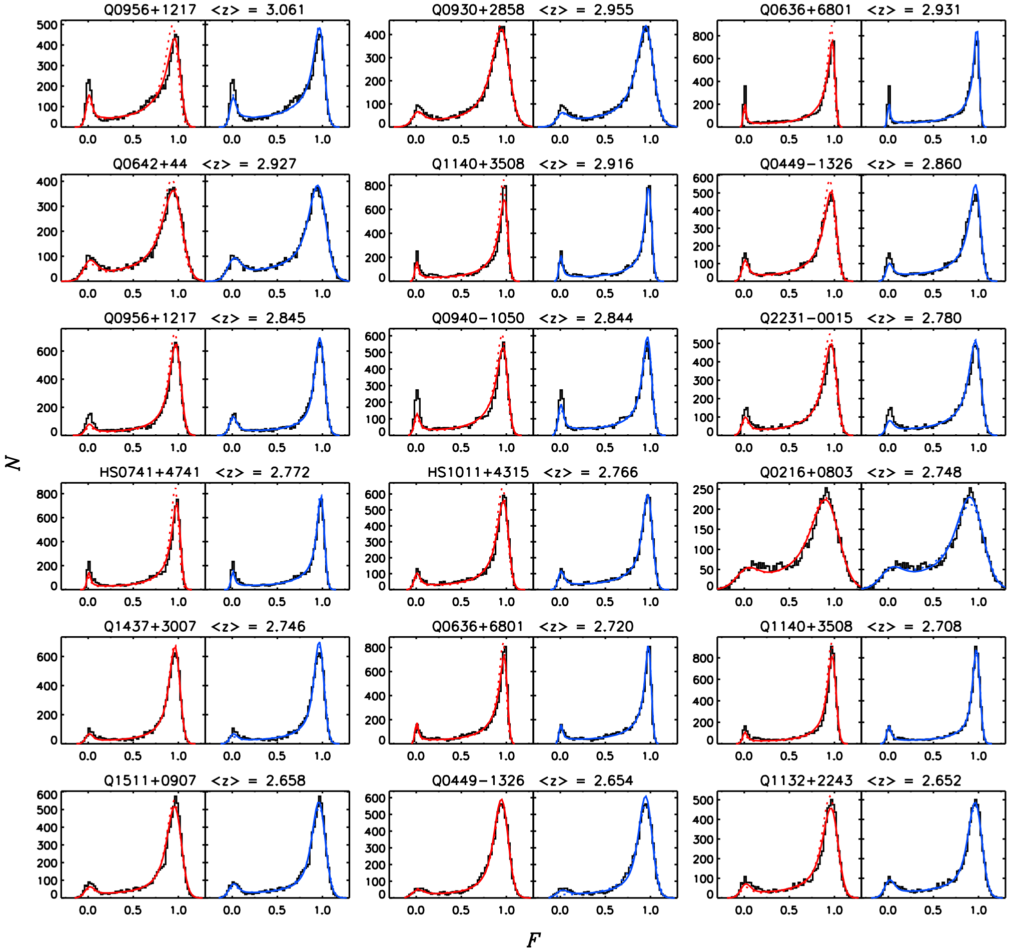

Figure 4.3 Fits to the Lyα flux probability distribution functions for QSOs in our sample, continued from Figure 4.1.

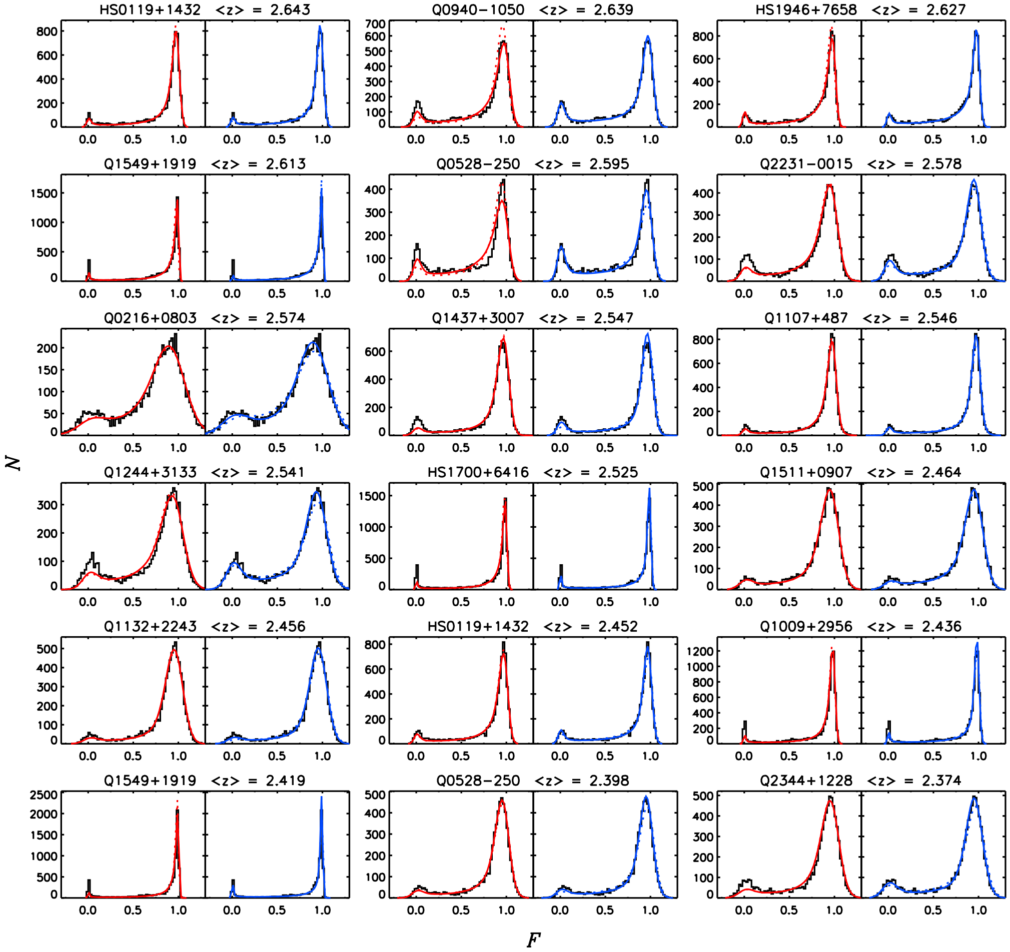

Figure 4.4 Fits to the Lyα flux probability distribution functions for QSOs in our sample, continued from Figure 4.1.

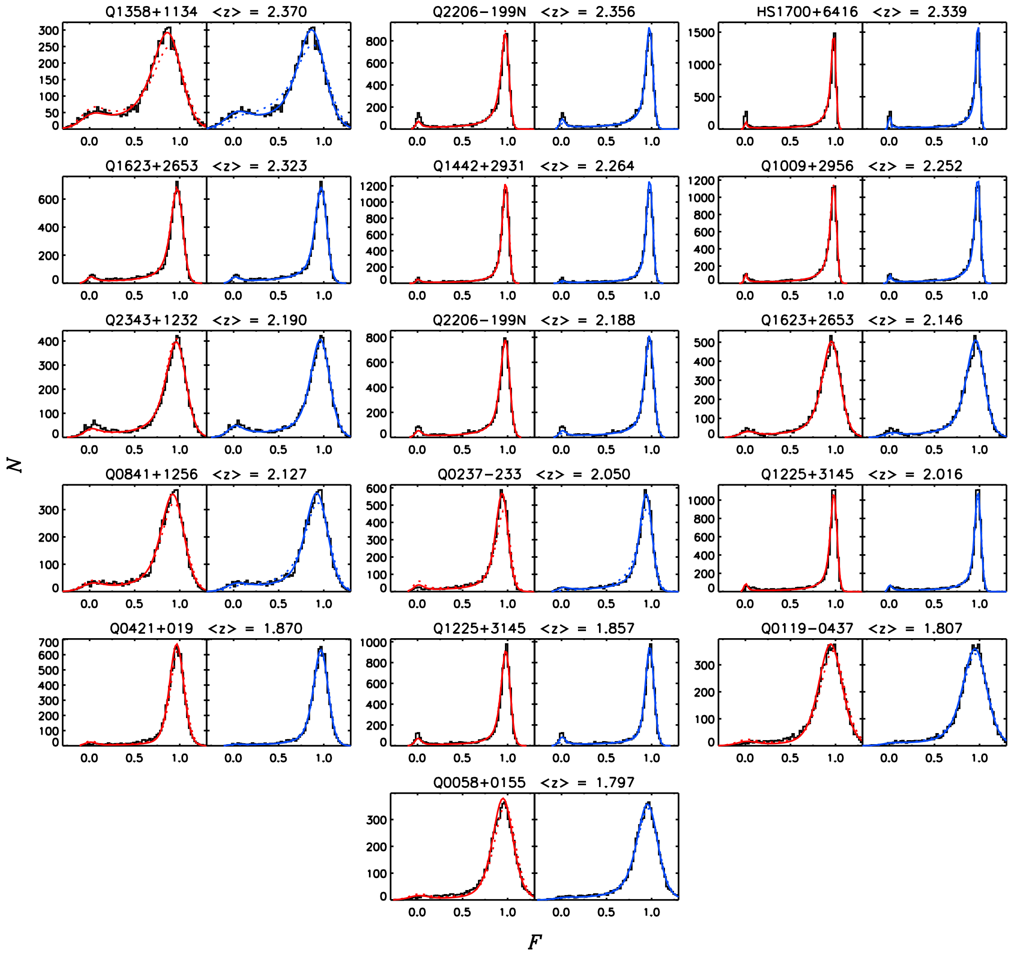

Figure 4.5 Fits to the Lyα flux probability distribution functions for QSOs in our sample, continued from Figure 4.1.

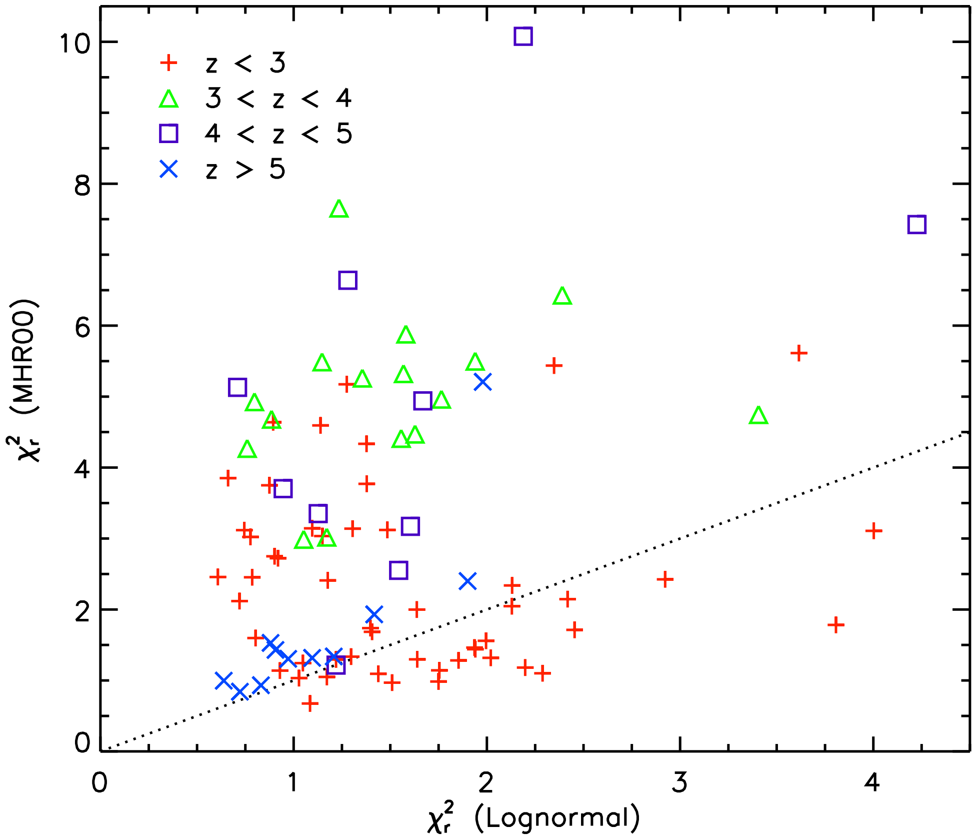

Figure 4.6 A comparison of the reduced χ^2 values for the best-fitting MHR00 and lognormal τ PDFs when the continuum and zero point are held fixed. Symbols indicate the mean absorption redshift of the fitted region of the Lyα forest. The dotted line indicates where $\chi^2_{\mathrm{r,\,MHR00}} = \chi^2_{\mathrm{r,\,Lognormal}}$. Roughly half of the Ly$\alpha$ regions at $z < 3$ are better fit by the MHR00 PDF. Otherwise, the lognormal PDF is preferred.

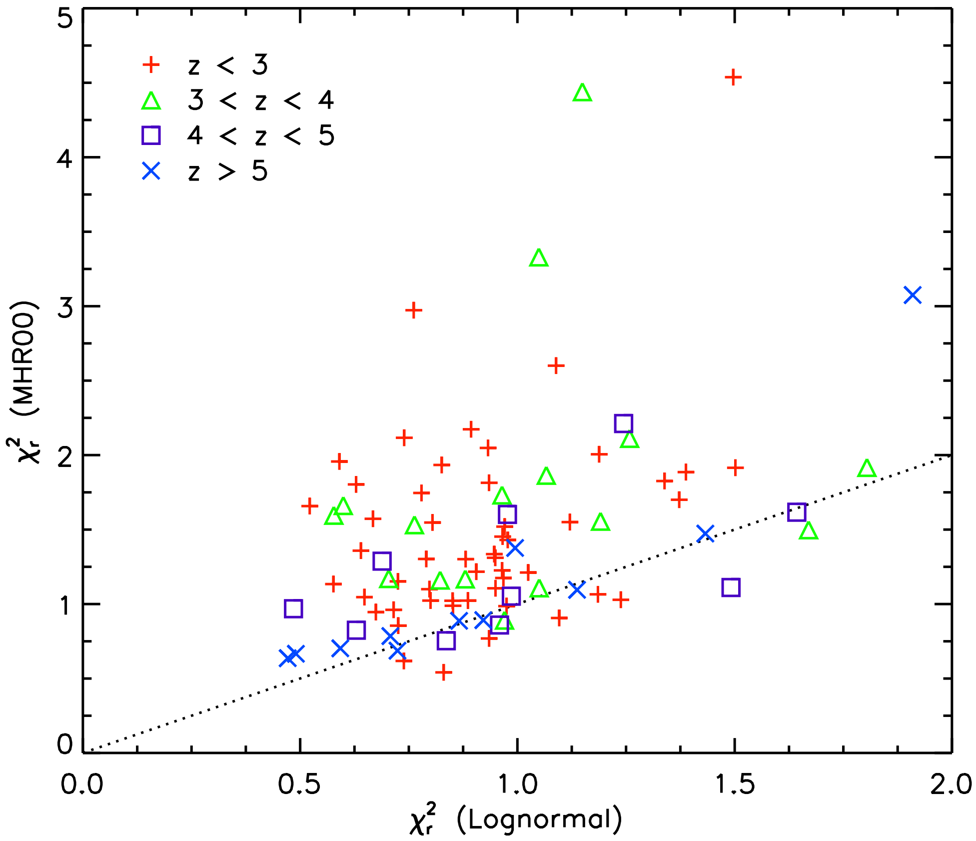

Figure 4.7 A comparison of the reduced χ^2 values for the best-fitting MHR00 and lognormal τ PDFs when the continuum and zero point are allowed to vary. Note the change in scale from Figure 4.6. Symbols indicate the mean absorption redshift of the fitted region of the Lyα forest. The dotted line indicates where $\chi^2_{\mathrm{r,\,MHR00}} = \chi^2_{\mathrm{r,\,Lognormal}}$. The lognormal PDF is preferred at all redshifts, particularly at $z < 5$.

theoretical distributions, since nearly all pixels have significant optical depth.

In Figure 4.9 we show examples of the best-fit continua overlaid on the corresponding regions of the Lyα forest. While the shape of a QSO continuum can be somewhat ambiguous when convolved with the response function of the instrument, no undue effort has been made to fit the continua across every transmission peak. The lognormal distribution fits the data well when the continua are near their intuitive values, while the MHR00 model requires the continua to be substantially higher. Fitting QSO continua is an inherently uncertain task. Even when the continuum is allowed to vary, however, the lognormal τ distribution produces a better fit than the MHR00 model.

In contrast to our results, Rauch et al. (1997) and McDonald et al. (2000) found good agreement between the observed flux PDFs from some of the same sightlines used here and the predictions from a numerical simulation with a density distribution similar to the MHR00 model. The reason for this appears to lie in their treatment of the continuum. Both works apply a strong correction to their simulated spectra by placing the continuum at the maximum transmitted flux level for each pass through the simulation box ($10h^{-1}$ Mpc, or ~ 30 Å at $z = 4$). This is a much higher-order correction than we consider here. In addition, McDonald et al. (2000) group all pixels with flux $F > 1$ into their bin at $F = 1$. This disguises the shape of the observed PDF for pixels with low optical depth, particularly at $z = 3-4$. By fitting pixels at all fluxes, we remain sensitive to the *shape* of the PDF near $F \sim 1$. Applying a low-order continuum correction is therefore not sufficient to obtain a good fit for the MHR00 distribution. This works well, however, in the lognormal case. Much of the discriminating power in the flux PDF occurs at very low optical depths. Therefore, unless more reliable continuum fits can be made, the success of the MHR00 model in this regime is at best unclear.

4.4 Redshift Evolution of Optical Depth

4.4.1 Lognormal Parameters

We have shown that a lognormal distribution of optical depths provides a good fit to the observed Lyα transmitted flux PDF at all redshifts $1.7 < z < 5.8$. In this section we examine the evolution of the lognormal distribution and use it to predict the evolution of the mean

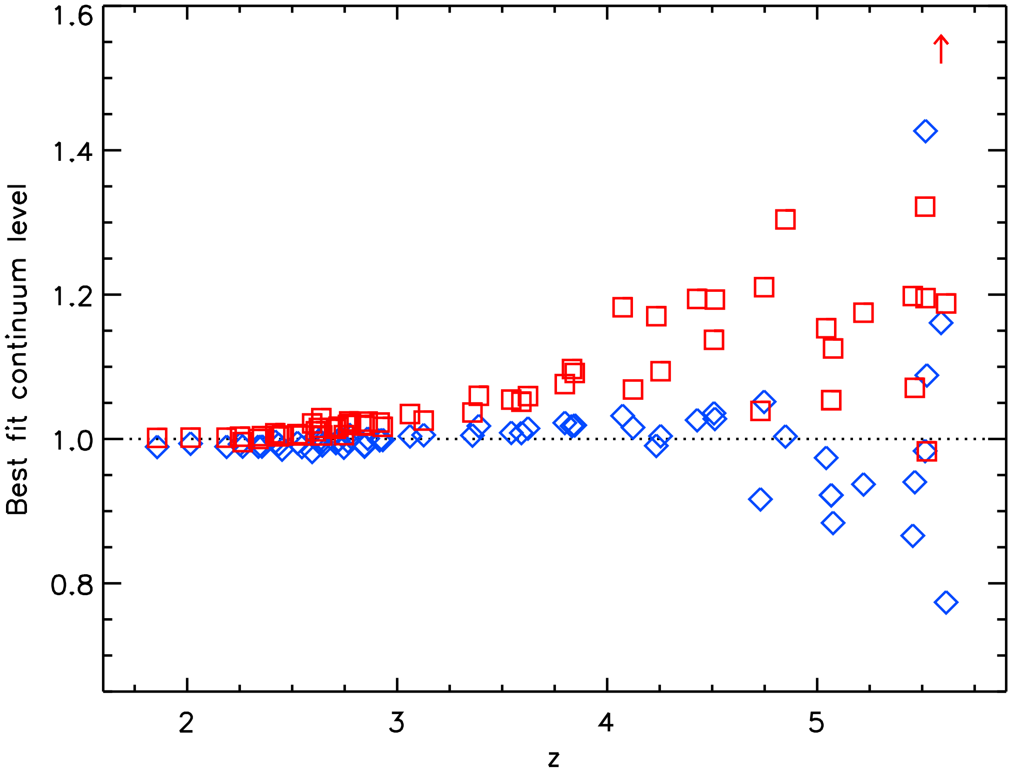

Figure 4.8 Continuum adjustments to the data that are required so that the observed distribution of Lyα fluxes are best fit by the theoretical distributions. Squares show the continuum adjustment needed for the MHR00 model. Diamonds show the continuum adjustment needed for the lognormal τ distribution. The MHR00 model value for SDSS J0818+1722 at $\langle z_{\rm abs} \rangle = 5.590$ lies outside the plot range, as indicated by the arrow. At $z < 4$, only the values for regions with median flux error < 0.05 are shown. The MHR00 distribution requires a steadily increasing continuum adjustment with redshift to account for the lack of pixels predicted to lie near the continuum. At $z > 5.4$ the best-fitting continuum has a large scatter for both distributions due to how little transmitted flux remains in the forest.

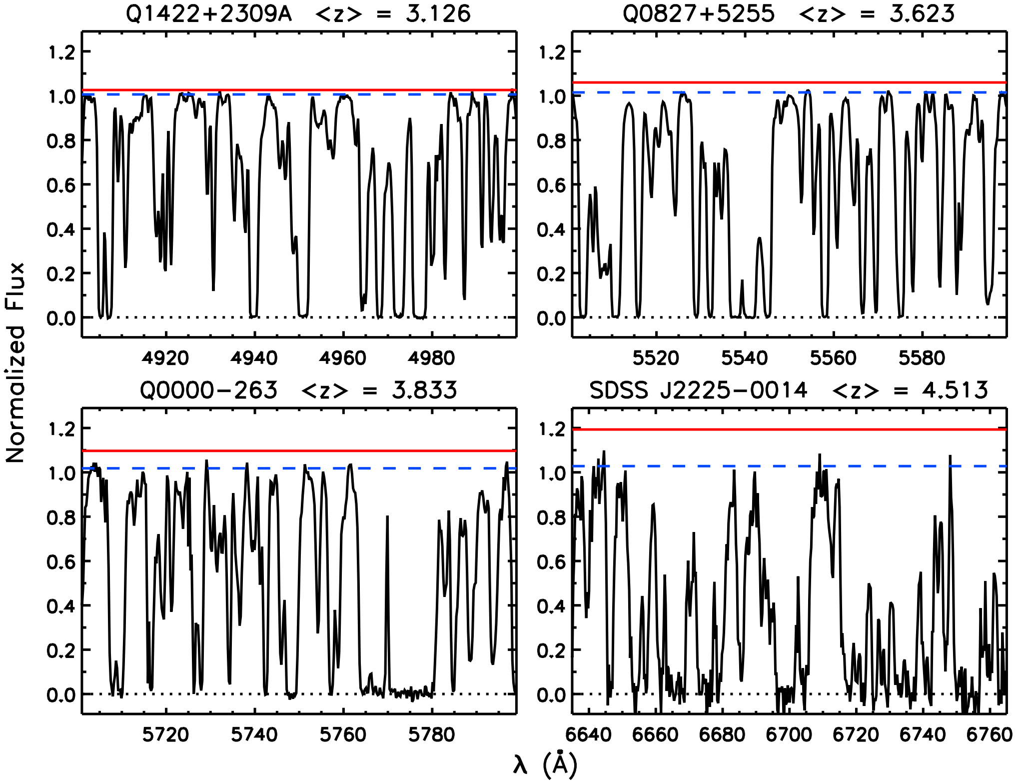

Figure 4.9 Four examples of continuum adjustments needed so that the observed flux PDFs are best fit by the theoretical distributions. Each panel shows a sample of the Lyα forest taken from the fitted region indicated by the QSO name and mean absorption redshift. The solid and dashed horizontal lines shows the continuum levels best fit by the MHR00 and lognormal τ distributions, respectively. The spectra have been binned to 13 km s^{-1} pixels for clarity.

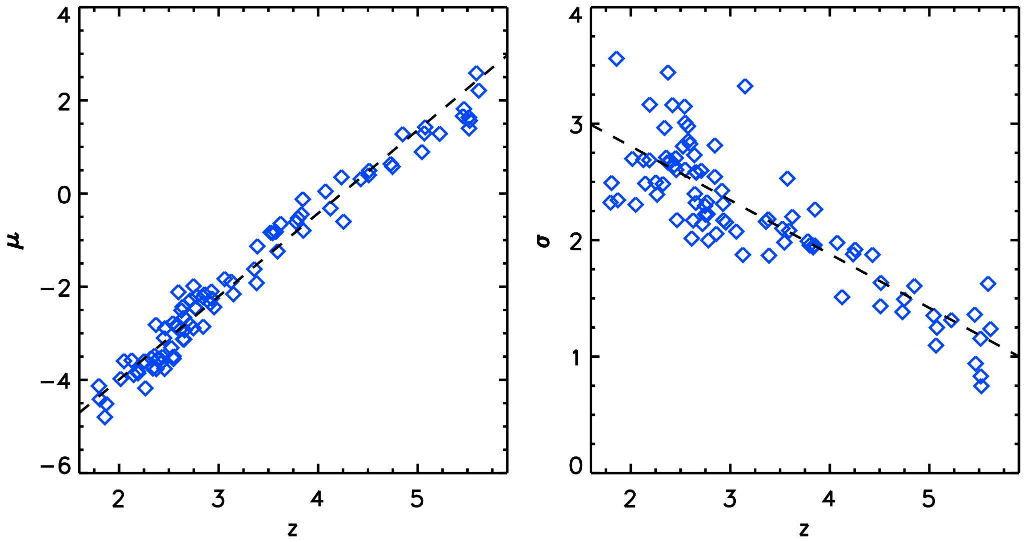

Figure 4.10 Parameters for the lognormal distribution of Lyα optical depths that produce the best fits to the observed flux PDFs. Here, $\mu = \langle \ln \tau \rangle$ and $\sigma = \mathrm{std\,dev}\,(\ln \tau)$. The dashed lines show the best linear fits from equations (4.10) and (4.11).

transmitted flux at $z > 6$. In Figure 4.10 we plot the lognormal parameters μ and σ as a function of z. Both parameters evolve smoothly with redshift, as should be expected if they reflect a slowly-evolving density field, UV background, and temperature-density relation. The increase in μ and decrease in σ with z can both be understood primarily in terms of the evolution of a self-gravitating density field. At earlier times, the density contrast in the IGM will be lower. This will tend to produce a higher volume-weighted median τ, which is given by e^{μ}, as well as a smaller logarithmic dispersion in τ, which is given by σ. Since we do not have an *a priori* model for how the lognormal parameters should evolve, for this work we choose the simplest possible parametrization. Excluding points at $z > 5.4$, where the lognormal parameters depend on highly uncertain continuum levels, a linear fit in redshift gives

$$\mu(z) = (-9.35 \pm 0.17) + (1.79 \pm 0.04)(1 + z)\,, \tag{4.10}$$

$$\sigma(z) = (4.19 \pm 0.16) - (0.46 \pm 0.03)(1 + z)\,. \tag{4.11}$$

These fits are plotted as dashed lines in Figure 4.10.

We can compare the evolution of the MHR00 and lognormal τ distributions and their predictions for the transmitted flux PDF. In Figure 4.11 we plot fiducial τ and flux distributions for $2 \leq z \leq 6$. Parameters for the lognormal distribution are calculated from equations (4.10) and (4.11). For the MHR00 model, values for Γ_{-12} are chosen to be consistent with the fitted values in Table 4.2. The vertical dotted lines indicate the range of optical depths that can be measured with good data. At $z = 2$ we are primarily sensitive to the high-τ tail in both distributions. At higher redshifts, the peaks of the distributions shift towards higher values of τ until we are sampling only the end of the low-τ tail at $z = 6$.

Differences in the shape of the transmitted flux PDF are largest at $3 \leq z \leq 5$, where $P_\tau(\tau)$ is well-sampled. The fact that the lognormal τ distribution is most strongly favored at these redshifts suggests that it is more likely to be useful in making predictions for the distribution of transmitted flux at $z > 6$. An important feature of the lognormal distribution is that it narrows with redshift more rapidly than the MHR00 distribution. It therefore predicts fewer pixels with measurable transmitted flux at $z \sim 6$ than does the MHR00 model with a slowly evolving UV background.

4.4.2 Mean transmitted flux

We can use the redshift evolution of the lognormal distribution to predict the the evolution of transmitted flux at $z \gtrsim 6$. The mean transmitted flux will be given by

$$\langle F \rangle = \int_0^1 F \, P_F(F) \, dF \, . \tag{4.12}$$

It is conventional to express the mean flux in terms of an effective optical depth $\tau_{\rm eff} = -\ln \langle F \rangle$. For a distribution of optical depths, $\tau_{\rm eff}$ will be smaller than the true mean optical depth. We show measurements of $\tau_{\rm eff}$ for Lyα from Songaila (2004) and Fan et al. (2006a) in Figure 4.12. The dashed line shows the best-fitting power-law to their data at $z < 5.5$ from Fan et al. (2006a). The deviation of the data from the power-law at $z > 5.7$ has been cited as the primary evidence for an abrupt change in the ionizing background at $z \sim 6$. We also show $\tau_{\rm eff}^\alpha$ as predicted by the evolution of the lognormal τ distribution given by equations (4.10) and (4.11) as a solid line. We emphasize that the lognormal parameters were fit only to measurements at $z < 5.4$. Even so, $\tau_{\rm eff}^\alpha$ calculated from the lognormal distribution both better fits the data at $z < 5$ and *predicts* the upturn in $\tau_{\rm eff}^\alpha$ at $z > 5.7$.

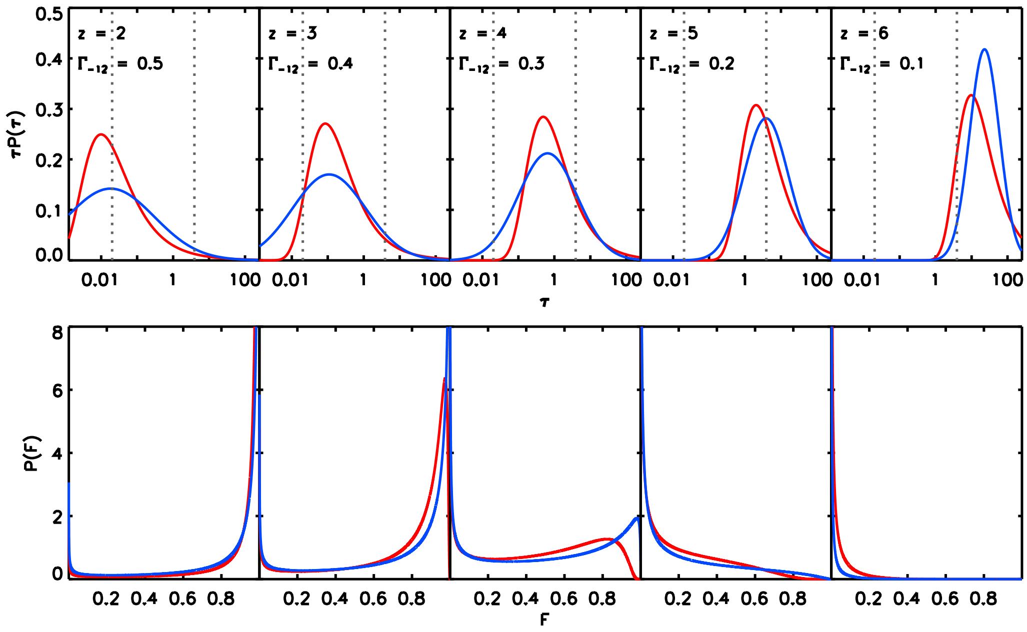

Figure 4.11 Redshift evolution of the theoretical Lyα optical depth and transmitted flux distributions. The top panels show the τ distributions for the indicated redshifts and ionization rates. Bottom panels show the corresponding transmitted flux PDFs. Distributions for the MHR00 model are shown in red. Distributions for the lognormal τ model are shown in blue. Parameters for the lognormal τ distribution were calculated from fits to μ and σ as a function of redshift (cf. equations 4.10 and 4.11). Vertical dotted lines indicate optical depths corresponding to 98% and 2% transmitted flux. The clearest differences in the predicted *shapes* of the flux PDFs occur at $3 < z < 5$. The lognormal τ distribution, which produces better fits to the data, narrows with redshift more rapidly than the MHR00 τ distribution. Hence, fewer pixels with measurable transmitted flux at $z = 6$ are predicted in the lognormal case.

In Figure 4.13 we include the lower-redshift measurements of Kirkman et al. (2005). The power-law underpredicts the amount of Lyα absorption at $z < 2.5$, while the lognormal distribution matches all observations at $1.6 < z < 6.2$.

Stronger constraints on the ionization state of the IGM can be set using Lyβ, which is a weaker transition than Lyα by a factor of 6.2. In the lognormal case, this produces a distribution of Lyβ optical depths with the same σ as Lyα but with $\mu_\beta = \mu_\alpha - \ln 6.2$. We can then compute the expected mean flux in the Lyβ forest at redshift z by multiplying the mean transmission resulting from Lyβ absorption at z by the mean transmission resulting from Lyα absorption at $z_\beta = (1+z)\lambda_\beta/\lambda_\alpha - 1$. We show the $\tau_{\mathrm{eff}}^{\beta}$ measurements from Songaila (2004) and Fan et al. (2006a) in Figure 4.14. These are computed directly from the transmitted flux and have not been corrected for foreground Lyα absorption. The dashed line again shows the best-fit power-law to the points at $z < 5.5$ from Fan et al. (2006a). The solid line shows the lognormal prediction. Here again, despite the fact that we have not used any Lyβ measurements to determine the optical depth distribution, $\tau_{\mathrm{eff}}^{\beta}$ predicted in the lognormal case is a better fit to the data at $z < 5$ and follows the upturn in $\tau_{\mathrm{eff}}^{\beta}$ at $z > 5.7$.

Our purpose here is not to fully characterize the evolution of transmitted flux at all redshifts. We have simply identified a distribution of optical depths that describes the observed distribution of transmitted fluxes better than the commonly used model. The fact that this distribution evolves smoothly with redshift, and that the same evolution describes changes in the Lyα forest as well at $z \sim 6$ as it does at $z \sim 3$ strongly suggests that the disappearance of transmitted flux at $z > 6$ is due to a smooth evolution of IGM properties. The lognormal prediction for $\tau_{\mathrm{eff}}^{\beta}$ falls slightly below some of the lower limits of Fan et al. (2006a) at $z \sim 6$, but the prediction does not take into account the expected scatter in the mean flux or any small deviation from our adopted linear redshift evolution of the lognormal parameters. The important point is that the evolution of the mean transmitted flux can be well described by a smooth evolution in the underlying optical depths. When sampling only the tail of the τ distribution, as at $z \sim 6$, a slight change in the optical depths will produce a large change in the transmitted flux.

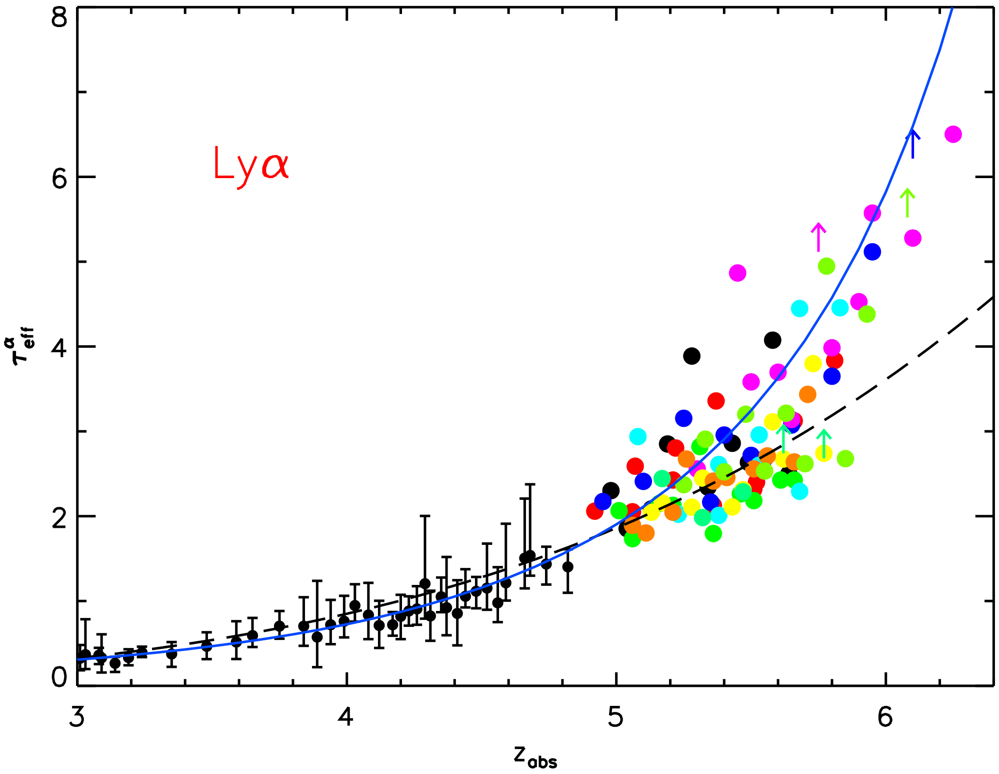

Figure 4.12 The evolution of Lyα effective optical depth with redshift, where $\tau_{\rm eff} = -\ln\langle F\rangle$. Data points are from Songaila (2004) (small circles) and Fan et al. (2006a) (large circles and arrows, with colors matching their Figure 2). The dashed line shows the best-fit power-law to $\tau_{\rm eff}^{\alpha}$ at $z < 5.5$ from Fan et al. (2006a). The solid line shows $\tau_{\rm eff}^{\alpha}$ calculated from the lognormal distribution of Lyα optical depths, for which the parameters were fit at $z < 5.4$. A simple evolution in the lognormal τ distribution predicts the upturn in $\tau_{\rm eff}^{\alpha}$ at $z > 5.5$ and produces a better fit to the observed $\tau_{\rm eff}^{\alpha}$ at $4 < z < 5$.

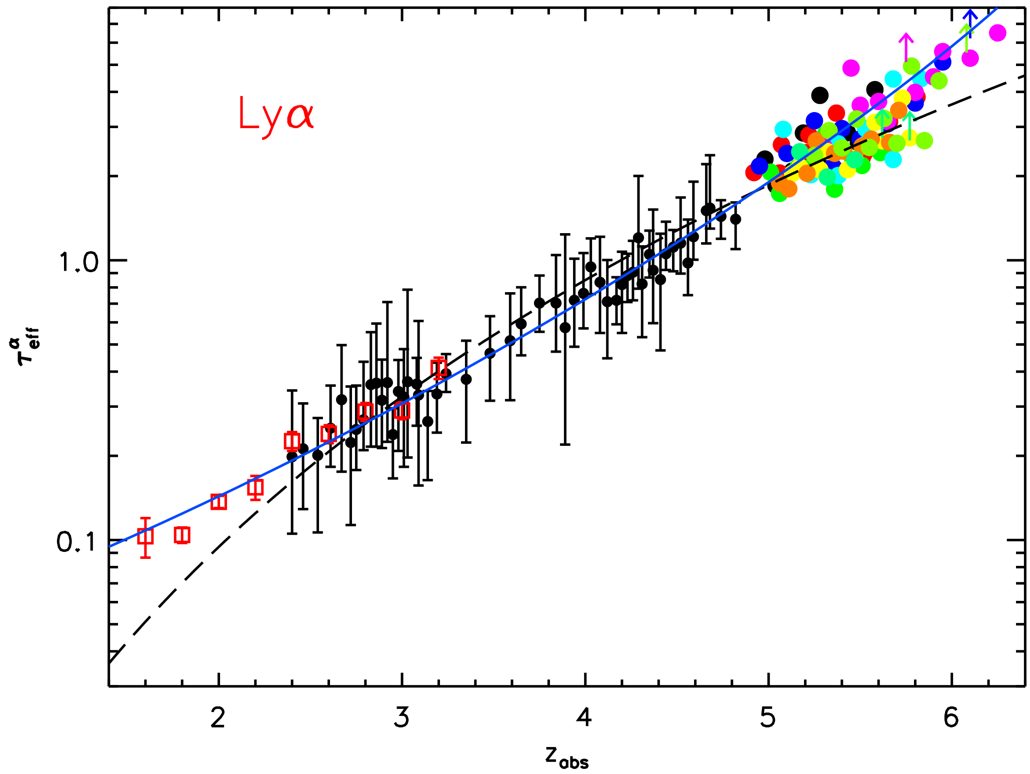

Figure 4.13 Same as Figure 4.12, with $\tau_{\rm eff}^{\alpha}$ on a logarithmic scale. We have also included lower-redshift measurements calculated from Kirkman et al. (2005), which exclude absorption from metal lines, Lyman limit systems, and damped Lyα systems. The Kirkman et al. (2005) points are plotted as open squares with errors in the mean measurements. The power-law fit from Fan et al. (2006a) (dashed line) underpredicts the amount of Lyα absorption both at $z > 5.7$ and at $z < 2.5$. In contrast, $\tau_{\rm eff}^{\alpha}$ calculated from the lognormal τ distribution (solid line), provides a simultaneously good fit to all points at $1.6 < z < 6.2$.

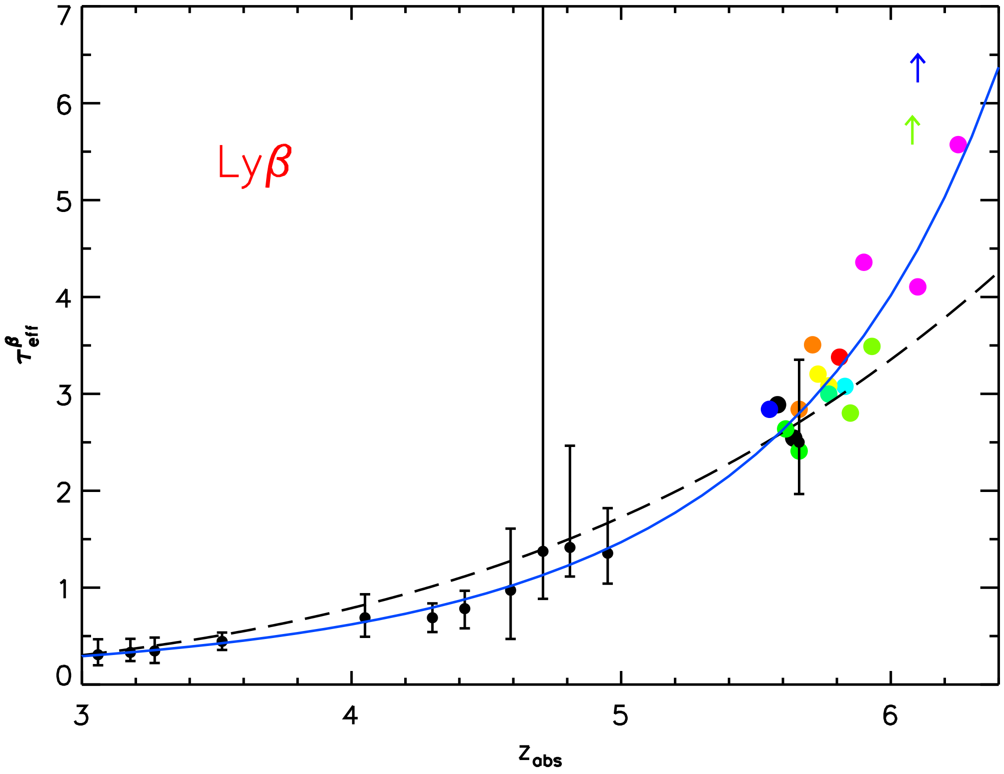

Figure 4.14 The evolution of Lyβ effective optical depths with redshift. Data points at from Songaila (2004) (small circles) and Fan et al. (2006a) (large circles and arrows, with colors matching their Figure 3). The data have *not* been corrected for foreground Lyα absorption. The dashed line shows the best-fit power-law to $\tau_{\rm eff}^{\beta}$ at $z < 5.5$ from Fan et al. (2006a). The solid line shows $\tau_{\rm eff}^{\beta}$ predicted purely from the lognormal distribution of Lyα optical depths. Even though no independent fitting of Lyβ fluxes was performed, the lognormal τ distribution captures the upturn in $\tau_{\rm eff}^{\beta}$ at $z > 5.5$ and produces a better fit to the observed $\tau_{\rm eff}^{\beta}$ at $4 < z < 5$.

4.4.3 UV background

Liu et al. (2006) recently demonstrated that a semi-analytic model based on a lognormal *density* distribution can reproduce the observed rise in $\tau_{\rm eff}$ at $z > 5.7$. However, they invoke a UV background that declines rapidly with redshift, decreasing by a factor of ~ 11 from $z = 3$ to 5, and by a factor of ~ 7 from $z = 5$ to 6. We have not assumed that the lognormal τ distribution used here arises directly from a lognormal density distribution. If we assume, however, a uniform UV background and an isothermal IGM, than we can calculate the H I ionization rate by inverting equation (4.4) and averaging over all densities. Doing so gives

$$\Gamma_{-12} = 0.05 \left(\frac{1+z}{7}\right)^{4.5} \frac{\tau_0}{\langle \tau^{1/2} \rangle^2} \,, \tag{4.13}$$

where $\langle \tau^{1/2} \rangle^2 = e^{\mu + \sigma^2/4}$, and we have used the fact that $\langle \Delta \rangle = 1$.

In Figure 4.15 we show Γ_{-12} calculated for each fitted region along with the mean values in bins of redshift. For comparison, the best-fit values of Γ_{-12} for the model distribution are also shown. The lognormal values are somewhat higher than the model values, which are in turn roughly consistent with previous measurements (McDonald et al. 2001; Fan et al. 2006a). We do not require, however, the strong evolution in Γ_{-12} given by Liu et al. (2006) for the lognormal model. Transforming from densities to optical depths depends on a number of factors, and we do not presume that the assumptions implicit in equation (4.13) are valid. We merely point out that a lognormal τ distribution is consistent with a slowly evolving UV background.

We can also calculate the mean volume-weighted neutral fraction,

$$f_{\rm H\,I} = (5.5 \times 10^{-5})\, h_{70}^{-1} \left(\frac{\Omega_{\rm m}}{0.3}\right)^{1/2} \left(\frac{\Omega_{\rm b}}{0.04}\right)^{-1} (1+z)^{-3/2} \langle \tau \rangle \,, \tag{4.14}$$

where we have used $H(z) \approx H_0 \Omega_{\rm m}^{1/2} (1+z)^{3/2}$. The mean optical depth for the lognormal distribution will be $\langle \tau \rangle = e^{\mu + \sigma^2/2}$. Calculating μ and σ from equations (4.10) and (4.11), this gives $f_{\rm H\,I} = [1.0, 1.2, 1.9, 4.0, 11, 20] \times 10^{-5}$ for $z = [2, 3, 4, 5, 6, 6.5]$. The mean optical depth will depend strongly on the high-τ tail of the distribution, which is poorly constrained at $z > 4$. The disappearance of transmitted flux at $z > 6$, however, is at least consistent with a highly-ionized IGM.

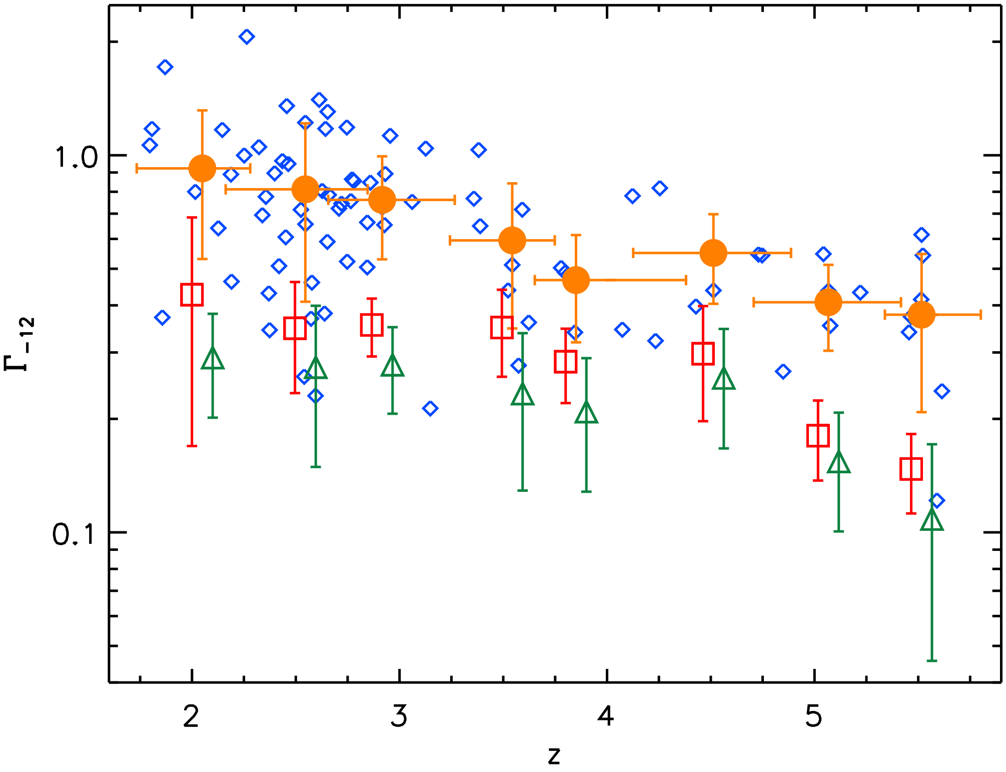

Figure 4.15 H I ionization rate as a function of redshift. Small diamonds show Γ_{-12} calculated from the lognormal fits to individual regions, assuming a uniform UV background (cf. equation 4.13). Points fit to high-S/N data are shown in blue. Filled circles show the mean Γ_{-12} for the lognormal model in redshift bins of 0.5, starting at $z = 2$. Vertical error bars show the standard deviation of points within a bin. Horizontal error bars show the range of redshift covered by all points within that bin. Squares show the mean Γ_{-12} from the MHR00 model fits for an isothermal IGM and uniform UV background ($\alpha = 0$). Triangles show the mean Γ_{-12} from the MHR00 model fits when α is allowed to vary.

4.5 An inverse temperature-density relation?

We have shown that the simplest transformation of the MHR00 gas density distribution to optical depths provides at best an uncertain fit to the observed distribution of transmitted fluxes. There are, however, several ways to modify the expected τ distribution. Here we consider a non-isothermal temperature-density relation. From equation (4.3) we have $\tau \propto T^{-0.7}\Gamma^{-1}\Delta^{2}$. We will address the general case where either T or Γ may depend on Δ. For a power law $T^{0.7}\Gamma \propto \Delta^{\alpha}$, this gives

$$\tau(\Delta) = \tau_0 \left(\frac{1+z}{7}\right)^{4.5} \left[\frac{0.05}{\Gamma_{-12}(z)}\right] \Delta^{2-\alpha}\,, \tag{4.15}$$

where Γ_{-12} is now the H I ionization rate at the mean density, and the temperature at the mean density is included in τ_0. For a uniform UV background, the equation of state index will be $\gamma = 1 + 1.43\alpha$.

Not surprisingly, adding a degree of freedom significantly improves the fits for many of our Lyα forest regions. The fitting results are summarized in Table 4.4, and a sample of the fits are shown in Figure 4.16. There is a large scatter in the best-fit α at all redshifts when the continuum and zero point are allowed to vary. The mean value $\langle\alpha\rangle = -0.36 \pm 0.45$ (sample variance), however, suggests that $T^{0.7}\Gamma$ *increases* towards lower densities. For a uniform UV background, this implies an equation of state $T(\Delta) \propto \Delta^{\gamma-1}$ with $\gamma \approx 0.5$. An index < 1 disagrees with previous measurements using the flux PDF (Choudhury et al. 2001; Lidz et al. 2006a; Desjacques & Nusser 2005). Those works, however, typically considered only $\gamma > 1$, which is expected following reionization if overdense regions experience more photoionization heating and less adiabatic cooling than underdense regions. Radiative transfer effects may create a complex temperature-density relation if underdense regions are reionized by a harder UV background than the dense regions near ionizing sources (Bolton et al. 2004). For the flux PDF, $\gamma < 1$ allows for a lower Γ (typically by $\sim 20\%$, see Figure 4.15), creating more saturated pixels, while at the same time maintaining a low τ in low density regions. The necessary continuum corrections also decrease, although they are still roughly half of those needed in the case of $\alpha = 0$. Of course, it is possible that we are not measuring the real equation of state, and that the added degree of freedom simply compensates for some other aspect of the model distribution. A more careful treatment of this problem will be reserved for future work.

4.6 Conclusions

We have analyzed the Lyα transmitted flux probability distribution in a high-resolution sample of 55 QSOs spanning the absorption redshift range $1.7 < z < 5.8$. Our main goal has been to assess how well the theoretical optical depth distribution commonly used to measure the H I ionization rate describes the observed flux PDF. We find that the MHR00 model, under the assumptions of a uniform UV background and an isothermal IGM, produces a poor fit to the observed flux PDF at all redshifts where the optical depth distribution is well sampled. This discrepancy eases only if large continuum corrections are applied.

In contrast, a lognormal distribution of optical depths fits the data well with only minor continuum adjustments. The parameters of the lognormal distribution evolve smoothly with redshift, as expected for a slowly evolving IGM, and reflect both an increase in the mean τ and a decrease in the relative scatter in τ with redshift. We have performed simple linear fits to the lognormal parameters at $z < 5.4$. The mean transmitted flux calculated from these fits matches the observations at $1.6 < z < 5.7$ better than the best-fitting power law (Fan et al. 2006a). In addition, extrapolating the lognormal evolution to $z > 6$ predicts the observed upturn in both Lyα and Lyβ effective optical depths. This strongly suggests that if a slowly evolving density field, ionizing background, and IGM temperature are responsible for the evolution of the Lyα forest at $z < 5$, then there is no reason to suspect a sudden change in the IGM at $z \sim 6$.

We emphasize that we have used the lognormal distribution as a phenomenological description of the optical depths only, and that the distribution may not hold for optical depths that are outside the dynamic range of the transmitted flux. Other factors, such a non-isothermal IGM or variations in the UV background are likely to be important in deriving the optical depth distribution from the underlying density field. We have explored the possibility of a non-isothermal IGM in the context of the MHR00 model. The best fits tend to favor an inverse temperature-density relation, where temperature increases with density. This is contrary to typical expectations for the balance between photoionization heating and adiabatic cooling (Hui & Gnedin 1997), and may be an artifact of some other feature that causes the MHR00 model to disagree with the data. However, as Bolton et al.

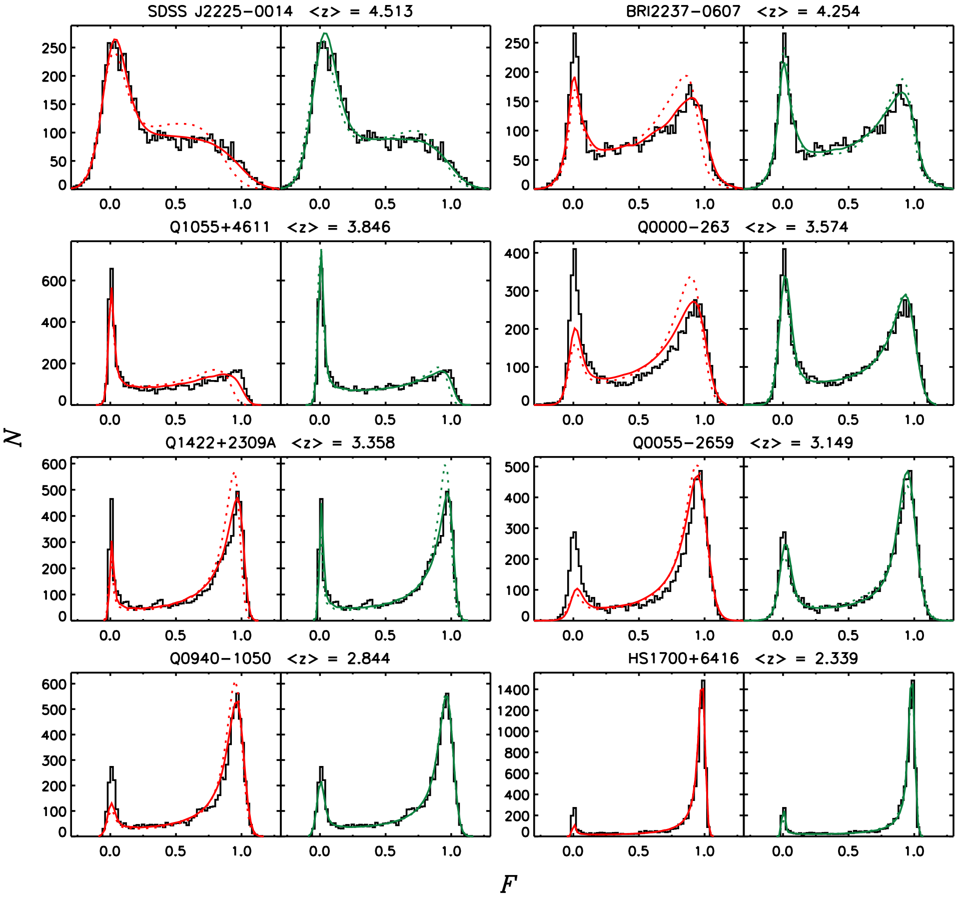

Figure 4.16 Examples of transmitted flux PDFs where the MHR00 model fit is significantly improved by allowing a non-isothermal temperature-density relation, or more generally, $T^{0.7}\Gamma \propto \Delta^{\alpha}$. Each set of panels is labeled with the QSO name and the mean absorption redshift. Histograms show the observed PDF. For each section, MHR00 model fits with $\alpha = 0$ are shown on the left-hand side (red lines), while fits with α treated as a free parameter are shown on the right-hand side (green lines). Dotted lines indicate the best fit without adjusting either the continuum or the zero point. Solid lines show the best fits when the continuum and zero point are allowed to vary. The mean value of α for all regions is $\langle\alpha\rangle \approx -0.4$. This may indicate that the UV background decreases with density, or that there exists an inverse temperature-density relation. Alternatively, finding $\alpha < 0$ may be an artifact of some other features of the MHR00 model that causes it to disagree with the data.

(2004) point out, radiative transfer effects may create a complex thermodynamic state in the IGM. If gas at a given density can have a range of temperatures and/or ionization rates, then a MHR00-like density distribution may give rise to a τ distribution that is closer to lognormal.

The largest source of uncertainty in fitting the flux PDFs remains the continuum level. Much of the disagreement between the MHR00 model and observed PDFs stems from the lack of pixels predicted to have very low optical depths at $z > 3$. This can be at least partially remedied by adjusting the continuum (see also McDonald et al. 2000). A dramatic change in the IGM, however, would still be required to explain the observed lack of transmitted flux at $z \sim 6.2$ (e.g., Fan et al. 2002, 2006a). Future observation of $z > 4$ gamma-ray bursts, whose continuum is a simple power law, may help to establish the correct flux PDF. For now, we have identified an optical depth distribution that both fits the data down to $z = 1.6$ and captures the evolution of the mean transmitted flux at $z > 5.7$. If the lognormal distribution truly reflects aspects of the real optical depth distribution, then the motivation for late reionization may be greatly diminished.

The authors would like to thank Martin Haehnelt for stimulating conversations, as well as Tom Barlow and Rob Simcoe for reducing much of the data. We especially thank the Hawaiian people for the opportunity to observe from from Mauna Kea. Without their hospitality this work would not have been possible. MR has been supported by the NSF under grant AST 05-06845.

Table 4.2. Best-Fit MHR00 Model Parameters (Isothermal)

QSO	$\langle z_{\rm abs}\rangle$[a]	$N_{\rm bin}$[b]	Continuum and zero point fixed		Continuum and zero point allowed to vary			
			Γ_{-12}[c]	χ_r^2	Γ_{-12}[c]	Cont.[d]	zero point[e]	χ_r^2
SDSS J1148+5251	5.614	49	0.14	1.32	0.12	1.188	0.005	0.67
SDSS J0818+1722	5.590	83	0.14	5.21	0.11	2.427	0.000	3.08
SDSS J1623+3112	5.522	76	0.15	0.93	0.14	0.983	0.005	0.89
SDSS J1048+4637	5.516	88	0.22	1.93	0.20	1.195	-0.006	1.38
SDSS J1030+0524	5.514	83	0.21	1.30	0.17	1.322	0.006	0.89
SDSS J0002+2550	5.465	68	0.13	1.34	0.12	1.071	0.009	1.10
SDSS J0836+0054	5.455	55	0.20	1.00	0.18	1.198	0.002	0.64
SDSS J0818+1722	5.221	73	0.23	1.53	0.20	1.175	0.006	0.78
SDSS J0002+2550	5.076	75	0.17	2.40	0.14	1.125	0.016	1.47
SDSS J0836+0054	5.067	56	0.16	0.84	0.16	1.054	0.003	0.70
SDSS J0231−0728	5.043	78	0.30	1.43	0.25	1.153	0.012	0.69
SDSS J0915+4244	4.849	71	0.19	3.35	0.16	1.304	0.007	0.97
SDSS J1204−0021	4.747	75	0.40	7.42	0.27	1.210	0.031	1.05
SDSS J0231−0728	4.730	77	0.27	1.22	0.25	1.039	0.012	0.86
SDSS J2225−0014	4.513	80	0.30	3.70	0.24	1.193	0.010	0.82
SDSS J0915+4244	4.509	77	0.33	3.17	0.26	1.137	0.017	0.75
SDSS J1204−0021	4.428	79	0.36	6.64	0.28	1.194	0.005	1.60
BRI2237−0607	4.254	84	0.64	4.94	0.50	1.094	-0.005	1.62
SDSS J2225−0014	4.234	86	0.28	5.13	0.21	1.170	-0.002	1.29
Q0246+1750	4.123	65	0.40	2.55	0.34	1.069	0.009	1.11
BRI1202−0725	4.074	87	0.29	10.08	0.23	1.182	0.011	2.21
Q0246+1750	3.851	78	0.55	5.26	0.39	1.073	-0.005	2.11
Q1055+4611	3.846	62	0.24	4.68	0.22	1.091	0.002	1.60

Table 4.2 (cont'd)

QSO	$\langle z_{\rm abs}\rangle$[a]	$N_{\rm bin}$[b]	Continuum and zero point fixed		Continuum and zero point allowed to vary			
			Γ_{-12}[c]	χ_r^2	Γ_{-12}[c]	Cont.[d]	zero point[e]	χ_r^2
Q0000−263	3.833	70	0.34	5.50	0.28	1.097	0.010	1.56
Q1645+5520	3.798	60	0.33	5.49	0.31	1.076	0.002	1.53
BRI0241−0146	3.779	67	0.40	6.43	0.29	1.076	0.019	1.86
Q0827+5255	3.623	55	0.31	4.93	0.32	1.059	0.000	1.66
Q1055+4611	3.591	63	0.51	7.66	0.41	1.052	0.004	1.73
Q0000−263	3.574	73	0.44	5.32	0.32	1.048	0.002	3.33
Q1645+5520	3.543	61	0.33	4.27	0.28	1.055	0.000	1.17
BRI0241−0146	3.523	74	0.32	4.96	0.26	1.064	0.000	1.92
Q0827+5255	3.389	61	0.33	5.88	0.27	1.060	0.004	1.17
Q0055−2659	3.381	67	0.69	3.02	0.51	1.030	0.010	1.11
Q1422+2309A	3.358	58	0.56	4.41	0.42	1.037	0.008	1.16
Q0055−2659	3.149	73	0.54	4.75	0.44	1.014	0.013	4.44
Q1422+2309A	3.126	57	0.44	2.99	0.37	1.025	0.004	0.89
Q0956+1217	3.061	64	0.37	4.47	0.29	1.035	0.001	1.50
Q0930+2858	2.955	74	0.49	1.24	0.44	1.011	···	1.02
Q0636+6801	2.931	56	0.50	3.02	0.39	1.017	···	1.30
Q0642+44	2.927	76	0.38	2.12	0.29	1.030	···	0.95
Q1140+3508	2.916	60	0.58	4.64	0.39	1.023	···	2.05
Q0449−1326	2.860	65	0.38	1.60	0.30	1.024	···	0.54
Q0956+1217	2.845	66	0.62	3.04	0.45	1.018	···	1.75
Q0940−1050	2.844	61	0.39	3.14	0.30	1.019	···	1.81
Q2231−0015	2.780	64	0.37	3.12	0.30	1.021	···	1.92
HS0741+4741	2.772	60	0.49	4.59	0.35	1.024	···	1.45

Table 4.2 (cont'd)

QSO	$\langle z_{\rm abs}\rangle$[a]	$N_{\rm bin}$[b]	Continuum and zero point fixed		Continuum and zero point allowed to vary			
			Γ_{-12}[c]	χ^2_r	Γ_{-12}[c]	Cont.[d]	zero point[e]	χ^2_r
HS1011+4315	2.766	63	0.44	2.46	0.32	1.019	···	1.13
Q0216+0803	2.748	86	0.21	1.30	0.19	1.010	···	1.23
Q1437+3007	2.746	65	0.49	1.14	0.45	1.005	···	1.03
Q0636+6801	2.720	56	0.35	2.75	0.27	1.017	···	1.22
Q1140+3508	2.708	61	0.56	3.12	0.40	1.014	···	1.66
Q1511+0907	2.658	70	0.42	1.74	0.35	1.011	···	1.34
Q0449−1326	2.654	69	0.39	1.18	0.45	0.990	···	0.91
Q1132+2243	2.652	71	0.39	2.72	0.27	1.022	···	1.55
HS0119+1432	2.643	58	0.54	1.34	0.48	1.005	···	1.15
Q0940−1050	2.639	66	0.38	3.85	0.24	1.029	···	1.80
HS1946+7658	2.627	59	0.36	2.45	0.28	1.015	···	1.10
Q1549+1919	2.613	53	0.50	3.14	0.43	1.011	···	1.17
Q0528−250	2.595	65	0.25	5.44	0.16	1.022	···	4.54
Q2231−0015	2.578	74	0.29	1.56	0.26	1.007	···	1.52
Q0216+0803	2.574	89	0.18	1.32	0.19	0.991	···	1.31
Q1437+3007	2.547	73	0.45	1.44	0.41	1.005	···	1.43
Q1107+487	2.546	72	0.55	1.05	0.49	1.005	···	0.96
Q1244+3133	2.541	81	0.22	2.34	0.20	1.011	···	2.12
HS1700+6416	2.525	54	0.57	2.41	0.44	1.007	···	1.57
Q1511+0907	2.464	76	0.31	1.03	0.30	1.002	···	1.02
Q1132+2243	2.456	74	0.43	1.28	0.48	0.994	···	1.21
HS0119+1432	2.452	60	0.32	1.46	0.29	1.005	···	1.36
Q1009+2956	2.436	56	0.48	2.05	0.43	1.004	···	1.83

Table 4.2 (cont'd)

QSO	$\langle z_{\mathrm{abs}} \rangle$[a]	N_{bin}[b]	Continuum and zero point fixed		Continuum and zero point allowed to vary			
			Γ_{-12}[c]	χ_r^2	Γ_{-12}[c]	Cont.[d]	zero point[e]	χ_r^2
Q1549+1919	2.419	55	0.68	3.77	0.48	1.008	···	2.60
Q0528−250	2.398	72	0.30	1.10	0.34	0.993	···	0.99
Q2344+1228	2.374	79	0.29	2.15	0.28	1.002	···	2.17
Q1358+1134	2.370	86	0.10	3.11	0.16	0.942	···	0.85
Q2206−199N	2.356	60	0.37	1.09	0.33	1.004	···	1.02
HS1700+6416	2.339	55	0.41	1.78	0.41	1.000	···	1.89
Q1623+2653	2.323	67	0.41	1.69	0.36	1.004	···	1.55
Q1442+2931	2.264	60	0.53	0.99	0.62	0.996	···	0.77
Q1009+2956	2.252	59	0.36	0.67	0.33	1.003	···	0.62
Q2343+1232	2.190	81	0.28	1.14	0.23	1.010	···	1.05
Q2206−199N	2.188	61	0.33	0.97	0.31	1.002	···	0.99
Q1623+2653	2.146	77	0.29	1.30	0.35	0.990	···	1.07
Q0841+1256	2.127	81	0.14	2.42	0.22	0.970	···	1.11
Q0237−233	2.050	67	0.13	5.61	0.28	0.967	···	1.30
Q1225+3145	2.016	62	0.32	2.00	0.30	1.002	···	2.01
Q0421+019	1.870	70	0.49	5.17	0.95	0.979	···	2.97
Q1225+3145	1.857	63	0.25	1.71	0.24	1.001	···	1.70
Q0119−0437	1.807	83	0.30	4.33	0.74	0.963	···	1.93
Q0058+0155	1.797	79	0.29	3.75	0.64	0.966	···	1.96

[a] Mean absorption redshift.

[b] Number of flux bins over which fit was performed.

[c] H I ionization rate, in units of 10^{-1} s^{-1}.

[d] Factor by which to multiply the continuum in order for the model to produce the best fit.

[e] Flux zero point that would allow the model to produce the best fit.

Table 4.3. Best-Fit Lognormal Parameters

QSO	$\langle z_{\rm abs} \rangle$[a]	$N_{\rm bin}$[b]	Continuum and zero point fixed			Continuum and zero point allowed to vary				
			μ[c]	σ[d]	$\chi^2_{\rm r}$	μ[c]	σ[d]	Cont.[e]	Zero pt.[f]	χ^2_r
SDSS J1148+5251	5.614	49	1.81	0.86	1.10	2.21	1.24	0.774	0.009	0.49
SDSS J0818+1722	5.590	83	2.71	1.83	1.98	2.59	1.63	1.161	0.002	1.91
SDSS J1623+3112	5.522	76	1.58	0.80	0.83	1.56	0.75	1.088	-0.001	0.87
SDSS J1048+4637	5.516	88	1.58	1.19	1.42	1.40	0.83	1.427	-0.010	0.99
SDSS J1030+0524	5.514	83	1.53	1.07	0.97	1.63	1.16	0.983	0.006	0.92
SDSS J0002+2550	5.465	68	1.61	0.79	1.21	1.82	0.94	0.940	0.009	1.14
SDSS J0836+0054	5.455	55	1.54	1.10	0.64	1.66	1.36	0.866	0.004	0.47
SDSS J0818+1722	5.221	73	1.19	1.15	0.88	1.29	1.31	0.937	0.007	0.71
SDSS J0002+2550	5.076	75	1.19	0.95	1.90	1.42	1.25	0.884	0.019	1.43
SDSS J0836+0054	5.067	56	1.29	1.00	0.72	1.29	1.10	0.922	0.000	0.59
SDSS J0231−0728	5.043	78	0.80	1.23	0.91	0.89	1.35	0.974	0.012	0.72
SDSS J0915+4244	4.849	71	1.12	1.49	1.13	1.28	1.61	1.004	0.011	0.48
SDSS J1204−0021	4.747	75	0.26	1.36	4.23	0.58	1.49	1.052	0.033	0.99
SDSS J0231−0728	4.730	77	0.63	1.17	1.22	0.64	1.38	0.916	0.009	0.96
SDSS J2225−0014	4.513	80	0.40	1.65	0.95	0.49	1.63	1.028	0.012	0.63
SDSS J0915+4244	4.509	77	0.26	1.40	1.60	0.40	1.43	1.036	0.014	0.84
SDSS J1204−0021	4.428	79	0.23	1.91	1.28	0.31	1.87	1.026	0.009	0.98
BRI2237−0607	4.254	84	-0.60	1.98	1.67	-0.60	1.92	1.004	0.008	1.64
SDSS J2225−0014	4.234	86	0.34	1.82	0.71	0.35	1.88	0.991	0.004	0.69
Q0246+1750	4.123	65	-0.35	1.56	1.54	-0.32	1.51	1.016	0.002	1.49
BRI1202−0725	4.074	87	-0.08	2.04	2.19	0.05	1.98	1.032	0.018	1.24
Q0246+1750	3.851	78	-0.74	2.16	1.36	-0.79	2.26	0.987	0.000	1.26
Q1055+4611	3.846	62	-0.15	2.02	0.89	-0.12	1.96	1.019	0.003	0.58

Table 4.3 (cont'd)

QSO	$\langle z_{\rm abs}\rangle$[a]	$N_{\rm bin}$[b]	Continuum and zero point fixed			Continuum and zero point allowed to vary				
			μ[c]	σ[d]	$\chi^2_{\rm r}$	μ[c]	σ[d]	Cont.[e]	Zero pt.[f]	χ^2_r
Q0000−263	3.833	70	-0.59	1.93	1.94	-0.45	1.94	1.018	0.010	1.19
Q1645+5520	3.798	60	-0.54	2.06	1.15	-0.53	1.96	1.022	0.002	0.76
BRI0241−0146	3.779	67	-0.78	1.85	2.39	-0.61	1.99	1.004	0.020	1.07
Q0827+5255	3.623	55	-0.58	2.30	0.80	-0.65	2.20	1.015	0.000	0.60
Q1055+4611	3.591	63	-1.31	2.15	1.23	-1.24	2.08	1.008	0.003	0.96
Q0000−263	3.574	73	-0.75	2.25	1.57	-0.82	2.53	0.981	0.008	1.05
Q1645+5520	3.543	61	-0.85	2.07	0.76	-0.85	1.98	1.009	0.002	0.70
BRI0241−0146	3.523	74	-0.82	2.07	1.76	-0.83	2.10	0.997	0.001	1.80
Q0827+5255	3.389	61	-1.22	1.97	1.58	-1.13	1.87	1.018	0.004	0.88
Q0055−2659	3.381	67	-1.88	2.04	1.17	-1.92	2.18	0.994	0.008	1.05
Q1422+2309A	3.358	58	-1.79	2.03	1.56	-1.62	2.16	1.005	0.007	0.82
Q0055−2659	3.149	73	-1.67	2.48	3.41	-2.16	3.32	0.970	0.011	1.15
Q1422+2309A	3.126	57	-1.95	1.98	1.05	-1.89	1.87	1.005	0.002	0.97
Q0956+1217	3.061	64	-1.85	2.16	1.63	-1.83	2.07	1.004	0.002	1.67
Q0930+2858	2.955	74	-2.28	1.99	1.05	-2.44	2.15	0.988	···	0.89
Q0636+6801	2.931	56	-2.23	2.13	0.78	-2.25	2.17	0.999	···	0.79
Q0642+44	2.927	76	-2.00	2.20	0.72	-2.10	2.31	0.992	···	0.67
Q1140+3508	2.916	60	-2.32	2.40	0.89	-2.35	2.43	0.998	···	0.93
Q0449−1326	2.860	65	-2.16	2.07	0.80	-2.16	2.06	1.001	···	0.83
Q0956+1217	2.845	66	-2.65	2.54	1.15	-2.86	2.81	0.991	···	0.78
Q0940−1050	2.844	61	-2.07	2.28	1.31	-2.22	2.54	0.990	···	0.93
Q2231−0015	2.780	64	-2.25	2.03	1.48	-2.20	2.00	1.003	···	1.50
HS0741+4741	2.772	60	-2.57	2.36	1.14	-2.46	2.22	1.006	···	0.97

Table 4.3 (cont'd)

QSO	$\langle z_{\rm abs}\rangle$[a]	$N_{\rm bin}$[b]	Continuum and zero point fixed			Continuum and zero point allowed to vary				
			μ[c]	σ[d]	$\chi^2_{\rm r}$	μ[c]	σ[d]	Cont.[e]	Zero pt.[f]	χ^2_r
HS1011+4315	2.766	63	-2.39	2.25	0.61	-2.45	2.33	0.997	···	0.58
Q0216+0803	2.748	86	-1.65	1.91	1.22	-1.99	2.22	0.971	···	0.96
Q1437+3007	2.746	65	-2.65	1.96	1.75	-2.89	2.29	0.988	···	1.24
Q0636+6801	2.720	56	-2.26	2.11	0.90	-2.28	2.14	0.999	···	0.91
Q1140+3508	2.708	61	-2.65	2.41	0.74	-2.81	2.60	0.994	···	0.52
Q1511+0907	2.658	70	-2.62	2.21	1.40	-2.93	2.58	0.987	···	0.95
Q0449−1326	2.654	69	-2.52	1.60	2.20	-3.13	2.32	0.974	···	1.10
Q1132+2243	2.652	71	-2.51	2.43	0.92	-2.66	2.59	0.993	···	0.80
HS0119+1432	2.643	58	-2.82	2.08	1.30	-3.13	2.40	0.991	···	0.73
Q0940−1050	2.639	66	-2.35	2.62	0.66	-2.43	2.73	0.996	···	0.63
HS1946+7658	2.627	59	-2.46	2.12	0.79	-2.51	2.17	0.998	···	0.80
Q1549+1919	2.613	53	-3.02	2.14	1.10	-2.92	2.01	1.003	···	0.97
Q0528−250	2.595	65	-1.68	2.41	2.35	-2.11	2.83	0.982	···	1.50
Q2231−0015	2.578	74	-2.37	2.26	2.00	-2.87	2.85	0.975	···	0.97
Q0216+0803	2.574	89	-1.90	1.97	2.02	-2.83	2.98	0.939	···	0.95
Q1437+3007	2.547	73	-3.00	2.34	1.94	-3.49	3.01	0.982	···	0.98
Q1107+487	2.546	72	-3.17	2.27	1.17	-3.55	2.61	0.989	···	0.72
Q1244+3133	2.541	81	-2.16	2.46	2.13	-2.78	3.15	0.966	···	0.74
HS1700+6416	2.525	54	-3.08	2.38	1.18	-3.31	2.81	0.995	···	0.67
Q1511+0907	2.464	76	-2.66	1.97	1.03	-2.88	2.17	0.989	···	0.85
Q1132+2243	2.456	74	-3.05	1.99	1.85	-3.76	2.60	0.979	···	1.02
HS0119+1432	2.452	60	-2.66	2.22	1.94	-3.10	2.71	0.985	···	0.64
Q1009+2956	2.436	56	-3.12	2.14	2.13	-3.50	2.64	0.992	···	1.34

Table 4.3 (cont'd)

QSO	$\langle z_{\rm abs}\rangle^{\rm a}$	$N_{\rm bin}{}^{\rm b}$	Continuum and zero point fixed			Continuum and zero point allowed to vary				
			$\mu^{\rm c}$	$\sigma^{\rm d}$	$\chi^2_{\rm r}$	$\mu^{\rm c}$	$\sigma^{\rm d}$	Cont.[e]	Zero pt.[f]	χ^2_r
Q1549+1919	2.419	55	-3.46	2.84	1.38	-3.63	3.16	0.996	···	1.09
Q0528−250	2.398	72	-2.79	2.02	2.29	-3.53	2.68	0.974	···	0.85
Q2344+1228	2.374	79	-2.91	2.60	2.42	-3.76	3.44	0.973	···	0.89
Q1358+1134	2.370	86	-1.63	1.47	4.00	-2.82	2.67	0.908	···	0.73
Q2206−199N	2.356	60	-3.07	2.15	1.44	-3.48	2.71	0.990	···	0.80
HS1700+6416	2.339	55	-3.16	1.97	3.81	-3.75	2.97	0.989	···	1.39
Q1623+2653	2.323	67	-3.24	2.26	1.41	-3.53	2.48	0.992	···	1.12
Q1442+2931	2.264	60	-3.58	1.83	1.75	-4.18	2.39	0.990	···	0.93
Q1009+2956	2.252	59	-3.30	2.10	1.08	-3.60	2.50	0.993	···	0.74
Q2343+1232	2.190	81	-3.37	2.74	0.93	-3.86	3.16	0.985	···	0.65
Q2206−199N	2.188	61	-3.34	2.17	1.51	-3.82	2.69	0.989	···	0.98
Q1623+2653	2.146	77	-3.18	1.89	1.64	-3.89	2.49	0.981	···	1.19
Q0841+1256	2.127	81	-2.43	1.72	2.92	-3.58	2.69	0.953	···	0.95
Q0237−233	2.050	67	-2.49	1.35	3.61	-3.59	2.31	0.961	···	0.88
Q1225+3145	2.016	62	-3.62	2.42	1.64	-3.98	2.70	0.994	···	1.19
Q0421+019	1.870	70	-3.81	1.92	1.27	-4.51	2.34	0.986	···	0.76
Q1225+3145	1.857	63	-3.91	2.56	2.45	-4.80	3.56	0.989	···	1.37
Q0119−0437	1.807	83	-3.36	1.87	1.38	-4.42	2.49	0.973	···	0.83
Q0058+0155	1.797	79	-3.39	1.87	0.87	-4.13	2.32	0.979	···	0.59

[a] Mean absorption redshift.

[b] Number of flux bins over which fit was performed.

[c] Lognormal parameter $\mu = \langle \ln \tau \rangle$.

[d] Lognormal parameter $\sigma = \mathrm{std\,dev}\,(\ln \tau)$.

[e] Factor by which to multiply the continuum in order for the model to produce the best fit.

[f] Flux zero point that would allow the model to produce the best fit.

Table 4.4. Best-Fit MHR00 Model Parameters (Non-Isothermal)

QSO	$\langle z_{\rm abs} \rangle^{\rm a}$	$N_{\rm bin}{}^{\rm b}$	Continuum and zero point fixed			Continuum and zero point allowed to vary				
			$\Gamma_{-12}{}^{\rm c}$	$\alpha^{\rm d}$	$\chi^2_{\rm r}$	$\Gamma_{-12}{}^{\rm c}$	$\alpha^{\rm d}$	Cont.[e]	Zero pt.[f]	χ^2_r
SDSS J1148+5251	5.614	49	0.13	-0.06	1.30	0.04	0.764	0.764	0.011	0.45
SDSS J0818+1722	5.590	83	0.01	-2.21	2.16	0.02	1.195	1.195	0.003	1.88
SDSS J1623+3112	5.522	76	0.20	0.25	0.86	0.17	1.050	1.050	0.003	0.89
SDSS J1048+4637	5.516	88	0.13	-0.49	1.51	0.19	1.431	1.431	-0.002	1.21
SDSS J1030+0524	5.514	83	0.16	-0.23	1.17	0.13	1.102	1.102	0.008	0.93
SDSS J0002+2550	5.465	68	0.18	0.23	1.24	0.10	0.986	0.986	0.010	1.11
SDSS J0836+0054	5.455	55	0.14	-0.37	0.61	0.11	0.981	0.981	0.005	0.47
SDSS J0818+1722	5.221	73	0.17	-0.30	1.21	0.16	1.081	1.081	0.008	0.77
SDSS J0002+2550	5.076	75	0.18	0.06	2.44	0.11	0.986	0.986	0.021	1.42
SDSS J0836+0054	5.067	56	0.16	0.01	0.84	0.18	1.136	1.136	0.001	0.69
SDSS J0231−0728	5.043	78	0.25	-0.19	1.27	0.23	1.119	1.119	0.014	0.70
SDSS J0915+4244	4.849	71	0.10	-0.74	1.90	0.09	1.100	1.100	0.012	0.49
SDSS J1204−0021	4.747	75	0.37	-0.18	7.44	0.24	1.166	1.166	0.033	1.04
SDSS J0231−0728	4.730	77	0.27	-0.01	1.27	0.23	1.006	1.006	0.013	0.90
SDSS J2225−0014	4.513	80	0.19	-0.61	1.82	0.20	1.120	1.120	0.015	0.65
SDSS J0915+4244	4.509	77	0.30	-0.11	3.14	0.26	1.126	1.126	0.018	0.76
SDSS J1204−0021	4.428	79	0.17	-0.92	1.95	0.18	1.086	1.086	0.012	0.80
BRI2237−0607	4.254	84	0.35	-0.78	1.99	0.43	1.056	1.056	-0.002	1.45
SDSS J2225−0014	4.234	86	0.13	-0.84	0.97	0.13	1.043	1.043	0.009	0.72
Q0246+1750	4.123	65	0.36	-0.12	2.44	0.38	1.090	1.090	0.007	1.06
BRI1202−0725	4.074	87	0.15	-1.03	3.94	0.16	1.090	1.090	0.022	1.40
Q0246+1750	3.851	78	0.23	-0.88	1.12	0.24	1.021	1.021	0.005	1.00
Q1055+4611	3.846	62	0.11	-0.87	1.91	0.13	1.049	1.049	0.004	0.72

Table 4.4 (cont'd)

QSO	$\langle z_{\rm abs}\rangle$[a]	$N_{\rm bin}$[b]	Continuum and zero point fixed			Continuum and zero point allowed to vary				
			Γ_{-12}[c]	α[d]	$\chi^2_{\rm r}$	Γ_{-12}[c]	α[d]	Cont.[e]	Zero pt.[f]	χ^2_r
Q0000−263	3.833	70	0.22	-0.62	3.52	0.21	1.063	1.063	0.012	1.22
Q1645+5520	3.798	60	0.16	-0.87	2.16	0.20	1.050	1.050	0.003	0.81
BRI0241−0146	3.779	67	0.30	-0.48	4.82	0.22	1.041	1.041	0.023	1.32
Q0827+5255	3.623	55	0.09	-1.19	1.08	0.13	1.034	1.034	0.001	0.43
Q1055+4611	3.591	63	0.27	-0.84	3.18	0.29	1.033	1.033	0.005	1.01
Q0000−263	3.574	73	0.15	-0.99	1.25	0.13	1.000	1.000	0.010	0.94
Q1645+5520	3.543	61	0.14	-0.83	1.30	0.18	1.032	1.032	0.001	0.53
BRI0241−0146	3.523	74	0.17	-0.70	1.79	0.18	1.033	1.033	0.005	1.31
Q0827+5255	3.389	61	0.22	-0.55	3.70	0.22	1.046	1.046	0.005	1.06
Q0055−2659	3.381	67	0.49	-0.41	1.74	0.43	1.017	1.017	0.012	0.86
Q1422+2309A	3.358	58	0.43	-0.38	3.47	0.30	1.024	1.024	0.008	0.79
Q0055−2659	3.149	73	0.19	-0.91	1.95	0.13	0.978	0.978	0.013	1.07
Q1422+2309A	3.126	57	0.30	-0.48	2.13	0.32	1.021	1.021	0.004	0.85
Q0956+1217	3.061	64	0.21	-0.68	2.27	0.24	1.026	1.026	0.003	1.45
Q0930+2858	2.955	74	0.44	-0.14	1.15	0.43	1.010	1.010	···	1.05
Q0636+6801	2.931	56	0.26	-0.60	1.30	0.29	1.010	1.010	···	0.94
Q0642+44	2.927	76	0.25	-0.48	0.91	0.26	1.015	1.015	···	0.77
Q1140+3508	2.916	60	0.27	-0.72	1.82	0.29	1.012	1.012	···	1.44
Q0449−1326	2.860	65	0.26	-0.40	0.98	0.29	1.021	1.021	···	0.56
Q0956+1217	2.845	66	0.28	-0.78	0.70	0.28	1.001	1.001	···	0.71
Q0940−1050	2.844	61	0.18	-0.69	1.01	0.18	1.003	1.003	···	1.00
Q2231−0015	2.780	64	0.31	-0.23	2.80	0.31	1.026	1.026	···	1.74
HS0741+4741	2.772	60	0.30	-0.59	2.64	0.32	1.020	1.020	···	1.41

Table 4.4 (cont'd)

QSO	$\langle z_{\mathrm{abs}} \rangle$[a]	N_{bin}[b]	Continuum and zero point fixed			Continuum and zero point allowed to vary				
			Γ_{-12}[c]	α[d]	χ^2_{r}	Γ_{-12}[c]	α[d]	Cont.[e]	Zero pt.[f]	χ^2_r
HS1011+4315	2.766	63	0.25	-0.55	1.08	0.27	1.011	1.011	$\cdots$	0.88
Q0216+0803	2.748	86	0.19	-0.13	1.25	0.19	1.002	1.002	$\cdots$	1.27
Q1437+3007	2.746	65	0.42	-0.16	1.02	0.43	1.002	1.002	$\cdots$	1.04
Q0636+6801	2.720	56	0.22	-0.46	1.67	0.24	1.013	1.013	$\cdots$	1.16
Q1140+3508	2.708	61	0.26	-0.69	0.95	0.26	1.004	1.004	$\cdots$	0.92
Q1511+0907	2.658	70	0.28	-0.42	1.04	0.28	0.999	0.999	$\cdots$	1.10
Q0449−1326	2.654	69	0.45	0.18	1.03	0.45	0.989	0.989	$\cdots$	0.94
Q1132+2243	2.652	71	0.22	-0.60	1.13	0.22	1.006	1.006	$\cdots$	1.10
HS0119+1432	2.643	58	0.43	-0.24	1.03	0.43	1.000	1.000	$\cdots$	1.09
Q0940−1050	2.639	66	0.12	-0.95	0.83	0.13	1.008	1.008	$\cdots$	0.75
HS1946+7658	2.627	59	0.25	-0.37	1.58	0.27	1.013	1.013	$\cdots$	1.08
Q1549+1919	2.613	53	0.29	-0.66	1.87	0.38	1.009	1.009	$\cdots$	1.14
Q0528−250	2.595	65	0.08	-0.80	2.31	0.08	0.991	0.991	$\cdots$	2.26
Q2231−0015	2.578	74	0.19	-0.38	1.05	0.18	0.989	0.989	$\cdots$	0.96
Q0216+0803	2.574	89	0.16	-0.10	1.33	0.15	0.952	0.952	$\cdots$	0.95
Q1437+3007	2.547	73	0.29	-0.45	0.93	0.27	0.991	0.991	$\cdots$	0.78
Q1107+487	2.546	72	0.45	-0.24	0.81	0.45	0.999	0.999	$\cdots$	0.81
Q1244+3133	2.541	81	0.12	-0.57	1.17	0.11	0.976	0.976	$\cdots$	0.80
HS1700+6416	2.525	54	0.20	-0.86	0.58	0.18	0.998	0.998	$\cdots$	0.57
Q1511+0907	2.464	76	0.32	0.05	1.01	0.31	1.009	1.009	$\cdots$	1.00
Q1132+2243	2.456	74	0.44	0.04	1.30	0.47	0.989	0.989	$\cdots$	1.21
HS0119+1432	2.452	60	0.22	-0.33	0.88	0.22	0.995	0.995	$\cdots$	0.81
Q1009+2956	2.436	56	0.28	-0.47	1.28	0.25	0.996	0.996	$\cdots$	1.26

Table 4.4 (cont'd)

QSO	$\langle z_{\rm abs}\rangle$[a]	$N_{\rm bin}$[b]	Continuum and zero point fixed			Continuum and zero point allowed to vary				
			Γ_{-12}[c]	α[d]	$\chi^2_{\rm r}$	Γ_{-12}[c]	α[d]	Cont.[e]	Zero pt.[f]	χ^2_r
Q1549+1919	2.419	55	0.15	-1.19	0.92	0.15	0.999	0.999	···	0.94
Q0528−250	2.398	72	0.31	0.03	1.09	0.32	0.985	0.985	···	0.88
Q2344+1228	2.374	79	0.18	-0.49	1.48	0.17	0.979	0.979	···	1.00
Q1358+1134	2.370	86	0.15	0.44	1.86	0.15	0.922	0.922	···	0.74
Q2206−199N	2.356	60	0.26	-0.33	0.77	0.26	0.998	0.998	···	0.77
HS1700+6416	2.339	55	0.30	-0.26	1.62	0.23	0.994	0.994	···	1.15
Q1623+2653	2.323	67	0.37	-0.12	1.56	0.37	1.003	1.003	···	1.63
Q1442+2931	2.264	60	0.63	0.20	0.85	0.63	0.996	0.996	···	0.82
Q1009+2956	2.252	59	0.29	-0.21	0.55	0.29	1.000	1.000	···	0.56
Q2343+1232	2.190	81	0.19	-0.46	0.72	0.19	0.996	0.996	···	0.72
Q2206−199N	2.188	61	0.29	-0.15	0.91	0.28	0.998	0.998	···	0.92
Q1623+2653	2.146	77	0.34	0.24	1.08	0.35	0.994	0.994	···	1.08
Q0841+1256	2.127	81	0.20	0.39	1.62	0.22	0.967	0.967	···	1.11
Q0237−233	2.050	67	0.27	0.68	1.63	0.29	0.975	0.975	···	1.19
Q1225+3145	2.016	62	0.30	-0.07	2.03	0.29	1.000	1.000	···	2.01
Q0421+019	1.870	70	0.54	0.72	1.60	0.48	1.008	1.008	···	1.58
Q1225+3145	1.857	63	0.19	-0.27	1.50	0.17	0.995	0.995	···	1.39
Q0119−0437	1.807	83	0.34	0.80	1.32	0.33	1.003	1.003	···	1.36
Q0058+0155	1.797	79	0.33	0.78	1.07	0.31	1.010	1.010	···	1.01

[a] Mean absorption redshift.

[b] Number of flux bins over which fit was performed.

[c] H I ionization rate, in units of 10^{-1} s^{-1}.

[d] Power-law index for the generalized temperature-density relation $T^{0.7}\Gamma \propto \Delta^{\alpha}$.

[e] Factor by which to multiply the continuum in order for the model to produce the best fit.

[f] Flux zero point that would allow the model to produce the best fit.

Chapter 5

The Metagalactic UV Background at $z = 4 - 5$ Measured Using the Quasar Proximity Effect[1]

Abstract

We present a measurement of the metagalactic UV background using the proximity effect in 16 QSOs at $4.4 < z < 5.1$. Our analysis uses a new method of directly estimating the size of a QSO's proximity region from the distribution of transmitted fluxes. Using accurate redshifts from Mg II emission lines, the start of the Lyα forest, and CO, we obtain a mean background H I ionization rate of $\Gamma^{\rm bg}_{-12} = 1.4^{+1.6}_{-0.7}$ (1σ), where $\Gamma^{\rm bg}_{-12}$ is in units of 10^{-12} s^{-1}. Including only the 13 QSOs with flux uncertainties $\leq 10\%$, our estimate becomes $\Gamma^{\rm bg}_{-12} = 1.3^{+0.6}_{-0.4}$. In order to test the photoionization model of the proximity effect, we have examined the dependence of the size of the proximity region on QSO luminosity. The proximity region size generally increases with the square root of a QSO's ionizing output, as expected. However, there is some evidence that the proximity regions around faint QSOs are disproportionately small. We tentatively attribute this to the effects of peculiar velocities in the absorbing gas, although it may indicate that a smaller fraction of ionizing photons escape from fainter QSOs. Our value of $\Gamma^{\rm bg}$ is consistent with measurements at $z \sim 3$ based on the proximity effect, the mean transmitted flux in the Lyα forest, and the integrated ionizing output of star-forming galaxies and QSOs. We are also marginally consistent with the values of $\Gamma^{\rm bg}$ derived from the Lyα forest at $4.5 < z < 5.3$. This agreement may improve with more

---

[1] Part of a manuscript in preparation for submission to *The Astrophysical Journal*; written with W. L. W. Sargent and M. Rauch

sophisticated treatment of the flux distribution in the proximity regions, as revised Lyα forest measurements based on updated cosmological parameters. .

5.1 Introduction

Over the past two decades, a consensus picture has emerged of the intergalactic medium (IGM) as a “cosmic web” of interconnected filaments, sheets, and voids (for a review, see Springel et al. 2006). These large-scale structures, which collapse by self-gravitation out of initial density perturbations, are the main baryon reservoir in the early Universe and the lattice out of which galaxies form. Our most sensitive probe of the IGM is absorption by residual neutral hydrogen in the photoionized gas, which gives rise to the Lyα forest. Therefore, considerable work has gone into understanding the relationship between the dark matter, which provides the underlying framework for the web, and the baryons, which are subject to ionization, heating, and feedback from galaxies and QSOs.

A key factor in determining the ionization state of the baryons is the intensity of the ionizing UV background. One approach to determining the UV background is to adopt a model for the gas density distribution and adjust the level of ionizing radiation such that the mean transmitted flux in the Lyα forest matches observations (e.g., Rauch et al. 1997; McDonald & Miralda-Escudé 2001; Fan et al. 2002, 2006a). The optical depth in the IGM, however, depends strongly on the assumed cosmology and, more importantly, on the temperature of the gas. It is also possible to infer the UV background from ionic ratios in metal-enriched systems (e.g., Songaila 1998). The results, however, depend somewhat on model parameters, such as absorber geometry and metallicity, and may be biased towards local ionizing sources (Boksenberg et al. 2003).

The quasar proximity effect offers an alternative means to measure the UV background. While the number density of absorption lines in the Lyα forest generally increase with redshift, a decrease is typically seen near the systemic redshift of a QSO (Weymann et al. 1981; Carswell et al. 1982; Murdoch et al. 1986; Tytler 1987). If this decrease is normally attributed to enhanced local photoionization by the QSO, as is generally assumed, then the UV background can be measured by balancing the ionizing flux from the background and QSO in the “proximity” region (Carswell et al. 1987; Bajtlik et al. 1988). For a given QSO luminosity, a larger proximity region indicates greater dominance by the QSO, and hence a lower background.

Several groups have used the proximity effect to measure the UV background at a variety of redshifts (Carswell et al. 1987; Bajtlik et al. 1988; Lu et al. 1991, 1996; Giallongo et al. 1993, 1996; Williger et al. 1994; Bechtold 1994; Cristiani et al. 1995; Fernandez-Soto et al. 1995; Savaglio et al. 1997; Scott et al. 2000, 2002; Liske & Williger 2001). The classical approach uses the observed change in the column density distribution of Lyα lines near $z \approx z_{\rm QSO}$ to determine the local impact of the QSO. This technique is best suited for high-resolution data at redshifts where where individual lines can be reliably identified ($z \lesssim 4$). At higher redshifts, or lower spectral resolution, the crowded nature of the forest makes it difficult to separate out discrete absorbers. Accurate QSO redshifts are essential, since errors in redshifts measured from high-ionization emission lines (up to a few thousand km s^{-1}) can be of the same order as the size of the proximity region. A large sample of QSOs is also necessary to overcome the stochastic nature of the Lyα forest. Scott et al. (2000, 2002) have conducted extensive proximity effect studies out to $z = 3.7$ using both reliable redshifts and large samples of QSOs. In contrast, measurements at $z > 4$ have so far relied on only a few sightlines (Williger et al. 1994; Lu et al. 1996; Cooke et al. 1997; Savaglio et al. 1997) and have not been supported by accurate redshifts.

A remaining challenge to the proximity effect is to demonstrate that the size of the proximity region scales correctly with QSO luminosity. Scott et al. (2000, 2002) and Liske & Williger (2001) find evidence that brighter QSOs show more transmitted flux near the QSO redshift, which is consistent with the photoionization model. It has not yet been shown, however, that the size of the proximity region depends on luminosity as $R \propto L^{1/2}$, which is an implicit assumption in proximity effect measurements. This relationship may change if QSOs reside in local overdensities. A large reservoir of gas near a QSO may decrease the apparent size of the proximity region, particularly for a low-luminosity QSO. Alternatively, additional nearby ionizing sources may increase the size of the proximity region. QSO variability may also be a factor if the ionization state of the gas does not rapidly respond to changes in QSO luminosity. Recombination timescales in a highly-ionized IGM are extremely long,

$$t_{\rm recomb} \sim \frac{1}{n_e \alpha_{\rm H}}$$

$$\sim \quad 10^{10}\ \mathrm{yr}\ \left(\frac{\Omega_{\mathrm{b}}h^2}{0.022}\right)^{-1}\left(\frac{\Omega_{\mathrm{m}}}{0.27}\right)^{-1}\left(\frac{1+z}{5.5}\right)^{-3}\left(\frac{T}{10^4\ \mathrm{K}}\right)^{-0.7}\Delta^{-1}\,, \qquad (5.1)$$

where α_{H} is the hydrogen recombination coefficient, T is the gas temperature, and $\Delta = \rho_{\mathrm{gas}}/\langle\rho_{\mathrm{gas}}\rangle$ is the gas overdensity. The time to replenish a low neutral neutral fraction $f_{\mathrm{H\,I}}$ will be much shorter,

$$t_{\mathrm{replenish}} \sim 10^5\ \mathrm{yr}\ \left(\frac{\Omega_{\mathrm{b}}h^2}{0.022}\right)^{-1}\left(\frac{\Omega_{\mathrm{m}}}{0.27}\right)^{-1}\left(\frac{1+z}{5.5}\right)^{-3}\left(\frac{T}{10^4\ \mathrm{K}}\right)^{-0.7}\left(\frac{f_{\mathrm{H\,I}}}{10^{-5}}\right)\Delta^{-1}\,. \qquad (5.2)$$

If a QSO varies significantly on these timescales, however, then the size of the proximity region may correspond to the peak luminosity rather than the instantaneous luminosity. In that case, QSOs that are currently faint may still have large proximity regions, leading to an underestimate of the UV background.

In this work, we present the first comprehensive proximity effect measurements at $z > 4$. Our sample includes 16 QSOs at $4.4 < z < 5.1$ with accurate redshifts determined from Mg II emission lines. The sample was chosen to cover a wide range in luminosity in order to test the photoionization model. The data are described in §5.2, along with our measurements of the QSO redshifts and luminosities. In §5.3 we describe the photoionization model of the proximity effect in mode detail. We also present a new method for determining the size of a QSO's proximity region based on the distribution of pixel optical depths, which can be applied to moderate resolution and highly absorbed data. In §5.4.1 we use this technique to determine a maximum likelihood estimate of the background H I ionization rate, Γ^{bg}. We examine the luminosity dependence of the size of the proximity region in §5.4.2. In §5.4.3 we perform a model-independent check on our results using the median transmitted flux as a function of distance from a QSO. We compare our results to other measurements of Γ^{bg} at high redshift in §5.5. Finally, our results are summarized in §5.6. Throughout this paper, we assume cosmological parameters favored by recent WMAP+SDSS results (Spergel et al. 2006): $\Omega_{\mathrm{b}}h^2 = 0.022$, $\Omega_{\mathrm{m}} = 0.27$, $h = 0.71$, $\sigma_8 = 0.77$.

5.2 The Data

5.2.1 Optical Spectra

Moderate- to high-resolution optical spectra for the 16 QSOs in our sample were obtained using Keck/ESI (Sheinis et al. 2002) and Keck/HIRES (Vogt et al. 1994). The sample was chosen partly to avoid Lyman limit systems (LLSs) within 12000 km s^{-1} of a QSO's systemic redshift, the region over which we measure the proximity effect, as well as to avoid associated broad metal absorption lines. Our observations are summarized in Table 5.1. The ESI data were reduced using the MAKEE package written by Tom Barlow. Relative flux calibration was performed for individual exposures using standard stars. The orders from all exposures were then combined, and a slowly varying spline was used to fit a single continuum to each object. Standard stars were also used to correct for telluric absorption. The majority of ESI observations were made using a $0\farcs75$ slit, which gives a typical spectral resolution of 60 km s^{-1}.

The HIRES data were also reduced using MAKEE. Rather than attempt to flux calibrate the individual exposures, however, a spline continuum was used to normalize each order separately. The normalized orders were then combined to create a final spectrum for each object. Observations were made using a $0\farcs86$ slit, which gives a resolution of 6.7 km s^{-1}.

5.2.2 IR Spectra

In order to measure accurate QSOs redshifts (see discussion below), we obtained low-resolution spectra of the Mg II emission line regions of our objects. At $z \sim 4-5$, Mg II falls in H-band, where we observed with Keck/NIRSPEC. The observations are summarized in Table 5.1. Individual exposures were processed using a custom set of IDL routines written by one of us (GDB). The reduction package attempts to minimize residuals from strong skylines by performing optimal sky subtraction (Kelson 2003). The 1D spectra were optimally extracted (Horne 1986). Relative flux calibration was then performed using standard stars. Standards were also used, along with models of atmospheric absorption, to correct for telluric features. We used a $0\farcs72$ slit, which gives a resolution of 220 km s^{-1}.

Table 5.1. Summary of Proximity Effect Observations

QSO	NIRSPEC		Optical		
	Dates	$t_{\rm exp}$ (hrs)	Instrument	Dates	$t_{\rm exp}$ (hrs)
PSS 0131+0633	2003 Nov	1.0	ESI[a]	2001 Jul	2.0
SDSS J0210−0018	2003 Nov	1.3	ESI	2000 Oct	0.8
SDSS J0211−0009	2003 Nov	1.5	ESI	2000 Oct	1.7
SDSS J0250+0046	2003 Nov	1.3	ESI	2000 Oct	1.7
SDSS J0310−0014	2003 Nov	1.0	ESI	2000 Oct	1.7
PSS 0439−0207	2003 Nov	1.0	ESI	2000 Mar	0.8
PSS 0747+4434	2003 Nov	1.3	ESI	2000 Mar	0.8
SDSS J0756+4104	2004 Mar	2.0	ESI[a]	2001 Mar	2.5
PSS 0808+5215	2003 Nov	1.2	ESI	2000 Mar	0.8
SDSS J0941+5947	2003 Nov	0.7	ESI[a]	2002 Dec	0.7
BRI 0952−0115	2003 Nov	1.3	ESI	2000 Mar	0.8
BR 1033−0327	2004 Mar	0.7	HIRES	1997 May	6.7
SDSS J1204−0021	2004 Mar	1.0	ESI	2000 Mar	1.7
GB 1428+4217	2004 Mar	1.0	ESI	2000 Mar	1.7
WFS 1612+5255	2004 Mar	1.0	ESI	2001 Apr	3.3
BRI 2237−0607	2003 Nov	0.5	HIRES	1994 Oct	10.8

[a] Spectrum provided by S. .G. Djorgovski.

5.2.3 Redshifts

The proximity region around a QSO generally extends at most several thousand km s^{-1}, and may be much smaller. Is is therefore essential to obtain accurate systemic redshifts, such that the redshift uncertainties are a small fraction of the proximity regions size. QSO redshifts are normally measured from broad, high-ionization emission lines such as Lyα and C IV. These lines, however, can have both an offset from the intrinsic QSO redshift (as measured from narrow forbidden lines or Balmer lines) and a large QSO-to-QSO scatter. The resulting redshifts errors can be up to a few thousand km s^{-1} (e.g., Tytler & Fan 1992; McIntosh et al. 1999; Vanden Berk et al. 2001; Richards et al. 2002). In this work we use three alternative redshift indicators: Mg II emission lines, the apparent beginning of the Lyα forest, and CO emission.

Mg II

Low-ionization lines such as Mg II have both smaller offsets and significantly less scatter ($\lesssim$ 100 km s^{-1}) than high-ionization lines. Several attempts have been made to determine the intrinsic offset of Mg II using both individual spectra (Tytler & Fan 1992; McIntosh et al. 1999) and composites (Vanden Berk et al. 2001). Tytler & Fan (1992) compared the peak wavelength of Mg II with respect to Hβ for 105 individual QSOs, which is most relevant to the present work. We, therefore, adopt their value of 2797.80 ± 0.43 Å for the intrinsic peak wavelength of the Mg IIemission line. This is 102 ± 46 km s^{-1} bluer than the laboratory wavelength of 2798.75 Å.

Figure 5.1 displays the Mg II emission line region for each of the QSOs in our sample. Mg II is a doublet transition. However, for sufficiently broad lines ($FWHM \gtrsim 2000$ km s^{-1}), the line profile is adequately described by a single Gaussian component. In Figure 5.1 we overplot our Gaussian fits, which include a linear term to account for the continuum and nearby Fe II emission. Vertical solid lines mark the peak wavelengths. The calculated redshifts are listed in Table 5.2. Uncertainties in $z_{\rm Mg\ II}$ include the formal errors in the fits, the error in the intrinsic Mg II wavelength, and a 100 km s^{-1} QSO-to-QSO scatter measured by Tytler & Fan (1992).

Table 5.2. QSO Redshifts

QSO	$z_{\rm Mg\ II}$[a]	$z_{\rm Ly\alpha}$[b]	$z_{\rm CO}$[c]	Preferred redshift
PSS 0131+0633	4.443 ± 0.002	4.437	···	Mg II
SDSS J0210−0018	4.734 ± 0.002	4.747	···	Lyα
SDSS J0211−0009	4.915 ± 0.004	4.917	···	Mg II
SDSS J0250+0046	4.778 ± 0.004	4.779	···	Mg II
SDSS J0310−0014	4.672 ± 0.002	4.671	···	Mg II
PSS 0439−0207	4.422 ± 0.002	4.410	···	Mg II
PSS 0747+4434	4.440 ± 0.002	4.424	···	Mg II
SDSS J0756+4104	5.093 ± 0.004	5.084	···	Lyα
PSS 0808+5215	4.479 ± 0.002	4.488	···	Lyα
SDSS J0941+5947	4.861 ± 0.003	4.855	···	Mg II
BRI 0952−0115	4.437 ± 0.002	4.435	4.4337 ± 0.0006[d]	CO
BR 1033−0327	4.527 ± 0.002	4.522	···	Mg II
SDSS J1204−0021	5.084 ± 0.003	5.090	···	Lyα
GB 1428+4217	4.756 ± 0.002	4.762	···	Mg II
WFS 1612+5255	4.950 ± 0.008	4.944	···	Lyα
BRI 2237−0607	4.568 ± 0.002	4.565	···	Mg II

[a] Redshift measured from the peak of the Mg II emission line.

[b] Redshift measured from the apparent start of the Lyα forest. Errors are assumed to be ±300 km s^{-1}($\Delta z \approx 0.005 - 0.006$).

[c] CO redshift.

[d] Guilloteau et al. (1999).

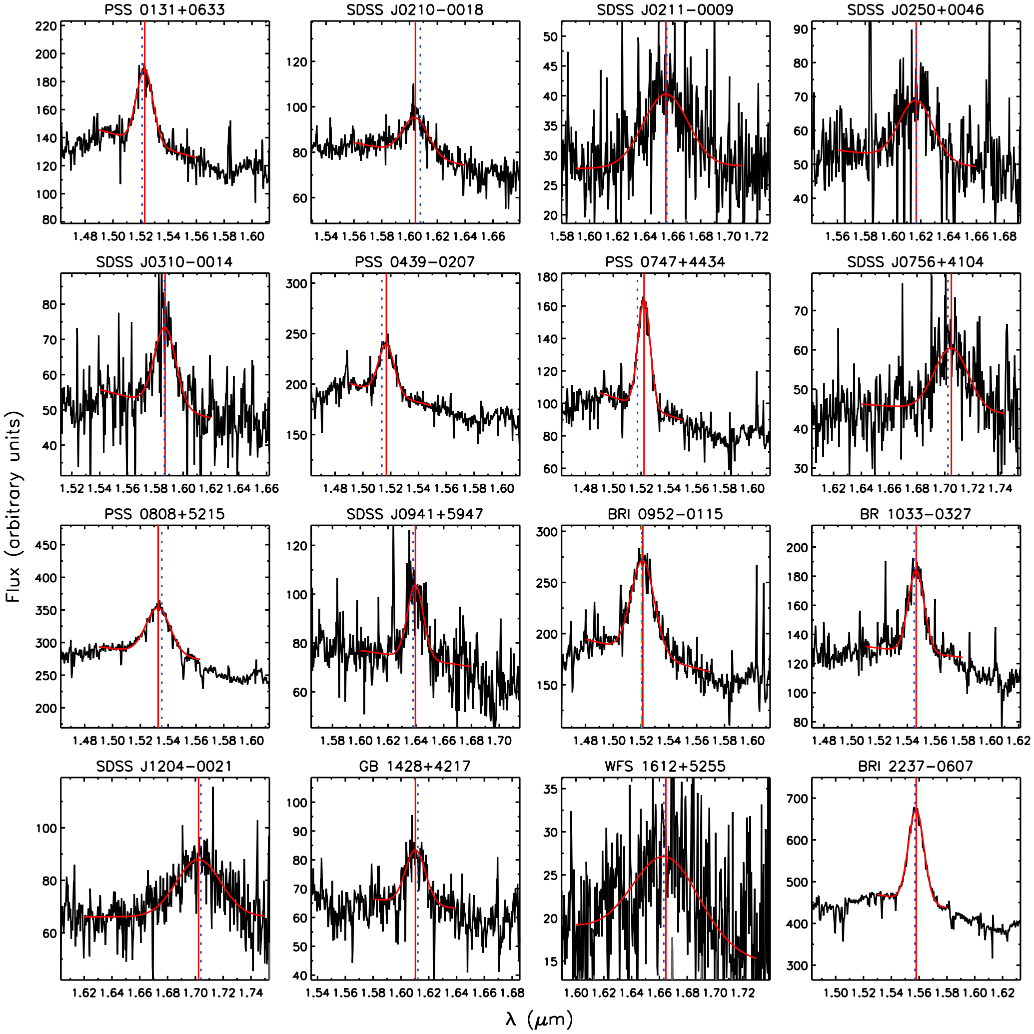

Figure 5.1 NIRSPEC H-band spectra of the Mg II emission line regions of the QSOs in our sample. Each panel covers 0.15 μm. Curved lines show the Gaussian + linear fit to the emission line. Vertical solid lines indicate the central wavelengths of the Gaussian component. Vertical dotted lines indicate where the peak would occur based on the QSO redshifts measured from the start of the Lyα forest. For BRI 0952−0115, a vertical dash-dotted line indicates the expected peak position based on the CO redshift.

Start of the Lyα forest

A QSO's intrinsic redshift may also, in principle, be determined from the start of the Lyα forest. This makes some assumptions, namely that there will be detectable Lyα absorption in the immediate vicinity of the QSO, that Lyα lines can be distinguished from intervening metal lines, and that there is no significant infall of absorbing material that would cause Lyα absorption to appear redward of the systemic redshift. Separating Lyα lines from metal lines is particularly challenging with ESI data, where intrinsically narrow metal lines will be smoothed to the same width as the Lyαlines. In many cases, however, the forest will begin with a strong Lyα line that is presumably associated with the QSO itself and can be verified by accompanying C IV absorption.

We have made a visual estimate of the start of the Lyα forest for each of the objects in our sample. The redshifts are listed in Table 5.2. In Figures 5.2 through 5.5 we display the proximity regions. A vertical dotted line marks the estimated start of the forest. In several cases (e.g., SDSS J0210−0018 and SDSS J0756+4104), we have confirmed the identity of strong Lyα lines with associated C IV. We also show the expected Lyα wavelength based on $z_{\mathrm{Mg\,II}}$ with a vertical solid line. In most cases, $z_{\mathrm{Ly}\alpha}$ agrees to within $1-2\sigma$ of $z_{\mathrm{Mg\,II}}$. The strongest disagreement occurs when $z_{\mathrm{Ly}\alpha}$ falls significantly blueward of $z_{\mathrm{Mg\,II}}$ (e.g., PSS 0747+4454). This may simply be due to a lack of Lyα absorption near the QSO, consistent with the proximity effect. On average, $z_{\mathrm{Ly}\alpha}$ is $\Delta z = 0.002$ ($\Delta v \approx 120$ km s^{-1}) bluer than $z_{\mathrm{Mg\,II}}$, with a scatter of 0.008 (500 km s^{-1}).

Preferred Redshifts

There are trade-offs in using either Mg II or the start of the Lyα forest for the intrinsic QSO redshift. The peak of the Mg II emission line is more objective, but difficult to measure for fainter objects. It also requires a correction for the intrinsic line shift. The start of the Lyα forest is easier to measure, but may be biased towards lower redshifts. To test the reliability of our results, we will measure the proximity effect using both sets of redshifts. In addition, we adopt a preferred redshift for each object based on the apparent merit of both indicators. We use the Lyα redshift in cases where the first Lyα line is strong and has associated C IVabsorption (SDSS J0210−0018, SDSS J0756+4104, PSS 0808+5215, and WFS 1612+5255), or where the forest clearly extends reward of $z_{\mathrm{Mg\,II}}$ (SDSS J1204−0021).

In one case, BRI 0952−0115, we use a CO redshift, which offers perhaps the best indicator of the systemic redshift of the QSO host galaxy (Guilloteau et al. 1999). This is displayed with a vertical dash-dotted line in Figures 5.2 through 5.5. For the remaining objects we use $z_{\mathrm{Mg\,II}}$. The preferred redshifts are listed in Table 5.2. While our choice of redshifts is somewhat subjective, we demonstrate below that all redshifts measured in this work give consistent results for the intensity of the UV background.

5.2.4 QSO Luminosities

We determined absolute flux calibrations for 14 of 16 QSOs in our sample using broad-band magnitudes. Photometric data were taken primarily from the Sloan Digital Sky Survey (SDSS, York et al. 2000), with some additional photometry from the Palomar-QUEST survey (Rabinowitz et al. 2003). A summary of the passbands we used is given in Table 5.3. For each filter, we convolved the relative flux-calibrated, non-atmospheric absorption-corrected ESI spectrum with the response function for the total photometric system, which includes the telescope, filter, detector, and atmosphere. The scaling factors obtained to convert to absolute flux levels were highly consistent for SDSS data, with results from r and i often agreeing to better than a few percent. This suggests that our relative flux calibration of the ESI data is typically accurate to this level over $\lambda \approx 5500 - 8200$. Much greater scatter was present in the QUEST results. At the time of writing, QUEST photometry still exhibits a number of systematic errors. We therefore adopt conservative 30% flux errors for these objects (A. Mahabal, private communication).

The calculated specific fluxes in the continuum are listed in Table 5.3. We measure the continuum level at $1285 \times (1 + z)$ Å, where there should be very little contamination from emission lines (Vanden Berk et al. 2001). For BRI 0952−0115 and BR 1033−0327, we use the spectrophotometric measurements of Storrie-Lombardi et al. (1996), obtained using a wide slit, and adopt their flux errors of 10%. The specific luminosities were then calculated as

$$L_{1285} = \frac{4\pi D_L^2(z) f_{1285}}{1+z}\,, \tag{5.3}$$

where $D_L(z)$ is the luminosity distance at redshift z. The results are listed in Table 5.3.

Finally, in order to compare the ionizing output of a QSO with the UV background,

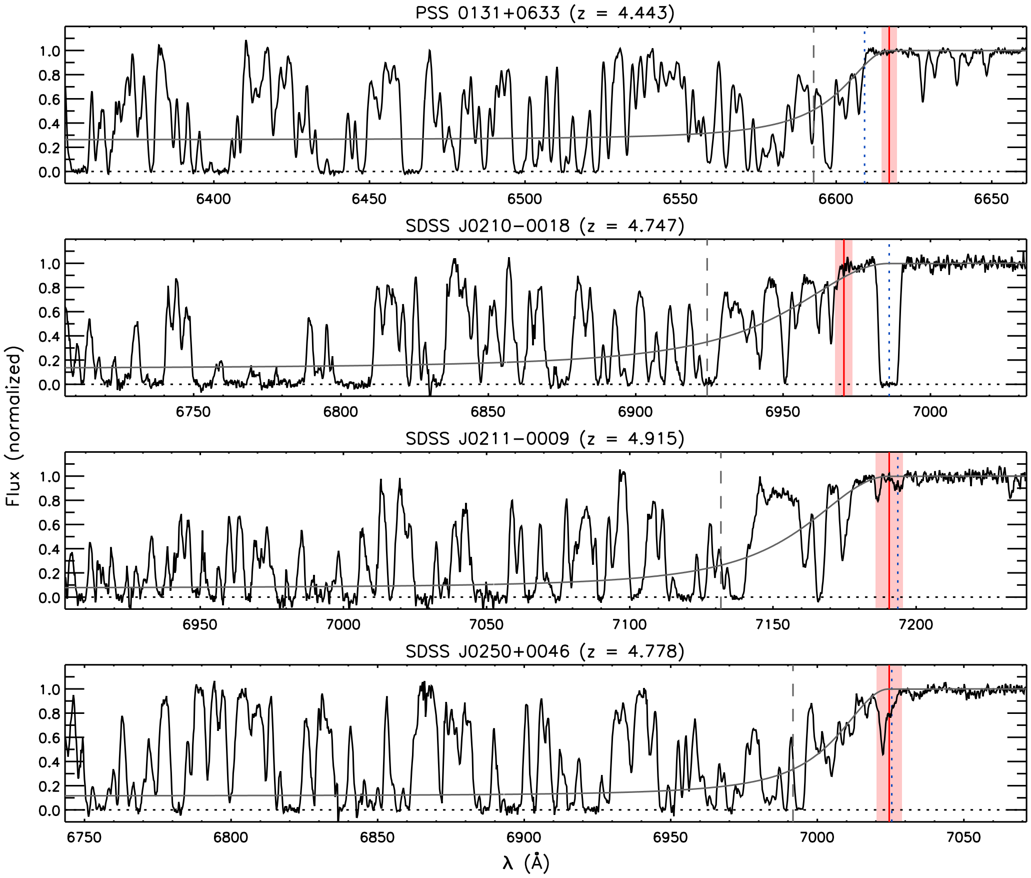

Figure 5.2 The Lyα forest near the QSO proximity regions. For each object, the normalized optical spectrum is displayed from 2000 km s^{-1} redward to 12000 km s^{-1} blueward of Lyα at the preferred systemic redshift. The HIRES data for BR 1033−0227 and BRI 2237−0607 has been binned to 13 km s^{-1} pixels for clarity. Vertical solid lines mark Lyα at the Mg II redshift. Shaded regions indicate the 1σ uncertainty in $z_{\text{Mg II}}$, including the expected 100 km s^{-1} QSO-to-QSO scatter. Dotted lines are visual estimates of the start of the Lyα forest. For BRI 0952−0115, a vertical dash-dotted line shows Lyα at the CO redshift. Solid lines decreasing towards the blue indicate the expected median transmitted flux based on the measured extent of the proximity regions and the model distribution of optical depths. Vertical dashed lines indicates the observed Lyα wavelength corresponding to R_{eq}, the best-fitting distance at which the H I ionization rate due to flux from the QSO equals the ionization rate due to the UV background.

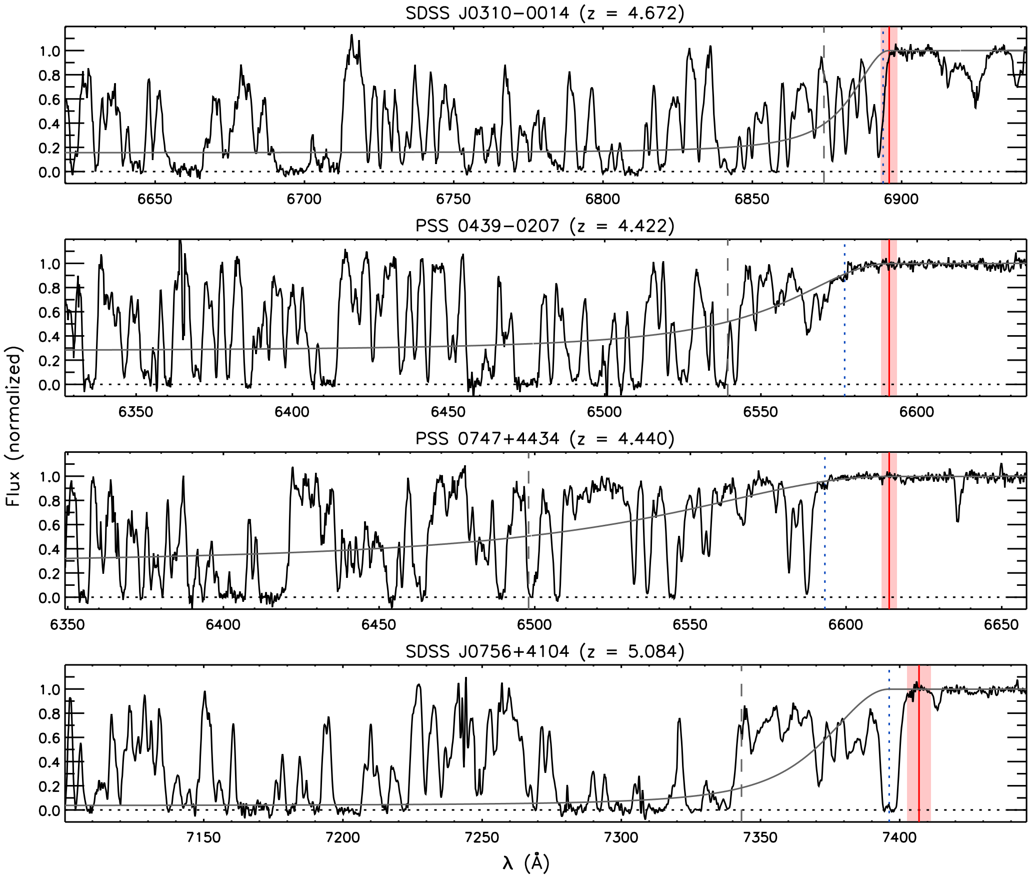

Figure 5.3 The Lyα forest near the QSO proximity regions, continued from Figure 5.2.

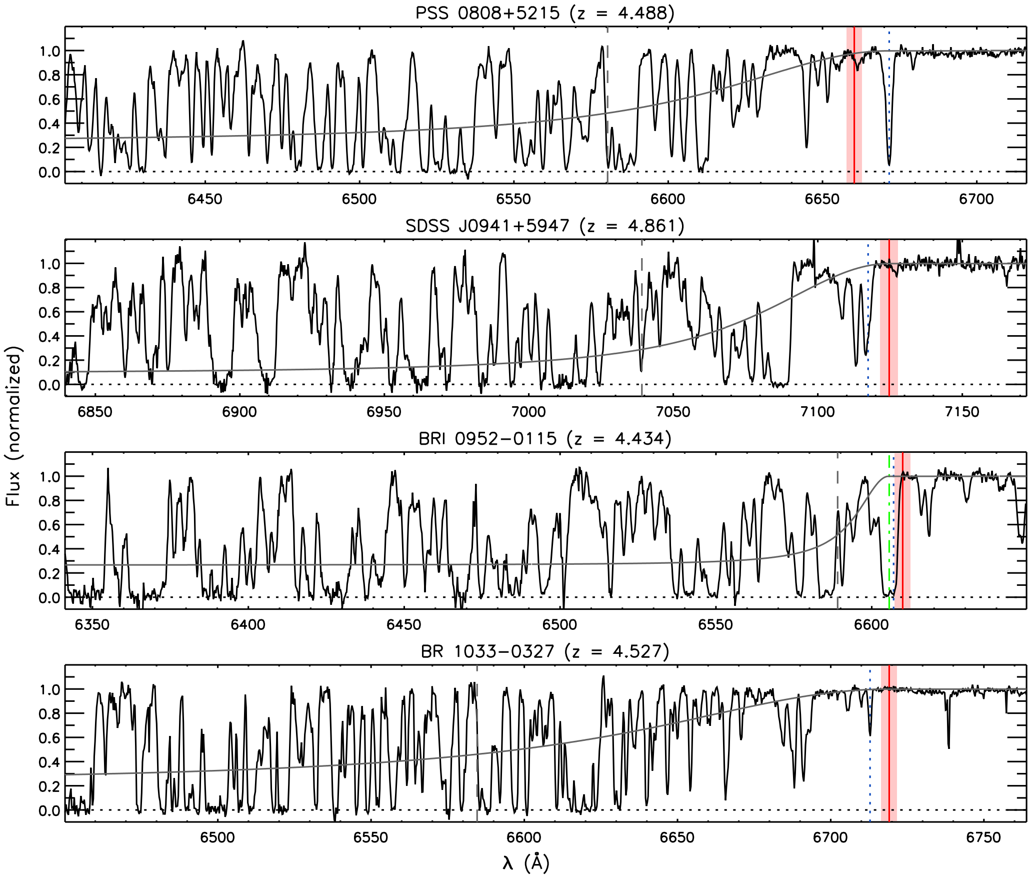

Figure 5.4 The Lyα forest near the QSO proximity regions, continued from Figure 5.2.

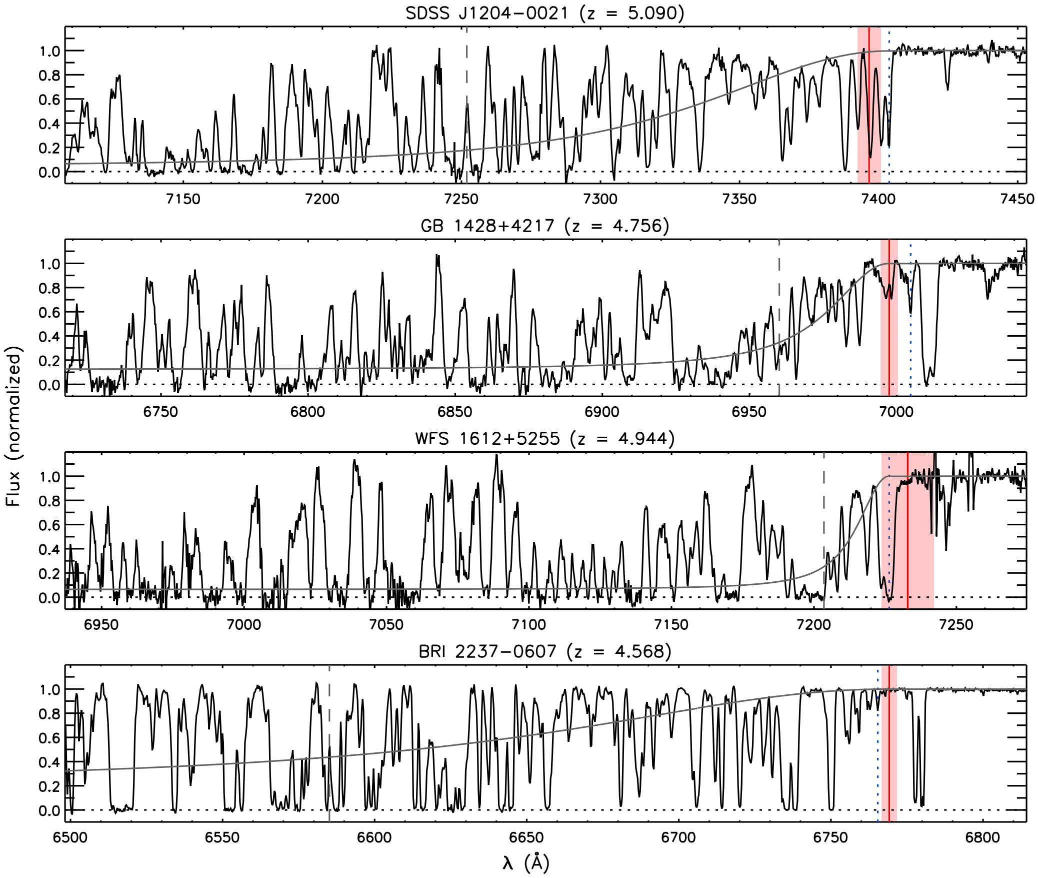

Figure 5.5 The Lyα forest near the QSO proximity regions, continued from Figure 5.2.

Table 5.3. QSO Continuum Properties

QSO	z	Photometry[a]	f_{1285}[b] (10^{-28} erg s^{-1} cm^{-2} Hz^{-1})	L_{1285}[c] (10^{31} erg s^{-1} Hz^{-1})	$\Gamma^{\mathrm{Q10}}_{-12}$[d]
PSS 0131+0633	4.443	QUEST *Rri*	8.08 ± 2.42	3.05 ± 0.91	0.58 ± 0.17
SDSS J0210−0018	4.747	SDSS *ri*	6.80 ± 0.13	2.83 ± 0.05	0.54 ± 0.02
SDSS J0211−0009	4.915	SDSS *ri*	3.47 ± 0.10	1.53 ± 0.04	0.29 ± 0.01
SDSS J0250+0046	4.778	SDSS *ri*	3.86 ± 0.10	1.64 ± 0.04	0.31 ± 0.01
SDSS J0310−0014	4.672	SDSS *ri*	3.35 ± 0.08	1.37 ± 0.03	0.26 ± 0.01
PSS 0439−0207	4.422	QUEST *ri*	9.86 ± 2.96	3.69 ± 1.11	0.70 ± 0.21
PSS 0747+4434	4.440	SDSS *ri*	5.22 ± 0.08	1.97 ± 0.03	0.38 ± 0.01
SDSS J0756+4104	5.084	SDSS *ri*	3.22 ± 0.09	1.50 ± 0.04	0.29 ± 0.01
PSS 0808+5215	4.488	SDSS *ri*	15.3 ± 0.2	5.85 ± 0.08	1.12 ± 0.04
SDSS J0941+5947	4.861	SDSS *ri*	5.45 ± 0.10	2.36 ± 0.04	0.45 ± 0.02
BRI 0952−0115	4.434	SL96[e]	9.76 ± 0.98	3.67 ± 0.37	0.70 ± 0.07
BR 1033−0327	4.527	SL96[e]	10.3 ± 1.0	3.99 ± 0.40	0.76 ± 0.08
SDSS J1204−0021	5.090	SDSS *ri*	8.29 ± 0.28	3.85 ± 0.13	0.73 ± 0.03
GB 1428+4217	4.756	SDSS *r*	5.40 ± 0.18	2.27 ± 0.08	0.43 ± 0.02
WFS 1612+5255	4.944	SDSS *ri*	1.69 ± 0.09	0.76 ± 0.04	0.14 ± 0.01
BRI 2237−0607	4.568	QUEST *Rri*	20.5 ± 6.1	8.06 ± 2.42	1.54 ± 0.46

[a] Filters: Gunn r, i; Johnson R.

[b] Observed flux at rest wavelength 1285 Å.

[c] Continuum luminosity at rest wavelength 1285 Å.

[d] H I ionization rate due to flux from the QSO at a distance of 10 proper Mpc, in units of 10^{-12} s^{-1}.

[e] Storrie-Lombardi et al. (1996) wide slit spectrophotometry.

which may have a different spectral shape, we calculate the total H I ionization rate,

$$\Gamma = \int_{\nu_0}^{\infty} \frac{4\pi J(\nu)\sigma_{\mathrm{H\,I}}(\nu)}{h\nu} d\nu \,. \tag{5.4}$$

Here, ν_0 is the frequency at the Lyman limit, $J(\nu)$ is the specific intensity at frequency ν, and $\sigma_{\mathrm{H\,I}}(\nu) = 6.3 \times 10^{-18} (\nu_0/\nu)^3$ cm^2 is the H I absorption cross section. For the flux from a QSO, $4\pi J(\nu) = L(\nu)/(4\pi R^2)$, where R is the distance from the QSO. We adopt a power-law QSO continuum, $f_\nu \propto \nu^{-\alpha}$, with $\alpha = 0.5 \pm 0.5$. For each QSO we compute the ionization rate at a distance of 10 proper Mpc, $\Gamma_{-12}^{\mathrm{Q10}}$, where Γ_{-12} is in units of 10^{-12} s^{-1}. These values are listed in Table 5.3. Errors include uncertainties in the observed flux as well as scatter in the power-law slope. We note that, due to the strong decrease in the absorption cross-section with frequency, Γ^{Q} does not depend sensitively on the choice of α within the range we assume.

5.3 Proximity Effect Model

Measuring the intensity of the UV background using the proximity effect requires determining the extent to which the ionizing flux from the QSO dominates over the background. The H I neutral fraction, and hence optical depth, will vary inversely with the total ionization rate, $\tau \propto \Gamma^{-1}$, where $\Gamma = \Gamma^{\mathrm{bg}} + \Gamma^{\mathrm{Q}}$ is the sum of the ionization rates due to the UV background and the QSO. We define R_{eq} to be the proper distance from a QSO at which $\Gamma^{\mathrm{Q}} = \Gamma^{\mathrm{bg}}$. In a uniform IGM, the optical depth would increase with distance as

$$\tau_{\mathrm{u}} = \frac{\tau_{\mathrm{bg}}}{1 + (R/R_{\mathrm{eq}})^2} \,, \tag{5.5}$$

where τ_{bg} is the optical depth far from the QSO. However, clustering in the IGM produces large variations in transmitted flux. In addition, the non-linear transformation between optical depth and flux makes it difficult to measure optical depths reliably. In classical proximity effect studies, H I column density distributions are measured as a way of overcoming these obstacles. At $z > 4$, however, lines in the forest are so strongly blended that identifying individual absorbers with moderate resolution data is extremely difficult.

One solution would be to simply median combine the spectra, taking advantage of the fact that, although the *mean* transmitted flux does not correspond to the *mean* optical depth, the *median* transmitted flux should correspond to the *median* optical depth. Due to the different QSO redshifts and luminosities, however, we would not expect the size of the proximity region to be the same for all objects. The median is also very noisy, even for a large number of spectra. We will return to this approach, nevertheless, as a consistency check in §5.4.3.

5.3.1 Transmitted Flux Distribution

In order to make the best use of the optical depth information encoded in the Lyα forest, we will instead examine how the distribution of transmitted fluxes changes a a function of distance from a QSO. In analogy to the column density distribution used by other authors, we adopt the lognormal τ distribution measured by Becker et al. (2006a). A slowly-evolving lognormal $P_\tau(\tau)$ was shown to correctly produce the observed distribution of transmitted fluxes over redshifts $1.7 < z < 5.8$. The distribution depends on two parameters, $\mu = \langle \ln \tau \rangle$, and $\sigma = \text{std dev}(\ln \tau)$, as

$$P_\tau(\tau) = \frac{1}{\tau\sigma\sqrt{2\pi}} \exp\left[-\frac{(\ln \tau - \mu)^2}{2\sigma^2} \right] . \tag{5.6}$$

For $F = e^{-\tau}$, this gives an expected distribution of transmitted fluxes,

$$P_F(F) = \frac{1}{(-\ln F)F\sigma\sqrt{2\pi}} \exp\left[-\frac{(\ln(-\ln F) - \mu)^2}{2\sigma^2} \right] , \tag{5.7}$$

for $0 \leq F \leq 1$, 0 otherwise. The observed flux distribution is constructed by convolving $P_F(F)$ with a smoothing kernel that incorporates the noise properties of the spectrum (Becker et al. 2006a).

For a uniform UV background, an increase in Γ due to flux from the QSO will not change σ, the logarithmic scatter in τ. However, μ will depend on Γ as $e^{\mu} \propto \Gamma^{-1}$. Hence, in the proximity region,

$$\mu(z, R) = \mu_{\text{bg}}(z) - \ln \left[1 + \left(\frac{R}{R_{\text{eq}}} \right)^{-2} \right] , \tag{5.8}$$

where $\mu_{\text{bg}} = \langle \ln \tau_{\text{bg}} \rangle$. For HIRES data, we use the redshift evolution of the lognormal parameters measured by Becker et al. (2006a),

$$\mu_{\rm bg}^{\rm HIRES}(z) = -9.35 + 1.79(1+z)\,, \tag{5.9}$$

$$\sigma_{\rm bg}^{\rm HIRES}(z) = 4.19 - 0.46(1+z)\,. \tag{5.10}$$

For ESI data, we have repeated the analysis of Becker et al. (2006a) after smoothing the HIRES data in that work to ESI resolution. The resulting parameters are

$$\mu_{\rm bg}^{\rm ESI}(z) = -7.50 + 1.43(1+z)\,, \tag{5.11}$$

$$\sigma_{\rm bg}^{\rm ESI}(z) = 2.72 - 0.28(1+z)\,. \tag{5.12}$$

Examples of the expected flux PDFs in the proximity region are shown in Figure 5.6. At $z = 4-5$, the values for μ are very similar in the high- and moderate-resolution cases. This is not surprising since the median optical depth and, hence, the median transmitted flux, depends only on μ, and the median flux is not changed greatly by smoothing. However, σ is somewhat lower at moderate-resolution than at high-resolution, which produces slight differences in the flux PDFs. The lower $sigma$ arises from the fact that smoothing tends to remove pixels from the continuum and from saturated regions, which narrows the apparent distribution of optical depths. We will return to the issue of resolution in §5.6. As evidenced by the similarity of the expected HIRES and ESI flux PDFs in Figure 5.6, it has only a minimal impact on our final results.

5.3.2 Maximum Likelihood Method

We can estimate the size of a QSO's proximity region by finding the value of $R_{\rm eq}$ that maximizes the probability that the observed fluxes near the QSO redshift are drawn from the expected flux distribution. This is analogous to the maximum likelihood method of Kulkarni & Fall (1993), which uses the distribution H I column densities. The expected transmitted flux PDF will evolve with distance from the QSO according to equations (5.7) and (5.8). For an individual QSO, we can construct a likelihood function of the form

$$\mathcal{L} = \prod_i P_F(F_i, z_i, R_i, R_{\rm eq})\,, \tag{5.13}$$

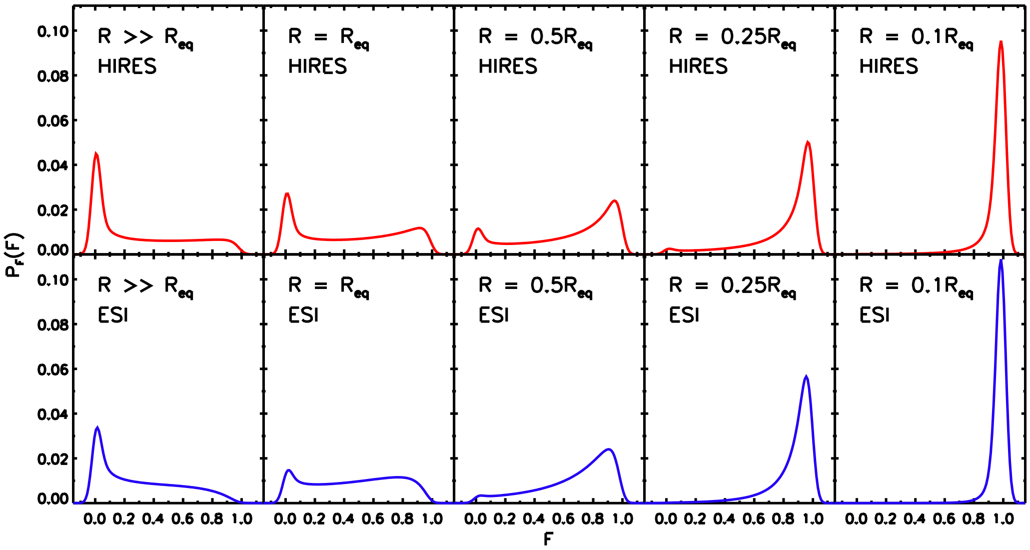

Figure 5.6 Theoretical transmitted flux probability distribution functions in the proximity region of a QSO at $z = 4.5$. In each panel we plot the expected flux PDF, computed from equation (5.7), at the indicated distance from the QSO. The lognormal parameters $\mu(z, R)$ and $\sigma(z)$ are computed from equations (5.8)–(5.12). Distances are expressed as a fraction of $R_{\rm eq}$, the distance at which $\Gamma^{\rm Q} = \Gamma^{\rm bg}$. The PDFs are smoothed to reflect a small amount of noise in the spectra ($r.m.s = 3\%$ of the continuum). Top panels are for HIRES resolution. Bottom panels are for ESI resolution. As the distance to the quasar decreases, the flux distributions shift towards higher values. The PDFs at the two resolutions are similar at all distances, although the high-resolution PDFs tends to have more pixels at $F \approx 0$.

where i refers to the ith pixel in the proximity region. The proper distance from the QSO is calculated for small distances as $R = \Delta v/H(z)$, where Δv is the velocity separation from the systemic redshift of the QSO, and $H(z)$ is the Hubble parameter at redshift z. For an ensemble of QSOs, the likelihood function becomes

$$\mathcal{L} = \prod_{Q}\prod_{i} P_F(F_i^Q, z_i^Q, R_i^Q, R_{\rm eq}^Q)\,, \tag{5.14}$$

where Q refers to an individual QSO. The expected $R_{\rm eq}^Q$ for an individual QSO will scale with $\Gamma^{\rm bg}$ as $R_{\rm eq}^Q = 10(\Gamma^{\rm Q10}/\Gamma^{\rm bg})^{1/2}$ Mpc. We can therefore estimate the UV background directly by maximizing $\mathcal{L}$ over a set of values for $\Gamma^{\rm bg}$. Since the quantity we are actually measuring is a length scale, however, we instead compute $\mathcal{L}$ by considering a QSO with a fiducial $\Gamma^{\rm Q10}$ and allow $R_{\rm eq}$ for that QSO to vary. For each fiducial $R_{\rm eq}$, the corresponding values of $R_{\rm eq}^Q$ for the QSOs in our sample are calculated according to their ionizing outputs, and our estimate of $\Gamma^{\rm bg}$ is the one that corresponds to the fiducial $R_{\rm eq}$ that maximizes $\mathcal{L}$. This approach gives the same result as computing $R_{\rm eq}^Q$ for each QSO directly over a range in $\Gamma^{\rm bg}$. It makes it easier, however, to estimate non-symmetric errors in $\Gamma^{\rm bg}$ that arise from the non-linear dependence of $\Gamma^{\rm bg}$ on $R_{\rm eq}$.

5.4 Results

5.4.1 Maximum Likelihood Estimates of $\Gamma^{\rm bg}$

We have determined maximum likelihood estimates of $\Gamma^{\rm bg}$ by maximizing equation (5.14) over the Lyα forest within $\Delta v \leq 12000$ km s^{-1} of the systemic redshift of each QSO. In order to avoid associated absorption, we do not include pixels within 200 km s^{-1}of the QSO redshift. Our primary estimate of $\Gamma^{\rm bg}$ was made by maximizing $\mathcal{L}$ simultaneously over all sightlines. Jackknife errors were used to estimate the uncertainty in $\Gamma^{\rm bg}$ due to cosmic variance, with jackknife replicants formed by leaving out one QSO at a time from the sample. We also computed errors due to uncertainties in the QSO redshifts and ionizing fluxes using Monte Carlo methods.

Our results are summarized in Table 5.4. For the full sample of 16 QSOs, using the preferred redshifts, we obtain $\Gamma_{-12}^{\rm bg} = 1.4^{+1.6}_{-0.7}$ (1σ), where $\Gamma_{-12}^{\rm bg}$ is the background H I

Table 5.4. UV Background Measurements

QSO subset	z type	$\Gamma^{\rm bg}_{-12}$[a]	Errors in $\Gamma^{\rm bg}_{-12}$		
			Jackknife[b]	MC[c]	Total
All	preferred	1.4	$^{+0.6}_{-0.4}$	$^{+1.4}_{-0.6}$	$^{+1.6}_{-0.7}$
All	Mg II	1.5	$^{+0.7}_{-0.4}$	$^{+1.2}_{-0.5}$	$^{+1.4}_{-0.7}$
All	Lyα	1.5	$^{+0.6}_{-0.4}$	$^{+1.5}_{-0.6}$	$^{+1.6}_{-0.7}$
Flux errors $\leq$ 10%	preferred	1.3	$^{+0.6}_{-0.4}$	$^{+0.2}_{-0.2}$	$^{+0.6}_{-0.4}$
$\Gamma^{\rm Q10}_{-12} > 1.0$	preferred	0.8	$^{+1.1}_{-0.4}$	$^{+0.4}_{-0.2}$	$^{+1.1}_{-0.4}$
$0.5 < \Gamma^{\rm Q10}_{-12} < 1.0$	preferred	1.3	$^{+1.7}_{-0.6}$	$^{+0.3}_{-0.2}$	$^{+1.8}_{-0.6}$
$\Gamma^{\rm Q10}_{-12} < 0.5$	preferred	1.9	$^{+0.9}_{-0.5}$	$^{+0.2}_{-0.2}$	$^{+1.0}_{-0.6}$

[a] Background H I ionization rate, in units of 10^{-12} s^{-1}.

[b] Jackknife errors, where jackknife replicants were formed by leaving out one QSO at a time from the subset.

[c] Monte Carlo errors compute for uncertainties in individual QSO z and $\Gamma^{\rm Q10}_{-12}$ values.

ionization rate in units of 10^{-12} s^{-1}. Very similar results are obtained when we use only redshifts determined from Mg II or the start of the Lyα forest, as shown in Table 5.4. The upper error is dominated by uncertainty in the luminosities of objects with QUEST photometry, particularly BRI 2237−0607, which is the brightest object in our sample. Using only the 13 objects with observed flux errors ≤ 10%, we obtain $\Gamma^{\rm bg}_{-12} = 1.3^{+0.6}_{-0.4}$.

5.4.2 Luminosity Dependence of Proximity Region Size

A key goal of this work is to demonstrate not only that the proximity region size increases with QSO luminosity, but that the shape of the luminosity dependence is what is expected for the photoionization model. The easiest way to do this is by dividing our QSO sample according to luminosity and estimating $\Gamma^{\rm bg}$ from each subset. If the photoionization model is correct, i.e., $R_{\rm eq} \propto L_{\rm QSO}^{1/2}$ (or more precisely, $R_{\rm eq} \propto (\Gamma^{\rm Q10})^{1/2}$), then the estimate of $\Gamma^{\rm bg}$ should be the same for all luminosities. We have divided our sample into three subsets according to their ionizing output: 2 QSOs with $\Gamma^{\rm Q10}_{-12} > 1.0$, 6 QSOs with $0.5 < \Gamma^{\rm Q10}_{-12} < 1.0$, and 8 QSOs with $\Gamma^{\rm Q10}_{-12} < 1.0$. For each group we repeated the maximum likelihood analysis. The results are given in Table 5.4. While the three values of $\Gamma^{\rm bg}$ are consistent within the errors, the fact that the fainter QSOs produce higher estimates of $\Gamma^{\rm bg}$ suggests that the proximity regions for faint QSOs may be disproportionately small.

In order to examine this issue more closely, we have determined maximum likelihood estimates of $R_{\rm eq}$ for each individual QSO. The results are listed in Table 5.5. In Figures 5.2 through 5.5, we overplot the corresponding median transmitted flux profiles in the proximity regions. The median flux is computed as $F_{\rm med} = \exp\left(-\tau_{\rm med}\right)$, where $\tau_{\rm med} = e^{-\mu}$, and μ is calculated from equations (5.8), (5.9), and (5.11). Note that the median flux will typically be smaller than the mean flux. Blueward of Lyα at a QSOs systemic redshift, the model median flux decreases asymptotically towards the background value. The wavelength corresponding to $R_{\rm eq}$ is marked with a vertical dashed line. In most cases, the estimated size of the proximity region agrees roughly with a visual estimate of the extent of the enhanced transmission.

In Figure 5.7, we plot $R_{\rm eq}$ vs. $\Gamma_{-12}^{\rm Q10}$ for all 16 QSOs in our sample. The solid line is the expected trend for our estimate of $\Gamma^{\rm bg}$ found by maximizing the likelihood function simultaneously over all sightlines. As expected from the highly random nature of the Lyα forest, there is a large scatter in $R_{\rm eq}$ at all levels of QSO ionizing output. Most QSOs fall below the solid line, indicating smaller than expected proximity regions. This might suggest that our estimate of $\Gamma^{\rm bg}$ is biased towards brighter QSOs, whose larger proximity regions will have greater leverage on the likelihood function. Still, the mean value of $R_{\rm eq}$ in each of our three luminosity bins is consistent with the expected trend in luminosity.

5.4.3 Median Transmitted Flux

Under the maximum likelihood approach, our estimate of $\Gamma^{\rm bg}$ depends on the model we assume for the underlying optical depth distribution. We can check our result by determining whether the median transmitted flux has the correct dependence on distance from the QSO. The median flux will be noisy for a small sample of QSOs, but it has the advantage of being nearly model-independent.

We expect the size of the proximity region to vary over the range of QSO luminosities in our sample. In order to preserve the shape of the transmitted flux profile when computing the median, therefore, we first adjust the distance scale for each sightline according to the

Table 5.5. Individual Proximity Region Estimates

QSO	z	$\Gamma_{-12}^{\mathrm{Q10}}$ [a]	R_{eq} [b] (proper Mpc)
PSS 0131+0633	4.443	0.58 ± 0.17	2.3
SDSS J0210−0018	4.747	0.54 ± 0.02	5.2
SDSS J0211−0009	4.915	0.29 ± 0.01	4.6
SDSS J0250+0046	4.778	0.31 ± 0.01	2.7
SDSS J0310−0014	4.672	0.26 ± 0.01	1.9
PSS 0439−0207	4.422	0.70 ± 0.21	5.0
PSS 0747+4434	4.440	0.38 ± 0.01	11.1
SDSS J0756+4104	5.084	0.29 ± 0.01	3.9
PSS 0808+5215	4.488	1.12 ± 0.04	8.6
SDSS J0941+5947	4.861	0.45 ± 0.02	6.8
BRI 0952−0115	4.434	0.70 ± 0.07	1.6
BR 1033−0327	4.527	0.76 ± 0.08	12.4
SDSS J1204−0021	5.090	0.73 ± 0.03	11.0
GB 1428+4217	4.756	0.43 ± 0.02	3.1
WFS 1612+5255	4.944	0.14 ± 0.01	1.8
BRI 2237−0607	4.568	1.54 ± 0.46	16.7

[a] H I ionization rate due to flux from the QSO at a distance of 10 proper Mpc, in units of 10^{-12} s^{-1}.

[b] Maximum likelihood estimate of the distance from the QSO at which $\Gamma^{\mathrm{Q}} = \Gamma^{\mathrm{bg}}$.

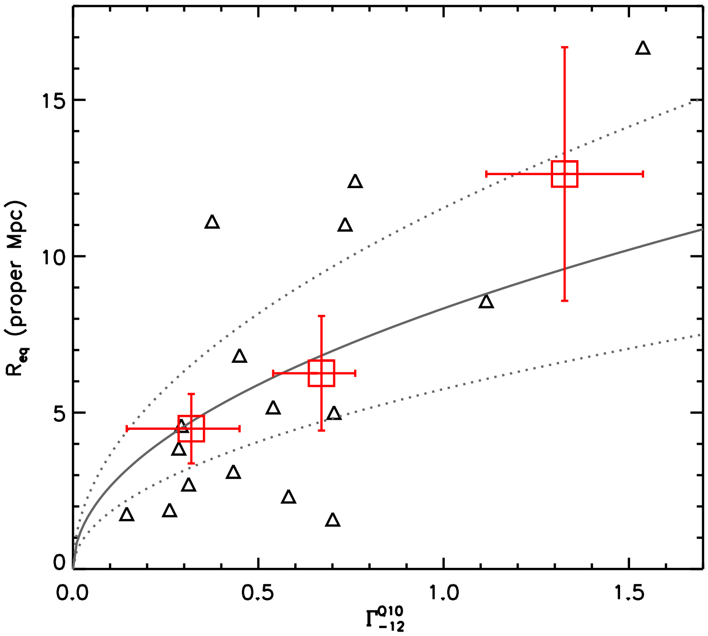

Figure 5.7 Proximity region size as a function of QSO luminosity. The horizontal axis is the H I ionization rate due to flux from the quasar at a distance of 10 proper Mpc. The vertical axis is the distance from the QSO at which $\Gamma^{Q} = \Gamma^{bg}$. Maximum likelihood values for individual sightlines are shown as triangles. The mean values in three luminosity bins are shown as squares. For each bin, horizontal error bars give the range in Γ_{-12}^{Q10} covered. Vertical error bars give the standard deviation in the mean R_{eq}. The solid line shows R_{eq} as a function of Γ_{-12}^{Q10} expected for the background Γ found by simultaneously fitting all sightlines. Dotted lines correspond to the 1σ uncertainties in the background Γ. The mean sizes of the proximity regions scale correctly with QSO luminosity, but with large scatter in the individual measurements.

QSO's ionizing output. We define the luminosity-scaled distance from a QSO as

$$R_S \equiv \left(\frac{\Gamma^{\mathrm{Q10}}}{\Gamma^{\mathrm{fid}}}\right)^{1/2} \frac{\Delta v}{H(z)}\,, \tag{5.15}$$

where Γ^{fid} is a fiducial ionization rate. The combined spectrum is then formed by taking the median of pixels from all sightlines in bins of R_S. This will tend to weight the median spectrum towards brighter QSOs, a consequence of preserving the transmitted flux profile in the proximity region. We are free, however, to compute the median in subsamples of QSOs luminosity.

The median transmitted flux profiles for the total sample and for our three luminosity subsets are shown in Figure 5.8. The HIRES data were rebinned to the ESI pixel size prior to combining. For each group, we take Γ^{fid} to be the median $\Gamma^{\mathrm{Q10}}_{-12}$ of the included QSOs. The expected flux profile is shown in each case for our maximum likelihood value of $\Gamma^{\mathrm{bg}} = 1.4^{+1.6}_{-0.7}$, the fiducial $\Gamma^{\mathrm{Q10}}_{-12}$, and the measured median flux far from the QSOs. For the three luminosity subsets, we also overlay the expected profile for the median $\Gamma^{\mathrm{Q10}}_{-12}$ of the total sample.

In general, the median transmitted flux profiles are consistent with our maximum likelihood estimate of Γ^{bg}. Although there is a large scatter in the flux, and adjacent points are correlated, the extent of the proximity region appears larger for QSOs with higher ionizing output. Still, in the lowest luminosity subset, there appears to be more absorption at $R_S \lesssim 3$ Mpc than expected. This may indicate that there is proportionately more neutral hydrogen around low-luminosity QSOs. The effects of line broadening, however, may also be important. The median optical depth should decrease as $\tau \propto [1 + (R/R_{\mathrm{eq}})^2]^{-1}$ only if the velocity width of Lyα absorbers depends primarily on the Hubble flow. If turbulent or thermal broadening is important, than a high column density absorber will remove flux from more pixels than it would otherwise. This effect would increase with the number of saturated lines. Hence, the proximity regions of low-luminosity QSOs may appear disproportionately small. More detailed modeling will be necessary to determine whether this is the case.

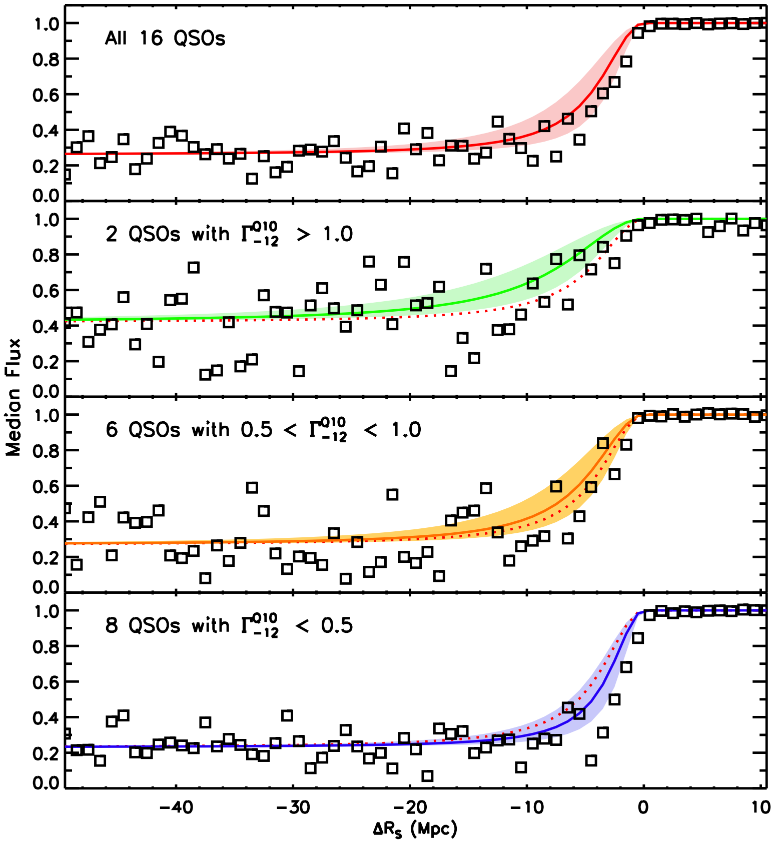

Figure 5.8 Median transmitted flux in the Lyα forest as a function of scaled distance from the QSO. In each group, the median flux in bins of 1 proper Mpc was computed after adjusting the distance scale for individual QSOs such that the expected scaled size of the proximity region is the same for all objects (cf. equation 5.15). The solid line in each panel shows the expected median flux based on the median Γ_{-12}^{Q10} for that group, our maximum likelihood estimate of Γ^{bg}, and the median flux far from the QSOs. Shaded regions reflect the 1σ uncertainties in Γ^{bg}. In the three lower panels, the expected profile for the median Γ_{-12}^{Q10} of the whole sample is shown with a dotted line. The extent of the enhanced transmission is larger for more luminous QSOs, consistent with what is expected for the photoionization model of the proximity effect. Although there is significant scatter in the median flux, however, and adjacent points are strongly correlated, there appears to be more absorption near the faintest QSOs than is expected from our estimate of Γ^{bg}.

5.5 Comparison with Previous Results

We can compare our results to other measurements of the UV background at high redshift. An important step will be to adjust all values to our adopted cosmology, as described below. Bolton et al. (2005) used a large suite of hydrodynamical simulations to determine $\Gamma^{\rm bg}$ from the mean opacity of the Lyα forest at $2 \leq z \leq 4$. Their work also examined the dependence of $\Gamma^{\rm bg}$ on various cosmological parameters. The optical depth in a uniform IGM will scale as $\tau_u \propto \left(\Omega_{\rm b} h^2\right)^2 \Omega_{\rm m}^{-0.5} h^{-1} T^{-0.7} \Gamma^{-1}$, where T is the gas temperature (Gunn & Peterson 1965; Weinberg et al. 1997). The mean transmission, however, will be highly sensitive to the gas distribution, which also depends on the cosmological parameters, including σ_8. Thus, determining $\Gamma^{\rm bg}$ from the mean transmitted flux is highly cosmology-dependent. The fiducial cosmological parameters used by Bolton et al. (2005) are very close to the WMAP+SDSS values. Their values for $\Gamma^{\rm bg}$ are therefore most likely limited by uncertainties in the gas temperature, and the fact that their simulations do not include radiative transfer, which may affect both the mean and the distribution of T (Bolton et al. 2004).

McDonald & Miralda-Escudé (2001) and Fan et al. (2006a) used the mean Lyα transmission to measure $\Gamma^{\rm bg}$ at $z > 4$. However, their values are based on a ΛCDM simulation that used somewhat outdated values for cosmological parameters ($\Omega_{\rm m} = 0.4$, Miralda-Escudé et al. 1996). We have used the $z = 4$ scaling relations from Bolton et al. (2005) to attempt to correct the McDonald & Miralda-Escudé (2001) and Fan et al. (2006a) measurements at $4.5 \leq z \leq 5.25$ to WMAP+SDSS cosmology. Including a decrease in the gas temperature from 2×10^4 K to 12500 K, which was used by Bolton et al. (2005) at $z = 4$ based on the measurement of Schaye et al. (2000), the corrected $\Gamma^{\rm bg}$ are roughly a factor of three larger than the published values. This is a great enough difference that the scaling relations given by Bolton et al. (2005) are unlikely to be accurate. We therefore regard the current measurements of $\Gamma^{\rm bg}$ based on Lyα transmission at $z > 4$ as rough estimates only.

We show our results for $\Gamma^{\rm bg}$ along with those from the Lyα forest in Figure 5.9. We also include $\Gamma^{\rm bg}$ measured by Scott et al. (2000) using the proximity effect in a large sample of QSOs at $1.7 < z < 3.8$. We have adjusted the Scott et al. (2000) values for cosmology by accounting for the change in luminosity distance and the (implicit) size of the proximity regions. The results are in excellent agreement with Lyα forest measurements at $2 \leq z \leq 4$. The proximity and Lyα forest values are also roughly consistent with the combined estimated contributions to $\Gamma^{\rm bg}$ at $z \sim 3$ from star-forming galaxies (Shapley et al. 2006) and QSOs (Hunt et al. 2004), which we show assuming spectral indices $\alpha_{\rm gal} = 1.8 \pm 1$ and $\alpha_{\rm QSO} = 0.5 \pm 1$, and neglecting changes in the spectral shape due to filtering through the IGM. This total may be lower if, for example, the escape fraction of ionizing photons from QSOs on the faint end of the luminosity function is less than 1.

Our proximity effect measurements at $z \sim 4.7$ are consistent with no evolution in $\Gamma^{\rm bg}$ from $z \sim 2$, although there are still large error bars at all redshifts. We are roughly consistent with, but somewhat higher than, the Lyα forest values at $z \geq 4.5$. As noted above, however, there are large uncertainties in the Lyα forest values related to cosmology, the IGM temperature, and radiative transfer effects. Future measurements using updated numerical simulations may be closer to our results. On the other hand, as we note above, our measurement of $\Gamma^{\rm bg}$ may be too high due to improper modeling of the expected flux distribution in the proximity region of faint QSOs. Our lower value of $\Gamma^{\rm bg}_{-12} \sim 0.8$ found using the brightest QSOs in our sample may therefore be the most accurate.

5.6 Conclusions

We have measured the mean H I ionization rate in the IGM at $4.4 < z < 5.1$ using the proximity effect in a sample of 16 QSOs. Accurate redshifts were derived from Mg II emission lines, supplemented by measurements based on the start of the Lyα forest and CO observations. In order to cope with the high levels of absorption at $z > 4$, where traditional methods based on counting individual lines would be difficult to apply, we have introduced a new method for determining the extent of a QSO's proximity region based on the expected distribution of pixel optical depths. For the complete sample, we obtain a maximum likelihood estimate of $\Gamma^{\rm bg}_{-12} = 1.4^{+1.6}_{-0.7}$ (1σ). Much of the error lies in the flux calibration of a few of our objects. Using only the 13 QSOs with flux uncertainties $\leq 10\%$, we obtain $\Gamma^{\rm bg}_{-12} = 1.3^{+0.6}_{-0.4}$.

We have further tested the photoionization mode of the proximity effect by examining the dependence of the size of the proximity region on QSO luminosity. For individual sightlines, maximum likelihood estimates of $R_{\rm eq}$, the distance from the QSO at which $\Gamma^{\rm Q} = \Gamma^{\rm bg}$, show a large scatter at all QSO luminosities. The mean values of $R_{\rm eq}$ in bins of $\Gamma^{\rm Q10}_{-12}$ are consistent with the expected $R_{\rm eq} \propto (\Gamma^{\rm Q10})^{1/2}$ trend, although most of the fainter

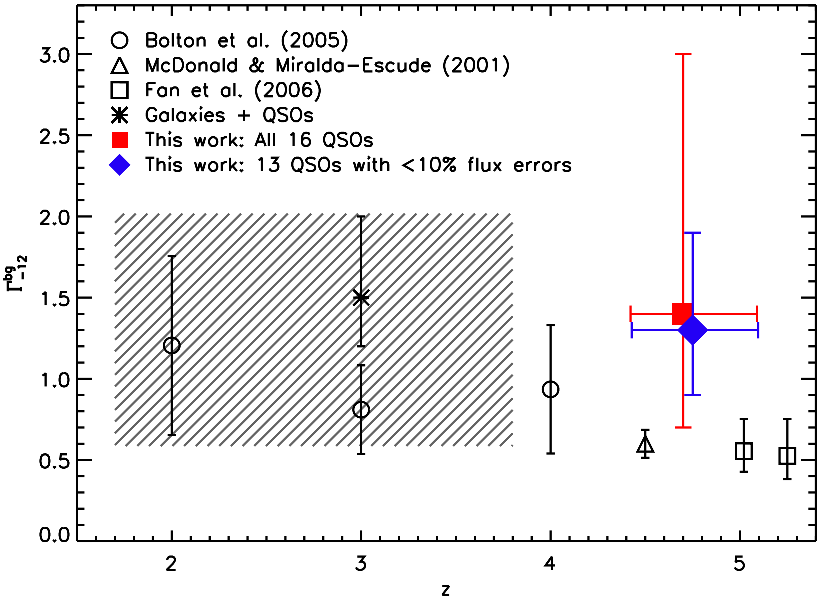

Figure 5.9 Measurements of the background H I ionization rate at $2 \lesssim z \lesssim 5$, corrected to WMAP+SDSS cosmology. Results from this work are shown with large filled symbols. Proximity effect measurements from Scott et al. (2000) are indicated by the shaded region. Values of $\Gamma_{-12}^{\mathrm{bg}}$ measured from the mean transmitted flux in the Lyα forest are shown from Bolton et al. (2005) (circles), McDonald & Miralda-Escudé (2001) (triangle), and Fan et al. (2006a) (open squares). The combined measured contributions from star-forming galaxies (Shapley et al. 2006) and QSOs (Hunt et al. 2004) at $z \sim 3$ are shown assuming spectral indices $\alpha_{\mathrm{gal}} = 1.8 \pm 1$ and $\alpha_{\mathrm{QSO}} = 0.5 \pm 1$, and neglecting filtering through the IGM (asterisk). Error bars for Bolton et al. (2005) include uncertainties in the cosmological model, while those for McDonald & Miralda-Escudé (2001) and Fan et al. (2006a) include only uncertainties in the mean transmitted flux. The corrections for cosmology applied to the McDonald & Miralda-Escudé (2001) and Fan et al. (2006a) points (a factor of ∼ 3) are highly uncertain (see text for details).

QSOs in our sample appear to have smaller than expected proximity regions. We have performed a model-independent check on our estimate of $\Gamma^{\rm bg}$ by computing the median flux as a function of luminosity-scaled distance for QSOs of different luminosities. Although the median flux is noisy, the observed profiles are generally consistent with our maximum likelihood estimate of $\Gamma^{\rm bg}$. The faintest QSOs show somewhat more absorption in the proximity region than expected. This may indicate that the sphere of influence around faint QSOs is disproportionately small, possibly due to a lower escape fraction of ionizing photons. On the other hand, the greater than expected decrease in transmitted flux may be due to peculiar velocities in the absorbing gas, which will tend to increase the amount of absorption caused by high-optical depth absorbers.

Our estimate of $\Gamma^{\rm bg}$ is consistent with no evolution from the proximity effect measurement of Scott et al. (2000) at $1.7 < z < 3.8$. Their value, when adjusted for cosmology, is in turn consistent with measurements at $z \sim 3$ based on the mean opacity of the Lyα forest (Bolton et al. 2005), and on the estimated combined contribution to $\Gamma^{\rm bg}$ from star-forming galaxies (Shapley et al. 2006) and QSOs Hunt et al. (2004). Our value for $\Gamma^{\rm bg}$ is consistent with, though somewhat higher than, estimates at $z > 4$ based on transmitted flux in the Lyα forest (McDonald & Miralda-Escudé 2001; Fan et al. 2006a). Those measurements, however, were made assuming cosmological parameters significantly different from the ones used here, and the corrections to $\Gamma^{\rm bg}$ are large and uncertain. Alternatively, accounting for any increased absorption due to peculiar velocities may lower out estimate of $\Gamma^{\rm bg}$.

The largest uncertainty in this work is our assumption about the underlying distribution of optical depths. We have used a lognormal τ distribution, which has been shown to produce the observed flux probability distribution function in high-resolution data (Becker et al. 2006a). It is not entirely clear, however, that a similar distribution should hold well enough for moderate-resolution data that the distribution of optical depths, and hence transmitted fluxes, can be accurately predicted in the proximity regions. In order to investigate possible systematic errors related to resolution, we have repeated our analysis using ESI data for all of our objects. The results are comparable to those found when we include the HIRES spectra. We have also estimated the sizes of individual proximity regions for HIRES objects before and after smoothing to ESI resolution. For the two HIRES objects in this sample, as well as others from Becker et al. (2006a), we find no clear dependence of $R_{\rm eq}$ on resolution. This is not entirely surprising, given the similarity of the expected flux PDFs for HIRES and ESI. Further modeling should be done, however, to account for resolution, as well as other effects including peculiar velocities and the local density profiles around QSOs. We therefore present this study as a demonstration that reasonable values for $\Gamma^{\rm bg}$ can be obtained using the proximity effect at large redshifts. Future measurements from the proximity effect, the opacity of the Lyα forest, and a deep counts of star-forming galaxies and QSOs should lead to a consensus on the ionization state of the $z > 4$ IGM.

We are grateful to George Djorgovski for providing some of the ESI spectra analyzed here, as well as to Sandra Castro and Milan Bogosavljevic for reducing those data.

Chapter 6

Epilogue

We have used a variety of means to explore the ionization state of the high-redshift IGM. Our results suggest a slowly varying H I ionization rate out to $z \sim 6.2$, with no evidence of a late reionization. A number of issue are worth pursuing further, however, and we offer some suggestions here.

The usefulness of O I as a tracer of neutral gas depends on the extent to which the IGM has been enriched with heavy elements. In order to resolve whether the non-detection of O I towards $z > 6$ quasars with Gunn-Peterson troughs indicates an ionized IGM, it must be established whether there are metals present in high-ionization states that we would not have seen in O I. Recent work suggests that the density of C IV remains constant out to $z \sim 6$ (Simcoe 2006), which would lend support to our finding that the IGM at $z \sim 6$ is highly ionized. Further deep near-IR spectra, at high enough resolution to suppress skylines, will be necessary to conduct a thorough census of metals at this epoch. However, if near-IR sky surveys can identify quasars at $z > 6.5$, then a “forest” of low-ionization metal lines may yet be discovered at higher redshifts.

Equally interesting is the nature of the excess O I systems towards SDSS J1148+5251. If these systems are associated with galaxies, then they give us a unique opportunity to study star formation and chemical enrichment at $z > 6$. The challenge will be to identify the galaxies themselves. Even a non-detection in deep imaging and/or spectroscopy would be interesting, as it might suggest a population below the detection limit of current efforts aimed at measuring the galaxy luminosity function at $z \sim 6$. Of course, we would also like to better quantify how rare these O I systems are. Searching a larger number of lower-redshift sightlines may reveal other case of unusually high number densities. Since publishing our first O I paper, however, we have discovered additional $z \sim 6$ systems along sightlines that were not included in that survey. There may, therefore, be a genuine increase in the number density of O I systems at high redshift. Observing additional $z > 6$ quasars at high resolution would be helpful, provided sky surveys uncover more suitably bright targets. Unfortunately, without major improvements in the throughput of echelle spectrographs, current facilities may not be capable of pursuing fainter targets than the ones we have already observed.

As we noted, our conclusions regarding the distribution of optical depths are sensitive to the quasar continuum levels. These are notoriously difficult to determine objectively, particularly if the continua must be fit one echelle order at a time. High-resolution spectra of even a small number of $z > 4$ gamma ray bursts, whose spectra are simple power-laws, would help determine how often transmission peaks reach the continuum in the high-redshift Lyα forest. Alternatively, accurately flux-calibrated echelle spectra would at least allow quasar continua to be drawn over longer wavelength intervals. In either case, establishing the correct transmitted flux distribution would tighten constraints on IGM models considerably, offering greater leverage with which to measure the ionization state and temperature-density relation of the high-redshift IGM.

We have presented a new method for measuring the UV background using the proximity effect at high redshift. For this work, we assumed a lognormal distribution of Lyα optical depths, but the technique can be generalized to any IGM model, particularly if simulations are used to calibrate the results. By decreasing the optical depth of structures that would otherwise produce saturated absorption, the enhanced photoionization near a quasar effectively extends the dynamic range of the transmitted flux distribution to probe the conditions of the gas. A successful model of the IGM should, therefore, reproduce both the distribution of observed fluxes in the general Lyα forest and the change in flux that occurs in quasar proximity regions. At $z > 6$, where the forest disappears, the proximity effect may ultimately be the best means of measuring the UV background, providing a clearer picture of the ionization of the IGM by galaxies and quasars in the early Universe.

Bibliography

Abel, T., Anninos, P., Zhang, Y., & Norman, M. L. 1997, New Astronomy, 2, 181

Adelberger, K. L., Steidel, C. C., Shapley, A. E., & Pettini, M. 2003, ApJ, 584, 45

Aguirre, A., Schaye, J., Kim, T.-S., Theuns, T., Rauch, M., & Sargent, W. L. W. 2004, ApJ, 602, 38

Alcock, C. & Paczynski, B. 1979, Nature, 281, 358

Aracil, B., Petitjean, P., Smette, A., Surdej, J., Mücket, J. P., & Cristiani, S. 2002, A&A, 391, 1

Bajtlik, S., Duncan, R. C., & Ostriker, J. P. 1988, ApJ, 327, 570

Barth, A. J., Martini, P., Nelson, C. H., & Ho, L. C. 2003, ApJ, 594, L95

Bechtold, J. 1994, ApJS, 91, 1

Bechtold, J., Crotts, A. P. S., Duncan, R. C., & Fang, Y. 1994, ApJ, 437, L83

Bechtold, J. & Yee, H. K. C. 1995, AJ, 110, 1984

Becker, G. D., Rauch, M., & Sargent, W. L. W. 2006a, ApJ, submitted

Becker, G. D., Sargent, W. L. W., Rauch, M., & Simcoe, R. A. 2006b, ApJ, 640, 69

Becker, R. H., Fan, X., White, R. L., Strauss, M. A., Narayanan, V. K., Lupton, R. H., Gunn, J. E., Annis, J., Bahcall, N. A., Brinkmann, J., Connolly, A. J., Csabai, I., Czarapata, P. C., Doi, M., Heckman, T. M., Hennessy, G. S., Ivezić, Ž., Knapp, G. R., Lamb, D. Q., McKay, T. A., Munn, J. A., Nash, T., Nichol, R., Pier, J. R., Richards, G. T., Schneider, D. P., Stoughton, C., Szalay, A. S., Thakar, A. R., & York, D. G. 2001, AJ, 122, 2850

Bi, H. & Davidsen, A. F. 1997, ApJ, 479, 523

Bi, H., Ge, J., & Fang, L.-Z. 1995, ApJ, 452, 90

Bi, H. G., Boerner, G., & Chu, Y. 1992, A&A, 266, 1

Boksenberg, A., Sargent, W. L. W., & Rauch, M. 2003, astro-ph/0307557

Bolton, J., Meiksin, A., & White, M. 2004, MNRAS, 348, L43

Bolton, J. S., Haehnelt, M. G., Viel, M., & Springel, V. 2005, MNRAS, 357, 1178

Bond, J. R. & Wadsley, J. W. 1997, in Structure and Evolution of the Intergalactic Medium from QSO Absorption Line System, ed. P. Petitjean & S. Charlot (Paris: Editions Frontieres), 143

Bouwens, R. J., Illingworth, G. D., Blakeslee, J. P., & Franx, M. 2005, astro-ph/0509641

Carilli, C. L., Gnedin, N., Furlanetto, S., & Owen, F. 2004, New Astronomy Review, 48, 1053

Carswell, R. F., Webb, J. K., Baldwin, J. A., & Atwood, B. 1987, ApJ, 319, 709

Carswell, R. F., Whelan, J. A. J., Smith, M. G., Boksenberg, A., & Tytler, D. 1982, MNRAS, 198, 91

Cen, R., Gnedin, N. Y., & Ostriker, J. P. 1993, ApJ, 417, 387

Chieffi, A. & Limongi, M. 2004, ApJ, 608, 405

Choudhury, T. R., Srianand, R., & Padmanabhan, T. 2001, ApJ, 559, 29

Churchill, C. W., Mellon, R. R., Charlton, J. C., & Vogt, S. S. 2003, ApJ, 593, 203

Churchill, C. W., Rigby, J. R., Charlton, J. C., & Vogt, S. S. 1999, ApJS, 120, 51

Coles, P. & Jones, B. 1991, MNRAS, 248, 1

Cooke, A. J., Espey, B., & Carswell, R. F. 1997, MNRAS, 284, 552

Cristiani, S., D'Odorico, S., Fontana, A., Giallongo, E., & Savaglio, S. 1995, MNRAS, 273, 1016

Croft, R. A. C., Weinberg, D. H., Katz, N., & Hernquist, L. 1998, ApJ, 495, 44

Crotts, A. P. S. & Fang, Y. 1998, ApJ, 502, 16

Davé, R., Hernquist, L., Katz, N., & Weinberg, D. H. 1999, ApJ, 511, 521

Desjacques, V. & Nusser, A. 2005, MNRAS, 361, 1257

Dinshaw, N., Impey, C. D., Foltz, C. B., Weymann, R. J., & Chaffee, F. H. 1994, ApJ, 437, L87

Djorgovski, S. G., Castro, S., Stern, D., & Mahabal, A. A. 2001, ApJ, 560, L5

D'Odorico, V., Cristiani, S., D'Odorico, S., Fontana, A., Giallongo, E., & Shaver, P. 1998, A&A, 339, 678

D'Odorico, V., Petitjean, P., & Cristiani, S. 2002, A&A, 390, 13

Dove, J. B. & Shull, J. M. 1994, ApJ, 423, 196

Ellison, S. L., Ibata, R., Pettini, M., Lewis, G. F., Aracil, B., Petitjean, P., & Srianand, R. 2004, A&A, 414, 79

Fan, X., Hennawi, J. F., Richards, G. T., Strauss, M. A., Schneider, D. P., Donley, J. L., Young, J. E., Annis, J., Lin, H., Lampeitl, H., Lupton, R. H., Gunn, J. E., Knapp, G. R., Brandt, W. N., Anderson, S., Bahcall, N. A., Brinkmann, J., Brunner, R. J., Fukugita, M., Szalay, A. S., Szokoly, G. P., & York, D. G. 2004, AJ, 128, 515

Fan, X., Narayanan, V. K., Lupton, R. H., Strauss, M. A., Knapp, G. R., Becker, R. H., White, R. L., Pentericci, L., Leggett, S. K., Haiman, Z., Gunn, J. E., Ivezić, Ž., Schneider, D. P., Anderson, S. F., Brinkmann, J., Bahcall, N. A., Connolly, A. J., Csabai, I., Doi, M., Fukugita, M., Geballe, T., Grebel, E. K., Harbeck, D., Hennessy, G., Lamb, D. Q., Miknaitis, G., Munn, J. A., Nichol, R., Okamura, S., Pier, J. R., Prada, F., Richards, G. T., Szalay, A., & York, D. G. 2001, AJ, 122, 2833

Fan, X., Narayanan, V. K., Strauss, M. A., White, R. L., Becker, R. H., Pentericci, L., & Rix, H.-W. 2002, AJ, 123, 1247

Fan, X., Strauss, M. A., Becker, R. H., White, R. L., Gunn, J. E., Knapp, G. R., Richards, G. T., Schneider, D. P., Brinkmann, J., & Fukugita, M. 2006a, AJ, 132, 117

Fan, X., Strauss, M. A., Richards, G. T., Hennawi, J. F., Becker, R. H., White, R. L., Diamond-Stanic, A. M., Donley, J. L., Jiang, L., Kim, J. S., Vestergaard, M., Young, J. E., Gunn, J. E., Lupton, R. H., Knapp, G. R., Schneider, D. P., Brandt, W. N., Bahcall, N. A., Barentine, J. C., Brinkmann, J., Brewington, H. J., Fukugita, M., Harvanek, M., Kleinman, S. J., Krzesinski, J., Long, D., Neilsen, Jr., E. H., Nitta, A., Snedden, S. A., & Voges, W. 2006b, AJ, 131, 1203

Fan, X., Strauss, M. A., Schneider, D. P., Becker, R. H., White, R. L., Haiman, Z., Gregg, M., Pentericci, L., Grebel, E. K., Narayanan, V. K., Loh, Y.-S., Richards, G. T., Gunn, J. E., Lupton, R. H., Knapp, G. R., Ivezić, Ž., Brandt, W. N., Collinge, M., Hao, L., Harbeck, D., Prada, F., Schaye, J., Strateva, I., Zakamska, N., Anderson, S., Brinkmann, J., Bahcall, N. A., Lamb, D. Q., Okamura, S., Szalay, A., & York, D. G. 2003, AJ, 125, 1649

Fang, Y., Duncan, R. C., Crotts, A. P. S., & Bechtold, J. 1996, ApJ, 462, 77

Fernandez-Soto, A., Barcons, X., Carballo, R., & Webb, J. K. 1995, MNRAS, 277, 235

Foltz, C. B., Weymann, R. J., Roser, H.-J., & Chaffee, Jr., F. H. 1984, ApJ, 281, L1

Fukugita, M., Nakamura, O., Schneider, D. P., Doi, M., & Kashikawa, N. 2004, ApJ, 603, L65

Furlanetto, S. R., Hernquist, L., & Zaldarriaga, M. 2004a, MNRAS, 354, 695

Furlanetto, S. R. & Loeb, A. 2003, ApJ, 588, 18

Furlanetto, S. R. & Oh, S. P. 2005, MNRAS, 363, 1031

Furlanetto, S. R., Zaldarriaga, M., & Hernquist, L. 2004b, ApJ, 613, 16

—. 2006, MNRAS, 365, 1012

Gaztañaga, E. & Croft, R. A. C. 1999, MNRAS, 309, 885

Giallongo, E., Cristiani, S., D'Odorico, S., Fontana, A., & Savaglio, S. 1996, ApJ, 466, 46

Giallongo, E., Cristiani, S., Fontana, A., & Trevese, D. 1993, ApJ, 416, 137

Gott, J. R. I., Jurić, M., Schlegel, D., Hoyle, F., Vogeley, M., Tegmark, M., Bahcall, N., & Brinkmann, J. 2005, ApJ, 624, 463

Grevesse, N. & Sauval, A. J. 1998, Space Science Reviews, 85, 161

Guilloteau, S., Omont, A., Cox, P., McMahon, R. G., & Petitjean, P. 1999, A&A, 349, 363

Gunn, J. E. & Peterson, B. A. 1965, ApJ, 142, 1633

Haiman, Z. & Cen, R. 2005, ApJ, 623, 627

Heger, A. & Woosley, S. E. 2002, ApJ, 567, 532

Horne, K. 1986, PASP, 98, 609

Hu, E. M. & Cowie, L. L. 2006, Nature, 440, 1145

Hu, E. M., Cowie, L. L., Capak, P., McMahon, R. G., Hayashino, T., & Komiyama, Y. 2004, AJ, 127, 563

Hu, E. M., Kim, T.-S., Cowie, L. L., Songaila, A., & Rauch, M. 1995, AJ, 110, 1526

Hui, L. & Gnedin, N. Y. 1997, MNRAS, 292, 27

Hui, L. & Haiman, Z. 2003, ApJ, 596, 9

Hui, L., Stebbins, A., & Burles, S. 1999, ApJ, 511, L5

Hunt, M. P., Steidel, C. C., Adelberger, K. L., & Shapley, A. E. 2004, ApJ, 605, 625

Kassim, N. E., Lazio, T. J. W., Ray, P. S., Crane, P. C., Hicks, B. C., Stewart, K. P., Cohen, A. S., & Lane, W. M. 2004, Planet. Space Sci., 52, 1343

Kelson, D. D. 2003, PASP, 115, 688

Kirkman, D., Tytler, D., Suzuki, N., Melis, C., Hollywood, S., James, K., So, G., Lubin, D., Jena, T., Norman, M. L., & Paschos, P. 2005, MNRAS, 360, 1373

Kulkarni, V. P. & Fall, S. M. 1993, ApJ, 413, L63

Lidz, A., Heitmann, K., Hui, L., Habib, S., Rauch, M., & Sargent, W. L. W. 2006a, ApJ, 638, 27

Lidz, A., Hui, L., Crotts, A. P. S., & Zaldarriaga, M. 2003, astro-ph/0309204

Lidz, A., Oh, S. P., & Furlanetto, S. R. 2006b, ApJ, 639, L47

Lin, W.-C. & Norman, M. 2002, astro-ph/0211177

Liske, J., Webb, J. K., Williger, G. M., Fernández-Soto, A., & Carswell, R. F. 2000, MNRAS, 311, 657

Liske, J. & Williger, G. M. 2001, MNRAS, 328, 653

Liu, J., Bi, H., Feng, L.-L., & Fang, L.-Z. 2006, ApJ, 645, L1

Lopez, S., Hagen, H.-J., & Reimers, D. 2000, A&A, 357, 37

Lopez, S., Reimers, D., Rauch, M., Sargent, W. L. W., & Smette, A. 1999, ApJ, 513, 598

Lu, L., Sargent, W. L. W., Womble, D. S., & Takada-Hidai, M. 1996, ApJ, 472, 509

Lu, L., Wolfe, A. M., & Turnshek, D. A. 1991, ApJ, 367, 19

Malhotra, S. & Rhoads, J. 2006, astro-ph/0511196

Malhotra, S. & Rhoads, J. E. 2004, ApJ, 617, L5

McDonald, P. & Miralda-Escudé, J. 1999, ApJ, 518, 24

—. 2001, ApJ, 549, L11

McDonald, P., Miralda-Escudé, J., Rauch, M., Sargent, W. L. W., Barlow, T. A., & Cen, R. 2001, ApJ, 562, 52

McDonald, P., Miralda-Escudé, J., Rauch, M., Sargent, W. L. W., Barlow, T. A., Cen, R., & Ostriker, J. P. 2000, ApJ, 543, 1

McGill, C. 1990, MNRAS, 242, 544

McIntosh, D. H., Rix, H.-W., Rieke, M. J., & Foltz, C. B. 1999, ApJ, 517, L73

Mesinger, A. & Haiman, Z. 2004, ApJ, 611, L69

Mesinger, A., Haiman, Z., & Cen, R. 2004, ApJ, 613, 23

Miralda-Escudé, J., Cen, R., Ostriker, J. P., & Rauch, M. 1996, ApJ, 471, 582

Miralda-Escudé, J., Haehnelt, M., & Rees, M. J. 2000, ApJ, 530, 1

Murdoch, H. S., Hunstead, R. W., Pettini, M., & Blades, J. C. 1986, ApJ, 309, 19

Oh, S. P. 2002, MNRAS, 336, 1021

Oh, S. P. & Furlanetto, S. R. 2005, ApJ, 620, L9

Osterbrock, D. E. 1989, Astrophysics of gaseous nebulae and active galactic nuclei (Mill Valley, CA: University Science Books)

Patnaik, A. R., Browne, I. W. A., Walsh, D., Chaffee, F. H., & Foltz, C. B. 1992, MNRAS, 259, 1P

Pentericci, L., Fan, X., Rix, H.-W., Strauss, M. A., Narayanan, V. K., Richards, G. T., Schneider, D. P., Krolik, J., Heckman, T., Brinkmann, J., Lamb, D. Q., & Szokoly, G. P. 2002, AJ, 123, 2151

Penton, S. V., Stocke, J. T., & Shull, J. M. 2000, ApJS, 130, 121

Péroux, C., McMahon, R. G., Storrie-Lombardi, L. J., & Irwin, M. J. 2003, MNRAS, 346, 1103

Petitjean, P., Aracil, B., Srianand, R., & Ibata, R. 2000, A&A, 359, 457

Petitjean, P., Surdej, J., Smette, A., Shaver, P., Muecket, J., & Remy, M. 1998, A&A, 334, L45

Petry, C. E., Impey, C. D., & Foltz, C. B. 1998, ApJ, 494, 60

Press, W. H., Teukolsky, S. A., Vetterling, W. T., & Flannery, B. P. 1992, Numerical recipes in C. The art of scientific computing, 2nd edn. (Cambridge: University Press)

Prochaska, J. X., Gawiser, E., Wolfe, A. M., Cooke, J., & Gelino, D. 2003, ApJS, 147, 227

Prochaska, J. X., Herbert-Fort, S., & Wolfe, A. M. 2005, ApJ, 635, 123

Prochaska, J. X., Wolfe, A. M., Tytler, D., Burles, S., Cooke, J., Gawiser, E., Kirkman, D., O'Meara, J. M., & Storrie-Lombardi, L. 2001, ApJS, 137, 21

Qian, Y.-Z. & Wasserburg, G. J. 2005a, ApJ, 635, 845

—. 2005b, ApJ, 623, 17

Rabinowitz, D., Baltay, C., Emmet, W., Hurteau, T., Snyder, J., Andrews, P., Ellman, N., Morgan, N., Bauer, A., Musser, J., Gebhard, M., Adams, G., Djorgovski, G., Mahabal, A., Graham, M., Bogosavljevic, M., Williams, R., Brucato, R., & Thicksten, R. 2003, BAAS, 203, 38.12

Rao, S. M., Turnshek, D. A., & Nestor, D. B. 2006, ApJ, 636, 610

Rauch, M., Miralda-Escude, J., Sargent, W. L. W., Barlow, T. A., Weinberg, D. H., Hernquist, L., Katz, N., Cen, R., & Ostriker, J. P. 1997, ApJ, 489, 7

Rauch, M., Sargent, W. L. W., & Barlow, T. A. 1999, ApJ, 515, 500

—. 2001a, ApJ, 554, 823

Rauch, M., Sargent, W. L. W., Barlow, T. A., & Carswell, R. F. 2001b, ApJ, 562, 76

Rauch, M., Sargent, W. L. W., Barlow, T. A., & Simcoe, R. A. 2002, ApJ, 576, 45

Richards, G. T., Fan, X., Schneider, D. P., Vanden Berk, D. E., Strauss, M. A., York, D. G., Anderson, Jr., J. E., Anderson, S. F., Annis, J., Bahcall, N. A., Bernardi, M., Briggs, J. W., Brinkmann, J., Brunner, R., Burles, S., Carey, L., Castander, F. J., Connolly, A. J., Crocker, J. H., Csabai, I., Doi, M., Finkbeiner, D., Friedman, S. D., Frieman, J. A., Fukugita, M., Gunn, J. E., Hindsley, R. B., Ivezić, Ž., Kent, S., Knapp, G. R., Lamb, D. Q., Leger, R. F., Long, D. C., Loveday, J., Lupton, R. H., McKay, T. A., Meiksin, A., Merrelli, A., Munn, J. A., Newberg, H. J., Newcomb, M., Nichol, R. C., Owen, R., Pier, J. R., Pope, A., Richmond, M. W., Rockosi, C. M., Schlegel, D. J., Siegmund, W. A., Smee, S., Snir, Y., Stoughton, C., Stubbs, C., SubbaRao, M., Szalay, A. S., Szokoly, G. P., Tremonti, C., Uomoto, A., Waddell, P., Yanny, B., & Zheng, W. 2001, AJ, 121, 2308

Richards, G. T., Vanden Berk, D. E., Reichard, T. A., Hall, P. B., Schneider, D. P., SubbaRao, M., Thakar, A. R., & York, D. G. 2002, AJ, 124, 1

Rollinde, E., Petitjean, P., Pichon, C., Colombi, S., Aracil, B., D'Odorico, V., & Haehnelt, M. G. 2003, MNRAS, 341, 1279

Santos, M. R. 2004, MNRAS, 349, 1137

Sargent, W. L. W., Young, P. J., Boksenberg, A., & Tytler, D. 1980, ApJS, 42, 41

Savage, B. D. & Sembach, K. R. 1996, ARA&A, 34, 279

Savaglio, S., Cristiani, S., D'Odorico, S., Fontana, A., Giallongo, E., & Molaro, P. 1997, A&A, 318, 347

Schaerer, D. 2002, A&A, 382, 28

Schaye, J., Theuns, T., Rauch, M., Efstathiou, G., & Sargent, W. L. W. 2000, MNRAS, 318, 817

Scheuer, P. A. G. 1965, Nature, 207, 963

Schneider, D. P., Fan, X., Strauss, M. A., Gunn, J. E., Richards, G. T., Knapp, G. R., Lupton, R. H., Saxe, D. H., Anderson, Jr., J. E., Bahcall, N. A., Brinkmann, J., Brunner, R., Csabai, I., Fukugita, M., Hennessy, G. S., Hindsley, R. B., Ivezić, Ž., Nichol, R. C., Pier, J. R., & York, D. G. 2000, AJ, 120, 2183

Scott, J., Bechtold, J., Dobrzycki, A., & Kulkarni, V. P. 2000, ApJS, 130, 67

Scott, J., Bechtold, J., Morita, M., Dobrzycki, A., & Kulkarni, V. P. 2002, ApJ, 571, 665

Shapley, A. E., Steidel, C. C., Pettini, M., Adelberger, K. L., & Erb, D. K. 2006, astro-ph/0606635

Sheinis, A. I., Bolte, M., Epps, H. W., Kibrick, R. I., Miller, J. S., Radovan, M. V., Bigelow, B. C., & Sutin, B. M. 2002, PASP, 114, 851

Shklovskii, I. S. 1965, Soviet Astronomy, 8, 638

Simcoe, R. A. 2006, astro-ph/0605710

Simcoe, R. A., Sargent, W. L. W., Rauch, M., & Becker, G. 2006, ApJ, 637, 648

Smette, A., Robertson, J. G., Shaver, P. A., Reimers, D., Wisotzki, L., & Koehler, T. 1995, A&AS, 113, 199

Smette, A., Surdej, J., Shaver, P. A., Foltz, C. B., Chaffee, F. H., Weymann, R. J., Williams, R. E., & Magain, P. 1992, ApJ, 389, 39

Songaila, A. 1998, AJ, 115, 2184

—. 2004, AJ, 127, 2598

—. 2005, AJ, 130, 1996

Songaila, A. & Cowie, L. L. 2002, AJ, 123, 2183

Spergel, D. N., Bean, R., Dore', O., Nolta, M. R., Bennett, C. L., Hinshaw, G., Jarosik, N., Komatsu, E., Page, L., Peiris, H. V., Verde, L., Barnes, C., Halpern, M., Hill, R. S., Kogut, A., Limon, M., Meyer, S. S., Odegard, N., Tucker, G. S., Weiland, J. L., Wollack, E., & Wright, E. L. 2006, astro-ph/0603449

Spergel, D. N., Verde, L., Peiris, H. V., Komatsu, E., Nolta, M. R., Bennett, C. L., Halpern, M., Hinshaw, G., Jarosik, N., Kogut, A., Limon, M., Meyer, S. S., Page, L., Tucker, G. S., Weiland, J. L., Wollack, E., & Wright, E. L. 2003, ApJS, 148, 175

Springel, V., Frenk, C. S., & White, S. D. M. 2006, Nature, 440, 1137

Steidel, C. C., Pettini, M., & Adelberger, K. L. 2001, ApJ, 546, 665

Steidel, C. C. & Sargent, W. L. W. 1992, ApJS, 80, 1

Stern, D., Yost, S. A., Eckart, M. E., Harrison, F. A., Helfand, D. J., Djorgovski, S. G., Malhotra, S., & Rhoads, J. E. 2005, ApJ, 619, 12

Storrie-Lombardi, L. J., McMahon, R. G., Irwin, M. J., & Hazard, C. 1996, ApJ, 468, 121

Storrie-Lombardi, L. J. & Wolfe, A. M. 2000, ApJ, 543, 552

Sunyaev, R. A. 1969, Astrophys. Lett., 3, 33

Suzuki, N. 2006, ApJS, 163, 110

Telfer, R. C., Zheng, W., Kriss, G. A., & Davidsen, A. F. 2002, ApJ, 565, 773

Theuns, T., Schaye, J., Zaroubi, S., Kim, T.-S., Tzanavaris, P., & Carswell, B. 2002, ApJ, 567, L103

Tozzi, P., Madau, P., Meiksin, A., & Rees, M. J. 2000, ApJ, 528, 597

Tytler, D. 1987, ApJ, 321, 49

Tytler, D. & Fan, X.-M. 1992, ApJS, 79, 1

Tzanavaris, P. & Carswell, R. F. 2003, MNRAS, 340, 937

Umeda, H. & Nomoto, K. 2002, ApJ, 565, 385

Vanden Berk, D. E., Richards, G. T., Bauer, A., Strauss, M. A., Schneider, D. P., Heckman, T. M., York, D. G., Hall, P. B., Fan, X., Knapp, G. R., Anderson, S. F., Annis, J., Bahcall, N. A., Bernardi, M., Briggs, J. W., Brinkmann, J., Brunner, R., Burles, S., Carey, L., Castander, F. J., Connolly, A. J., Crocker, J. H., Csabai, I., Doi, M., Finkbeiner, D., Friedman, S., Frieman, J. A., Fukugita, M., Gunn, J. E., Hennessy, G. S., Ivezić, Ž., Kent, S., Kunszt, P. Z., Lamb, D. Q., Leger, R. F., Long, D. C., Loveday, J., Lupton, R. H., Meiksin, A., Merelli, A., Munn, J. A., Newberg, H. J., Newcomb, M., Nichol, R. C., Owen, R., Pier, J. R., Pope, A., Rockosi, C. M., Schlegel, D. J., Siegmund, W. A., Smee, S., Snir, Y., Stoughton, C., Stubbs, C., SubbaRao, M., Szalay, A. S., Szokoly, G. P., Tremonti, C., Uomoto, A., Waddell, P., Yanny, B., & Zheng, W. 2001, AJ, 122, 549

Viel, M., Haehnelt, M. G., & Lewis, A. 2006, MNRAS, 370, L51

Viel, M., Matarrese, S., Mo, H. J., Haehnelt, M. G., & Theuns, T. 2002, MNRAS, 329, 848

Vogt, S. S., Allen, S. L., Bigelow, B. C., Bresee, L., Brown, B., Cantrall, T., Conrad, A., Couture, M., Delaney, C., Epps, H. W., Hilyard, D., Hilyard, D. F., Horn, E., Jern, N., Kanto, D., Keane, M. J., Kibrick, R. I., Lewis, J. W., Osborne, J., Pardeilhan, G. H., Pfister, T., Ricketts, T., Robinson, L. B., Stover, R. J., Tucker, D., Ward, J., & Wei, M. Z. 1994, in Proc. SPIE Instrumentation in Astronomy VIII, ed. D. L. Crawford & E. R. Craine, Vol. 2198, 362

Weinberg, D. H., Miralda-Escude, J., Hernquist, L., & Katz, N. 1997, ApJ, 490, 564

Weymann, R. J., Carswell, R. F., & Smith, M. G. 1981, ARA&A, 19, 41

Weymann, R. J. & Foltz, C. B. 1983, ApJ, 272, L1

White, R. L., Becker, R. H., Fan, X., & Strauss, M. A. 2003, AJ, 126, 1

—. 2005, AJ, 129, 2102

Williger, G. M., Baldwin, J. A., Carswell, R. F., Cooke, A. J., Hazard, C., Irwin, M. J., McMahon, R. G., & Storrie-Lombardi, L. J. 1994, ApJ, 428, 574

Williger, G. M., Smette, A., Hazard, C., Baldwin, J. A., & McMahon, R. G. 2000, ApJ, 532, 77

Woosley, S. E. & Weaver, T. A. 1995, ApJS, 101, 181

Wyithe, J. S. B. & Loeb, A. 2004a, Nature, 432, 194

—. 2004b, Nature, 427, 815

—. 2005a, ApJ, 625, 1

Wyithe, S. & Loeb, A. 2005b, astro-ph/0508604

Yan, H. & Windhorst, R. A. 2004, ApJ, 612, L93

York, D. G., Adelman, J., Anderson, Jr., J. E., Anderson, S. F., Annis, J., Bahcall, N. A., Bakken, J. A., Barkhouser, R., Bastian, S., Berman, E., Boroski, W. N., Bracker, S., Briegel, C., Briggs, J. W., Brinkmann, J., Brunner, R., Burles, S., Carey, L., Carr, M. A., Castander, F. J., Chen, B., Colestock, P. L., Connolly, A. J., Crocker, J. H., Csabai, I., Czarapata, P. C., Davis, J. E., Doi, M., Dombeck, T., Eisenstein, D., Ellman, N., Elms, B. R., Evans, M. L., Fan, X., Federwitz, G. R., Fiscelli, L., Friedman, S., Frieman, J. A., Fukugita, M., Gillespie, B., Gunn, J. E., Gurbani, V. K., de Haas, E., Haldeman, M., Harris, F. H., Hayes, J., Heckman, T. M., Hennessy, G. S., Hindsley, R. B., Holm, S., Holmgren, D. J., Huang, C.-h., Hull, C., Husby, D., Ichikawa, S.-I., Ichikawa, T., Ivezić, Ž., Kent, S., Kim, R. S. J., Kinney, E., Klaene, M., Kleinman, A. N., Kleinman, S., Knapp, G. R., Korienek, J., Kron, R. G., Kunszt, P. Z., Lamb,

D. Q., Lee, B., Leger, R. F., Limmongkol, S., Lindenmeyer, C., Long, D. C., Loomis, C., Loveday, J., Lucinio, R., Lupton, R. H., MacKinnon, B., Mannery, E. J., Mantsch, P. M., Margon, B., McGehee, P., McKay, T. A., Meiksin, A., Merelli, A., Monet, D. G., Munn, J. A., Narayanan, V. K., Nash, T., Neilsen, E., Neswold, R., Newberg, H. J., Nichol, R. C., Nicinski, T., Nonino, M., Okada, N., Okamura, S., Ostriker, J. P., Owen, R., Pauls, A. G., Peoples, J., Peterson, R. L., Petravick, D., Pier, J. R., Pope, A., Pordes, R., Prosapio, A., Rechenmacher, R., Quinn, T. R., Richards, G. T., Richmond, M. W., Rivetta, C. H., Rockosi, C. M., Ruthmansdorfer, K., Sandford, D., Schlegel, D. J., Schneider, D. P., Sekiguchi, M., Sergey, G., Shimasaku, K., Siegmund, W. A., Smee, S., Smith, J. A., Snedden, S., Stone, R., Stoughton, C., Strauss, M. A., Stubbs, C., SubbaRao, M., Szalay, A. S., Szapudi, I., Szokoly, G. P., Thakar, A. R., Tremonti, C., Tucker, D. L., Uomoto, A., Vanden Berk, D., Vogeley, M. S., Waddell, P., Wang, S.-i., Watanabe, M., Weinberg, D. H., Yanny, B., & Yasuda, N. 2000, AJ, 120, 1579

Young, P. A., Impey, C. D., & Foltz, C. B. 2001, ApJ, 549, 76